
Article:
Wahlund, J.-E. orcid.org/0000-0002-2107-5859, Bergman, J.E.S., Åhlén, L. et al. (158 more authors) (2025) The Radio & Plasma Wave Investigation (RPWI) for the JUpiter ICy moons Explorer (JUICE). Space Science Reviews, 221. 1. ISSN 0038-6308

https://doi.org/10.1007/s11214-024-01110-0

Space Science Reviews (2025) 221:1
https://doi.org/10.1007/s11214-024-01110-0

The Radio & Plasma Wave Investigation (RPWI) for the JUpiter ICy moons Explorer (JUICE)

J.-E. Wahlund · J.E.S. Bergman · L. Åhlén · W. Puccio · B. Cecconi · Y. Kasaba et al. ***[full author details at the end of the article]***

Received: 4 October 2023 / Accepted: 10 September 2024

Abstract
The Radio & Plasma Wave Investigation (RPWI) onboard the ESA JUpiter ICy moons Explorer (JUICE) is described in detail. The RPWI provides an elaborate set of state-of-the-art electromagnetic fields and cold plasma instrumentation, including active sounding with the mutual impedance and Langmuir probe sweep techniques, where several different types of sensors will sample the thermal plasma properties, including electron and ion densities, electron temperature, plasma drift speed, the near DC electric fields, and electric and magnetic signals from various types of phenomena, e.g., radio and plasma waves, electrostatic acceleration structures, induction fields etc. A full wave vector, waveform, polarization, and Poynting flux determination will be achieved. RPWI will enable characterization of the Jovian radio emissions (including goniopolarimetry) up to 45 MHz, has the capability to carry out passive radio sounding of the ionospheric densities of icy moons and employ passive sub-surface radar measurements of the icy crust of these moons. RPWI can also detect micrometeorite impacts, estimate dust charging, monitor the spacecraft potential as well as the integrated EUV flux. The sensors consist of four 10 cm diameter Langmuir probes each mounted on the tip of 3 m long booms, a triaxial search coil magnetometer and a triaxial radio antenna system both mounted on the 10.6 m long MAG boom, each with radiation resistant pre-amplifiers near the sensors. There are three receiver boards, two Digital Processing Units (DPU) and two Low Voltage Power Supply (LVPS) boards in a box within a radiation vault at the centre of the JUICE spacecraft. Together, the integrated RPWI system can carry out an ambitious planetary science investigation in and around the Galilean icy moons and the Jovian space environment. Some of the most important science objectives and instrument capabilities are described here. RPWI focuses, apart from cold plasma studies, on the understanding of how, through electrodynamic and electromagnetic coupling, the momentum and energy transfer occur with the icy Galilean moons, their surfaces and salty conductive sub-surface oceans. The RPWI instrument is planned to be operational during most of the JUICE mission, during the cruise phase, in the Jovian magnetosphere, during the icy moon flybys, and in particular Ganymede orbit, and may deliver data from the near surface during the final crash orbit.

Keywords JUICE · RPWI · Ganymede · Europa · Callisto · Jupiter

Published online: 16 December 2024

1 Introduction & Overall Description

The Radio & Plasma Wave Investigation (RPWI) consist of three groups of instruments that provides a highly versatile set of electric and magnetic measurements associated with ambitious observational capabilities (cf. Sect. 2), with the aim to address numerous science objectives regarding foremost the Jovian space environment but also the interior and surface of the large icy moons and their interactions with the space environment (cf. Sect. 3). The instrument is described in Sect. 4 and its related software/firmware in Sect. 5. The RPWI planned operations and data products are described in Sects. 6 and 7. This paper give substantial information for using the RPWI data for science, although it is recommended that a contact is made with the PI and/or expert Co-I's institutes to understand possible caveats/features detected during flight. The RPWI instrumentation is a result of a long-term plan to investigate the Jovian system, which started at the beginning of the new millennium (Blomberg et al. 2005; Wahlund et al. 2005a,b; Cecconi et al. 2010). ESA selected the RPWI instrument package for implementation in 2013.

1.1 The RPWI Basic Performance

The RPWI instrument measures the electromagnetic fields and cold plasma (Table 1). From these parameters it is possible to derive several other physical characteristics within and around the icy moons and within the magnetospheres of Ganymede and Jupiter (cf. Sect. 2). We partially include some of the latest in-flight raw data in this paper, although the in-flight calibration results are not ready at the time of the manuscript submission, that show how the in-flight data and performance are compliant with predictions.

1.2 The RPWI Team

The RPWI team consists of hardware and software/firmware providers, ground segment and data archiving experts, and of course scientists skilled in analysis of data products, but also theory modellers that can put the observations into context, and public outreach specialists. The team has 50 science Co-Investigators, engineers, and associated scientists from 9 countries, as well as ESA and Airbus Defence and Space (ADS) supporting engineers/managers and independent companies used for manufacturing of instrument parts. A summary of design developers is given in Table 2.

Table 1 Basic measurement output from RPWI. Samples per second (sps)

RPWI Measured Quantity	Range	Max time resolution
Electric field vector, $\delta\mathbf{E}$(f)	DC – 45 MHz	763 sps continuously
		Snapshots or frequency sweeps every 30 s
Magnetic field vector, $\delta\mathbf{B}$(f)	0.1 Hz – 20 kHz	763 sps continuously
		49ksps snapshots every 30 s
Cold plasma parameters	Ne: 10^{-4} – 10^{5} cm^{-3}	Nominally every 30 s, or 763 sps
	Ni: 1 – 10^{5} cm^{-3}	Nominally every 30 s, or 763 sps
	Te: 0.01 – 20 eV	Nominally every 30 s
	Vdi: 0.1 – 200 km/s	Nominally every 30 s, or 763 sps
Density fluctuations (δn/n)	DC – 10 kHz	49 ksps snapshots every 30 s
Spacecraft potential (Usc)	$\pm$80 V	763 sps continuously

Table 2 Providers involved in the development of RPWI design of hardware, software, calibration, theory support, archiving, operations, and public outreach. In addition, several companies have been involved in the manufacturing of the flight hardware (not included in this list)

Institute/institution/company	Roles	Country
Swedish Institute of Space Physics (IRF), Uppsala	PI institute	
Royal Institute of Technology (KTH), Stockholm	CoI institute	
Uppsala University, Uppsala	H/W developer	
Linköping University, Linköping	H/W developer	
Laboratoire d'Etudes Spatiales et Instrumentation en Astrophysique (LESIA), Paris	Co-PI institute	
Laboratoire de Physique des Plasmas (LPP), Paris	CoI institute	
Laboratoire de Physique et Chimie de l'Environnement et de l'Espace (LPC2E), Orléans	CoI institute	
Institut de Recherche en Astrophysique et Planétologie (IRAP), Toulouse	CoI institute	
Université de Versailles Saint-Quentin (LATMOS), Paris	CoI institute	
Office National d'Etudes at de Reserches Aérospatiales (ONERA), Toulouse	CoI institute	
Laboratoire Plasma et Conversion d'Energie (LAPLACE), Toulouse	CoI institute	
Space Research Centre of the Polish Academy of Sciences (SRC-PAS), Warsaw	Co-PI institute	
Astronika, LTD., Warsaw	H/W developer	
Institute of Atmospheric Physics (IAP), Prague	Co-PI institute	
Astronomical Institute (AsI), Prague	CoI institute	
Imperial College London, Department of Physics	Co-PI institute	
University of Sheffield, Space instrumentation group, Sheffield	CoI institute	
Space Research Institute (SRI), Austrian Academy of Sciences, Graz	CoI institute	
University of Cologne, Cologne	CoI institute	
Dublin Institute for Advanced Studies (DIAS), Dublin	CoI institute	
Tohoku University, Sendai	Co-PI institute	
Tokyo University of Science, Tokyo	CoI institute	
Kyoto University, Kyoto	CoI institute	
Kanazawa University, Kanazawa	CoI institute	
Nagoya University, Nagoya	CoI institute	
Meisei Electric Co., Ltd., Isesaki	H/W developer	

1.3 RPWI Novel Capabilities

The RPWI focuses, apart from cold plasma studies, on the understanding of how, through electrodynamic and electromagnetic coupling, the momentum and energy transfer occur in the surrounding space environments and with the icy Galilean moons. In Ganymede orbit, in-situ measurements by RPWI of the electric coupling between any sub-surface ocean, the ionosphere and magnetosphere will provide constraints on the physical characteristics of this ocean.

The RPWI instrument has outstanding new or enhanced capabilities that have not been available to previous missions to the outer planets and that are crucial to answer several fundamental science objectives of the JUICE project. Among them are:

- The capability of four Langmuir probes to measure the vector electric field from near DC to 1.5 MHz, as well as plasma convection ($\mathbf{E} \times \mathbf{B}$ drift, ion flux), thereby allowing the investigation of plasma electrodynamics in the Jovian system and how the sub-surface oceans and ionospheres of the icy Galilean moons couple electrodynamically to the highly variable Jovian magnetosphere.
- The capability of a tri-axial search coil, together with the Langmuir probes' ability to measure the vector magnetic and electric fields simultaneously below 20 kHz to identify Alfvén and Whistler waves, filamentary currents, flux ropes and electrostatic structures involved in the momentum and energy transfer between different particle populations involved in the interaction between the Jovian magnetosphere and the conducting ionised exospheres around the icy Galilean moons.
- The significantly enhanced capability of using both passive and semi-active methods to infer the cold ($<$100 eV) plasma characteristics. The implemented methods also include the capability to infer the bulk ion drift speed.
- The capability of three electric dipole antennae to fully characterize radio emissions at Jupiter (Carozzi et al. 2001; Bergman and Carozzi 2007), making it possible to determine source locations and polarization of radio emissions from the aurora, Jupiter's magnetosphere, Ganymede's magnetosphere, and characterize their variability with time and response to external forcing.
- The capability to monitor electrically charged dust properties and identify any dust-plasma interactions. This type of study on open versus closed magnetic field lines at Ganymede, and the direct observations of the electric field vector accelerating these particles toward the surface, will give insight to surface sputtering processes and their effect on the icy surfaces and atmospheres.
- The capability to directly measure in-situ the thermal and dusty plasma and electrodynamics within the partly ionized gas exhaust of water-rich plumes above active surface regions on the icy moons.
- The capability to use the Jovian radio emissions to carry out occultation of the icy moon ionospheres and passive sub-surface radar (PSSR) of the icy crust of the moons. The former gives the altitude density profiles from the radio cut-offs. The latter potentially determines the conductivity and the subsurface features of the icy crust.

1.4 RPWI Instrument Parts & Science Experiments

The top-level block diagram (Fig. 1) illustrates the overall RPWI baseline configuration. The RPWI instrument consists of 10 sensors, grouped in three sets, and connected to 3 receivers. The RPWI instrument have four Langmuir probes (LP-PWI) for thermal plasma and electric field measurements, three axes search coil magnetometer (SCM) for magnetic

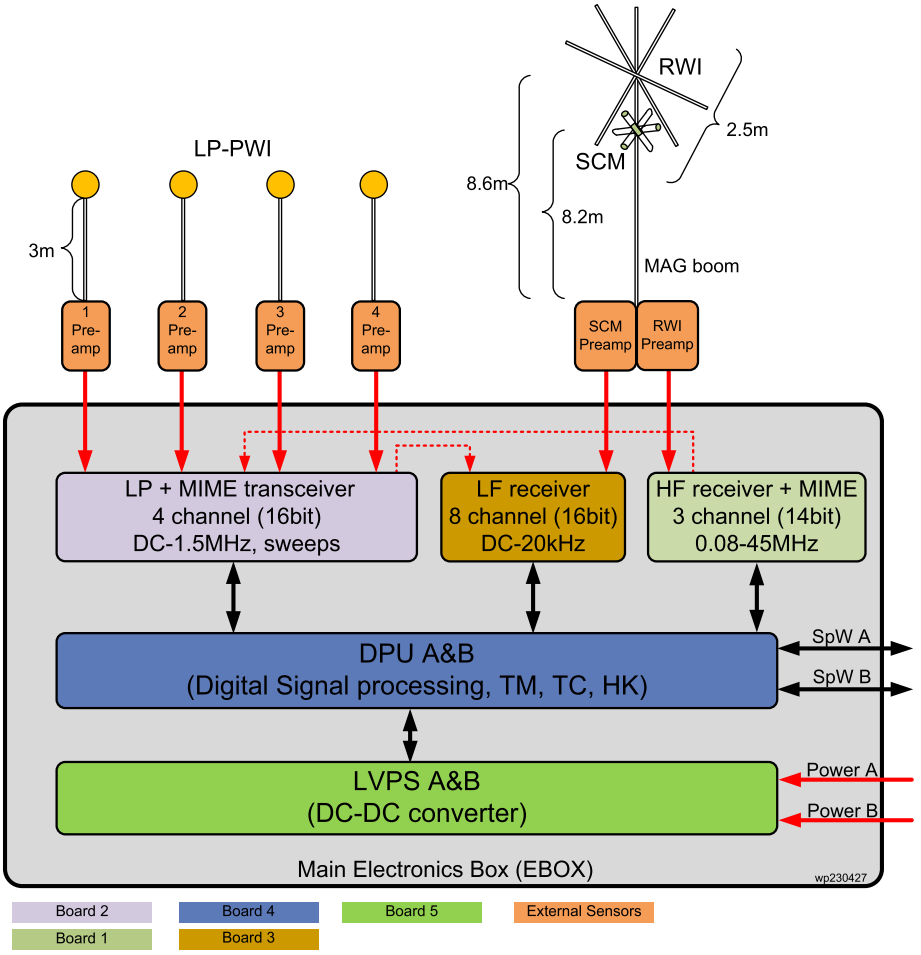

Fig. 1 JUICE/RPWI instrument configuration

fields measurement, and three dipole antennas (RWI) for radio measurements. The RPWI system is built up around a main Electronics Box (EBOX), which houses dual redundant Low Voltage Power Supplies (LVPS A&B) and Digital Processing Units (DPU A&B) that serve the Langmuir Probe & Mutual IMpedance Experiment (LP-MIME) transceiver, the Low Frequency (LF) receiver, and the High Frequency (HF) receiver. The LVPS and DPU units are hardwired to each other, such that LVPS A is connected to DPU A and LVPS B is connected to DPU B. A backplane inside the EBOX distributes the analogue and digital signals, the different voltages, and a clock signal, which is generated by dual redundant crystal oscillators on the LVPS board. The LP-MIME transceiver is connected internally to the LF receiver, for which it provides single-ended and differential signals from the Langmuir probes. It also contains driver circuits for the MIME transceiver. The MIME drivers can furthermore be synchronized to the mixer frequency of the HF receiver, used for mutual impedance measurements at high frequencies. External harnesses connect the LP-PWI, SCM, and RWI sensors to the circuit boards inside the EBOX.

The EBOX is housed in the payload vault in the centre of spacecraft. Each LP-PWI sensor has a 3 m long deployable boom with the 10 cm diameter Langmuir probe at its end and with the preamplifier mounted separately near the boom root. The SCM is mounted on the MAG boom (Arce and Rodriguez 2019) and has its preamplifiers mounted inside the mechanical structure, which supports the sensors. The RWI antenna subsystem, also mounted on the MAG boom, consist of six BeCu antenna rods with the length of 1.25 m and the diameter of 1 cm, attached on a cubic mechanical chassis which stores the preamplifier electronics inside. Those six antenna rods form three dipole antennas with the tip-to-tip length of 2.5 m.

The RPWI instrumentation can alternatively be divided into experiments (GANDALF, MIME, SAMWISE, JENRAGE) for easier reference to science topics. GANDALF (GANymede plasma Density And Low-Frequency wave experiment) uses the four Langmuir probes and the LP receiver part. MIME makes use of both the four Langmuir probes and the RWI antenna together with the LP-MIME transceiver. SAMWISE (Search-coil and Analyzer Module for Waves and Instabilities Science Experiment) makes use of both the four Langmuir probes and the SCM together with the LF receiver. Finally, JENRAGE (Jupiter ENvironment Radio Astronomy and Ganymede Exploration) uses the RWI antenna and the HF receiver.

1.5 RPWI Theory Support

The RPWI investigation will benefit from tight integration of instrument data analysis with state-of-the-art numerical modelling of atmospheres and space environment (example shown in Fig. 2). The RPWI institutes access together the capability of simulating all environments relevant for RPWI investigations. The models generate parameters including plasma densities and composition, temperatures, and velocities as well as electric and magnetic fields on 3-D grids as a function of time. Simulations are driven by external input parameters describing solar wind and radiation forcing as well as neutral atmosphere properties, but otherwise respond to basic physical laws. RPWI furthermore provide simulation tools to calculate radio wave propagation (direction, polarization, intensity) through the relevant environments.

By solving well known coupled non-linear equations of continuity, energy and momentum for plasma and neutral gas distributions as well as Maxwell's equations for electric and magnetic fields, our models complement the observations, which considerably widen the scientific gain. As an example, models of Ganymede's ionosphere are driven in part by the assumed neutral atmosphere and by the magnetospheric environment. By driving such models using observed boundary conditions (magnetic fields, plasma energy distributions, etc.) and matching simulations to observed quantities at locations along the spacecraft trajectory, the local (along-track) observations are placed into a global context (e.g., Galand et al. 2025). Furthermore, the models provide key information on the origins of observed behaviour, of the physical drivers behind it, thereby enabling a considerably deeper scientific analysis of behaviour than otherwise possible. Radio emission modelling (Louis et al. 2019a) will allow us to predict the occurrence of the observable radio emissions as well as their polarization, and thereby will be used to optimize the instrument observation planning (Cecconi et al. 2021).

The in-flight calibration of the RPWI observations will take advantage of the Spacecraft Plasma Interaction Software (SPIS) simulations (cf. Sect. 2.7, Sarrailh et al. 2015) to predict the behaviour of the plasma close to the spacecraft. RPWI plan to use full 3D spacecraft rolls in the Solar Wind together with SPIS model predictions to account for the asymmetric spacecraft electric potential pattern when measuring near DC electric fields.

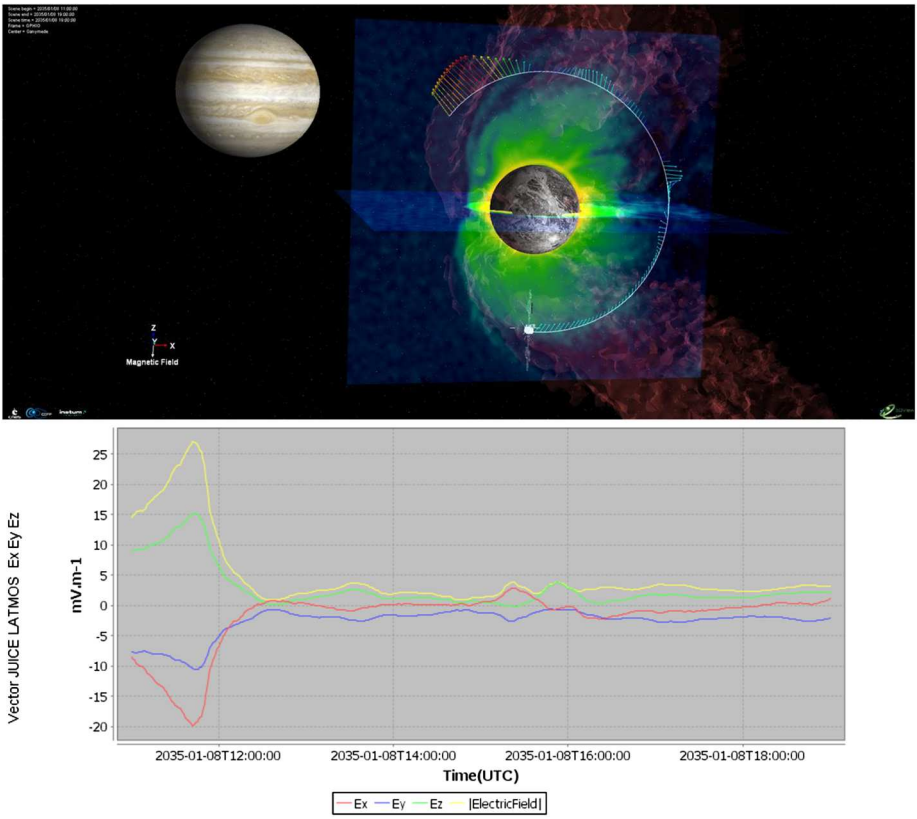

Fig. 2 Three-dimensional view of Ganymede's global magnetosphere (top panel, from a hybrid model), viewed from the upstream flank side with Jupiter in the background. The model simulates the interaction between Ganymede's and Jupiter's magnetospheres (Modolo et al. 2018). Plasma populations from Ganymede's ionosphere and Jupiter's magnetosphere are included and the model computes the time-dependent electromagnetic field. Colour code indicates the electron density for different plane cuts where yellow indicates high density and blue low density. The white line shows a segment of a JUICE orbit trajectory. Vectors along the JUICE s/c indicates the simulated electric field values while the reddish structure represents the Alfvén wings emphasized with an iso-surface based on a velocity value. The bottom panel gives the electric field components along the JUICE trajectory. It illustrates the RPWI team capability of simulating RPWI observations by tracing physical parameters along the spacecraft trajectories (e.g., using the 3dview tool, http://3dview.cdpp.eu, Génot et al. 2018, of the French plasma physics datacentre CDPP)

2 The RPWI Experiment Capabilities

2.1 Design Drivers

The RPWI science objectives are numerous, and the most important ones are listed in Sect. 3. To fulfil them the RPWI instrument needs to measure the complete electric and magnetic field vectors, as well as the thermal plasma properties in a wide frequency range and/or with high temporal/spatial resolution. Special ElectroMagnetic Compatibility (EMC) mitigating methods have also been implemented throughout the instrument and spacecraft development to make the RPWI measurements as free as possible from potential electromagnetic noise sources. The full assessment of remaining EMC interferences has been investigated

extensively during on-ground tests and will be further verified in-flight. For instance, the RPWI near DC electric field measurements will be compared to the $\mathbf{v}_{\text{ion, PEP}} \times \mathbf{B}_{\text{J-MAG}}$. Here, the Particle Environment Package (PEP) estimates the ion moments to derive the ion speed, and the JUICE MAGnetometer (J-MAG) estimates the near DC magnetic field components. Special periods of in-flight calibrations, involving full spacecraft rolls in reasonably known conditions, in the solar wind and near Earth, will characterize the influence of the electric and plasma environment around a large asymmetric spacecraft on the RPWI measurements before JUICE enters the Jovian system. The RPWI measurements and data analysis will also be supported by SPIS spacecraft environment interaction simulations (See Sect. 2.7, Sarrailh et al. 2015).

A special focus was put on the low frequency measurements below approximately 100 Hz, which the Galileo/PWS did not cover well. For instance, RPWI provides the first ever measurements of the near DC electric field vector, as well as providing detailed cold plasma measurements with several techniques (including active methods like mutual impedance and Langmuir probe sweep techniques), in the Jovian system. RPWI also provides very sensitive monitoring of the medium-frequency magnetic and electric fields. This approach also provides a very good complement to the PEP hot plasma (Barabash et al. 2025, this collection) and J-MAG magnetic field (Dougherty et al. 2025, this collection) measurements, and a focus on the planetary objectives related to the interaction of the icy moons with the magnetosphere of Jupiter. The characteristic spatial and temporal scales encountered by JUICE and the RPWI parameter coverage is displayed in Fig. 3. RPWI will be able to do science investigations in all parts of the Jovian system traversed by JUICE, and the intention is to carry out basically continuous measurements starting 3 months before Jupiter Orbit Insertion (JOI).

Another design driver has been to make omnidirectional or full vector measurements, and not be dependent on spacecraft attitude or field-of-view (FoV). This makes operation planning much easier, being only dependent on restrictions in telemetry (TM) volume and power from the spacecraft. Nevertheless, particularly the low frequency and near DC measurements by the LP sensors will depend on their exposition to ram flow and sunlight. At times, one or more LPs will be in shadow or wake. To minimize the scientific impact of this, we have designed the operation modes, so the use of probes is often redundant and/or used for different purposes.

The radio measurement design drivers are the remote sensing capabilities of the Jovian system in the spectral range up to 45 MHz. Three axis electric field antenna measurements constitute a 'goniopolarimetric' (Cecconi 2013) system, i.e., with direction finding and polarization capabilities, enabling studies of the Jovian radio sources, which are widely distributed in the Jovian magnetosphere (Cecconi and Zarka 2005). Passive sounding of natural radio emissions will further enable ionospheric radio occultations of the icy moons and enable studies of the reflected signals from the surface and sub-surfaces of these moons. Passive sub-surface radar (PSSR) measurements are planned to sound the icy crusts of Galilean satellites by using the reflections of Jovian radio emissions (HOM/DAM). Here, there exist also the capability to sample the full waveform below a few MHz in a broad frequency window.

With these capabilities, RPWI will survey the harsh space environment around Jupiter, and its interaction with icy moons, as well as monitor these moons' surface and subsurface characteristics.

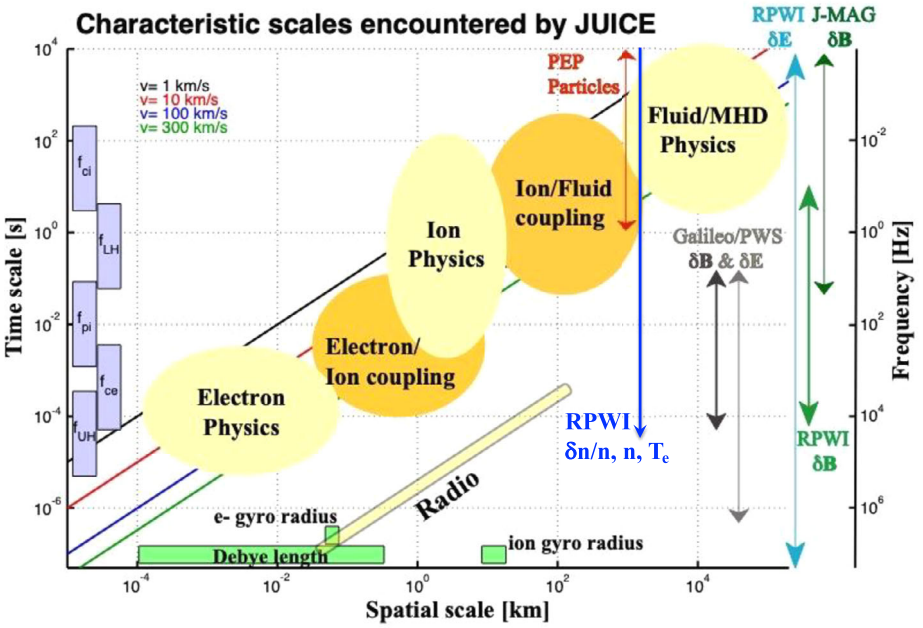

Fig. 3 The RPWI measurements will cover all expected spatial and temporal scales to be encountered by JUICE, except for magnetic variations below 0.1 Hz that will instead be covered by the J-MAG payload. The electric field and cold plasma parameters, at the lowest frequencies below about 100 Hz, have never been measured accurately before in the Jovian system. The radio waves are used for remote sensing and the spatial scale indicated refers here to their wavelengths, not to local scales in the plasma as the case is for other parameters to be measured by RPWI. See Sect. 3 for references on typical encountered plasma conditions. The following natural frequencies are ion cyclotron (f_{ci}), Lower Hybrid (f_{LH}), ion plasma (f_{pi}), electron cyclotron (f_{ce}), and the Upper Hybrid (f_{uh})

2.2 GANDALF

This experiment makes use of the LP-PWI sensors together with the LP-MIME receiver part of the electronics. The LP-PWI sensors sample electric voltages or currents, which is the basis of the inferred physical parameters. The probes can therefore be operated in two different modes: current sampling mode (used as Langmuir probes) for plasma diagnostics (e.g., N_e, N_i, T_e, V_{di}) or voltage sampling mode (used as electric field probes) for measurement of the electric field (**E**), where two of the primary tasks are to sample the near DC electric field vector and to diagnose plasma waves. The spacecraft potential (U_{SC}) is always measured independent of operational mode. The spacecraft potential can be used as an electron number density proxy down to very low densities (10^{-4} cm^{-3}), a method that has been conducted successfully by related instruments with booms of similar size in a variety of solar system environments including the Saturn magnetosphere (Morooka et al. 2009), the solar wind (Khotyaintsev et al. 2021; Mozer et al. 2022), and the coma of comet 67P (Johansson et al. 2021).

2.2.1 Electric Field Mode

When used as electric field probes, the electric field components are obtained from the measurements of the potential (voltage) difference between probe pairs, while feeding these

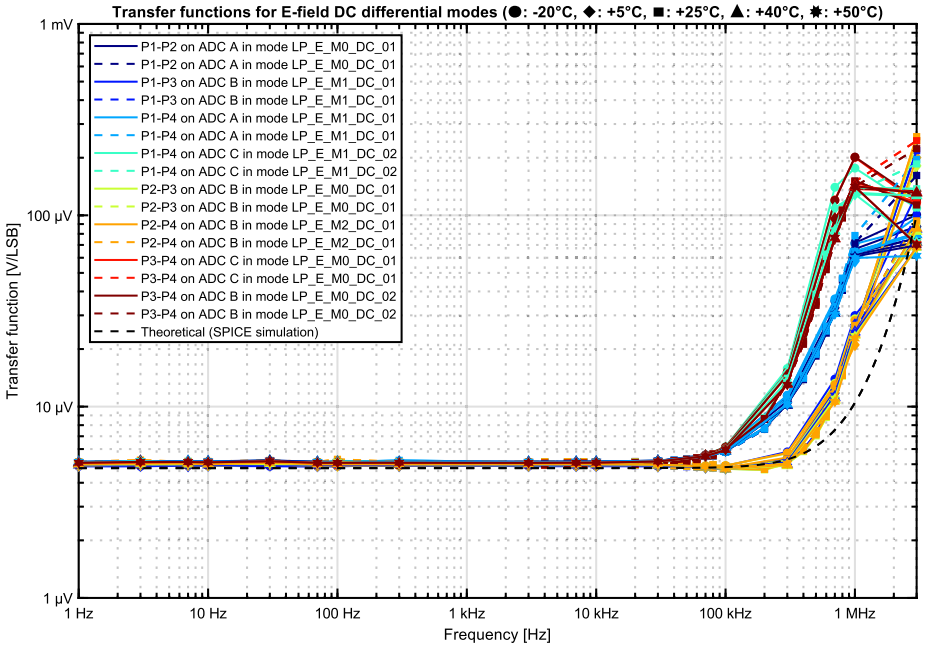

Fig. 4 PFM LP-MIME transfer functions for all electric field DC differential modes. Results from the on-ground calibration for different ADCs and temperatures

probes with a constant bias current. Most of the time, RPWI will sample a selection of three probe potential differences, and one single ended (for monitoring the spacecraft potential). The LP-PWI probes will therefore allow estimates of the full vector electric field from near DC up to 1.5 MHz. GANDALF will carry out continuous sampling at 763 samples per second (lowpass), and snapshots of various sample length (usually 16 ksamples) at higher frequencies (now set at 49 ksps or 694 ksps) to ensure relevant wave electric emissions are monitored. The snapshots are either time-tagged or triggered within a sequence cycle (usually every 30 s but can be longer). There also exists a spectrum sweep sampling mode up to 1.5 MHz. It is possible to use interferometer measurements between pair of probes to estimate the phase speed of electric field fluctuations.

Several processes affect in-flight measurement performance with Langmuir probes: photoelectrons (and secondary electrons) emitted from the spacecraft, differential charging of large insulating surfaces, asymmetric structures affecting the potential pattern around the S/C, and the plasma environment itself. It has therefore been important to make the exterior of the S/C and solar panels conducting (and electrically connected) to limit the disturbances and simplify their characterization. The near DC electric field, together with the J-MAG magnetic field measurements, will enable us to continuously give values of the $\mathbf{E} \times \mathbf{B}$ convection (i.e., wherever JUICE is traversing in the Jovian system).

The instrument itself is very accurate in DC E-field mode. The resolution is of the order of 5 µV/6.2 m (double probe minimum distance) ≈0.9 µV/m for DC (see Fig. 4) and better in AC (Fig. 5). The asymmetric spacecraft (with variable solar panel positions and plasma ram flow directions) itself will be the largest error source, and we can only determine this source during in-flight calibration with S/C roll manoeuvres in know plasma environments (e.g., solar wind conditions). However, a detailed EMC programme was run during the de-

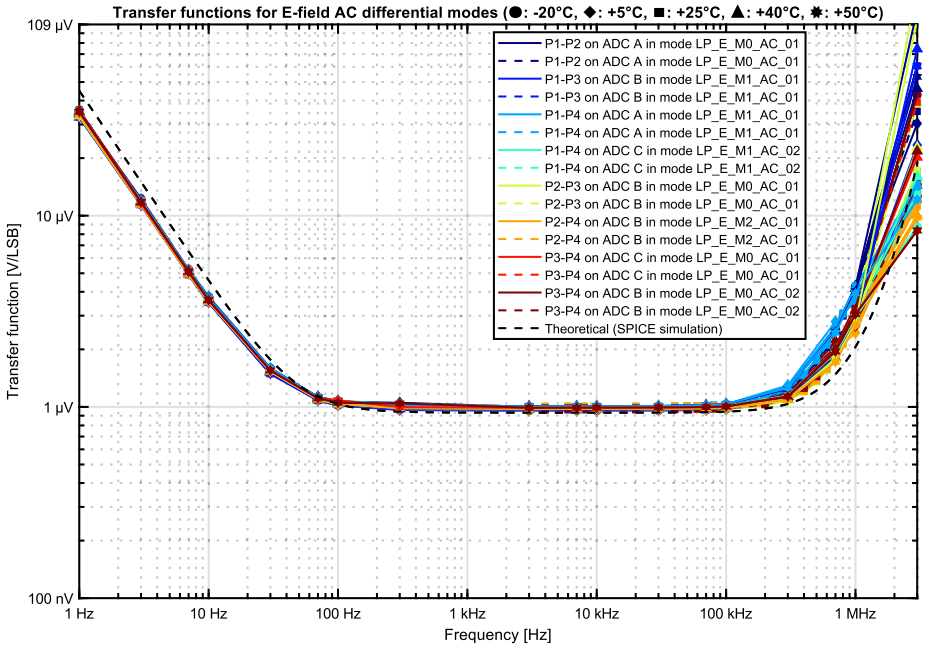

Fig. 5 PFM LP-MIME transfer functions for all electric field AC differential modes. Results from the on-ground calibration for different ADCs and temperatures

sign and implementation of the JUICE spacecraft, which made sure most of the surfaces were conductive, thus mitigating differential charging of the surface and resulting influence of the potential pattern around the spacecraft. Our experience with near DC electric field measurements on Rosetta and Solar Orbiter with shorter booms indicate that a rather accurate DC electric field is achievable. On JUICE, in-flight calibrations of the RPWI DC **E**-field with the $\mathbf{v} \times \mathbf{B}$ electric field are planned together with J-MAG and PEP in the solar wind. Likewise, full spacecraft rolls campaigns are planned (also together with J-MAG and PEP) to map in detail the potential disturbance of the S/C on the DC electric field measurements.

Another error source is the temperature stability of the preamplifiers and the receiver, which therefore will be continuously measured in-flight for potential electric field offset corrections for each probe. The temperature stability shown in Figs. 4 and 5 can in this regard be noted. Moreover, GANDALF will intermittently measure the electric field over a known internal resistor for stability calibration purposes, detecting any ageing of the instrument. SPIS simulation (Sarrailh et al. 2015) results will also help us understand the potential error sources and give better reduction of the sampled data around the spacecraft. Similar considerations have successfully been carried out on several space physics related spacecraft before (e.g., Cluster and Solar Orbiter). Examples of in-flight data in the solar wind near Earth show a good quality of the data (Figs. 6 and 7). We therefore believe that a true DC electric field vector measurement is possible with specified accuracy over a longer time. The reference to a "*near* DC" capability notifies the above-mentioned difficulties to achieve the true DC electric field vector at all times of the mission.

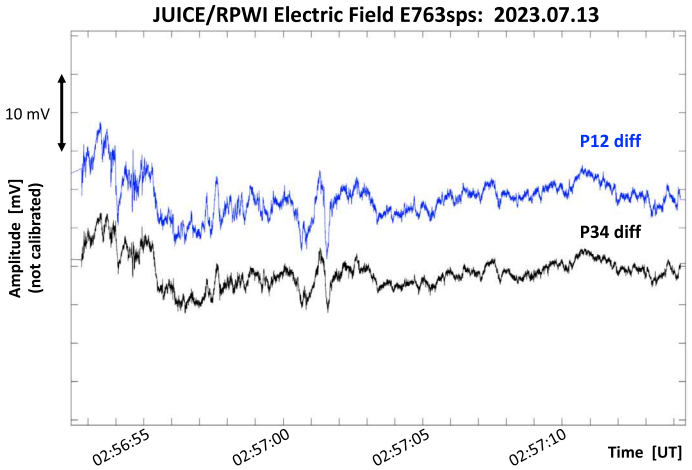

Fig. 6 In-flight electric waveforms in the solar wind near Earth sampled at 763 samples-per-second (low pass at 350 Hz). Voltage differentials between probe pairs 1 – 2 (blue) and 3 – 4 (black) are shown. The probe inter-distance is about 6.3 m and 9.6 m respectively. Probes 3 and 4 has the JUICE spacecraft in between, while P1-2 do not. The DC offset is not yet corrected for, so only the relative differences can be compared here. Even so, the almost exact match is promising for the RPWI capability to measure the near DC electric field. In-flight calibrations remain to be carried out

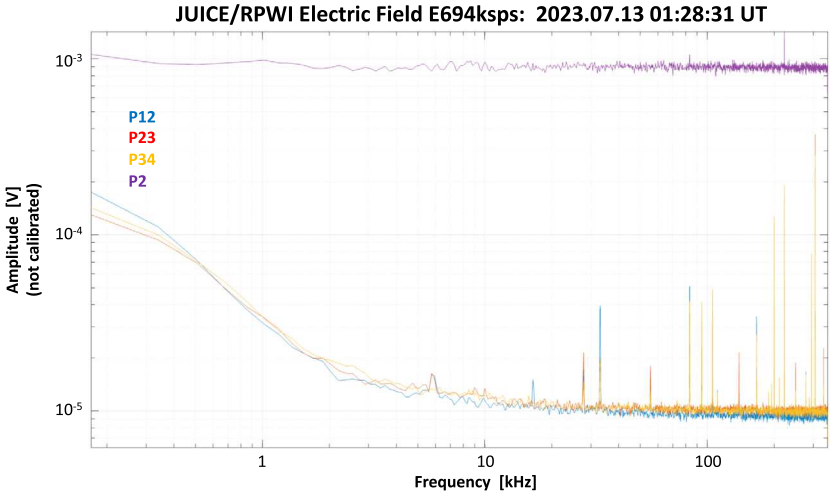

Fig. 7 In-flight AC electric field spectrum sampled at 694 ksps in the solar wind near Earth. The differential signals (P12, P23, P34) are very similar and indicates the noise floor. A nice correspondence between the power spectral densities versus frequency exist. Interference lines at the higher frequency end is partly due to the S/C power system but such lines appearing in the Langmuir probe data can easily be removed on board at a later stage. A single ended (P2) signal measures versus the S/C and is used for S/C potential estimations

2.2.2 Density Mode

When used as Langmuir probes, the probes are biased to a specific voltage (positive or negative) or stepped in bias voltage (a so-called Langmuir sweep, see an example in Fig. 8),

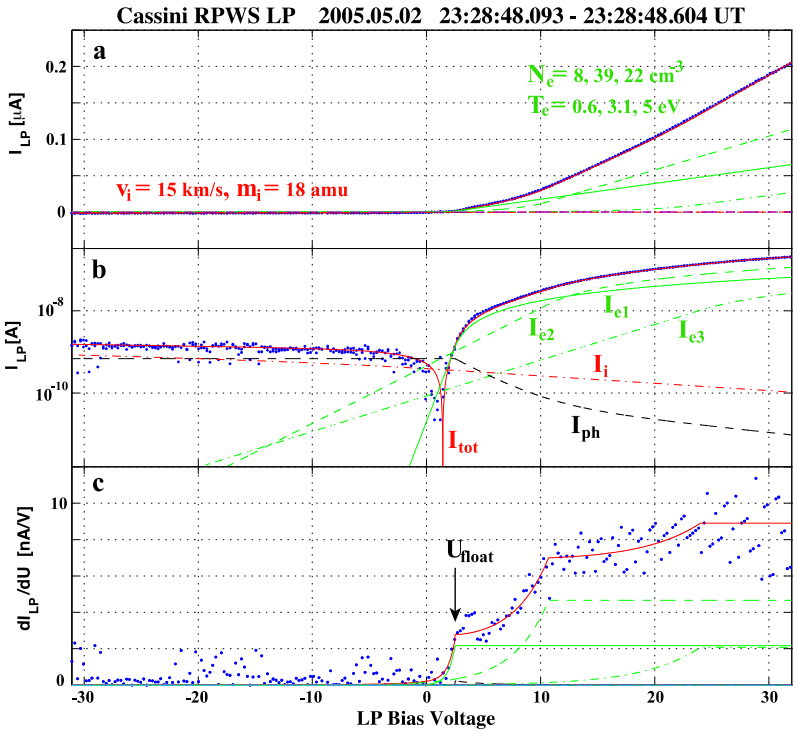

Fig. 8 Example of a Langmuir probe voltage sweep from the Cassini RPWS/LP in the magnetosphere of Saturn (Gustafsson and Wahlund 2010). Panel a, b and c are respectively linear, logarithmic and the derivative of the same data. Blue dots = sweep data, red line = total fitted current based on Sheath Limited (SL) theory, red dashed = ion current, various green lines = electron currents from spacecraft photoelectrons and ambient electrons, black dashed = photoelectron current from the probe

and the probe current is measured (Mott-Smith and Langmuir 1926). When the probe is biased negatively, the current is dominated by ions attracted to the probe and/or photoelectrons emitted from a sunlit probe. When the probe is positively biased, attracted electrons dominate the probe current. RPWI can operate the probes in the bias voltage range ±80 V, which allows for plasma measurements in a wide range of different plasma environments. The sweeps can be sampled at 3 mV resolution and with a rate of 3 ksps. RPWI has different sweep bias tables that can be used. During cruise we make use of 128 bias steps with 20 samples each (at 3 ksps). For instance, the bias voltage range of ±80 V and instrument sensitivity will be good enough to derive the bulk drift speed (V_{di}) directly from the sweep response (see Fig. 10) in most encountered regions. The bulk ion drift speed can be derived from the sweep characteristic for negative bias (ion sampling) and for a drifting Maxwellian ion distribution as (e.g., Whipple 1965; Fahleson et al. 1974; Holmberg et al. 2012):

$$I_i \approx q_i n_i A_{LP} \sqrt{V_{di}^2/16 + k_B T_i/2\pi m_i} \left(1 - \frac{U_{bias} + U_{float}}{W_i}\right). \quad (1)$$

where T_i, m_i, q_i and W_i is the temperature, mass, charge, and energy of the ions respectively, and A_{LP} is the surface area of the probe. Normally the ion thermal energy is $\ll$ ion kinetic ram energy, and the $k_B T_i/2\pi m_i$ term is neglected. This puts an upper constraint to the ion

temperature. Therefore, in most cases it represents the ram ion flux to the probe. Having the plasma density, gives the ion drift speed relative the spacecraft motion. For Jupiter's magnetosphere, RPWI will use PEP ion thermal energy estimates as input to the analysis.

The voltage-biased probes can be sampled continuously up to 763 sps, and in snapshots up to 49 ksps, allowing thermal plasma electron density and ion flux to be monitored at high rates. It also allows for performing a frequency spectrum of the density variations (δn/n) of plasma waves or structures. In addition, measurements from several probes can be combined (in current sampling mode) allowing for interferometric measurements to estimate the velocity of plasma structures. It is possible to discern the propagation direction and velocity in 3D of plasma inhomogeneities (e.g., LaBelle et al. 1986; Kintner et al. 1987; Holmgren and Kintner 1990; Wahlund et al. 1998, 2009; and references therein). Except for the need to have density inhomogeneities with enough amplitude in the plasma, the used probes should preferably not be in the wake of the spacecraft yet have a reasonable alignment with the plasma flow direction, and the speed need be slow enough to give a measurable time difference (0.1 – 1 ms), which gives a speed limit of about 10 – 100 km/s. Furthermore, some probes may operate at positive bias voltage, while others operate at negative bias potential simultaneously. This allows for directly comparing electron and ion inhomogeneities as well as detect regions with significant amounts of charged dust (e.g., in plumes, see Wahlund et al. 2009). Now, electric field (voltage, bias current) and number density (current, bias voltage) measurements cannot be made simultaneous with the same probe. Likewise, the electron density (positive voltage bias) and ion density (negative voltage bias) cannot be made simultaneous with the same probe. However, RPWI has four probes. We have therefore different operation modes that need be selected and planned for when to operate (cf. Sect. 6.3). Nominally the electric field components are measured with all four probes, and any density (δn/n) mode need be specially selected. However, RPWI always carry out Langmuir probe and MIME sweeps (takes about 3 s) each measurement cycle (usually 30 s long, see Table 18).

The accuracy of the Langmuir probes to measure the ambient electron population (electron sampling side, positive bias) is to a large degree dependent on the number of photoelectrons and secondaries emitted from the S/C, which in turn will be affected by the spacecraft potential and geometry of the spacecraft. The method works best for denser thermal plasma conditions and negative spacecraft potential where the photoelectrons escape radially away from the S/C and pose a much less of a problem (see top panel in Fig. 10).

The capability of the Langmuir probes to detect the ion (usually ram) currents in thin plasma depends largely on the LP-PWI preamplifier noise level, the leakage current level, the large size of probes (10 cm) and bias voltage range (e.g., $\pm$80 V). The photoelectron emission from the probes is relatively constant with time (variation on time durations of the solar intensity, days) and can be corrected for. An example of a JUICE RPWI Langmuir probe sweeps just after launch is shown in Fig. 9, where the noise level can be accounted for in an Operational Domain diagram (Fig. 10), where the expected encountered plasma domains can be superposed. The upcoming Earth flyby in August 2024 is expected to give an increased understanding for the potential limitations of the Langmuir probe sweeps carried out by the four probes.

The instrument leak currents of a few pA (see Table 3 and Fig. 11) were measured on the 4xFM and FS LP-PWI booms + Langmuir probe sensors before delivery to the spacecraft. The probe to inner shield is the important one for science measurements. The pre-amplifiers have lower or similar leak currents (for $\sim$TOhm resistance). The LP-MIME DC current receiver responses are shown in Fig. 11. These values can be compared to the Cassini LP noise limit of $\approx$100 pA (e.g., Wahlund et al. 2009).

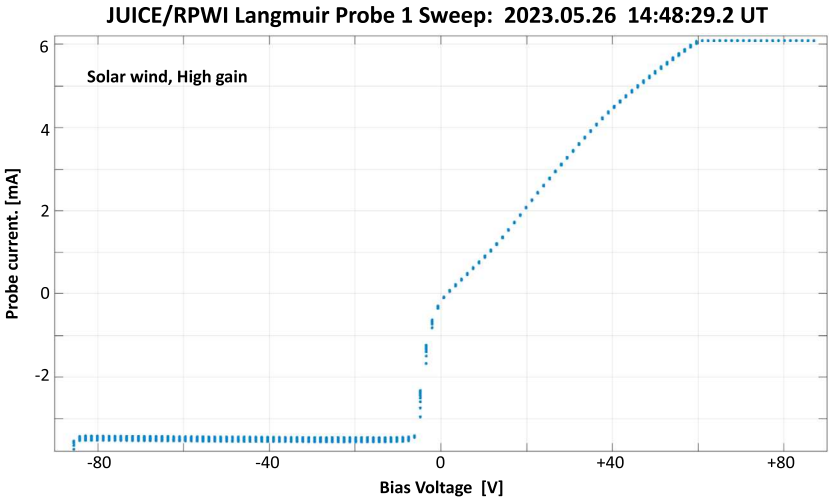

Fig. 9 An in-flight Langmuir probe sweep in the solar wind. Instrument saturation occurs at 6 μA for this high-gain sweep, which results in a flat response after +60 V. Twenty samples are sampled for each bias step to see the impedance response (which flattens out in time after about 3 ms). A sweep takes less than 2 seconds. In the solar wind the sweep is dominated by the photoelectrons emitted from the probe and the spacecraft. This sweep is uncalibrated. Further analysis will reveal if solar wind ion flux and electron temperature can be extracted. However, already from this sweep it is possible to infer a spacecraft surface potential of about +5 V, as the U-I-characteristic photo-electron exponential drop is shifted roughly −5 V compared to $U_{bias} = 0$ V and knowing $U = U_{float} + U_{bias}$

Although the frequency dependence of the transfer functions is not very dependent on the preamplifier and receiver temperatures (as seen in Fig. 11), the DC offset is. Therefore, RPWI employs regularly in-flight calibration sweeps over two know resistors to correct for this effect. The transfer functions for AC current measurements (Fig. 12 and 13) gives the sensitivity and phase stability for the δn/n measurements.

2.3 MIME

This RPWI/MIME experiment is the mutual impedance probe of JUICE. Mutual impedance probes (Storey et al. 1969) are electrical instruments designed to measure certain characteristic parameters of plasmas, such as electron density and temperature (Chasseriaux et al. 1972). The measurement method is based on the electrical coupling between a pair of electrical antennae (transmitting and receiving) and the plasma in which the antennae are immersed (Grard 1969). In practice, an oscillating electrical signal produced by a current generator at a given frequency is injected into the plasma to be diagnosed by a first, transmitting electrical antenna (monopolar or dipolar). Simultaneously, the electrical signal propagating through the plasma is measured by means of the electrical potential difference produced on the second, receiving antenna (generally dipolar) at the frequency of the transmission signal. The ratio between the receiving voltage and the transmitting current is called the mutual impedance. This operation, consisting of simultaneous transmission and reception at a given frequency, is repeated over several discrete frequencies, step by step, in a predefined frequency range of interest, selected within the range 3 kHz–3 MHz in the case of the RPWI/MIME experiment. The mutual impedance is then calculated successively for each

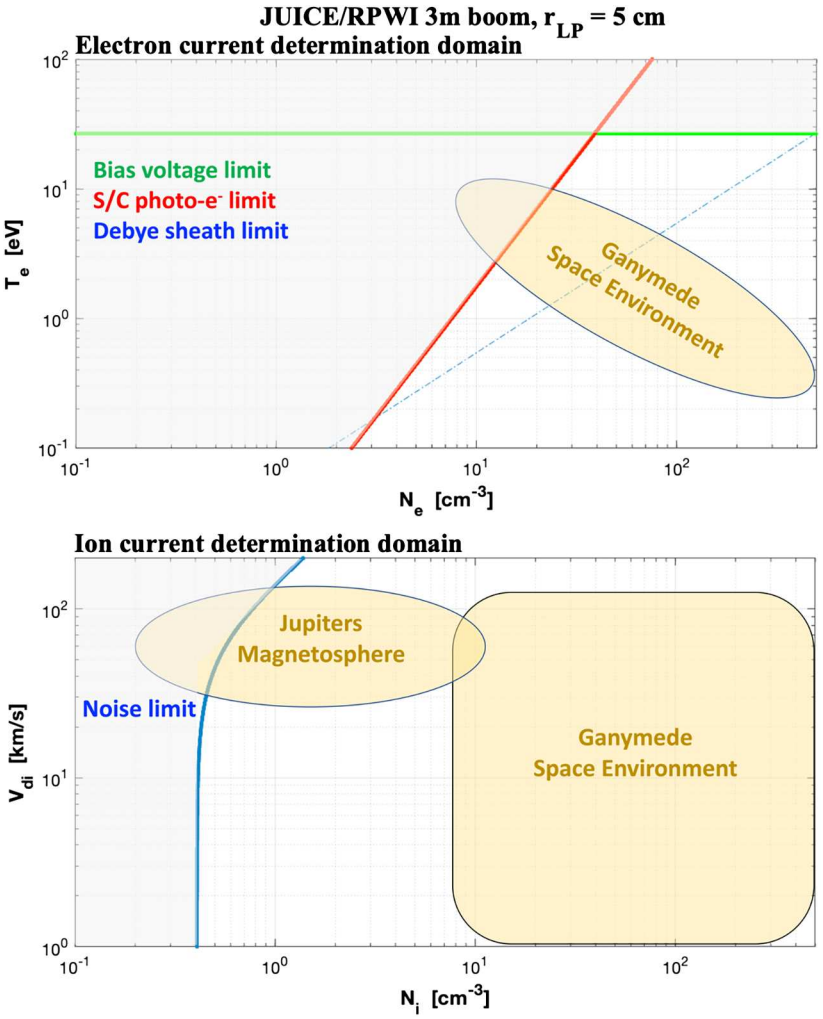

Fig. 10 The operational domains for the JUICE/RPWI Langmuir probes. Top panel: Electron current determination domain. A worst-case, with a positive S/C potential in excess of +2 V, would give a dominating photoelectron cloud near the spacecraft (red). When the probes are inside the S/C Debye sheath (blue-dashed line limiter) a less accurate parameter determination may result. The bias Voltage limit (green) is about 1/3 of the maximum sweep range. Bottom panel: Ion current determination domain. The large sensor, sensitive receiver electronics, and the +/−80 V bias voltage sweep range makes it possible to measure the ion current in large parts of Jupiter's magnetosphere, and determine, e.g., the ion drift speed. The electron density and plasma convection can also be determined in several complementary ways by RPWI. See Sect. 3 for references on typical encountered plasma conditions

of these frequencies in order to construct the mutual impedance spectrum which constitutes the observable of the MIME experiment.

To perform such a measurement, a mutual impedance experiment is therefore composed of (i) several electric sensors to transmit and receive the electric signal, (ii) electronics boards to generate the transmitted signal and treat the received signal, and (iii) an on-board software to define the transmitted signal and perform the on-board analysis of the received signal.

Table 3 Measured leakage currents from the 4 FM booms + sensors and the FS. The original requirement was $<12pA$

FM boom/sensor	Probe to inner shield	Outer shield to inner shield
LP1 (blue)	1.95 ± 0.1 pA	2.0 ± 0.2 pA
LP2 (yellow)	1.9 ± 0.2 pA	2.4 ± 0.3 pA
LP3 (orange)	0.7 ± 0.1 pA	1.0 ± 0.2 pA
LP4 (green)	0.9 ± 0.2 pA	2.0 ± 0.15 pA
LP spare (pink)	1.2 ± 0.2 pA	0.5 ± 0.3 pA

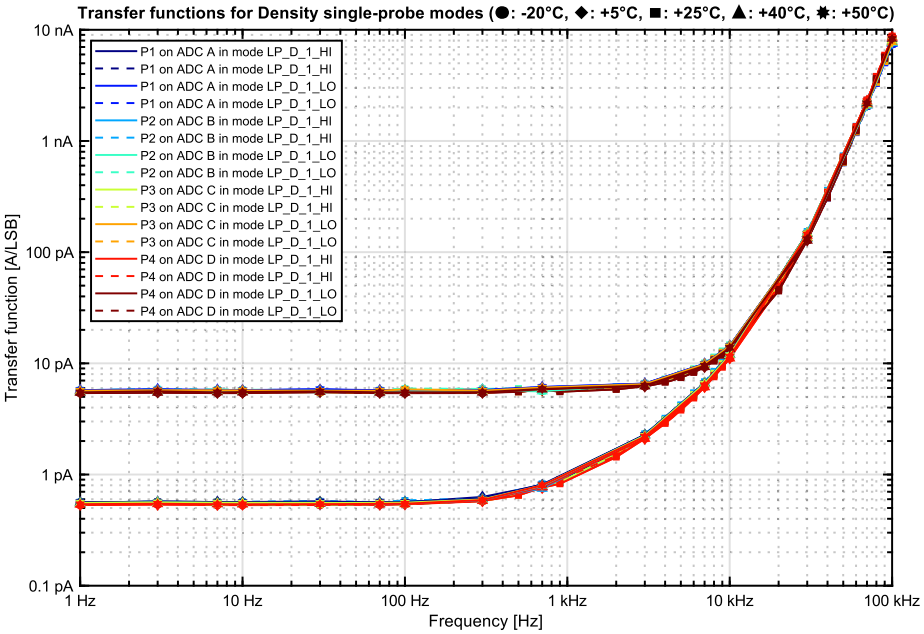

Fig. 11 PFM LP-MIME transfer function for density (i.e., current) single-probe modes, with both high (HI) and low (LO) gain levels. Results from the on-ground calibration showing a good stability versus temperature

Within RPWI, the MIME experiment makes use of (i) both the LP-PWI and RWI sensors, with (ii) the LP-MIME electronic board and (iii) a specific MIME sub-software within the RPWI onboard software.

Practically, for science purposes, MIME transmission and reception can be configured to select one or two Langmuir Probes as transmitter(s); and either another pair of Langmuir Probes or the RWI antennas as receiver. The emitted signal voltage is kept small enough to avoid spurious nonlinear plasma responses (Bucciantini et al. 2022). Reception on the Langmuir probes is performed in the nominal MIME frequency range (low frequency mode: 3 kHz–1.5 MHz), that can be extended to higher frequency by performing the reception on RWI antennas (high frequency mode: 80 kHz–3 MHz). However, the MIME transmitted signal can in principle be received by any other electric or magnetic field sensor, which makes it also possible to use MIME for calibrations and cross calibrations. The active measure-

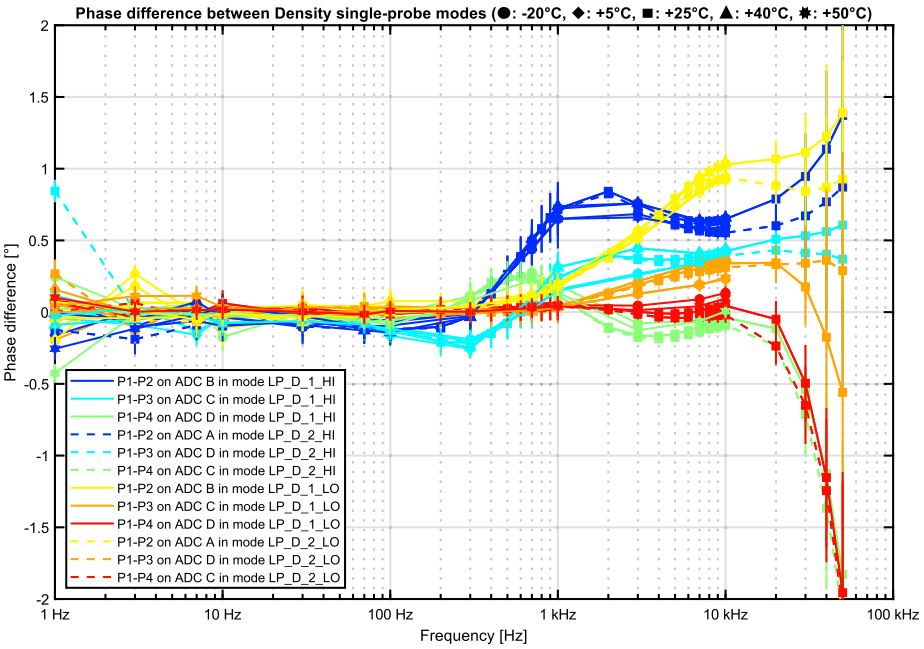

Fig. 12 PFM LP-MIME phase difference between two single-probe in density (i.e., current) measurement mode, for both high (HI) and low (LO) gain levels as a function of frequency. Results from the on-ground calibration showing a good stability versus temperature and a phase difference $<1°$ below 10 kHz

ments performed by MIME are near-field measurements, which is a standard technique for antenna calibration.

The functionality of the MIME subsystem in LP-MIME is that of a laboratory network analyser, which is an advanced Ohm-meter used to measure the frequency dependent complex impedance of an unknown device or medium, namely in this case the space plasma to be diagnosed. Details on the implementation of the LP-MIME electronics are described in Sect. 4.2.5.

MIME is a highly versatile experiment whose onboard acquisition modes can be selected by telecommand from ground to adapt to different environments encountered and to different scientific objectives. Several operation modes have been defined to prioritize either the time or frequency resolution, all within a constant telemetry envelope. Moreover, MIME has the capability to simultaneously process signals from several receiving sensors among the Langmuir Probes (when in low frequency mode) or RWI antennas (when in high frequency mode), leading to the simultaneous acquisition of two or three mutual impedance spectra from different receiving paths, useful to increase the robustness of the measurement and the subsequent plasma diagnostic as well as useful for internal calibration. This results in 96 transmission/reception configuration possibilities and in 9 nominal science modes. Calibration campaigns during the cruise phase and in the early mission phase will give insight for identifying the most appropriate subset of MIME configurations that will be used in nominal science operations. In addition to these science modes, 2 technological modes have been developed to offer the capability to:

- track the plasma dynamics with a higher time resolution. Within 1 sec, the associated operating mode performs 6 successive acquisitions over a reduced bandwidth centred on

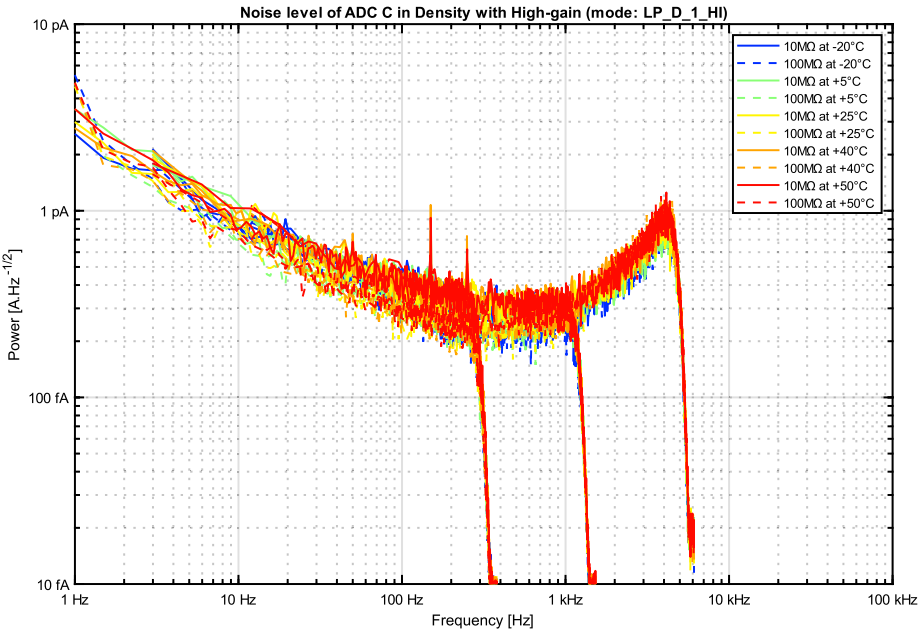

Fig. 13 Example of PFM LP-MIME noise level for density (i.e., current) measurement, here in high gain (HI) and measured on ADC C. Similar measurements were performed during the on-ground calibration for all four ADC (A, B, C & D) and for each gain level (HI & LO). These measurements give the equivalent noise level for $\delta n/n$ measurements

a spectral characteristic associated to the plasma frequency previously determined on-board.

- assess the value of the magnetic field magnitude. The associated mode performs 3 synchronous high-resolution acquisitions in 3 reduced frequency ranges associated to the electron gyrofrequency and its two first harmonics (previously determined on-board), hence allowing to precisely derive the magnetic field magnitude.

MIME can produce electric field spectra either while transmitting an electric signal into the plasma to produce a mutual impedance spectrum (*active* spectrum) or without transmitting any electric signal into the plasma to produce an electric field spectrum (*passive* spectrum). The passive spectrum is used to identify any electric fluctuation present in the plasma independently of the MIME transmitted signal. In science mode, MIME outputs one passive electric spectrum for reference and one or several mutual impedance spectra that will allow ground-based analysis of the local plasma.

Physically, MIME measures the plasma transfer function, in other words, MIME is used to obtain the dielectric permittivity of the plasma. The mutual impedance spectrum is in fact expressed as an integral function of the inverse of the plasma dielectric which determines what kind of wave modes (i.e. eigenmodes) the plasma supports. The plasma's eigenmodes correspond to the frequencies at which the dielectric cancels out, so the mutual impedance spectrum contains resonances at frequencies close to the plasma's eigenmodes.

For instance, the electron plasma frequency depends only on the electron density. In an unmagnetized plasma, this resonance appears as a sharp peak or a cut-off, depending on the electron temperature, in the MIME frequency mutual impedance spectrum. It is this frequency that is sought with a mutual impedance probe to obtain an absolute measurement of

the electron density. The plasma eigenmode known as the Langmuir wave, found at frequencies equal or slightly higher than the plasma frequency, has dispersion properties that depend directly on the temperature of the electrons. In a plasma characterized by a weak magnetic field, it is this natural mode that makes it possible to identify the electron temperature.

If the plasma is magnetized, the upper hybrid and gyro-harmonic resonance frequencies (i.e. the electron Bernstein modes) appear as resonances in the mutual impedance spectra, and enable the retrieval of both the magnetic field strength and the plasma density.

In practice, it is essential that the plasma frequency, or the upper hybrid frequency, is contained within the frequency range of the instrument, in order to measure the electron density and, under certain conditions, the electron temperature. MIME measurements are therefore based on a frequency measurement, which is very well-controlled experimentally.

On the one hand, the MIME onboard products are electric spectra that are either mutual impedance spectra (also referred as *active* spectra) and electric field spectra (*passive* spectra). On the other hand, the final physical products of MIME are the electron density and temperature. They are derived from the telemetered MIME mutual impedance spectra with a ground calculation that is based on a detailed numerical modeling of the MIME experiment to produce synthetic mutual impedance spectra. This MIME experimental model uses a two-step approach.

First, we compute the electric potential emitted by a point-like charge embedded in the plasma. At this stage a hypothesis is made on the actual electron velocity distribution function, usually considered as Maxwellian, bi-maxwellian (Gilet et al. 2017) or kappa (Gilet et al. 2019).

Second, we compute the electric potential generated by MIME at the receiving sensor's location, that is influenced by the spacecraft conductive surfaces, and potentially also by the effect of the inhomogeneous plasma sheath surrounding the JUICE spacecraft on the propagation of the MIME signal (Wattieaux et al. 2019; Bucciantini et al. 2023). For this purpose, we take into account the shape of the different electric sensors as well as their interaction with the conducting spacecraft body using the so-called Discrete Surface Charge Model (hereafter DSCD). This model, first developed in Béghin and Kolesnikova (1998) was proved successful in the context of the Rosetta RPC-MIP mutual impedance experiment (Gilet et al. 2020; Wattieaux et al. 2020). This model enables us to take into account the influence of the different conductive surfaces, including the large JUICE solar panels, on the mutual impedance measurement.

In this computation, we have considered the following electric coupling between the different parts of the spacecraft and the different parts of the MIME experiment: a 4.7 nF link capacitance between the transmitter and the LP sensors used as emitting sensors, 1.92 Ω resistance and 480 pF capacitance for the harness connecting the LPs sensors to the receivers electronics, and 25 pF for the capacitance of the receiver RWI amplifiers.

We present in Fig. 14 different synthetic mutual impedance spectra expected in an unmagnetized plasma composed of a Maxwellian electron population, with electron density of 200 cm^{-3} and temperature of 1 eV, as expected at Ganymede at an altitude of about 500 km from the surface (Eviatar et al. 2001). By unmagnetized, we mean that the electron cyclotron frequency is considered negligible compared to the electron plasma frequency. To illustrate the versatility of the MIME experiment, we consider in this computation different sets of electric sensors, both in emission and reception, corresponding to three cases presented in Figs. 44 and 45 (namely cases A, B, and C). The different colors correspond to measurements on different reception antennas. We consider the following antenna configurations: dipole emission on Langmuir Probes LP1-LP4 with dipole reception on Langmuir Probes LP2-LP3 for mode A (left panel), monopole emission on Langmuir Probe LP4 with

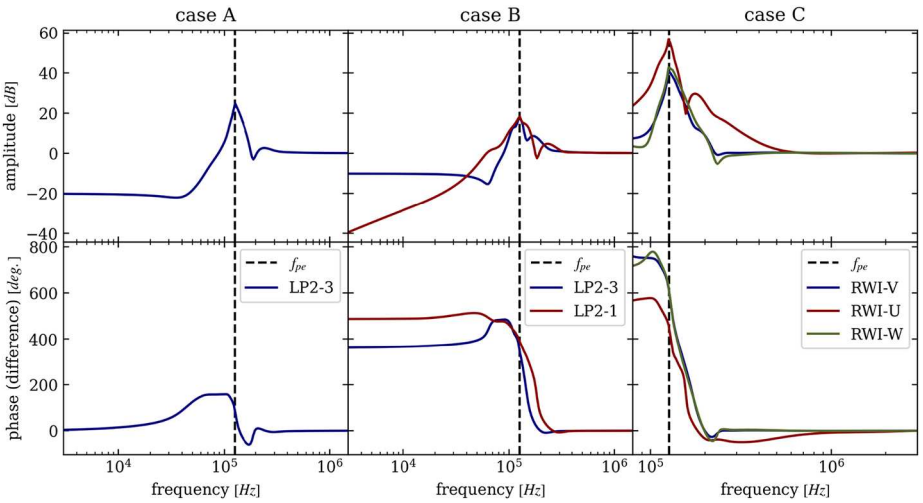

Fig. 14 Synthetic mutual impedance spectra of the RPWI/MIME experiment, using different instrumental modes and antenna configuration. Cases A, B, and C correspond to the transmission-reception RPWI sensor configurations described in Figs. 44 and 45. The plasma is modeled as composed of a Maxwellian electron population of density 200 cm^{-3} and temperature of 1 eV

dipole reception on both Langmuir Probes LP2-LP3 and Langmuir Probes LP2-LP1 for mode B (middle panel), dipole emission on Langmuir Probes LP2-LP4 with dipole reception on the RWI triad antenna for mode C (right panel). Note that the frequency range of operation chosen here is the entire available frequency range for MIME in LF mode (left and middle panels) and HF mode (right panel). The amplitude and phase of the complex mutual impedance spectra are shown in the top and bottom panels, respectively. The mutual impedance spectra expected in the plasma have been normalized to the mutual impedance spectra expected in vacuum. In this example, each synthetic mutual impedance spectrum, whatever the chosen electric sensors configuration, exhibits a clear resonance at the plasma frequency (∼130 kHz, indicated by a vertical dashed line) that would be used to retrieve the absolute plasma density. Note that a significant phase rotation is also expected at the plasma frequency, which can also be used to diagnose the plasma density. The electron temperature controls the actual shape of the mutual impedance spectrum, and would be retrieved experimentally from a best fit procedure between the measured and the modeled mutual impedance spectra.

2.4 SAMWISE

By integrating several closely related subsystems, SAMWISE (Search-coil and Analyzer Module for Waves and Instabilities Science Experiment) aims at measurements of electromagnetic waves and instabilities, which can interact with different particle populations in the surrounding plasma medium. It primarily makes use of the three axial Search Coil Magnetometer antenna (SCM, see Sect. 4.2.11) for vector (3D) measurements of the fluctuating magnetic field. SAMWISE also uses the measurements of the vector (3D) electric field fluctuations, and variations of the plasma density (δn/n) by the four Langmuir Probe sensors (LP-PWI, see Sect. 4.2.8 – 4.2.10). All seven analogue input signals from these sensors are conditioned, sampled, and analysed by the Low Frequency Receiver (LFR, see Sect. 4.2.6),

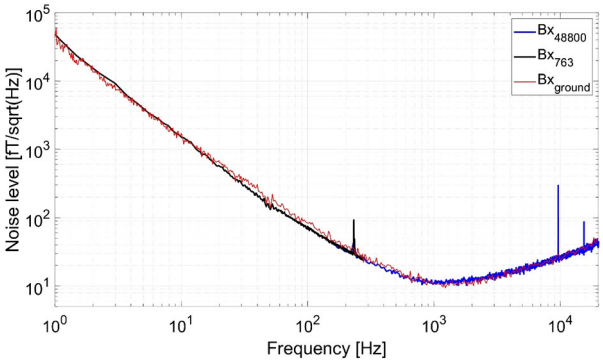

Fig. 15 SCM in-flight noise level for the X component as a function of frequency, obtained in the near-Earth solar wind superposing spectrum from high-frequency snapshots (48.8 ksps; blue line) and from continuous waveforms (763 Hz; black line). Spectrum from high-frequency snapshots is plotted between 150 Hz and 20 kHz. Spectrum from continuous waveforms is plotted from 1 Hz to 280 Hz. Noise level measured on ground in red. The behaviour of Y and Z components is similar to that of the X-component. Note that preliminary calibrations have been applied

which also controls power for the SCM preamplifier. Higher-level data analysis procedures are implemented in the LFR flight software executed by the RPWI DPU (see Sect. 4.2.4, and 5.1), which also makes use of real time J-MAG magnetic field data sent on-board to RPWI.

The SAMWISE frequency range is defined by the SCM working frequency band, which covers a broad interval from 0.1 Hz to 20 kHz. Figure 15 (black and blue lines) shows the in-flight noise level which corresponds to the SCM sensitivity. This noise level is obtained combining the spectrum obtained from high-frequency snapshot waveforms (48.8 ksps) and the spectrum obtained from continuous waveforms (763 sps). The measurements have been obtained in the near-Earth solar wind during the first JUICE in-flight interference campaign after commissioning phase (July 2024). The red line shows the noise level measured on ground during SAMWISE calibrations. The agreement between these first in-flight data and on-ground measurements is overall very good, confirming that the performance of the SCM sensor satisfies RPWI science requirements. The lowest value of the noise level corresponds to the best sensitivity of about 10 fT $Hz^{-1/2}$ close to 1 kHz. The in-flight SAMWISE data also indicate that the interferences from the JUICE platform are rather limited below 20 kHz, mostly because SCM has been accommodated on the MAG boom at about 8.2 m from the platform. Nevertheless, a few interferences have been observed. The detailed analysis of such interferences is ongoing, and they will be reported elsewhere (Retino et al., in preparation), together with the full description of the SCM sensor and performance. The two narrowband emissions above 9 kHz in Fig. 15 are related to the drive frequency of the MAG-IBS instrument. They were expected from ground measurements, are stable and can be removed by post-processing. Narrowband peaks above the noise level around 200 Hz are likely due to emissions from the reaction wheels. Such emissions can also be removed with postprocessing. Although calibrations of the SAMWISE data are preliminary, these first in-flight data already show that the performance of the SAMWISE experiment is adequate to properly resolve key plasma waves, especially Alfvén-, magnetosonic- and Whistler mode waves as well as radio waves (especially the QP and b-KOM), in the Jupiter system.

Beside the full multidimensional waveforms sampled at variable rates, which served for first in-flight measurements shown in Fig. 15, SAMWISE will also run on-board analysis procedures to reduce the telemetry volume by science-based data compression. These data

products include time and frequency averaged multidimensional spectral matrices involving the full vector of magnetic field fluctuations, the full vector of electric field fluctuations, and fluctuations of plasma density. The spectral matrices contain information on amplitudes, mutual phases, and coherences of all these signals. High level on-board processing in the LFR software result in the very compressed set of wave polarization and propagation parameters (with a heritage from the Van Allen probes missions), which will be used as preview data set for selective download of full waveform data. Another high-level data set of on-board processed data (with a heritage from the Solar Orbiter mission) is based on automatic recognition of dust impacts on the spacecraft and wave-like features from the waveforms. Spectral matrices, wave polarization and propagation data, or data products based on waveforms will be also alternatively used to trigger the full resolution waveform captures.

2.5 JENRAGE

JENRAGE (Jovian ENvironment Radio Astronomy and Ganymede Exploration) processes the electric field signals sampled by the three-dipole antenna (Radio Wave Instrument, RWI, see Sect. 4.2.12) and the High Frequency Receiver (HFR, see Sect. 4.2.7). Within RPWI, JENRAGE covers the high frequency range from 80 kHz up to 45 MHz. The RWI is mounted on the MAG-boom at 8.6 m away from the spacecraft body. Radio signals detected by three RWI dipole antenna are picked up by sensitive wide-band RWI preamplifiers (cf. Sect. 4.2.13), and are transferred to the HFR board in the RPWI-EBOX via the long RWI-HF harness with the length of 17 m. After a low path filter at the entrance of HFR, 3 channels are sampled with the rate of 90 Msps and digitally filtered into ∼300 kHz bands. The DPU in EBOX converts those digital signals to the power and cross spectra.

2.5.1 Planned Operation Modes

Each dipole antenna element of the RWI has no intrinsic directivity. However, the combination of the three-axis electric field components enables detailed radio observations with the goniopolarimetric capabilities. It can provide the direction of arrival, the flux density and the polarization state and degree of observed radio waves, as a full-sky radio imager orbiting Jupiter and Ganymede. Such capabilities are applicable in the short antenna regime, i.e., when the effective electric lengths of the antennas are much shorter than the observed wavelength. The power of the three-axis radio wave detection has been proved in the Kronian system studies by the RPWS/HFR instrument aboard the Cassini spacecraft up to 2 MHz with 3 monopole antennas (10 m physical length) (Gurnett et al. 2004; Cecconi and Zarka 2005). The experiment will employ goniopolarimetry in the Jovian system, where simulations have shown that an accuracy of 2 degrees can be achieved below 1.5 MHz (Fischer et al. 2021). The in-flight RWI calibrations will provide the effective electrical length and direction of each of the three RWI antenna. JENRAGE's telemetry modes are summarized in Sect. 5.8 and 6.3. There are at least three primary modes of operation:

- The most basic mode is 'Radio-Full (nominal-sweep)', which is used during the Jovian orbiting phase, when the JENRAGE aims to monitor the Jovian radio emissions continuously. In this mode, spectra are taken once per sequence cycle (usually every 30 s but can be longer) in the frequency range 80 kHz – 45 MHz with semi-logarithmic 256 frequency channels, after averaging in frequency.
- The 'Radio-burst' mode is primary used for occultations of intense Jovian radio emission by icy moons and their ionospheres. In this mode, spectra are taken once per 0.2, 0.5, 1 or 2 seconds in 80 kHz – 2.096 MHz with linear-spacing 72 frequency channels after averaging in frequency.

- The 'passive sub-surface radar (PSSR)' modes target the electric characteristics of the crust and sub-surfaces of Europa, Ganymede, and Callisto, using the reflections of penetrated Jovian radio emissions (HOM/DAM) (e.g., Kumamoto et al. 2018). JENRAGE have three PSSR modes:
  - o 'PSSR1' mode takes a spectrum matrix with 4320 frequency channels (rich) or a power spectrum of 540-frequency channels (survey) once per 30 seconds. It can potentially show an 'interferometry pattern' appeared in a frequency-time spectrogram, which is caused by the differences of the resonance between the waves directly from Jupiter and the waves reflected from icy moons in different wavelengths. This mode is for coherent and continuous Jovian radiation during the waiting time of the arrival of reflected waves from icy moons.
  - o 'PSSR2' mode takes the down-converted waveforms with selected 16 frequency channels (rich) or their autocorrelation in measured 45 frequency channels (survey) once per 30 seconds. It is for incoherent and short Jovian radiation like 's-burst'. Io-DAM s-burst with dispersive fine spectral structures is the useful incident for PSSR, because its short duration of several 10 s msec can be potentially used like Chirp radar signals.
  - o 'PSSR3' is the simplest, which obtains 11.2 msec down-converted waveforms at a single frequency. The signals are transmitted to the Earth without any data processing in DPU, and all correlation analyses will be made on the ground.

2.5.2 Sensitivity Characteristics

Figure 16 shows the geometry of the three dipole antenna elements of the RWI on the MAG-boom. Six antenna elements are BeCu antenna rods with the length of 1.25 m and the diameter of 1 cm, attached on the cubic chassis which stores the preamplifier electronics inside. The measured components are called U, V and W with right-handed coordinates.

Because it was impossible to deploy S/C appendices (such as RWI antenna, MAG-boom, and solar panels) in any final ground tests, numerical antenna simulations were performed by Fischer et al. (2021). Moreover, the actual performance of the effective antenna lengths and directions can only be measured after the launch. Planned in-flight calibrations for direction finding and polarization are associated with the Earth flyby operations, using the radio signals from known source locations and wave polarization. Suitable sources are Auroral Kilometric Radiation (AKR) from the Earth in 100 – 800 kHz. When JUICE is not too far from Earth solar type-III bursts in wider frequency range can also be used for the flux calibration with simultaneous detections by Earth-orbiting spacecraft like Wind WAVES (Bougeret et al. 1995) and Arase PWE (Kasahara et al. 2018) up to 10 MHz. JUICE will make a flyby of Earth in August-2024, and two more in 2026 and 2029 respectively doing simultaneous measurements with other spacecraft (see also Sect. 6.4).

Just after the in-flight RWI antenna deployment operation it was detected that JENRAGE suffers multiple harmonic lines of noise from 200 kHz (not shown) and upward with a wideband enhancement in the 3 – 10 MHz range (see Fig. 17). RPWI suffers no science loss due to the strong Jovian radiation, but it may impact the objectives requiring weak signal detections in the frequency range 3 – 10 MHz, like PSSR. The upcoming Earth flyby in August 2024 will characterise this interference and mitigation methods will be applied like the line noise elimination logic in the onboard HF software in the DPU. The real performance of JENRAGE and its suitable operation with the revised telemetry definitions will be carefully established during the long cruise.

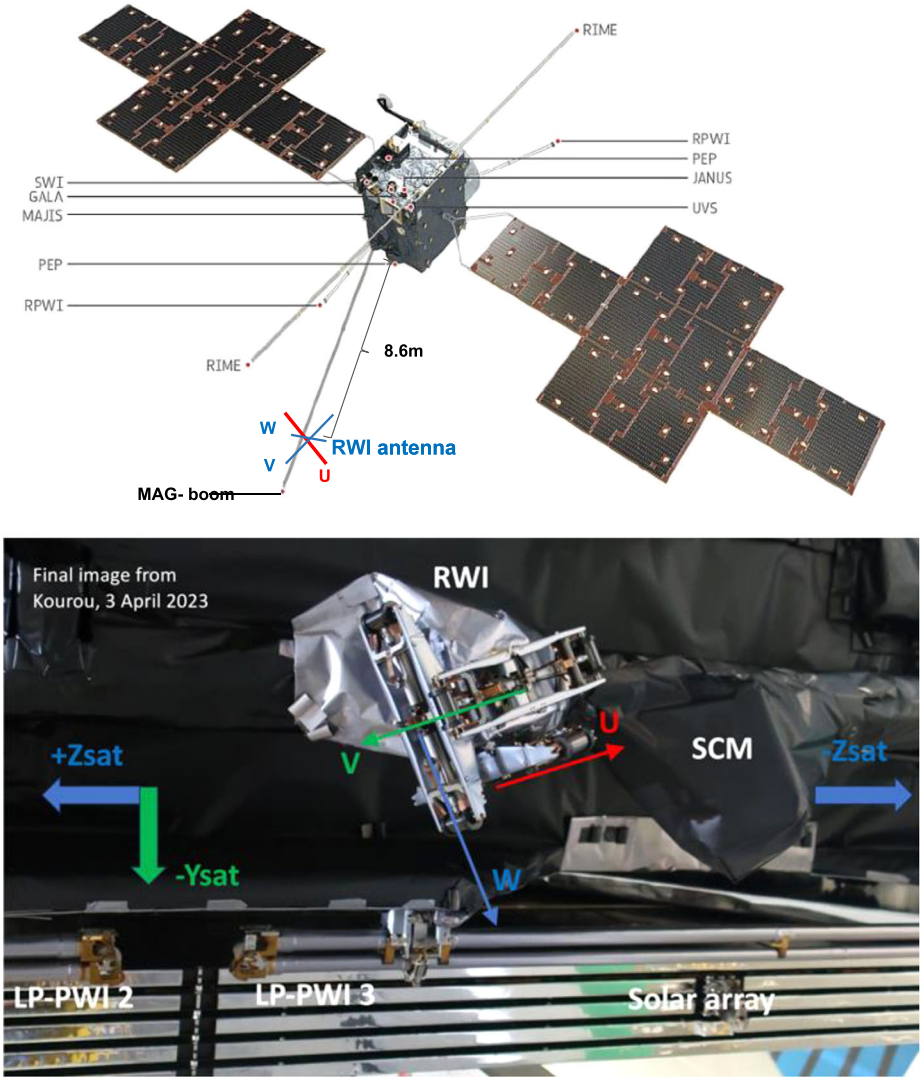

Fig. 16 The Radio Wave Instrument (RWI), a tri-dipole antenna system which consist of 3-axis electric field antenna with 2.5 m tip-to-tip length. (above) The location of the RWI on the MAG-Boom deployed from the spacecraft. (below) The axis configuration of the RWI just before launch. Side note, compared to Fig. 2 in Fischer et al. (2021) the V and W antennas became interchanged during integration

2.5.3 Numerical Antenna Calibration for RWI

Antenna pattern is critically important for the JENRAGE science for the direction finding and polarization analyses. The numerical analysis presented by Fischer et al. (2021) describes the expected reception properties of the RWI antennas by calculating the so-called effective antennas. Table 4 gives the spherical coordinates of the physical RWI antennas in comparison to the effective antennas for a capacitive load of 25pF. The angle γ in the last column gives the angular deviation of the effective antenna from the physical one, which

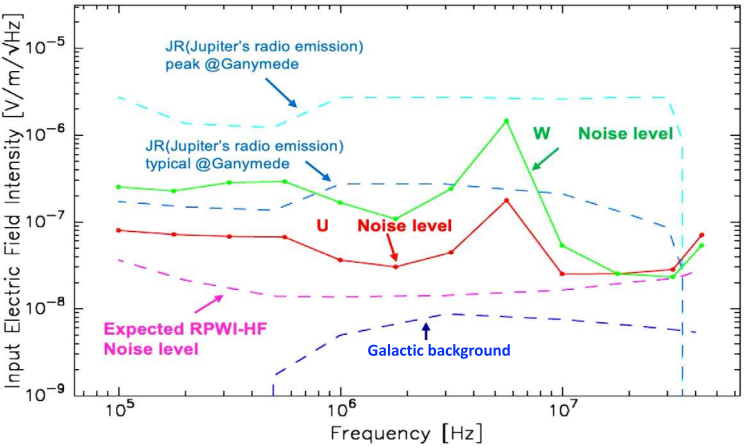

Fig. 17 Detection capability of the electric field by JENRAGE is due to the combination of RWI and HF. RWI preamplifier temperature is assumed to be −140 °C. Real antenna calibration is not executed yet. The noise floor expected before launch is in pink dashed line. Green and red lines show the noise level seen after the launch suffered by the radiation of the spacecraft system. Expected levels of Jovian radiation at Ganymede (peak and typical) and the galactic background radiation are also shown

is caused by the induced currents on the conductive surface of the spacecraft. The deviations lead to U-V, V-W, W-U angles between the effective dipoles of 72.7°, 82.1°, and 92.6°, respectively.

As described in Sect. 2.5.2, Table 4 shows that the effective length of the W antenna is around twice that compared to the U and V antenna. The reason for this is most likely that the currents on the MAG boom induce larger currents in the V-dipole, since the angle between the MAG boom and the V dipole is just 28°, whereas the angles between the U and W-dipole and the MAG boom are 74° and 68°, respectively.

The results in Table 4 were calculated for a frequency of 300 kHz, which is in the so-called quasi-static frequency range where the wavelength is still large in comparison to the dimensions of the spacecraft. Fischer et al. (2021) found that the effective angles deviate by less than 2° up to 1.5 MHz, so reasonable direction-finding and polarization measurements can be done up to this frequency. At higher frequencies, the effective antennas become complex quantities depending on frequency and incoming wave direction. The gain pattern of each dipole changes from a torus-like shape at quasi-static frequencies to a pattern with multiple lobes at higher frequencies as Fig. 18 shows. Actual performance will be confirmed by in-flight calibration using the received signals of known source locations and wave polarization, for example Auroral Kilometric Radiation (AKR) from the Earth.

2.6 Positions and Alignment of RPWI Sensors

The locations of the RPWI sensors on the JUICE spacecraft are shown in Fig. 19. The origin of the spacecraft coordinate system is defined to be located at the separation plane between the S/C and the launch adapter, in the centre of the launch adapter, i.e., slightly outside the spacecraft body at the bottom of Fig. 19.

The LP-PWI probe mechanical positions are given in Table 5, where also the LP-to-LP separation vectors, based on the LP SPICE positions, and the hardware limited simultaneous sensor combinations of LP-PWI are given. The hardware constrains the combinations

Table 4 Spherical coordinates of physical and effective RWI antennas with loaded ports ($25pF$). The letter h denotes the effective length, the angle θ is the colatitude, and φ is the azimuth in the JUICE spacecraft coordinate. The angle γ gives the deviation of the effective antennas from the physical ones. Table adapted from Fischer et al. (2021)

Antenna name	Physical antennas			Effective antennas loaded ports (25 pF)			
	h [m]	θ [deg]	φ [deg]	h [m]	θ [deg]	φ [deg]	γ [deg]
U+U-	2.5	69.6	−22.1	0.26	45.1	−25.9	24.7
V+V-	2.5	22.1	134.4	0.48	27.7	155.9	10.6
W+W-	2.5	98.1	64.9	0.23	84.8	73.1	15.6

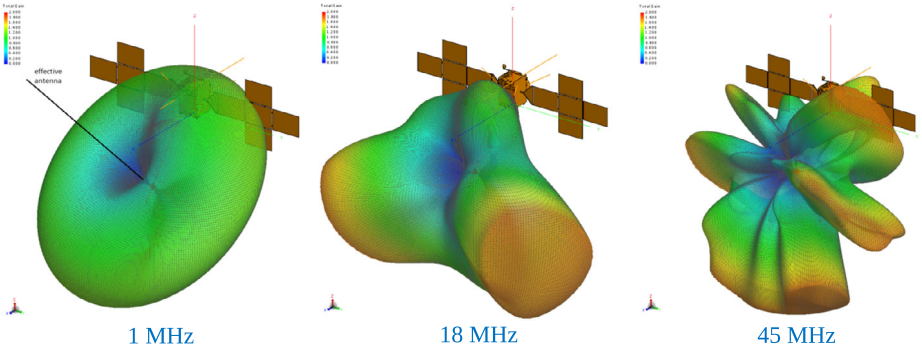

Fig. 18 Far-field gain pattern of U-antenna for 1 MHz (left), 18 MHz (middle), and 45 MHz (right). The colour scales go from 0 (dark blue) to 2 (red) and denote the total linear gain

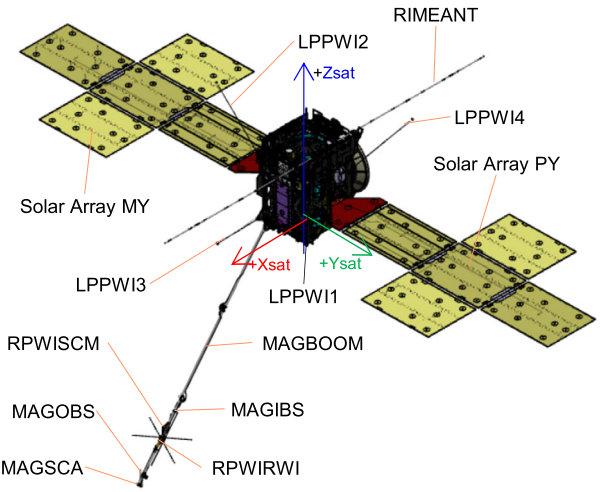

Fig. 19 RPWI (and other) sensor locations on the JUICE spacecraft: LP-PWI 1 through 4, RWI, and SCM. In this representation the launch adapter is on the side facing below and not visible

to only four possible differential modes, while allowing all four single-ended modes. The single ended modes can of course be further combined to all 6 differential components by on-ground analysis.

Table 5 Langmuir probes URF (SPICE) mechanical positions

LP-PWI	Spacecraft coordinates [mm]			Separation [mm]
	X	Y	Z	
LP-PWI 1 (LP1)	2484	2895	4377	
LP-PWI 2 (LP2)	1455	−3238	5303	
LP-PWI 3 (LP3)	1455	−3238	−1849	
LP-PWI 4 (LP4)	−2768	2686	4432	
LP1-LP2	1029	6133	−926	6287.3
LP1-LP3	1029	6133	6226	8799.8
LP1-LP4	5251	209	−55	5256.4
LP2-LP3	0.00	0.00	7153	7152.0
LP2-LP4	4223	−5924	872	7327.1
LP3-LP4	4223	−5924	−6281	96114
Possible AC & DC differential modes	ΔU1	ΔU2	ΔU3	
Mode 0 [3D] (default)	LP1-LP2	LP2-LP3	LP3-LP4	
Mode 1 [2D]	LP1-LP4	LP1-LP3	LP3-LP4	
Mode 2 [2D]	LP1-LP2	LP2-LP4	LP1-LP4	
Mode 3 [1D]	LP1-LP4	LP1-LP4	LP1-LP4	

Table 6 Electric field vector ($\boldsymbol{E}$) transformation matrix for Mode 0

Voltages U [V]	Transformation matrix M [m]			E-field [V/m]
ΔU_{12}	1.029	6.133	−0.926	E_x
ΔU_{23}	0.0	0.0	7.153	E_y
ΔU_{34}	4.223	−5.924	−6.281	E_z
E-field [V/m]	Inverse transformation matrix M^{-1} [m^{-1}]			Voltages U [V]
E_x	0.1852	0.1923	0.1917	ΔU_{12}
E_y	0.1320	−0.0112	−0.0322	ΔU_{23}
E_z	0.0	0.1398	0.0	ΔU_{34}

For the default LP Mode 0 [3D], to obtain the electric field vector, E, in S/C coordinates, from the measured voltage differences, ΔU, the transformation matrix M and its inverse M^{-1} ($\Delta U = \mathsf{M}E$ or equivalently $\mathsf{M}^{-1}\Delta U = E$), are given in Table 6.

The SCM and sensor axes are shown in Fig. 20, where with W-axis of the SCM unit points towards the spacecraft. The SCM and RWI (SPICE) sensor positions in spacecraft coordinates are given in Table 7 and 8.

2.7 Surface Charging of JUICE

The interaction between a spacecraft and its space environment will charge the spacecraft and give it a surface potential (e.g., DeForest 1972; Wahlund et al. 1999a,b; Eriksson et al. 1999; Eriksson and Wahlund 2006). Differential surface charging will occur since there are different dielectric surfaces on the spacecraft, such as the HGA and the radiators. Since spacecraft surface charging modifies the near spacecraft plasma environment it can im-

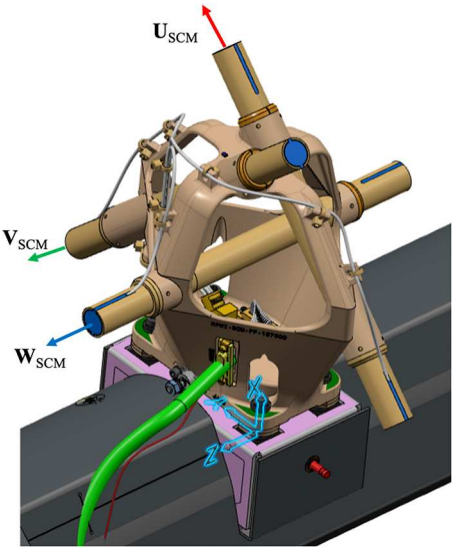

Fig. 20 SCM sensor directions. The SCM W sensor is parallel with the MAG boom and the U and V sensors are rotated by 45 degrees around this axis. The spacecraft frame is not given here

Table 7 SCM (SPICE) mechanical positions in spacecraft coordinates and rotation matrix from sensor frame to S/C frame. The position of the SCM is in the centre of the unit

SCM	Spacecraft coordinates [mm]			
SCM position	6541	−857	−6205	
B-field [T] S/C	Rotation matrix (SPICE)			B-field [T] SCM
B_X	−0.0677	0.7742	−0.6293	B_U
B_Y	−0.9962	−0.0872	0	B_V
B_Z	−0.0548	0.6269	0.7771	B_W

Table 8 RWI (SPICE) mechanical positions in spacecraft coordinates and rotation matrix from sensor frame to S/C frame. The position of the RWI is the reference hole of the unit reference frame (URF)

RWI	Spacecraft coordinates [mm]			
RWI position	6750	−836	−6719	
E-field [V/m] S/C	Rotation matrix (SPICE)			E-field [V/m] RWI
E_X	−0.8749	0.2683	−0.4031	E_U
E_Y	0.3303	−0.2779	−0.9020	E_V
E_Z	−0.3541	−0.9224	0.1546	E_W

pact the measurements of both particles and fields. In preparation for the RPWI operations we have performed several studies of the spacecraft environment and surface charging of JUICE. These studies include conditions in the Jovian magnetosphere, the ionospheres of Jupiter's moons Ganymede and Europa, and the solar wind at 1 AU. For these simulations (Holmberg 2020, 2023, Bochet et al. 2023) we have used the Spacecraft Plasma Interaction Software (SPIS, Sarrailh et al. 2015); a 3D model of the JUICE spacecraft; a catalogue

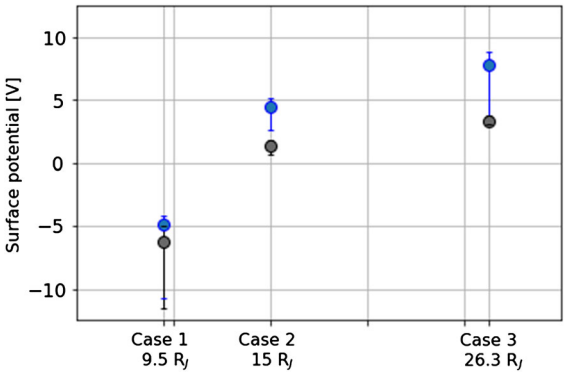

Fig. 21 The surface potential of the JUICE spacecraft in sunlight (blue) and eclipse (black) at 9.5, 15, and 26.3 R_J from the centre of Jupiter, in the densest region of the plasma disk. The bars give the potential range of the different spacecraft surfaces

of each spacecraft surface materials and its properties; and descriptions of each simulated environment. Examples of JUICE spacecraft surface charging typically encountered in the Jovian magnetosphere is presented in Fig. 21. The charging within Ganymede's and Europa's ionospheres at 400 km can reach down to −20 V. The modification of the spacecraft plasma environment from such surface potentials, even at the distant locations of the Langmuir probes, is important to understand. For RPWI the effects are mitigated by the Langmuir probe sweep range of up to ±80 V, when estimating the thermal plasma properties. The surface charging of JUICE in the solar wind at 1 AU is expected to vary between −42 V to +12 V for typical solar wind conditions (Holmberg et al. 2024). One of the first RPWI Langmuir probe sweep measurements in the solar wind during near Earth commissioning indicated an average spacecraft surface potential of about +5 V (see Fig. 9). This is in excellent agreement with the SPIS simulations, which shows an average spacecraft surface potential of around +6 V for a typical solar wind environment (Holmberg et al. 2024).

2.8 Summary of RPWI Capabilities

The RPWI science products and related performances are given in Table 9. RPWI ensures that the *electron density*, n_e, can be determined in all plasma environments encountered by JUICE. This is achieved by measuring n_e through several complementing techniques, ensuring good measurements in all plasma regions as well as accuracy evaluation by method comparisons:

- LP-PWI bias voltage sweeps (see Fig. 10, for $n_e > 10$ cm^{-3}).
- Derive the upper hybrid resonance frequency (f_{uh}) from natural upper hybrid emission bands (for $n_e > 0.01$ cm^{-3}).
- Monitoring the spacecraft potential (U_{SC}) and calibrating toward f_{uh} (or possibly the PEP electron spectrometer). (for $n_e < 1$ cm^{-3})
- Continuous high time resolution sampling of the probe current (allows ms time resolution, $\delta n/n$, for $n_e > 10$ cm^{-3}).
- Active mutual impedance measurements (MIME, for $n_e > 0.01$ cm^{-3}).
- Refractive index measurement near radio frequency wave cut-offs (e.g., during ionosphere remote sounding, for $n_e > 10$ cm^{-3}).

The *ion density*, n_i, can be determined by

- Langmuir probe sweeps in denser plasmas ($n_i > 1$ cm^{-3}).

The *thermal electron temperature* (T_e) is determined through two techniques:

Table 9 RPWI science products and performance verified mostly from ground measurements and pending in-flight calibrations

RPWI Measured Quantity	Range/Product	Error/Sensitivity
Electric field vector, $\delta\mathbf{E}$(f)	DC – 1.5 MHz	DC: $\approx$ 0.9 μV/m (instrument)
	Dust detection.	(Calibration for S/C influence needed in flight)
	Polarization with $\delta\mathbf{B}$(f).	
	Poynting flux with $\delta\mathbf{B}$(f).	Spectral (differential):
		$<$1 μV/m/$\sqrt{}$Hz ($>$500 Hz)
Electric field vector, $\delta\mathbf{E}$(f)	80 kHz – 45 MHz	30 – 50 nV/m/$\sqrt{}$Hz (at 10 MHz)[1)]
	Wave vector ($\delta\mathbf{k}$)	$\sim$1° (at 5 MHz)
	Polarization	$\sim$10% (at 5 MHz)
		(Direction finding & sensitivity calibration needed in-flight)
Magnetic field vector, $\delta\mathbf{B}$(f)	0.1 Hz – 20 kHz	8 pT/$\sqrt{}$Hz (at 1 Hz)
	Polarization with $\delta\mathbf{E}$(f).	0.6 pT/$\sqrt{}$Hz (at 10 Hz)
	Poynting flux with $\delta\mathbf{E}$(f).	0.06 pT/$\sqrt{}$Hz (at 100 Hz)
		20 fT/$\sqrt{}$Hz (500 Hz-10 kHz)
Electron density (n_e)	10^{-4} – 10^5 cm^{-3}	$<$10% ($>$10 cm^{-3})
		Leak current $\approx$0.5pA $<$100 Hz
Density fluctuations (δn/n)	DC – 10 kHz	$<$5% below 1 kHz
$\delta\mathbf{E}$ or δn interferometry	$<$1000 km/s	Phase accuracy $<$1° for $<$20 kHz.
		Phase response correctable.
Ion density (n_i)	1 – 10^5 cm^{-3}	$<$20%
Electron temperature (T_e)	0.01 – 100 eV	$<$20%
Ion drift speed (V_{di})	0.1 – 200 km/s	$<$20%
Ion temperature (T_i) upper constraints	0.02 – 20 eV	Constrained by $<mV_{di}^2/2e$
Spacecraft potential (Usc)	±80 V	$<$10%
Integrated solar EUV flux	$<$1 Hz	Res. 0.003 Gphotons/cm^2/s
PSSR: Max Ice depth / Resolution	$<$20 km (depend on ice conductivity/salinity)	$<$1 km

[1)]Need in-flight verification.

- LP-PWI bias voltage sweeps (see Fig. 10, $0.01 < T_e < 20$ eV).
- Active mutual impedance measurements (MIME, $0.01 < T_e < 100$ eV).

The absolute value of *ion drift speed* (V_{di}), and limits on the ion temperature (T_i), is determined from

- LP-PWI bias voltage sweeps (see Fig. 10).
- $\mathbf{E} \times \mathbf{B}$ drift (together with J-MAG **B** data).

The combined measurements by RPWI allow determination of:

- Wave vector, energy flux (Poynting vector), and wave polarization estimates of different plasma waves and radio waves.
- Remote radio source location.

- Interferometry of plasma waves and density inhomogeneities (δn/n), giving phase speeds and plasma drift speeds.
- Poynting flux associated with field-aligned currents.
- Dust distribution ($>$ 1 μm size).

The *spacecraft potential*, U_{SC}, can be determined in most plasma environments by LP-PWI, i.e., where the spacecraft charges within $+/-80$ V. The active measurement techniques (MIME), applied to the RPWI sensors, will furthermore allow to determine the effective antenna electric lengths, deployment lengths and electric sensor calibration to increase the accuracy of the passive RPWI measurements.

3 The RPWI Science Objectives

The main RPWI science objectives are listed below as science topics for easy reference. It is by no means to be a complete list or a complete account for the science to be made by RPWI. The intention is instead to give a resumé of the main science questions that need an answer, and how RPWI intends to answer these questions with what measured parameters.

The main science focus of RPWI is to monitor the energy and momentum transfer processes dealing with electromagnetism in the whole Jovian system, especially near the icy moons. This includes many aspects of the information gained by measuring the vector electric fields (near DC to 45 MHz), vector magnetic fields (0.1 Hz – 20 kHz) and bulk plasma properties. In short, the RPWI will focus on characterizing electric currents and its dynamos, electric acceleration structures, e.g., in auroral energisation regions, plasma boundary processes, and all types of waves, e.g., dispersive Alfvén waves, Whistler waves, plasma waves and their role in transporting energy and momentum in the magnetospheres and ionospheres. The dynamics and particle energisation processes can further be monitored by radio waves, which also will be used to monitor the icy moons ionospheres and sub-surface properties. Most processes related to coupling between the magnetospheres, ionospheres, charged dust, thin atmospheres, surfaces, and the conductive interior of the icy moons will be addressed by RPWI. One major objective is to contribute to the study of sub-surface ocean structure(s) and possibly mapping of ocean flows. The focus will also be to determine the properties of bulk plasma and dust in the space environment in the magnetosphere of Jupiter and in the regions near the icy moons. Here the ionospheric structure (and chemistry), conductivity and transport near the icy moons is of special interest, and their role in closing electric current systems. The dust particle size distribution in the Europa and Io tori as well as potential exhaust plumes will be studied. This will allow for studies of possible dust-plasma interaction and acceleration of charged dust by electric fields. Table 10 summarize the main

Table 10 Main RPWI science goals

Addressed RPWI science process	Experiment contribution
Sub-surface induction at icy moons	GANDALF, flybys Sect. 3.1
Sub-surface ocean tides at Ganymede	GANDALF, in Ganymede orbit Sect. 3.1
Auroral oval "wiggling" at Ganymede	GANDALF, in Ganymede orbit Sect. 3.2

Table 10 (*Continued*)

Addressed RPWI science process	Experiment contribution
Structure of icy crust of icy moons	JENRAGE, flybys, in Ganymede orbit
	Sect. 3.3
Jovian and Ganymede magnetospheric plasma waves, their boundary processes	GANDALF, SAMWISE, near Ganymede, in Jupiter orbit and approach, high latitude
	Sect. 3.5
Ionosphere–magnetosphere couplings at Ganymede	GANDALF, MIME, SAMWISE, near Ganymede
	Sect. 3.6
Structure and variability of the ionosphere and magnetosphere of Ganymede, electrodynamics, Alfvén wings, thermal plasma outflow	GANDALF, MIME, SAMWISE, JENRAGE, near Ganymede
	Sect. 3.7
Ganymede auroral processes	GANDALF, MIME, SAMWISE, near Ganymede
	Sect. 3.8
Europa's ionosphere, related electrodynamics, ion outflows, interaction with Jovian magnetosphere	All RPWI experiments, Europa flybys
	Sect. 3.9
Europa plume dust, structure, and electrodynamics	GANDALF, MIME, SAMWISE, Europa flybys
	Sect. 3.10
Europa torus	GANDALF, SAMWISE,
	Sect. 3.11
Dust near icy moons	SAMWISE, near icy moons
	Sect. 3.11
Callisto's ionosphere, related electrodynamics, ion outflows, interaction with Jovian magnetosphere	All RPWI experiments, Callisto flybys
	Sect. 3.12
Co-rotation breakdown in the Jovian magnetosphere	GANDALF, SAMWISE, Jupiter orbit, high latitude phase
	Sect. 3.13
Jovian radio emissions & magnetosphere dynamics	JENRAGE, Jupiter orbit, high latitude phase
	Sect. 3.14
Io torus dynamics	JENRAGE, Jupiter orbit
	Sect. 3.15
Wave emissions from Jupiter atmosphere lightning	SAMWISE, JENRAGE, close to Jupiter
	Sect. 3.16
Cruise science	All RPWI experiments,
	Sect. 3.17
Upstream solar wind	GANDALF, SAMWISE
Global Jovian magnetosphere structure and convection	GANDALF
Jovian current/plasma sheet	GANDALF, SAMWISE

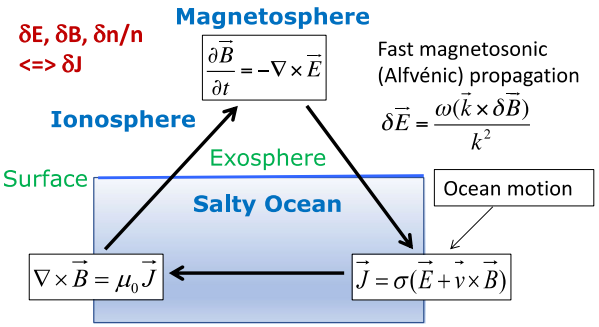

Fig. 22 The induction process coupling the local space plasma where the spacecraft is situated to the electric currents in a conductive sub-surface ocean. The red parameters are measured in orbit (or during flybys) of the icy moons by RPWI and J-MAG onboard JUICE. The quasi-periodic magnetospheric induction disturbance dominantly from Jupiter's magnetodisc propagates down to the sub-surface ocean in an Alfvénic manner, and there generates an induction current. The ocean (e.g., tidal) motion also contributes to an electric current. The total induction response in the ocean propagates outward through the ionosphere to the magnetosphere, where the JUICE spacecraft measures the disturbed electric and magnetic fields at many frequencies (days, hours, minutes). Various other electric current sources, such as ionospheric electric currents, also contribute to the measured electric and magnetic fields and must be separated out from the contribution of the sub-surface ocean. For instance, the induction response itself generates electric currents in the ionosphere, and for Callisto, this ionospheric induction response can dominate the measurements

processes that RPWI focus on. This can be compared with more general science goals for JUICE (Fletcher et al. 2023; Masters et al. 2024; Tosi et al. 2024; Van Hoolst et al. 2024; Witasse et al. 2025, all in this collection).

3.1 Mapping of Sub-Surface Induction Electromagnetic Fields at the Icy Moons, and Ocean Tides at Ganymede

The near dipole magnetic field of Jupiter is tilted by about 9.8 degrees to the planet's spin axis and the magnetosphere rotates roughly with the planet's sidereal period (9.93 h), at least out to the co-rotation breakdown in the middle magnetosphere (e.g., Kennel and Coroniti 1975; Hill 1979, 2001; Cowley and Bunce 2001). A magnetodisc is formed mainly due to mass loading stress of volcanic material ejected from Io (e.g., Bagenal and Sullivan 1981; Khurana and Kivelson 1999; Khurana et al. 2004). The magnetodisc will therefore undergo a quasi-periodic motion past the large icy moons of Jupiter, i.e., Europa, Ganymede and Callisto. There are also other magnetospheric processes that will contribute to a highly time-variable magnetospheric environment (e.g., Kivelson et al. 2002; Duling et al. 2014) in the icy moons Keplerian and equatorial orbits around Jupiter (cf. Masters et al. 2024; Van Hoolst et al. 2024, both in this collection).

According to Faraday's law of induction (see Fig. 22) a time-varying magnetic field causes a rotation of the electric field, which in the presence of a conducting (salty) ocean gives rise to induced electrical currents in this ocean that in turn generate a secondary (induced) and opposing magnetic field (e.g., Khurana et al. 1998; Neubauer 1998; Kivelson et al. 2000; Saur et al. 2010, 2015). The primary magnetic field change in the magnetosphere and the induced secondary response in the conducting material will propagate via an Alfvénic disturbance (Alfvén 1942) at the Alfvén speed.

Using induction models and data from the Galileo spacecraft, the existence of an ocean at Ganymede was confirmed (Kivelson et al. 1999). It was however not yet constrained in

terms of its depth and conductivity. To achieve that, suitable coverage (over a wide range of longitudes and latitudes) of the surface of Ganymede is needed for the largest oscillation signals. This was somewhat achieved by Kivelson et al. (2002) by calculating variations in the internal dipole field over a full sidereal rotation period of Jupiter and the five available Galileo flybys. Lack of data did however not yet allow for a clear distinction between a time-varying dipole and a collection of fixed multipoles. This is an issue that JUICE will easily resolve. At Europa, similar methods have already confirmed the presence of a large ocean-induced dipole via the study of the dominant 11 h rotation period oscillation (Kivelson et al. 2000).

RPWI will measure the near DC electric (**E**, and δ**E**) field and the density (δn/n) components of the disturbance, map the ionosphere and magnetosphere currents and their contribution to the induction, and monitor the plasma density and (**E** × **B**) convection of the surrounding variable Jovian (and Ganymede) magnetosphere on a continuous basis. J-MAG will measure the near DC magnetic (**B**, and δ**B**) field. RPWI (and J-MAG) will, for this purpose, use both flybys and the orbital phases of JUICE at Ganymede.

The amplitude and phase delay of the induction response, in the case of a spherical conducting shell and a uniform oscillating magnetic field across it, can be used to determine the radial conductivity structure of the shell. The largest variation in Jupiter's inducing magnetic field is caused by the dipole tilt and occurs for the synodic rotation period (around 10 h for the icy moons), but smaller effects are expected for the orbital periods of the icy moons due to their orbital eccentricities. However, a broad spectrum of electromagnetic variability will affect the icy moons, and this can also be used for sounding the interior impedance at various depths (e.g., Grimm et al. 2020, 2021). In this case where the magnetotelluric method (e.g., Vozoff 1991; Simpson and Bahr 2005; Chave and Jones 2012) is applied, the horizontal electric (E_x) and the orthogonal magnetic (B_y) fields in a broad frequency range is measured above the surface of the icy moons. The source field does not need to be known with this method. The apparent conductivity is calculated from

$$\sigma_a(\omega) = (\omega/\mu)\left|B_y/E_x\right|$$

where the conductivity with depth σ(z) is calculated from the $\sigma_a(\omega)$ by, e.g., Occam's inversion (Constable et al. 1987). The frequency range from micro-Hz to 100 Hz is reachable with RPWI **E**-field and J-MAG **B**-field measurements. The JUICE spacecraft will be in near polar orbit around Ganymede toward the end of the mission, slowly pre-cessing above the surface so as it covers all longitudes by time. It is therefore possible to construct a map of the inferred conductivity profile with depth.

To infer internal ocean properties, the measurements from JUICE RPWI and J-MAG will drive and constrain theoretical induction models which calculate the ocean induction and secondary electric and magnetic fields as a function of the inducing (Jovian) field and ocean properties. Accurate knowledge of the inducing magnetic field is of essence, obtained partly from local measurements and from theoretical models. Note that because the region of interest here is located well within the magnetosphere, random variations in the current sheet due to the solar wind or other external factors are limited. Over the long term, irregular ejections of plasma from Io's volcanic surface may produce additional variations in the plasma-sheet that may not be predicted in any reliable way. Another source of influence on the induced signal may lie within the moons' conductive ionospheres and may account for all the induction signal detected near the moon Callisto (Hartkorn and Saur 2017). Theoretical calculations of ocean induction in the presence of an ionosphere have revealed that the electric field does not seem to decay due to the presence of an ionosphere: large increases in the Alfvén speed counteract the ($1/R^3$) decay in the electromagnetic perturbation.

Mapping of tidal flows in Earth's salty conductive ocean have been made by the Swarm and CHAMP spacecraft by using a spherical harmonic analysis (Egbert and Erofeeva 2002; Grayver et al. 2016, 2017; Tyler et al. 2017; Grayver and Olsen 2019). We plan to combine the RPWI and J-MAG measurement using a similar method to infer the sub-surface ocean tides of Ganymede (if existing) when JUICE is in near polar circular orbit of this moon at 200 and 500 km altitude respectively for numerous Ganymede orbits around Jupiter (a total of 1000+ such orbits are currently planned). This would open the possibility to study also other suggested ocean movements, like a suggested electromagnetically driven equatorial jet (Gissinger and Petitdemange 2019).

3.2 Sub-Surface Ocean Conductivity Determination by Mapping of Auroral Processes

The magnetosphere and the auroral ovals of Ganymede are moving near the surface in latitude as a response to the periodical Jovian magnetodisk flapping motion past this icy moon. An electrically conductive ocean would cause the externally time-varying magnetosphere to reduce the response in Ganymede's magnetosphere due to the induction response within the sub-surface ocean. This has been demonstrated by observation with HST of the oval oscillatory position (Saur et al. 2015), suggesting that a sub-surface ocean indeed does exist at Ganymede and giving constraints on the conductivity of such an ocean.

The JUICE spacecraft will be in near polar orbit around Ganymede toward the end of the mission, slowly pre-cessing above the surface so as it covers all longitudes by time. This means the JUICE spacecraft will pass the south and north auroral ovals 4 times each orbit (see Fig. 23). The position of the auroral oval can be determined by, e.g., the near DC electric field convection identification of the so called low-latitude boundary layer (LLBL, e.g., Morooka et al. 2004; Vines et al. 2017) separatrix to an accuracy of a few km. A sharp poleward boundary was detected by the JUNO Ultraviolet Spectrograph (UVS) (Greathouse et al. 2022). Other auroral indicators can be used as well. Determining the oval position requires ± 10 minutes of electric field measurements over the predicted auroral zone boundary crossings. RPWI need at least 100 crossings (out of at least 4000+ planned such JUICE crossings) to gain enough statistics to determine the auroral oval wiggling variation with longitude and Jovian plasma disk variations, and thereby determine the average internal conductivity variation with longitude, thus further constraining the internal structure of Ganymede's sub-surface and ocean.

3.3 Structure of Icy Crusts

RPWI is designed to be operated as a passive radar sounder to explore the icy moons interior (Fig. 24; Romero-Wolf et al. 2015; Hartogh and Ilyushin 2016; Kumamoto et al. 2018; Schroeder et al. 2016; Carrer et al. 2020; Gerekos et al. 2019; Di Paolo et al. 2020; Roberts et al. 2021; Gassot et al. 2021). The science objectives for RPWI are to characterise the icy moons ice shells and to look for past and present activity. The wide frequency range of RPWI enables us to carry out these radar observations by using intense Jovian radio emissions, such as DAM/HOM (0.4–40 MHz) and bKOM (20–400 kHz), which were observed during the Jupiter flybys by Voyager and Cassini (e.g., Zarka et al. 2004; Cecconi et al. 2012, 2021). The Jovian emission locations can be predicted in advance (Louis et al. 2019a; Cecconi et al. 2021). A correlation is made between the recorded incoming signal from Jupiter with its reflections from the surface and subsurface of a given target icy moon. From the correlation output, it is possible to locate the target features and their respective depths. The

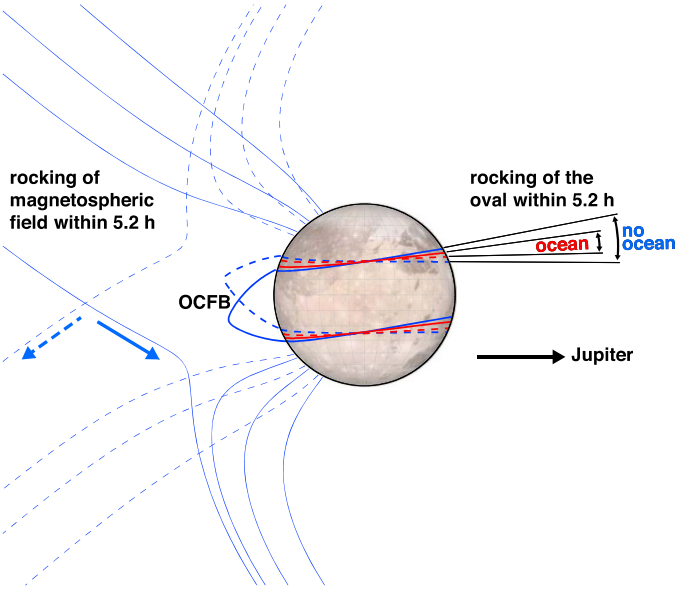

Fig. 23 Simplified sketch of selected magnetic field lines and locations of auroral ovals when Ganymede is above (dashed lines) and below the current sheet (solid lines), respectively. The ovals are located where the open-closed field line boundary (OCFB) intersects Ganymede's surface. The JUICE spacecraft in polar orbit and slowly pre-cessing around Ganymede will encounter a periodically motion of the auroral ovals of Ganymede due to the Jovian magnetodisk motion past this moon. The oscillatory varying location of the oval can be determined with in-situ measurements by RPWI with very high accuracy, thereby giving constraints on the internal conductivity of the moon (picture and partly Figure text from Saur et al. 2015)

frequency range of RPWI observations make it also possible to characterize the roughness of the surface. The possibility to detect subsurface feature by a passive radio acquisition depends on several conditions: (i) the Jovian radio flux density value, (ii) the radar bandwidth, (iii) the integration time, (iv) the surface roughness (v) the attenuation in the ice, (vi) the total electron content (TEC) of the icy moons' ionospheres, and (vii) the orbit altitude.

The RPWI freedom of frequency choice allows us to select frequencies where the noise from the S/C is minimized, but also allows for a correction for the ionosphere delay. One mode of operation centres around 1 MHz and use a bandwidth of about 300 kHz. The TEC of Ganymede's ionosphere was reported to be up to 0.6×10^{16} el./m^2 (Buccino et al. 2022), but can also be provided by the RIME measurements (Bruzzone et al. 2025, this collection). The equivalent distance to the ionospheric delay can be estimated by $c\tau = 40$ TEC / f^2 where f is frequency of the radio wave. It is < 240 km at 1 MHz.

The amplitude of the echoes from the subsurface boundaries will be affected by attenuation in the ice and roughness of the boundaries. Since the conductivity of the ice doesn't depend significantly on the frequency (e.g., Evans 1965; Fujita et al. 2000), low attenuation cannot be expected by changing the observation frequency. On the other hand, the roughness of surface and subsurface boundaries determines the frequency dependence of the echo power, which can be estimated by the radar equation for targets with rough surfaces (Bruzzone et al. 2011):

$$P_{RX} \propto \int_0^\infty \exp\left(-2s^2k^2t^{2H}\right) t\,dt,$$

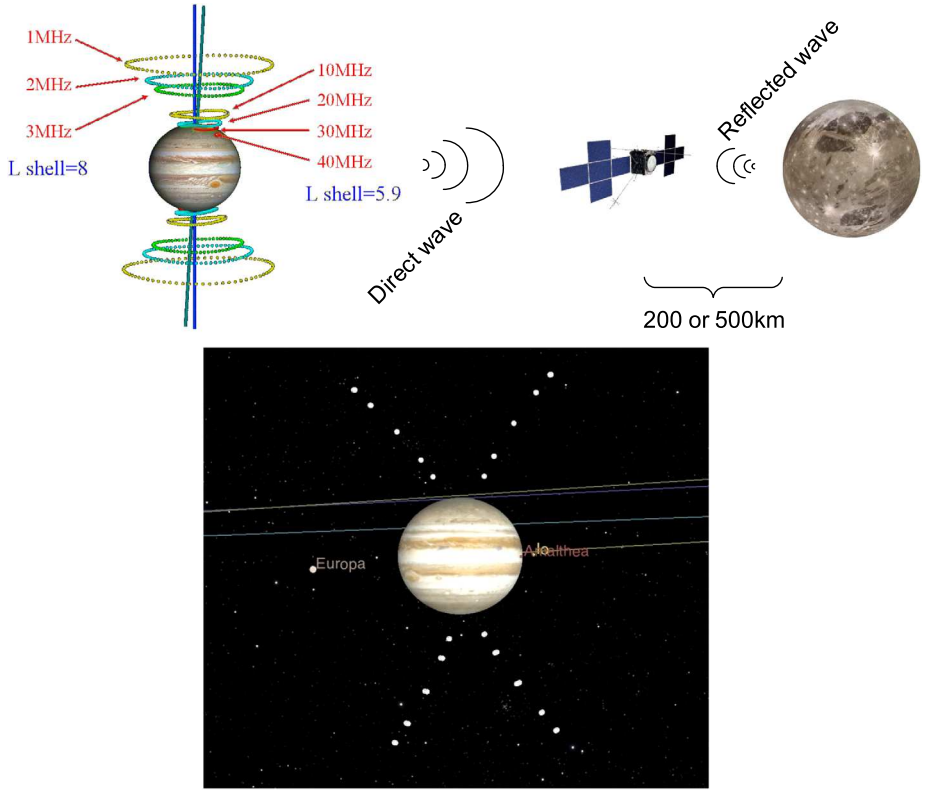

Fig. 24 (a) Illustration of passive radar using Jovian radio waves in wide frequency range by RPWI. (b) The view of Jupiter, the moons, and visible Jovian radio wave sources from RPWI around Ganymede

where k is wave number, s is RMS height for 1 m distance, and H is Hurst exponent (an incident angle of 0 is assumed for simplicity). Typical roughness parameters H and s in several areas of Europa were reported as $(H, s) = (0.75, 0.2)$, and $(0.5, 1.5)$ (Nimmo and Schenk 2008; Steinbrugge et al. 2018). The ratio of the echo power P_{RX} at 1 MHz with respect to 10 MHz is estimated to be 20 dB in the former area while it is estimated to be 40 dB in the latter area. The RPWI observations covering a wide frequency range will thereby be useful to determine roughness of the surface, but also characterise subsurface boundaries.

RPWI plans to operate in three different passive subsurface radar modes, PSSR-1, 2 and 3. When the radio wave propagates from Jupiter to the spacecraft orbiting around the icy moon, and if the radio wave is continuous and its duration is longer than the round-trip delay between the spacecraft and icy moon surface (1.3 ms or 3 ms for a S/C height of 200 km or 500 km respectively, at the sub-Jovian position), the direct radio wave is superimposed by the radio waves reflected at the surface and subsurface boundaries of the icy moon. Due to the superposition of the direct and reflected waves, the amplitude of the wave becomes larger or smaller depending on the phase difference, which also depends on the wavelength. The radio wave spectrum with the interference patterns can be measured in PSSR-1 mode (Kumamoto et al. 2018). Similar interference was observed by the Kaguya spacecraft in orbit around Earth's moon (Ono et al. 2010). In the spectrogram of auroral kilometric ra-

diation (AKR), interference patterns between AKR directly from the Earth and reflected at the surface of the Moon was observed. For Jovian radio bursts with a shorter duration than the round-trip delay in PSSR-2 or continuous noise bursts in PSSR-3, the waveforms of the bursts are sampled directly from Jupiter and reflected at the surface and subsurface boundaries of the icy moons (for monitor and burst observations, respectively). By applying correlation and autocorrelation analysis, time delays, Doppler and polarization (utilizing the three RWI antennas) of the surface and subsurface echoes can then be determined.

3.4 Mapping Jovian Magnetosphere Processes

RPWI will nominally monitor the Jovian magnetosphere continuously in a low telemetry mode, where the electric field (**E**) is sampled at 24 sps and any waves sampling (16k snapshots) and active Langmuir probe or MIME sweeps are made with a long duty cycle (once per 10 minutes or more). Triggered burst measurements (for example using an enhanced DC electric field power trigger, and/or selective downlink of burst data) will be carried out during bow shock and magnetopause crossings, and occasional radio burst measurements will occur during observations of Jovian auroral acceleration events when JUICE is in the high latitude phase. The RPWI measurements in the Jovian magnetosphere aims to study the following conditions/processes:

- Upstream solar wind.
- Global magnetosphere mapping of plasma density (n_e), convection ($\mathbf{E} \times \mathbf{B}$, together with J-MAG), and Jovian radio emissions and their dynamics.
- Current/plasma sheet.
- Co-rotation breakdown (see Sect. 3.13).
- Io torus (remote radio, Sect. 3.15) and Europa torus (in-situ, Sect. 3.11) plasma transport.
- Jupiter aurora (radio, see Sect. 3.14).
- Electromagnetic and plasma wave energy transport (see Sect. 3.5).
- Bow shock and magnetopause (see Sect. 3.5).
- Reconnection in Jovian magnetotail and magnetopause (see Sect. 3.5).
- Whistler and radio waves from Jovian lightning (see Sect. 3.16).

We will not describe these magnetospheric processes in detail here but refer to the given sub-sections and to the associated JUICE review (Masters et al. 2024, this collection).

3.5 Characteristics of Alfvén Waves, Whistler Waves, Plasma Waves in the Jovian and Ganymede Magnetospheres Including Their Boundary Processes

There have been sporadic reports from plasma wave measurements within the Jovian magnetosphere from many spacecraft (Pioneers, Voyagers, Ulysses, and Galileo) in the past (e.g., Gurnett et al. 1983a; Stone et al. 1992; Shprits et al. 2018), but few in-depths interpretations. Somewhat more efforts have been put into Ultra Low Frequency (ULF) waves and turbulence, such as electromagnetic ion cyclotron waves (EMIC), and their role in Jupiter's magnetosphere (e.g., Petkaki and Dougherty 2001; Tao et al. 2015; Manners and Masters 2020). Also there exist several reports on plasma waves during close encounters with the Galilean moons (see further Sects. 3.7 through 3.12).

However, recent Juno observations in the auroral acceleration regions closer to Jupiter (Sulaiman et al. 2022; and references within) have shown that auroral bidirectional energetic electron acceleration, proton acceleration, and field-aligned currents are associated with large amplitude broadband Alfvén wave activity and plasma density cavities, and it has

been suggested that an ionospheric Alfvén resonator (Polyakov 1976; Sato 1978; Belyaev et al. 1990) can account for the broad energy of the field-aligned electrons (e.g., Saur et al. 2018; Lysak et al. 2021) and electric currents are set up in the ionosphere (auroral electrojet, Boström 1964). On Earth plasma auroral density cavities are related to auroral acceleration processes (e.g., Persoon et al. 1988; Paschmann et al. 2003; Alm et al. 2014, 2015), and it is further related to two main types of acceleration processes; inverted-V electric potential structures (Alfvén 1958; see further Sect. 3.8) and ionospheric dispersive Alfvén wave cascade (Hasegawa 1976; see further Sect. 3.8). The latter process is believed to be more important for the generation of Jupiter's aurora (Clark et al. 2018). Dispersive Alfvén waves on Earth generate broadband emissions (e.g., Gurnett and Frank 1977; Chmyrev et al. 1989; Boehm et al. 1990; Louarn et al. 1994; Wahlund et al. 1994, 1998, 2003; Stasiewicz et al. 2000a,b; Chaston et al. 2001, 2008; Streltsov and Karlsson 2008) and are observed together with upgoing transversely heated ionospheric ions (e.g., Temerin and Roth 1986; André et al. 1988) and down going field-aligned electrons (e.g., Boehm et al. 1990). This has been interpreted as a positive feedback mechanism, whereby small-scale Alfvén waves cascade to higher ion mode frequencies and erode the auroral ionosphere by facilitating transverse ion acceleration and resulting ion outflow, which in turn leads to deeper density cavities that maintain the production of small-scale Alfvén waves via refraction and phase mixing of incoming large-scale Alfvén waves (e.g., review by Haerendel 2011, and references therein; see further Sect. 3.8). The inertial Alfvén waves are associated with a parallel electric field component, which accelerates electrons as beams along the magnetic field.

JUICE will during its high-inclination phase reach between 33 – 38° jovi-graphic latitude during 15 – 18 flybys (depending on finally selected JUICE trajectory), using gravity assist by Callisto each occasion. This high latitude phase allows for the first prolonged studies of the mid-latitudes of the Jovian magnetosphere with high-resolution in situ measurements at distances near to $\sim 25 R_J$ at ∼45° magnetic latitude. This would allow, for example, for a long temporal baseline study of the Jovian auroras including remote sensing in UV and IR wavelengths in combination with monitoring of magnetospheric dynamics through RPWI Alfvén and plasma waves measurements. It also allows for a detailed analysis of the plasma flows at mid-high magnetic latitudes which will magnetically map to the outer magnetosphere and tail, tackling the major question of solar wind versus co-rotation effects. This, in turn, will make it possible to study the correlation of reconnection or injection events in the magnetosphere with resulting auroral emissions and detailed studies of the moon footprints. Furthermore, it facilitates detailed studies of the region of the magnetosphere where the rigid corotation of the plasma flow breaks down (region of field-aligned current maps into the main auroral oval – inner pair of dashed green lines in Fig. 25, see further Sect. 3.13), and beyond to higher latitudes. The high-latitude orbits give coverage of the field lines and field-aligned current systems well poleward of the main oval into the polar region - to the edge of the open field lines according to this simple model.

RPWI will be able to determine the full electrodynamic and electromagnetic environment along the JUICE trajectory. For instance, all waves will be sampled with the full vector electric and magnetic fields giving polarization and Poynting flux as well as waveform, and in some operation modes also $\delta n/n$, near-continuously below 180 Hz, and with a duty cycle below 20 kHz. The electric waveform can be sampled up to 1.5 MHz, giving information on electron wave modes. RPWI therefore provides excellent capabilities to measure plasma waves and plasma density which will allow characterization of the boundary processes in the magnetosphere of Jupiter and Ganymede. Measurements of the full vector electric ($\delta \mathbf{E}$) and magnetic ($\delta \mathbf{B}$) components of waves in a broad frequency range together with high resolution plasma density measurements (by several methods) allow for identification of

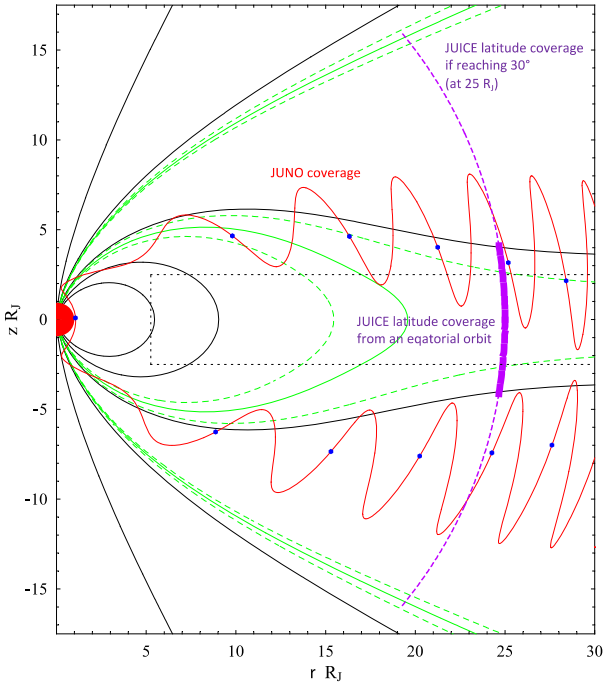

Fig. 25 Jupiter's magnetic field (black and green) in magnetic coordinates, where the green field lines (dashed and solid) mark the regions planned to be covered by JUICE in its high-latitude and equatorial phases at a 25R$_J$ conjugate radial position (using Callisto flybys to reach the higher latitudes). The regions where field-aligned currents map into the main auroral oval is marked with pairs of dashed green lines. Trajectory coverage show the arc (purple) of a circular orbit at 25R$_J$ that will be covered by a 30°inclined phase in magnetic coordinates. The heavy dashed purple line near the equator shows the coverage for an equatorial orbit, i.e., ±9.5° about the equator as the magnetic dipole rotates. The lighter dashed purple parts correspond to a 30° orbit, which extends the range to ±39.5° about the equator. An example Juno orbit is shown in red for comparison (adapted from Cowley et al. 2008 by Emma Bunce, credit Stan Cowley, University of Leicester)

low-frequency waves as kinetic Alfvén waves (KAW), medium frequency waves such as lower hybrid drift waves (LHDI), whistlers, electrostatic solitary waves, and high frequency Langmuir and upper-hybrid waves, and beam wave modes. All these waves provide important information about the kinetic plasma processes related to plasma heating and particle acceleration, as well as energy and plasma transport at magnetospheric boundaries.

Waves can be used for identification and characterization of plasma boundaries. RPWI plasma density measurements will allow to identify density gradients. High-resolution measurements of magnetic field measurements by SCM and J-MAG will allow to identify thin current sheets. It is difficult to determine the boundary speed and thus the spatial scale, and presence of strong lower-hybrid drift waves can be used as an indicator of thin ion-scale boundaries with strong density gradients (Graham et al. 2019), such as the magnetopause boundary close to a reconnection site. Waves around reconnection regions provide a unique footprint, and this can be used to identify reconnection regions (Khotyaintsev et al. 2019). Detection of Whistler waves, knowledge of their wave-normal angle and direction of propagation from the Poynting flux can be used to identify open-closed field boundaries. Reconnection leads to creation of a loss-cone electron distribution close to the open-closed boundary; such distributions are difficult to resolve in the particle data but can be identified

through whistlers propagating towards the reconnection site. Also, KAWs can indicate that a region is connected along the magnetic field lines to an active reconnection X-line. Separatrices - the regions where field-aligned electrons beams are often present can be identified from Langmuir waves, and electrostatic waves (Viberg et al. 2013). Regions of active magnetic flux pile-up like at the fronts of reconnection jets can be identified using field-aligned Whistler waves (Khotyaintsev et al. 2011).

Plasma waves which will be measured by RPWI will allow us to characterize several different processes in different boundary regions. At the magnetopause the waves processes participate in plasma entry and mixing across the boundary, cross-field diffusion, reconnection, finite gyro-radius effects, unsteady reconnection. The magnetopause of Ganymede will be crossed multiple times, so we will collect a large database to quantify these processes (see further Sects. 3.6 and 3.7). In the magnetotail the waves contribute to plasma heating and acceleration, particle dynamics at reconnection jet fronts, pitch-angle scattering, energy transport by wave Poynting flux (whistlers and KAWs). In the Alfvén wings we expect the waves drive plasma heating and ion outflow.

3.6 Determine the Magnetospheres-Ionosphere Couplings at Ganymede

Ganymede has, unlike most other moons in the solar system, an intrinsic magnetic field strong enough to produce a mini magnetosphere of its own residing in the vastly much larger magnetosphere of Jupiter (Kivelson et al. 1996). As the ambient plasma flow in Jupiter's magnetosphere is both sub-Alfvénic and sub-magnetosonic at the orbit of Ganymede there is no bow shock forming but instead Alfvén wings are formed (Neubauer 1998). The ionosphere of Ganymede (see Sect. 3.7) is created by ionisation of its atmosphere. Magnetosphere-ionosphere coupling involves the process of transporting energy and momentum from one region within a plasma environment to another. This typically involves electric currents, often mediated by Alfvén disturbances, that travel along magnetic field lines on a global scale. The global current systems that are set up in this system are strongly affected by the coupling between Jupiter's magnetosphere and Ganymede's magnetosphere. An interaction region upstream, between the southward directed magnetic field of Jupiter and the northward directed magnetic field of Ganymede (not unlike the situation arising between a southward magnetic field in the solar wind and Earth's magnetosphere for instance) sets up a system of complex electromagnetic interactions. At the magnetopause upstream of Ganymede, magnetic reconnection is likely to occur, as are the formation of current sheets (e.g., Tóth et al. 2016; Zhou et al. 2020). Accelerated particles triggered by the reconnection processes, including acceleration by dispersive Alfvén waves and electrostatic potential structures on auroral field-lines (see Sect. 3.8), can travel to either the atmosphere of Jupiter or Ganymede itself and cause auroral emissions there. Tailward of the moon, a magnetic wake forms with somewhat stretched out magnetic field lines, allowing for field-aligned currents to flow and possibly also cause ion outflows via the plasma sheet (e.g., Jia et al. 2009). As the Jovian magnetospheric flow is sub-magnetosonic the magnetosphere will become cylinder-shaped with the axis aligned with the external magnetic field direction, in contrast to the parabola-shaped magnetosphere of a body embedded in the solar wind.

JUICE instruments including RPWI will sample this interaction region via several close flybys (12 planned) and during the Ganymede orbiting phases toward the end of the mission. These begins with 122 days (≈240 orbits) in highly elliptic (300 km – 10,000 km) or high altitude (5000 km) orbits, followed by circular orbits at 500 km and 200 km altitude for 156 days (≈1150 orbits). This may change somewhat depending on the final trajectory decision still to be made. Thus, there are many passes through relevant regions of the magnetosphere

of Ganymede where the dynamic electrodynamic coupling can be studied, and wherefrom a coherent observational picture can be formed.

RPWI is planned to do continuous measurements of the electric field and thermal plasma near Ganymede and will investigate the physical processes occurring in the interaction region between Ganymede and the ambient Jovian magnetosphere by utilizing a wide range of measurements and associated data products. Cold plasma (ion and electron) density, temperature and flow velocity and associated (thermal) pressure terms will be measured using the GANDALF and MIME experiments. Three-dimensional electric ($\mathbf{E}$, $\delta\mathbf{E}$) and magnetic fields ($\delta\mathbf{B}$) using both GANDALF and SAMWISE will be measured which will allow for detection of certain wave modes present that are involved in the energy and momentum transfer in this coupling region (see further below and Sect. 3).

3.7 Mapping Structure and Variability of the Ionosphere and Magnetosphere of Ganymede and Related Electrodynamics and Thermal Plasma Outflow

The ionosphere and magnetosphere of Ganymede was detected by the Galileo plasma wave and magnetic field instruments (Gurnett et al. 1996; Kivelson et al. 1996), while the on-board radio sounding experiment gave upper constraints for the electron density near the surface of a few 1000 cm^{-3} and the uncertainty was attributed to the possible non-spherical geometry of the limb observation toward the wake (Kliore 1998). Further analysis of the plasma wave and plasma analyser (Frank et al. 1997) data and associated preliminary modelling gave an O_2^+-O^+ dominated ionosphere with near surface densities not more than 2500 cm^{-3} for the two closest Galileo G1 and G2 flybys (Eviatar et al. 2001). The plasma wave observations furthermore showed a variety of emissions common in planetary magnetospheres, like whistlers, cyclotron waves, upper hybrid waves, broadband noise at the lower frequencies below the ion plasma frequency, but also possible radio waves created in the magnetosphere of Ganymede (Gurnett et al. 1996; Kurth et al. 1997).

Recent measurements by the Juno spacecraft during a distant flyby (c/a 1046 km) provided both new plasma (Allegrini et al. 2022; Valek et al. 2022), waves (Kurth et al. 2022) and new ionospheric occultation results (Buccino et al. 2022). The wave data revealed broadband emissions (dispersive Alfvén wave cascade?) in the magnetospheric wake possibly related to reconnection and heavy ions (3 – 24 cm^{-3}), Whistler waves and electron cyclotron harmonics emissions, and an obliquely propagating chorus associated with few 100 eV precipitating electrons contributing to Ganymede's aurora. The two-limb radio occultations gave no ionospheric peak signatures but rather an exponential increase toward the surface with maximum electron densities of about 1000 – 2000 cm^{-3} close to the surface. The error in the egress signal (on closed magnetic field lines) was large though and could be a non-detection. The ingress signal on the other hand was a detection and occurred for open magnetic field lines, indicating that electron impact ionization was important. The ion composition data revealed ionospheric ions (O_2^+, O^+, H_2^+, H^+, and H_3^+), but the inferred positively charged ion density was ∼2.5 times larger than the electron density from the plasma wave data (Allegrini et al. 2022; Valek et al. 2022). These ions were flowing outward along the magnetic field and belonged to a cold ionospheric plasma (thermal energies up to tens of eV). The peak outward flux of O_2^+ was about 5×10^{11} ions/m^3/s. Detailed theory investigations have studied the atmosphere-ionosphere-magnetosphere coupling processes and their variability under different conditions (e.g., Leclercq et al. 2016; Fatemi et al. 2016; Leblanc et al. 2017; Poppe et al. 2018; Carnielli et al. 2019, 2020a,b; Vorburger et al. 2022; Leblanc et al. 2023). Photo- and particle-impact ionization of the atmosphere gives rise to an ionospheric plasma, which fills most of the magnetosphere (Galand et al. 2025). For an

atmosphere dominated by O_2 close to the surface, the most abundant ionospheric species inferred are O_2^+ followed by O^+, H_2^+, and H_2O^+ (e.g., see Table 3 in Carnielli et al. 2019). Though a large part of the oxygen ions impacts the surface and constitute a source for the atmosphere (Carnielli et al. 2020b), the rest of the oxygen ions as well as most of the other ionospheric ions flows outward and escapes the magnetosphere through the Alfvén wings or through the plasma tail (in co-rotation direction).

Cold plasma with temperatures only slightly higher than the corresponding atmospheric source of ions can dominate the number density of the space environment of the icy moons and within their tails along their orbits within the Jovian magnetosphere. Such cold plasma outflow can drastically change the Alfvén speed and the conditions for magnetic reconnection (Toledo-Redondo et al. 2021) and it is in this respect interesting that broadband dispersive Alfvénic activity seems to exist in the wake of Ganymede (Kurth et al. 2022). The (cold) plasma also significantly influences the spacecraft charging (e.g., Morooka et al. 2009; Bergman et al. 2020), which will be continuously monitored by RPWI. Hence mapping the locations, transport and energisation of cold plasma may be complicated but is important for understanding the Jovian system.

RPWI will study the ionosphere and magnetosphere of Ganymede with several in-situ techniques (cf. Sect. 2.8), but also apply ionosphere occultation cut-off of Jovian radio emissions (with a radio burst mode, cf. Sect. 2.5.1 and 5.8.2). The RPWI instrument has several important advantages for measuring the densities of the bulk ion and electron components, including the possibility of detecting the negatively charged ion and nm-sized dust populations (if existing). This will be sampled nominally every 30 – 600 s with Langmuir probe sweeps (cf. Sect. 2.2) and mutual impedance sweeps (cf. Sect. 2.3), but density monitoring can, if needed, be sampled continuously at a rate of 763 sps to detect sharp density gradients. Different Langmuir probes can simultaneously sample the electron and positive ion densities separately. These can usually be cross calibrated against upper hybrid, Langmuir wave and other plasma wave emissions. The plasma convection ($\mathbf{E} \times \mathbf{B}$) can be inferred from combined RPWI and J-MAG measurements. This will give needed information of plasma transport within the Jovian plasma disc and Ganymede magnetosphere, the icy moons outflow flux and other plasma flow patterns. The RPWI full vector capabilities of measuring electrostatic and electromagnetic waves ($\delta\mathbf{E}$ and $\delta\mathbf{B}$) up to 20 kHz will be used to study the energy transport (Poynting flux, polarization) between local particle populations, or over long distances with (dispersive) Alfvén waves.

3.8 Characterize Ganymede Auroral Processes

The first indications of auroral emissions from Ganymede was made by UV oxygen emission lines by the HST (Hall et al. 1998). It was inferred from the analysis of these lines (130.4 and 135.6 nm) that they were produced by electron impact ionizations of an O_2 dominated atmosphere. Further HST observations revealed the auroral ovals, and these were located at a higher latitude on Ganymede's hemisphere facing the co-rotation plasma stream of the Jovian magnetosphere and that the emissions varied strongly with time and longitude (Feldman et al. 2000; McGrath et al. 2013; Molyneux et al. 2018; Marzok et al. 2022). MHD models of the Jovian magnetosphere interaction with the magnetosphere of Ganymede supported the idea that the Ganymede aurora occurred near the boundary between open and closed magnetic field lines (e.g., Jia et al. 2009; Zhou et al. 2019). The higher resolution Juno UVS measurements showed an intense narrow auroral curtain ($<5°$) with a sharp poleward boundary ($<2°$) near the open-closed magnetic field boundary, and there are less intense emissions equatorward of the curtain on closed magnetic field lines (Greathouse et al.

2022). The emissions were inferred to originate from within 25 – 50 km of the surface of Ganymede. The JUNO in-situ plasma wave measurements (Kurth et al. 2022) showed both broadband (Alfvénic?) emissions in the wake magnetosphere of Ganymede possibly related to reconnection, and an obliquely propagating chorus associated with few 100 eV precipitating electrons contributing to Ganymede's aurora. JUNO encountered only open magnetic field-lines.

It is tempting to compare with the auroral processes on Earth. However, the interaction with Jupiter's nearly co-rotating magnetosphere is sub-magnetosonic (and sub-Alvénic), causing the Ganymede magnetosphere to develop Alfvén wings from the polar regions and a bow shock should not form upstream the magnetopause (Neubauer 1998; Kivelson et al. 1998, 2004). The Alfvén wings are connected via magnetic flux tubes to Jupiter itself, and there cause an auroral footprint. These emissions produced in the Jovian upper atmosphere are caused by dispersive Alfvén waves with Poynting fluxes of $\sim$100 mW/m^2, creating electron acceleration up to several keV toward Jupiter's atmosphere (Szalay et al. 2020b). This Alfvén wave activity should also propagate in the other direction along the magnetic flux tube toward Ganymede and there these waves would become inertial when hitting its polar ionosphere (increased Alfvén speed) and produce field-aligned precipitating electrons. The Juno UVS did not detect corresponding emissions in the Ganymede polar cap, but could be due to the electron energies involved, and this need be studied more in detail by JUICE.

On Earth there are two main auroral forms: diffuse aurora and discrete arcs. It could be reasonable to relate these to the two forms detected by JUNO UVS (Greathouse et al. 2022). Diffuse aurora (which can pulsate) is mostly associated with precipitating electrons or ions injected from mostly the plasma sheet and scattered into a loss cone by plasma waves (e.g., Sandahl et al. 1980; Newell et al. 2009; Nishimura et al. 2020). Scattering of electrons by chorus waves accounts for intense inner magnetosphere electron precipitation (e.g., Cully et al. 2011), while electrostatic electron cyclotron harmonic waves dominate the nightside at high L-shells (e.g., Ni et al. 2011; Kurita et al. 2014). Scattering by electromagnetic ion cyclotron (EMIC) waves is also a lead candidate for ion precipitation (e.g., Yahnin et al. 2021).

Discrete aurora is also associated with several different acceleration processes of charged particles. The suggestion that parallel electric fields, aligned with Earth's magnetic field, accelerate particles producing aurora was first made by Alfvén (1958). Experimental evidence of parallel electric fields has since been presented from both sounding rockets and satellite missions (e.g., Mozer and Bruston 1967; Block 1972; Mozer et al. 1977; Lindqvist and Marklund 1990; Chust et al. 1998; Mozer and Kletzing 1998; Ergun et al. 1998, 2002, 2004; Marklund et al. 2001, 2011), and the resulting acceleration of electrons creates what is often called an "inverted-V" structure. The theory behind auroral cavities and electrostatic potential drops are in good agreement with theoretical modelling (Block and Fälthammar 1968; Knight 1973; Janhunen et al. 2002), and reviews on the subject exist (e.g., Karlsson et al. 2020; Borovsky et al. 2020; Lysak et al. 2020).

Another acceleration process is caused by inertial Alfvén waves and broadband Extremely Low Frequency (ELF) waves. Hasegawa (1976) showed that Alfvén waves with small perpendicular scale lengths could support a finite fluctuating parallel electric field in the magnetosphere or topside ionosphere above the aurora. Broadband ULF/ELF emissions have been observed on many spacecraft in the boundary between the auroral oval and the polar cap, being the transition between open and closed magnetic field lines (e.g., Gurnett and Frank 1977; Chmyrev et al. 1989; Boehm et al. 1990; Louarn et al. 1994; Wahlund et al. 1994, 1998, 2003; Seyler et al. 1998; Stasiewicz et al. 2000a,b; Chaston et al. 2001, 2008; Streltsov and Karlsson 2008). These emissions have been interpreted as turbulent Alfvénic

activity (or Alfvénic aurora) propagating down the magnetic field lines and breaking up to higher frequency components below the ion plasma frequency and is characterized by large downward Poynting flux (e.g., Volwerk et al. 1996; Wahlund et al. 2003; Keiling et al. 2002, 2019a,b) and a transfer of its energy into precipitating electrons up to keV energies, transverse ion acceleration and resulting ion outflow in a divergent magnetic field. The theory behind dispersive Alfvén waves (DAW) and its turbulent cascade is reasonably understood (e.g., Goertz 1984; Lysak and Lotko 1996; Schukla and Stenflo 2000; Stasiewicz et al. 2000b; Chaston et al. 2008; Lysak 2023), but the observed processes also include several non-linear wave-wave and wave-particle interactions which needs further studies.

The JUICE mission can characterize the processes responsible for the aurora on Ganymede, where RPWI, J-MAG, PEP and UVS will all contribute to understand this phenomenon to a knowledge level we already have of aurora at Earth. The near polar orbital phase of JUICE with a slow precession around Ganymede, and at different altitudes from 5000 km down to 200 km will globally cover the study of Ganymede auroral acceleration regions, both the in-situ processes and remote effects. There are four crossings of the auroral oval each orbit, and RPWI will do high-resolution measurements ± 10 minutes across each. The RPWI sensors measuring plasma and electromagnetic waves ($\delta\mathbf{E}$, $\delta\mathbf{B}$) can identify the wave characteristics like polarization and Poynting flux, and the near DC electric field ($\mathbf{E}$) can identify both large and small scale electrostatic potential drops on auroral magnetic field lines, and RPWI (together with J-MAG and PEP) can infer the electric currents and related instabilities causing the particle precipitation and plasma outflow processes in detail.

3.9 Determine the Structure of the Europa Ionosphere & Related Electrodynamics and Ion Outflows During the Flybys

The Jovian magnetospheric interactions with the icy moons are characterized by the formation of Alfvén wing structures (e.g., Drell et al. 1965; Neubauer 1998, 1999; Kivelson et al. 1999, 2004; Volwerk et al. 2007). The interaction is a result of a sub-Alfvénic magnetized plasma flow with a conducting body, e.g., with its ionosphere or a sub-surface conducting material. In the case of Europa, ion pickup mass-loads the magnetic field lines and divert and slow them down, creating electric currents which exert a $\mathbf{j} \times \mathbf{B}$ force doing the deacceleration. The flow is basically un-affected at the poles of Europa, and this forms a velocity shear along a bended structure from the poles. The electromagnetic disturbance is propagated along the polar flux tubes by the Alfvén speed, and Alfvén wings are created. The bending angle is roughly given by $\theta_A = \tan^{-1}\left(\upsilon_{flow}/\upsilon_A\right)$. More detailed MHD and hybrid interaction scenarios of involved processes have been presented (e.g., Blöcker et al. 2016; Harris et al. 2021; Addison et al. 2021). At the Jupiter endpoint of the Alfvén wing flux tubes of the icy moons (the magnetic footprints) there exist auroral like emissions (e.g., Bonfond et al. 2017, and references therein). The electron precipitation caused by, and associated field-aligned currents carried by, dispersive Alfvén waves near these magnetic footprints of the icy moons have been observed by the JUNO spacecraft instruments (e.g., Szalay et al. 2020a; Allegrini et al. 2020b; Rabia et al. 2023).

Much published knowledge of the thermal plasma environment of Europa comes from Galileo flybys and numerical simulations, but also a recent Juno flyby. The review by Bagenal and Dols (2020) summarises many relevant studies and their Figs. 1 and 10 give an overview of the Io-Europa space environment and the thermal ion sources at Europa, respectively. A major source of ions at Europa is the impact of electrons giving approximately 20 kg/s O_2^+, with photo ionization being a less important source (Saur et al. 1998; Dols et al. 2016). Simulations suggest that a few times 10^{24} thermal (about 100 eV) O^+ ions per second

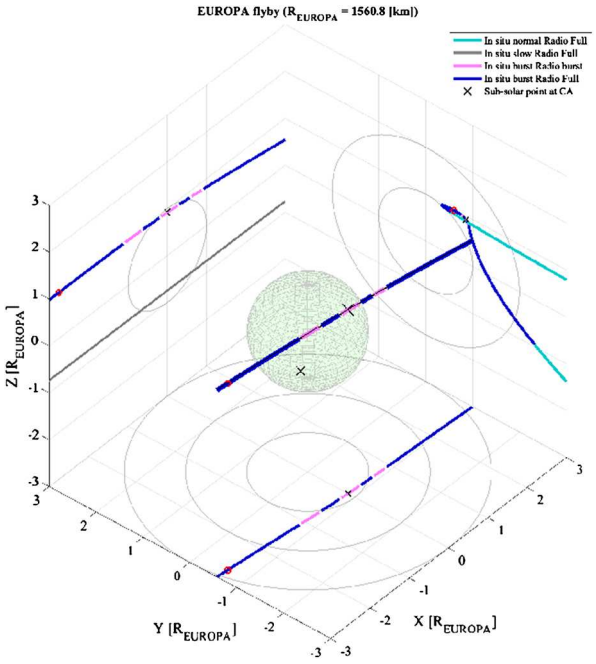

Fig. 26 The first JUICE flyby of the moon Europa. The second one occurs in the south, but with a similar path through the tail. Detailed operation requests and related planning have so far only been carried out for the first flyby. RPWI measures in electric field burst mode for the in-situ measurements with the Langmuir probes and SCM. Radio burst (pink) is used for Jovian radio occultation measurements of the ionosphere range profile. The Europa wake region is marked with circles in the Z-Y-plane projection. JUICE will spend a long time in the Europa wake

from the plasma disc co-rotating with Jupiter cause sputtering of particles from the moon's surface, while another significant part of the plasma disc flow is diverted due to interaction with the ionosphere (Harris et al. 2022).

The ionosphere of Europa was detected during five (of six) limb radio occultation measurements onboard Galileo (Kliore et al. 1997), which showed a rather dense ionospheric plasma up to $10^4 cm^{-3}$ close to the surface. The altitude profiles assume a spherically symmetric configuration, which is probably not the case for Europa's ionosphere, so the exact altitude profiles can be inaccurate. This ionosphere is also a conductive region affecting the electrodynamic interaction with the magnetosphere of Jupiter (e.g., Saur et al. 1998) and where there are electric currents flowing in response to the corotation convection electric field across Europa and where the field-aligned currents in the Alfvén wings close. The interaction causes the ionosphere to be strongly asymmetric by the magnetospheric convection and dragged through the tenuous atmosphere (and frictionally heated) and out into a tail "behind" the moon (in corotation direction). The Galileo plasma wave measurements during nine flybys detected electron cyclotron harmonics on the upstream ram side, widespread Whistler (or chorus) emissions and upper hybrid resonance enhancements within $2R_E$ of the moon, as well as highly variable electrostatic noise in the plasma wake (Gurnett et al. 1998; Kurth et al. 2001). Recent Juno plasma wave observations during a high inclination flyby at 355 km distance and through the wake region (Kurth et al. 2023) also detected chorus emissions, upper hybrid band and broadband electrostatic waves (ESW) below a few kHz with a magnetic component at the lowest frequencies. The ESW coincide with periods of bi-directional magnetic field-aligned electron beams at energies below 300 eV. The ESW could therefore be the cascade of Alfvénic turbulence to higher frequencies, like what is observed in the auroral region of Earth (cf. Sect. 3.8).

Two flybys of the moon Europa at 400 km altitude are planned for JUICE. These occur over geologically active regions near closest approach and pass inside and along the

plasma wake (Fig. 26). For the first flyby RPWI focus on the near DC electric field (**E**) and waves (δ**E**, δ**B**) and electrodynamics. Continuous electric field measurements up to 763 sps, and 16k snapshots up to 694ksps are planned. For the second flyby, see Sect. 3.10. Associated with the JUICE spacecraft moving along the trajectory, Jovian radio emission sources ($<$1 MHz) will gradually become occulted by the ionospheric plasma near the surfaces of the icy moons. From the radio cut-off frequencies of these emissions, we hope to gain range profiles of the topside ionosphere, with the cooperation of the occurrence of Jovian radio emissions. This remote sensing capability can provide the vertical distributions of the ionospheric densities, as well as episodic plume ejections triggered by crustal activities (cf. Sect. 5.8.2).

3.10 Characterize the Plasma, Dust, and Electrodynamics of Possible Plumes

There are putative Europa plume candidates observed in far-ultraviolet spectroscopy and imaging observation by the Hubble Space Telescope (HST, e.g., Saur et al. 2011; Roth et al. 2014a; Sparks et al. 2016) as well as Galileo spacecraft in-situ measurements (Jia et al. 2018; Arnold et al. 2019). However, the HST spectroscopic image detection could not be repeated (Roth et al. 2014b), and the pure imaging observations are associated with uncertainties and was explained by purely statistical fluctuations (Giono et al. 2020). Therefore, there is no definitive evidence for plumes at Europa from the UV observations. The in-situ measurements by Galileo stems from magnetic and electron density measurements in reasonable agreement with MHD models applied to one event (Kurth et al. 2001; Kivelson et al. 2009; Jia et al. 2018). The electron density is estimated from plasma wave data but consist of only two enhanced samples, while the magnetic field data indicate the presence of local electric currents nearby the spacecraft. It is clear though that a close encounter provides the best opportunities to resolve the issue and give detailed information of the physics and chemistry state of potential plume(s) (e.g., Vorburger and Wurz 2021). JUICE aims to target its two flybys above active surface regions of Europa, and its current trajectory seems to encounter possible plume material (Winterhalder and Huybrighs 2022). The JUICE Jupiter tour, however, need freeze by mid-2028, so any tweaks of the JUICE trajectory due to a detection of more exact plume location will be restricted.

A great deal of information on how to probe active plumes can be gained from the detailed studies by the Cassini spacecraft of the geysers emanating from the geologically active south polar region on the small icy moon Enceladus. From there gas and ice grains are continuously being expelled and form a water rich plume (Dougherty et al. 2006; Porco et al. 2006; Spahn et al. 2006; Waite et al. 2006; Morooka et al. 2011; Postberg et al. 2018). Many in depth studies have been conducted with various instruments regarding the plume physics based on direct fly-through observations by the Cassini spacecraft (e.g., Spitale and Porco 2007; Cravens et al. 2009; Krupp et al. 2012; Engelhardt et al. 2015). The plume material is for instance salty and contains phosphates (e.g., Postberg et al. 2009, 2011, 2023). The plume has also been found to contain partially ionized material including negatively charged nanograins (e.g., Tokar et al. 2006, 2009; Jones et al. 2009; Morooka et al. 2011; Shafiq et al. 2011; Hill et al. 2012; Farrell et al. 2010; Dong et al. 2015), where the densities of electrons, ions and negatively charged dust increase to several orders of magnitude compared to the surrounding magnetosphere of Saturn. Newly ejected material from the plume (both ions and charged dust) becomes picked up and accelerated by the Kronian magnetospheric flow (e.g., Tokar et al. 2008; Pontius and Hill 2006; Fleshman et al. 2010; Farrell et al. 2012, 2014). Enceladus is the primary source of sub-micron sized dust in the E-ring (e.g., Kurth et al. 2006; Spahn et al. 2006), which consists predominantly of negatively charged water

ice (Kempf et al. 2006, 2008, 2010; Hillier et al. 2007), and plays an important role in the dust plasma interaction there (Wahlund et al. 2005, 2009; Farrell et al. 2017). Enceladus and its electrically conductive plume act as an obstacle to Saturn's magnetospheric plasma flow and causes large scale perturbations around the moon (e.g., Dougherty et al. 2006; Saur et al. 2007; Engelhardt et al. 2015). The magnetospheric flow slows down due to mass loading of material from the plume, and results in a magnetic field pileup region upstream of Enceladus' plume (Dougherty et al. 2006; Morooka et al. 2011). The neutral-ion collisions generate perpendicular (Pedersen and Hall) currents inside the plume, which are then thought to close along the magnetic field lines (Kriegel et al. 2011; Simon et al. 2014; Engelhardt et al. 2015) and cause an auroral footprint in Saturn's ionosphere (Pryor et al. 2011). Clear signatures of accelerated electrons are observed at the edges of the plume, which are also associated with auroral hiss emissions (Gurnett et al. 2011; Leisner et al. 2013) also closer to Saturn (Sulaiman et al. 2018). These are along wedge shaped regions (the so-called Alfvén wings) like those observed at Io (Neubauer 1980). These Alfvén wings are the magnetic wakes caused by a moving plasma flow around a stationary conductive obstacle, in this case the plume. Many of the findings from Enceladus can with advantage be considered also for the Europa plume since both are the results from expulsion of dominantly water from a subsurface and therefore should have some general physical similarities. There are also distinct differences: Due to Europa's larger mass and gravity, most of the ejected material will return to the surface. Only the fastest particles, with speeds exceeding the 2 km/s escape speed will be fed directly into the environment. Moreover, Europa possesses a global atmosphere, maintained by charge particle sputtering and sublimation of the surface and consisting primarily of O_2 (Hall et al. 1995, 1998; Johnson et al. 2009; McGrath et al. 2009). Near the sub-solar point, H_2O might be equally or more abundant than O_2 (Roth 2021; de Kleer et al. 2023), also affecting the ionosphere (Li et al. 2020). Therefore, any signals affected by the gas and plasma environment must be interpreted carefully to distinguish between different sources of the gas, including possible active plumes.

The RPWI, with its ambitious *in-situ* sensor suite, can further the science of the electrodynamics and structure of a Europa plume to an unprecedented level not possible by any other spacecraft instrumentation. Potential cracks in the ice on any of the large icy moons and potential associated plume formation can be detected much more easily by *in-situ* studies close to these moons. For Europa, RPWI considers two different sets of measurements for the two JUICE flybys, one focusing on the near DC electric field ($\mathbf{E}$) and waves ($\delta\mathbf{E}$, $\delta\mathbf{B}$) and electrodynamics, the other focusing on high time resolution simultaneous electron (n_e) and ion (n_i) density and inhomogeneity measurements ($\delta n_e/n_e$ and $\delta n_i/n_i$, at 763 sps and 49ksps) and the structure of a potential dust-plasma interactions in a water exhaust plume. Both sets include μm-sized dust measurements from RPWI.

3.11 Characterize the Plasma and Dust of Europa Torus and Near the Icy Moons

The plasma environment near the moon Europa (and Io) has recently been reviewed (Bagenal et al. 2015; Bagenal and Dols 2020; Masters et al. 2024, this collection). A dominant source of plasma in the orbit of Europa originates from the volcanic moon Io. An extensive cloud of neutrals and dust is expelled from Io (estimates are 1 – 2 ton/s), which is partly ionized and expand outward toward the orbit of Europa in a few tens of days and fills most of the magnetosphere of Jupiter with a heavy mass plasma (e.g., O^+, S^+, SO^+, SO_2^+, Na^+, H^+, and multiple charge states, Bagenal et al. 2017a; Huscher et al. 2021). Typical densities in the disk range from about 30 to 0.1 cm^{-3} at 10 to 30 R_J, and thermal energies increase from about 100 eV in the Io torus to several keV at tens of R_J. This Io torus is also generating powerful Alfvén waves mediating strong electric currents along the magnetic field

toward Jupiter, radio, and plasma waves. Charge exchanges between co-rotating plasma and this neutral cloud further produce a sizable amount of energetic neutral atoms detectable by, e.g., the JUICE PEP-Hi instrument (see Barabash et al. 2025, this collection). The characteristics of the plasma and dust in the orbit of Europa is also affected by expelled (and ionized) material from the moon Europa itself which forms a possible additional torus in its orbit (e.g., Mauk et al. 2003; Smith et al. 2019; Szalay et al. 2022; Roth et al. 2023) consisting mostly of molecular hydrogen and oxygen and being ionized mostly to H_2^+, H^+. This constitutes the Europa torus, which is embedded within the Io torus variations.

A dust component of μm-sized grains may also exist within both the Io and Europa tori, but also close to the icy moons (e.g., Krüger et al. 1999, 2003; Thiessenhusen et al. 2000; Krivov et al. 2002; Liu and Schmidt 2019; Kurth et al. 2023), which are different populations as compared to the electric antenna detection of similar sized dust around the ring plane near Jupiter (Ye et al. 2020) by the JUNO spacecraft. The belief here is that hypervelocity impacts of interplanetary micrometeorids ejects dust particles from the moons. RPWI measurements electric pulses with four Langmuir probes can reveal from where and when the ejected dust particles leave the surface of the moons. There exists clear decrease of 0.2 – 2 μm-sized grains outward with radial distance from Jupiter (Soja et al. 2013) with a few 100 grains/km^3 close to Europa. This number was predicted to increase by 2 – 3 orders of magnitude during flybys of the icy moons at closest approach.

The RPWI sensors will monitor the electric field (**E**), wave activity, plasma density, and dust hits within the orbit of Europa and close to Europa. Several JUICE flybys through the predicted Europa torus exist including two close flybys of Europa itself, and frequent close encounter visits exist of Ganymede and Callisto, including the orbital phase of Ganymede. While the plasma density variation of the Europa plasma torus could be hard to separate out from the plasma disc variations, the wave activity and electric fields affecting charged particles (and charged dust) will be continuously monitored. The dust counting will be made with the four Langmuir probes in electric field modes as well as when sampling currents (density mode). This is very similar to the method of electric field spikes detected with antenna on several other missions (e.g., Aubier et al. 1983; Gurnett et al. 1987, 1983b, 1991; Kurth et al. 2006; Meyer-Vernet et al. 1996, 2009; Zaslavsky et al. 2012; Ye et al. 2014, 2016, 2019, 2020). The dust counting algorithm that RPWI uses is based on the one used on Solar Orbiter (Zaslavsky et al. 2021; Soucek et al. 2021). An important difference here is that RPWI will make use of the four Langmuir probes instead of the RWI antenna elements, and the Langmuir probes make use of both differential and single ended measurements simultaneously and almost continuously at 49ksps (up to 25% duty cycle). With this method we expect 0.01 – 10 dust hits/s to be detected in the relevant regions.

3.12 Determine the Structure of the Callisto Ionosphere & Related Electrodynamics and Ion Outflows During the Flybys

Callisto has a dense ($\sim 10^4$ cm^{-3}), asymmetric, and highly variable ionosphere (Kliore et al. 2002) that interacts with the nearly corotating and highly time variable magnetosphere of Jupiter (e.g., Khurana et al. 1998) forming Alfvén wings and a plasma wake around Callisto (e.g., Neubauer 1999). The plasma environment at the Callisto orbit has been observed by Galileo and Juno (Bagenal et al. 2016; Kim et al. 2020; Huscher et al. 2021). The Jovian plasma disc at this orbital distance includes O^+, S^{2+} (about 60% of the total charge density) together with other charge states of O and S, with typical densities and energies of about 0.3 cm^{-3} and 1 – 10 keV. Much of the predictions of the local plasma around Callisto comes from simulations (e.g., Lindkvist et al. 2015; Galli et al. 2022). Atmospheric models indicate

densities from 10^6 to above 10^8 cm^{-3} (depending on conditions and assumptions) for H_2, H_2O and O_2 at altitudes of a few hundred km (e.g., Carberry Mogan et al. 2022).

The ionosphere was best detectable on the magnetospheric nearly co-rotating ram side at the same time this hemisphere was sunlit (Kliore et al. 2002), indicating that both plasma impact ionization and photoionization in an impact sputtered atmosphere are important for its formation. This ram-dayside ionosphere had a clear peak at about 25 – 50 km altitude and similar scale heights. The Galileo magnetic field data also for this icy moon revealed a strong induction signature indicative of induced electric currents in a salty conductive sub-surface ocean (Khurana et al. 1998). However, results from an atmosphere-ionosphere model of Callisto (Hartkorn et al. 2017; Hartkorn and Saur 2017) pointed to that induced electric fields and electric currents in a conductive ionosphere could instead account for a large part of the observed induction response. The salty sub-surface ocean would in this case not exist or be situated deeper in Callisto's interior. On the other hand, the asymmetry of Callisto's ionosphere and atmosphere, affecting the Pedersen and Hall conductivities, together with an applied magnetospheric motional electric field ($\mathbf{E} \sim 10$ mV/m) and a highly time variable electric field, $\delta\mathbf{E}$(t), induced by the streaming and variable Jovian magnetosphere give rise to complex electrodynamic system not easily inferred by theory alone. A detailed mapping of the ionosphere-atmosphere-surface and its dynamic interaction with the Jovian magnetosphere and inferring the electric current system around Callisto must be carried out to resolve the issues.

Some Galileo spacecraft flybys, using the plasma wave instrument, show plasma densities up to 400 cm^{-3} at altitudes just above 500 km (Gurnett et al. 2000). This is about three orders of magnitude higher than the ambient thermal plasma density in the Jovian plasma disc, showing that significant plasma outflow may be expected. The JUICE trajectory during more than 20 flybys of Callisto will often have a closest approach around 200 km, which is well above the ionospheric peak, but RPWI in-situ measurements can nevertheless give information on cold plasma properties like the topside ionospheric plasma density, electron temperature and scale heights. Galileo plasma wave observations also reveal upper hybrid band emissions and broadband electrostatic wave activity (Gurnett et al. 2000).

RPWI will employ the full in-situ electric field and thermal plasma measurements during most Callisto flybys (see Sect. 2.7). Here the 22 JUICE flybys where several are as close as 200 km altitude will be extra important. An example is shown in Fig. 27. An example RPWI will also carry out radio occultation measurements using Jovian radio emission cut-offs. A coverage of these with respect to solar zenith angle (SZA) and plasma ram angle is displayed in Fig. 28.

3.13 Characterize Processes Behind the Co-Rotation Breakdown in the Jovian Magnetosphere

As a consequence of Jupiter's intense internally generated magnetic field and rapid rotation, much of Jupiter's magnetosphere is in a so-called "rotationally-dominated" regime, in which the dynamics of the magnetospheric plasma are largely controlled by coupling via the ionosphere to the rotating neutral atmosphere. However, the (radial) extent of this control is ultimately limited, such that enforcement of a state of rigid corotation is maintained only out to distances of $\sim$15 – 20 R_J, beyond which the plasma sub-corotates, having azimuthal velocities that are only a fraction of the local corotation velocity (McNutt et al. 1979). Prior to the arrival of Juno at Jupiter, the generally accepted framework held that mechanical stresses, transferred along magnetic field lines between the polar ionosphere(s) and equatorial magnetosphere by field-aligned currents were primarily responsible for the main auroral

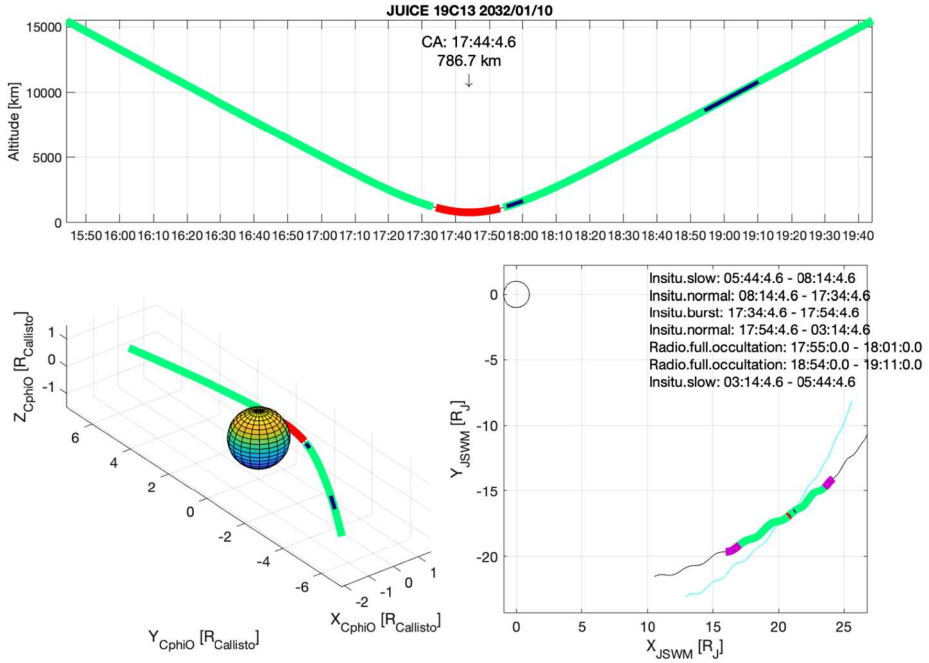

Fig. 27 RPWI planned operations near a distant flyby of Callisto. We plan to do in-situ burst operations for Langmuir probes in electric field modes and SCM at closest approach (red). Ionospheric occultation of Jovian radio emissions is planned at special times when these radio waves pass through the ionosphere of Callisto (two cases, black)

emissions observed at Jupiter (see e.g., summaries provided by Achilleos et al. 2015 and Bagenal et al. 2017b). This paradigm has been extensively explored in models ranging from one-dimensional purely analytical approximations to spatially resolved numerical simulations (e.g., Hill 1975, 1979; Cowley and Bunce 2001; Nichols 2011; Chané et al. 2013), and was generally found to reproduce well both the available in-situ particle and field data from missions such as Voyager and Galileo, as well as remote observations of auroral emissions made, e.g., by HST (e.g., Clarke et al. 2009). However, more recent observations made by Juno instrumentation of auroral structures, plasma waves, precipitating particle distributions and the Jovian field at high latitudes have in some respects challenged the accepted model of the Jovian main emissions (e.g., Bonfond et al. 2020). Specifically, evidence in both particles and fields for significant energy fluxes into the polar ionosphere carried by broadband-accelerated electrons and Alfvenic fluctuations appears to suggest a component of the Jovian magnetosphere-ionosphere-atmosphere coupling due to aspects not originally considered (see e.g., Gershman et al. 2019; Kotsiaros et al. 2019; Allegrini et al. 2020a; Mauk et al. 2020).

The measurements to be made by RPWI in the Jovian magnetosphere are expected to contribute to studies of the process of corotation breakdown in the equatorial plasma in several ways, all of which are intrinsically related to studies of the general spatial and temporal structure of the equatorial magnetosphere and magnetodisc. For example, quasi-continuous monitoring of the local plasma density is obtained by RPWI using various methods, which together can be used to construct maps of the magnetospheric thermal plasma structure, as well as its thermal and kinetic energy content (dominated by its azimuthal velocity). Spatial

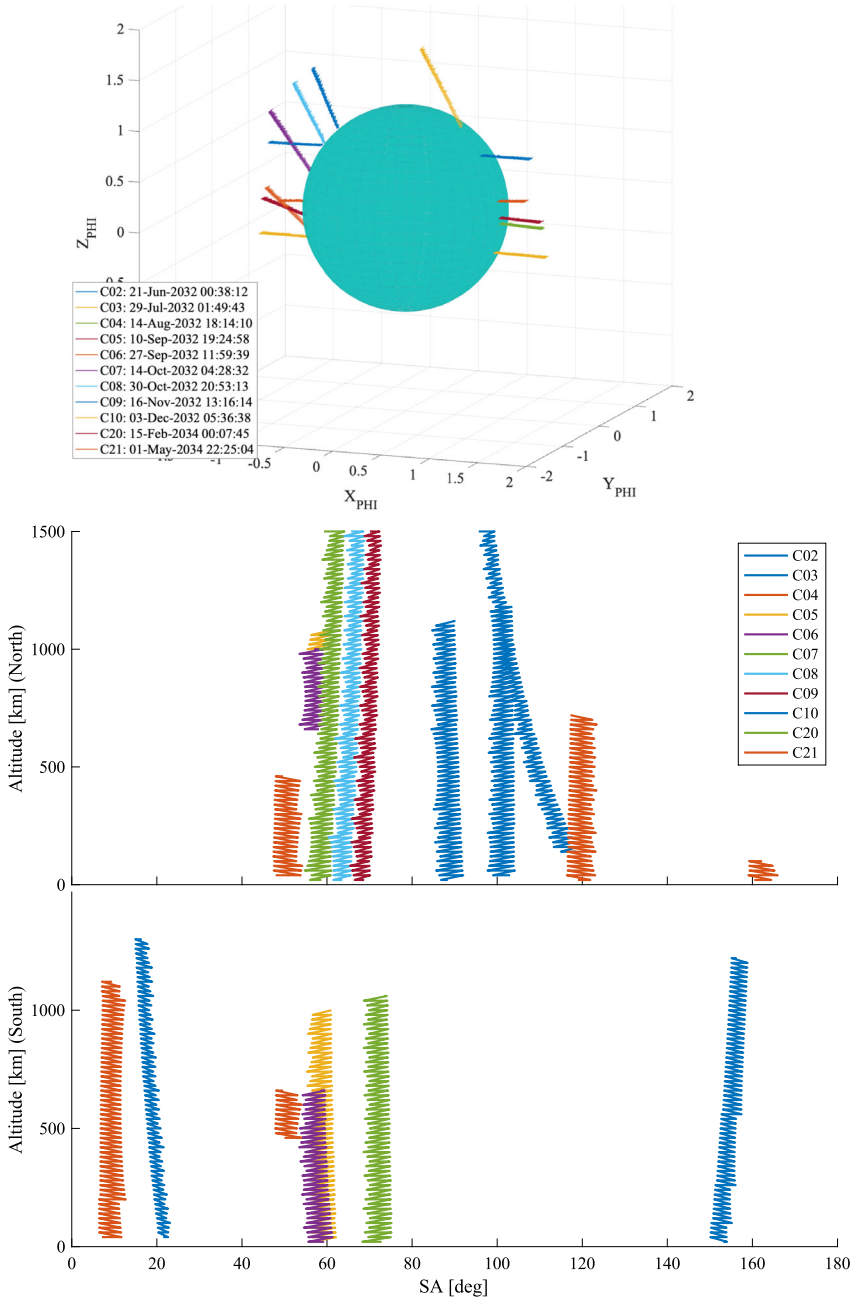

Fig. 28 Coverage of ionosphere measurements from RPWI radio occultations of Jovian decametric radio emissions. Panel A: The magnetospheric plasma ram arrives from −X (+X is Callisto wake). The different coloured lines are the radio occultation traces with altitude up to 1500 km. The ionosphere plasma is expected to be encountered below about 300 km with a peak in the 50 – 100 km range. Both the ram-side and the wake-side can be covered. Panels B & C show the coverage of radio occultations with respect to solar zenith angle (SZA) and where B is North hemisphere and C the South hemisphere

gradients and inhomogeneities in these parameters yield information as to the forces acting on and within the plasma in the magnetodisc. Such observations can be used to provide further constraints on, e.g., the action of the interchange instability and radial plasma transport, the spatial (local time and radial) extent over which corotation breakdown occurs, as well as externally and internally forced temporal variability in these processes. Measurements of the quasi-DC electric field combined with J-MAG data can give the $\mathbf{E} \times \mathbf{B}$ drift velocity of the ambient plasma. From this, departures from rigid corotation can be quantified both in terms of their magnitude and spatial variation throughout the regions sampled by JUICE, as well as monitoring any temporal variations associated, e.g., with magnetospheric compressions and expansions. Similarly, in certain circumstances, interferometry techniques can be employed to study the motion of plasma structures (δn/n) across the spacecraft, yielding measurements of ambient plasma flow over a limited range of relative velocities (e.g., LaBelle et al. 1986; Kintner et al. 1987; Holmgren and Kintner 1990; Wahlund et al. 1998, 2009; and references therein; see also Sect. 2.2.2).

Simultaneous measurements of Jovian auroral radio emissions provide a mechanism to infer both the internal state of the magnetosphere, as well as detecting any transient changes associated with external forcing by solar wind variations - critical drivers of the system that may otherwise generally only be inferred by extrapolated solar wind conditions from other solar system missions and heliospheric modelling. Local plasma wave measurements over a broad frequency range, including wave propagation characteristics including polarization and Poynting flux provide information as to the transfer of energy between different regions, which can be analysed together with, e.g., estimates of quasi-DC field aligned currents provided by J-MAG.

3.14 Determination of Dynamics of the Jovian Magnetosphere Through Radio Emissions

The first measurements of radio waves from the neighbourhood of Jupiter were reported by Burke and Franklin (1955) and since then many different types of observations have been made in the radio spectrum both from ground and from spacecraft. The JENRAGE experiment will have the sensitivity to detect all components of the Jovian magnetospheric radio emissions (high latitude auroral and satellite-induced Cyclotron-Maser (CM) emissions, low-latitude plasma emissions, e.g., from the Io torus, atmospheric lightning radio waves) from the kilometer to the decameter wavelength range (Zarka 1998; Zarka et al. 2004; Louis et al. 2021). Figure 29 summarizes the source location and beaming for most of these components.

JENRAGE only has a marginal capability of detecting the fast-drifting S-bursts (Zarka et al. 1996; Mauduit et al. 2023), but all other emissions varying slower than a few seconds will be observed in flux density and polarization together with the direction of arrival of the waves, thanks to JENRAGE's goniopolarimetric capability. Dynamic spectra of CM emissions will be compared to simulations done using the code ExPRES (Louis et al. 2019a) and relying on the most recent Jovian magnetic field model (Connerney et al. 2022). Refracted propagation paths from the sources, especially at low frequencies, will be studied using the ARTEMIS-P code (Gautier 2013). Finally, RPWI radio measurements will be complemented or correlated with measurements from other remote sensing instruments onboard JUICE (particles, UV aurorae, magnetic field, etc.), as well as with other ground-based and space radio observations.

As its trajectory will not bring JUICE much closer to Jupiter than the orbit of Europa, radio measurements will rather be of synoptic nature. They will allow us to address the

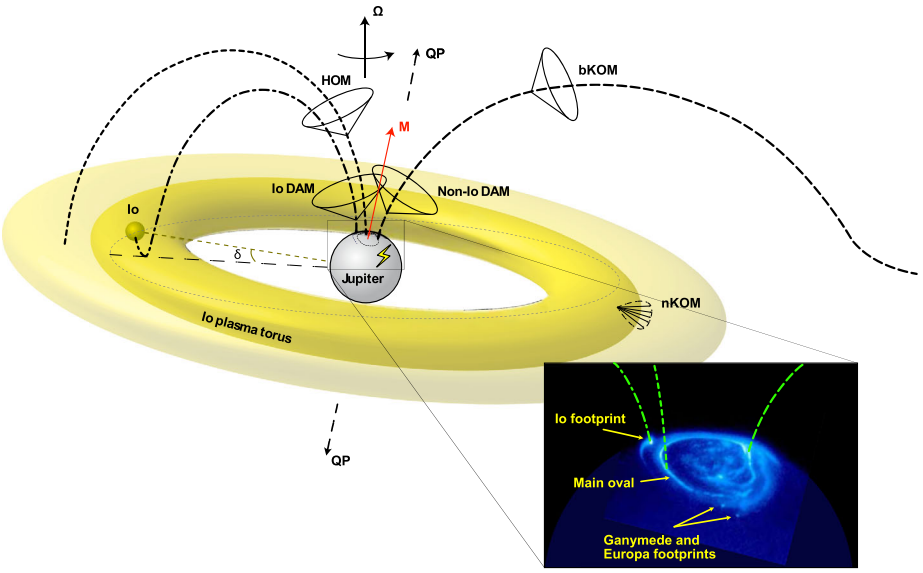

Fig. 29 Jovian natural radio sources observable by JUICE/RPWI. The radio emissions are mostly produced in the jovian auroral regions, by energetic particles traveling along magnetic field lines and resulting in unstable distribution functions. The radio emission pattern is not isotropic: the radio waves are emitted along a thin hollow cone represented in the Figure. The approximate location of the io-controlled decametric (Io-DAM), auroral decametric (non-Io-DAM), hectometric (HOM), narrow-band kilometric (nKOM), brand-band kilometric (bKOM) and quasi-periodic bursts (QP) components. For instance, Io-DAM emissions are only visible when the emission cone is illuminating the observer. The longitudinal lag between the magnetic longitude of Io and that of the Io-controlled radio sources (the so-called lead-angle) is represented by the δ angle. Vector M and Ω represent the magnetic and rotation axes of Jupiter, respectively. In the bottom-right corner, sub-figure shows an HST UV image of the Jovian auroral components (Galilean moon footprints, main oval and polar emissions), which are produced by the same populations of particles as the radio components. The lightning symbol in Jupiter represents the electromagnetic counterpart of atmospheric lightnings. This plot is modified from Zarka 2000 & Cecconi et al. 2012

following objectives concerning the dynamics of the Jovian magnetosphere, to understand better:

(1) the internally controlled dynamics by observing the so-called energetic events (Louarn et al. 2014, 2015), that correspond to outward centrifugal plasma transport and particle injections associated to radio intensifications; RPWI measurements will allow us to compare the variations of all Jovian radio components together with plasma variations, and to document the recurrence time of these events and their relationship with Io's volcanic activity (see Sect. 3.15). It will explore the origins of the so-called system IV period, related to corotation lag within Io's torus (Reiner et al. 1993) but also affecting more surprisingly some auroral decameter emissions (Panchenko et al. 2010, 2013).

(2) the externally controlled dynamics by measuring the response of radio emissions to interplanetary shocks (forward and reverse) (Hess et al. 2014; Louis et al. 2023), the delay between excitation and response, the different behaviour of the different parts of the magnetosphere (dawn- or dusk-side).

Following Zarka et al. (2021) who proposed a method for comparing quantitatively the level of internal versus external control for each radio component, Boudouma et al. (2023) established that the hectometer (HOM) emission mainly originates from the dusk side of Jupiter's magnetosphere, where the plasma disc is thicker and more turbulent (Kivelson and

Southwood 2005) and the aurora brighter (Bonfond et al. 2015). The question remains open for other components. Combined with ground-based and Juno radio observations, RPWI observations may allow us to address longer-term variations depending on Jovian season or the solar cycle.

JENRAGE measurements will also address questions related to the generation of radio waves:

- The strongly needed long-term (3.5 years) goniopolarimetric measurements will allow us to precisely identify the source location of all radio components, from decametric to kilometric range (in particular the surprising but well-defined decameter components A' and A", Marques et al. 2017). Lower frequency radio components, such as QP-bursts (MacDowall et al. 1993; Morioka et al. 2006; Kimura et al. 2012), or the narrowband low-frequency – nLF – component (Louis et al. 2021), will be observed with GANDALF since JENRAGE only observes down to 80 kHz. CM radio sources will be related to the auroral morphology (diffuse aurora, zones I & II, Louis et al. 2019b; Sulaiman et al. 2022; Collet et al. 2023). The radio beaming, measured along with source location, is important both for, e.g., improving ExPRES simulations and for being applied to exoplanetary radio emissions to derive emitted power from measured flux densities (Callingham et al. 2021).
- Measurements up to $\sim 30^\circ$ latitude may allow us to identify the transition from observed circular to elliptical polarization (Reiner et al. 1995) as a function of the frequency (with measurable Faraday rotation when elliptical polarization is present (Lecacheux et al. 1991), that can be modelled with ARTEMIS-P and has deep implications on the wave generation and near-source plasma content (Lecacheux 1988).
- CM radio emissions seem to be mostly produced at an oblique angle relative to the magnetic field in the sources (Hess et al. 2008; Mottez et al. 2010), via the loss-cone driven CM instability (Louarn et al. 2017) whereas growth rates are generally higher for shell-driven CM instability (Hess et al. 2007, 2008).
- What is the origin of peculiar emissions in Jovian radio dynamic spectra such as Zebra (Panchenko et al. 2018) or the high frequency "splitting" at the upper frequency of decameter radio emission (Leblanc and Rubio 1982)?

3.15 The Io Torus Dynamics and Related Radio Emissions

Radio emissions induced by the interaction of Galilean satellites with Jupiter's magnetic field are not limited to the case of Io. Ganymede- and Europa-induced emissions have been unambiguously identified (Louis et al. 2017; Zarka et al. 2018; Jacome et al. 2022) and their detailed characteristics will be studied by JENRAGE and compared to the plasma environment of these satellites. For such radio sources restricted to a single magnetic flux tube, JENRAGE observations will be used together with an accurate Jovian internal field model (Connerney et al. 2022) and be compared to ExPRES simulations to give strong constraints on the radio beaming angle (possibly azimuth-dependent (Galopeau and Boudjada 2016; Louis et al. 2017)), the Alfvén propagation time between the satellite and Jupiter and the energy of emitting electrons (Lamy et al. 2022, 2023; Zheng et al. 2023). Despite the tentative detection of a UV footprint associated to Callisto (Bhattacharyya et al. 2018), the existence of CM radio emissions induced by Callisto remains an open question which will be tackled by JENRAGE.

The torus also generates emissions at or near the local plasma frequency, such as the narrowband kilometer - nKOM (Reiner et al. 1993) and perhaps the nLF (Louis et al. 2021)

components. The variations of nKOM are related to the system IV period and to energetic events (see previous section). The dynamics of the torus, and that of the Jovian magnetosphere at large fed by the torus plasma, can be affected by Io's volcanism (Yoneda et al. 2010, 2013). This variability can be studied via that of the Io- and Io torus related radio components (nKOM, Io-decameter).

3.16 Characterize Wave Emissions from Lightning at Jupiter

The first detections of lightning in Jupiter's turbulent atmosphere were made with the Voyagers spacecraft when bright spots on Jupiter's nightside were imaged with the camera (Cook et al. 1979) and whistlers were detected with the radio instrument onboard Voyager 1 (Gurnett et al. 1979). Those were long dispersion whistlers lasting for several seconds, recorded at frequencies of a few kHz in the Io plasma torus between 5 to 6 Jovian radii. Surprisingly, none of the radio instruments on-board the Voyagers, Ulysses, Galileo, Cassini or Juno ever detected sferics (radio signals from the atmosphere) at Jupiter in a frequency range of 1 to 40 MHz. This is in marked contrast to Saturn, where Saturn Electrostatic Discharges are $\sim 10^4$ times more intense than terrestrial lightning radio emissions in this high frequency (HF) range (Fischer et al. 2008). The reason for this is unclear, but it could be due to strong absorption of these radio waves in Jupiter's lower ionospheric layers (Zarka 1985). Farrell et al. (1999) attributed the non-detection of the HF component to the decrease of the spectral power with increasing frequency. However, this is in contradiction to the surprising detection of prevalent lightning sferics at 600 MHz with the Juno Microwave Radiometer (Brown et al. 2018). New Jovian lightning detections with Juno were also made below 150 kHz: The so-called Jupiter dispersed pulses (JDPs) were recorded by the Juno Waves instrument at frequencies between 10 and 150 kHz with dispersions in the millisecond range at distances below 5.5 Jovian radii. They might propagate in the free-space ordinary mode through low density regions of Jupiter's ionosphere (Imai et al. 2019). Furthermore, close to Jupiter, rapid whistlers at frequencies from 50 Hz to 20 kHz with dispersions from units of milliseconds to tens of milliseconds were also detected (Kolmašová et al. 2018). Recently, groups of radio pulses (JDPs and rapid whistlers) with typical time separations of one millisecond were identified in the Juno Waves data. This finding suggests step-like extensions of Jovian lightning channels and indicates that lightning initiation processes at Jupiter are similar to the initiation of intracloud lightning at Earth (Kolmašová et al. 2023). All these detections with Juno have led to the largest data set on Jovian lightning collected to date. Due to the large periapsis distances of JUICE ($\sim$9 to 20 Jovian radii) it will be much more difficult for JUICE to detect lightning radio pulses compared to Juno. However, it is not excluded that RPWI will detect whistlers from very high latitudes, JDPs passing through ionospheric holes, or maybe the missing HF component. Further details about optical thunderstorm and lightning observations with JUICE can be found in the paper by Fletcher et al. (2023, in this collection).

3.17 Cruise Science by RPWI

Any cruise science by JUICE is for the moment on best effort basis by the project. The launch of JUICE (April 14, 2023) allows though for a close flyby of the moon, a Venus flyby, three flybys of Earth and measurements through the asteroid belt. Conjunctions are also looked for with another spacecraft such as Solar Orbiter, Parker Solar Probe, BepiColombo and the soon to be launched Europa Clipper. We here provide a short list of the RPWI cruise science opportunities.

- *Earth flyby*:
  - o Compare with radio emissions & whistlers from lightning $\pm 20\ R_{Earth}$
  - o Compare with measurements from Wind/WAVES and Cluster allowing for two-point measurements of the beaming of AKR
  - o Part of calibration runs near Earth
- *Moon flyby*:
  - o Test Passive Sub-Surface Radar (PSSR) with AKR as source
  - o Lunar wake measurements
- *Solar system dust & solar wind interaction characterization:*
  - o LP-PWI & SCM to do continuous monitoring of plasma and dust counts
  - o ... in the orbits of Venus and Earth
  - o ... make a dust count profile through the asteroid belt.
- *Conjunctions with another spacecraft for solar wind studies:*
  - o BepiColombo, Solar Orbiter, Parker Solar Probe, Europa Clipper conjunctions within 5° latitude/longitude and within 0.1 AU to be able to probe the same solar wind plasma. Here RPWI will monitor solar wind ion flux, $\mathbf{E} \times \mathbf{B}$ (with J-MAG), and plasma turbulence.

4 Instrument Design

4.1 General Design

Figure 30 shows the RPWI overall block diagram, where a redundant set of Data Processing Units (DPU) and Low Voltage Power Supplies (LVPS) controls the four main experiments of the instrument package. Physically, the SCM and RWI preamplifiers are installed inside the SCM and RWI sensors boxes (chassis), while the LP-PWI preamplifiers are situated at the roots of the LP-PWI booms near the S/C surface (i.e., not within the spherical Langmuir probes).

The RPWI consists of products, as shown in Fig. 30.

- EBOX, which is the main electronic unit where all data from the sensors is collected and processed as well as power distribution and TM/TC communication to the S/C.

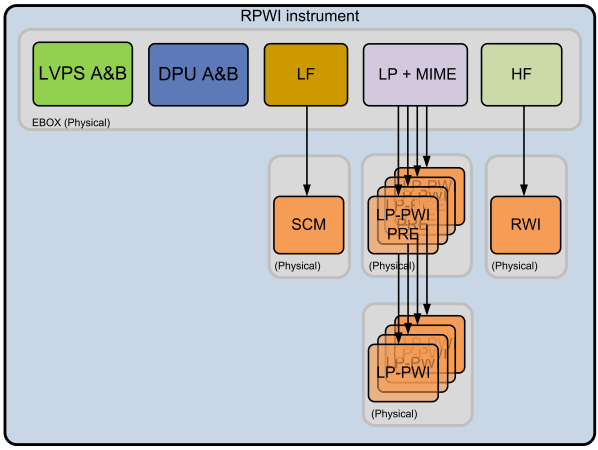

Fig. 30 RPWI physical architecture

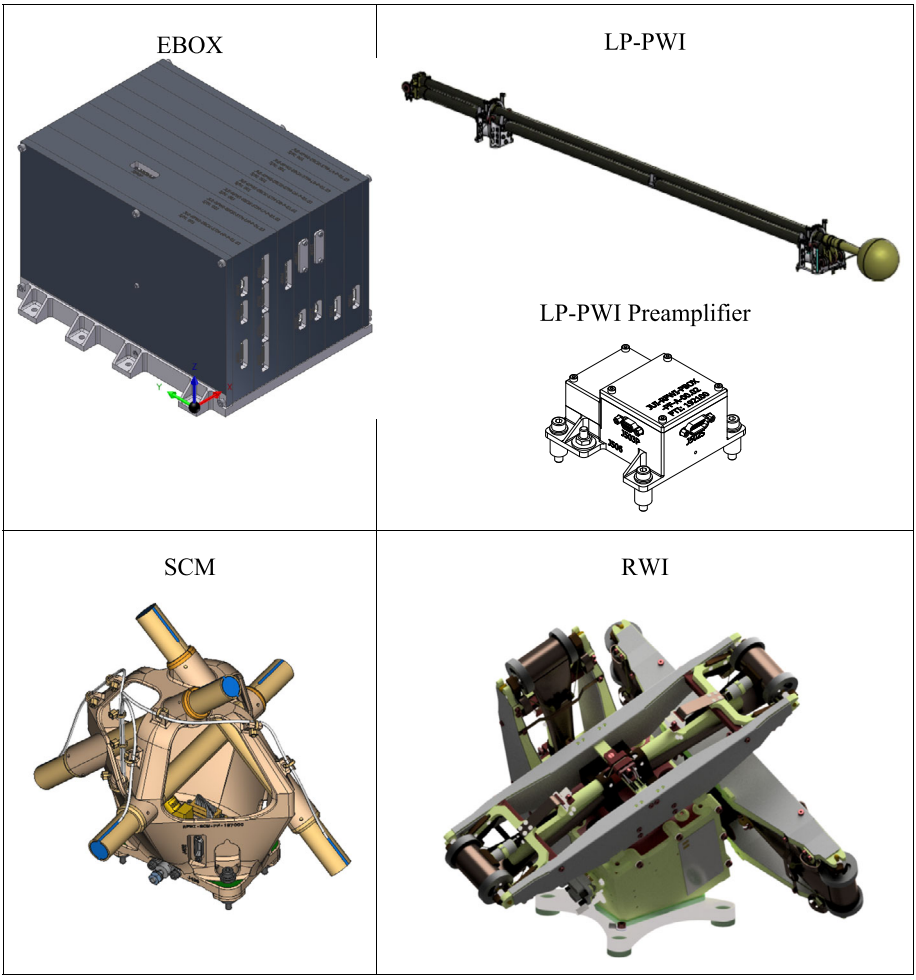

Fig. 31 Main RPWI units. Top left: main electronics box (EBOX), Top right: LP-PWI boom unit and preamplifier. Bottom left: Search-coil magnetometer (SCM). Bottom right: RWI antenna system (stowed). The SCM and RWI boxes are covered by their multi-layer insulations (MLI)

  - o LVPS (A&B), Low Voltage Power Supply. Primary and redundant side.
  - o DPU (A&B), Digital Processing Unit. Primary and redundant side.
  - o LF (Low Frequency) Receiver.
  - o LP-MIME (Langmuir Probe & Mutual Impedance Measurement) Transceiver.
  - o HF (High Frequency) Receiver.
- LP-PWI, which consists of four Langmuir probes and (deployable) booms.
- LP-PWI Preamplifiers, which consists of four LP preamplifiers, and external harnesses.
- SCM, which consists of the tri-axes search coil antenna and preamplifier with an external harness along the MAG boom.
- RWI, which consists of the three collocated (deployable) dipole antennas and preamplifiers, with its external harness along the MAG boom.

The RPWI subsystems are shown in Fig. 31.

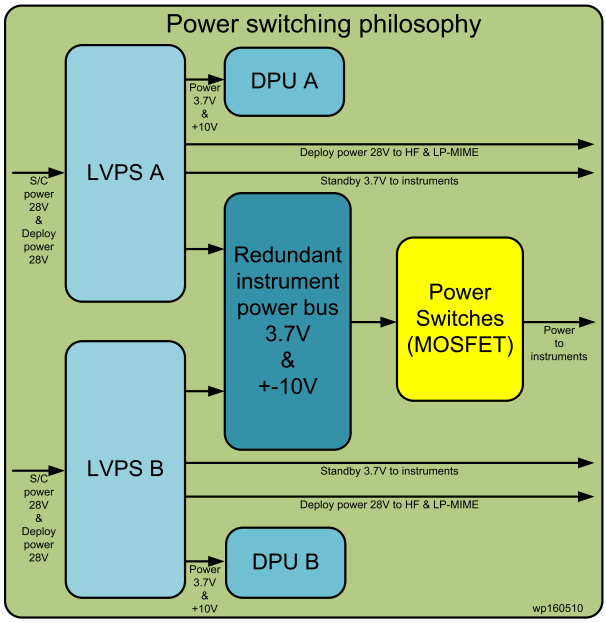

Fig. 32 LVPS and DPU power switching philosophy

The RPWI system is built up around a main Electronics Box (EBOX), which houses dual redundant Low Voltage Power Supplies (LVPS A&B) and Digital Processing Units (DPU A&B). These serve the Low Frequency (LF) receiver, the High Frequency (HF) receiver, and the Langmuir Probe & Mutual IMpedance Experiment (LP-MIME) transceiver. The duplicated (redundant) LVPS and DPU adds to robustness and immunity to single point failure. LVPS A is hardwired to DPU A and LVPS B is hardwired to DPU B. The power switching philosophy is shown in Fig. 32.

A backplane inside the EBOX distributes the analogue and digital signals, the different voltages, and a clock signal, which is generated by dual redundant crystal oscillators on the LVPS circuit board. The LP-MIME transceiver is connected internally to the LF receiver, for which it provides single-ended and differential signals from the Langmuir probes. It also contains driver circuits for the MIME transmitter. The MIME drivers can furthermore be synchronized to the mixer frequency of the HF receiver, for mutual impedance measurements at high frequencies. External harnesses connect the LP-PWI, SCM, and RWI sensors to the circuit boards inside the EBOX.

The EBOX is housed inside the payload vault of the spacecraft, where it is relatively well protected from the space environment. The RPWI sensors are mounted on the outside and face a more severe temperature and radiation environment. For optimal performance, all preamplifiers are mounted as close as possible to the sensors. While the sensors themselves are immune to the harsh radiation and thermal environments around Jupiter, the preamplifier electronics is less resilient. Special considerations have therefore been taken as to their radiation hardness, shielding, and thermal management. The units mounted on the outside will be subject to both high and low temperatures and are therefore protected by MLI.

Each LP-PWI sensor has a deployable boom with the Langmuir probe at its end and with the preamplifier mounted close to its root. The LP-PWI preamplifier housings are attached directly to the spacecraft body on standoffs and under MLI. Survival heaters are mounted

just under the preamplifier housings. This protects them from radiation from one side and simplifies their thermal management.

The SCM is mounted on the MAG boom. Its preamplifier is a custom-made ASICs, which is designed to withstand the radiation levels and to work in a wide temperature range. They are mounted inside the mechanical structure that supports the three sensors and acts as the boom interface. The SCM preamplifier ASIC has been tested down to −196 °C.

The RWI antenna subsystem is also mounted on the MAG boom close to the SCM. Its preamplifiers are housed inside a preamp box that is designed to provide radiation shielding and thermal balance. The early engineering models (mechanically representative chassis and electrically representative preamplifiers but without any antennas) was successfully turned on and worked in thermal vacuum between −180 °C and +90 °C. The preamplifier box supports the antenna elements and acts as a mechanical interface to the boom. Survival heaters are mounted on the RWI box.

Deployment power for the deployable units (including heaters) is the direct bus power provided by the spacecraft. However, RPWI is designed to measure very low-level electric and magnetic signals, which makes it special in this respect. Any cable that is galvanically connected from the spacecraft to the RPWI sensors is a potential source of noise (even after deployment). For this reason, the deployment lines are referenced to RPWI instrument ground when deployment is not active.

4.2 Electronics Box

The EBOX, which is made of 8 mm thick CNC machined Aluminium, houses seven A5 sized (210 × 148 mm) printed circuit boards (PCB), which are interconnected by a backplane with floating connectors. The backplane block diagram is shown in Fig. 33. The FM PCBs are displayed in Fig. 34. As can be seen in the diagram, each receiver (LP-MIME, LF, and HF) has its own PCB, the DPU A & B have separate PCBs, and the LVPS A & B have separate PCBs. Each unit is mounted in a separate frame. They are stacked vertically, with thin Aluminium plates between them for electromagnetic shielding. The frames are held together by long bolts. This construction makes the EBOX very rigid and practically insensitive to shocks and vibrations. Using frames is also very convenient during the development of the different subsystems, as the frames provide mechanical protection for the PCBs and support for electric connectors, which makes it much safer and easier to handle them than compared to handling bare PCBs.

The backside of each frame has connectors for the backplane and the front has connectors for the sensors, which makes it possible to connect individual PCBs safely to laboratory test equipment during the development phase, for instance to the electric ground support equipment (EGSE) during tests. External harnesses connect the sensors to the different receivers inside the EBOX.

4.2.1 Backplane

The purpose of the backplane inside the EBOX is to route all the signals and power lines between the instruments, the DPUs and the LVPS PCBs. A block diagram of the backplane is shown in Fig. 35. The backplane ground, with 3 dedicated planes, creates a low resistance star grounding point between all the stacked PCBs, and the EBOX chassis, which has single connection to the spacecraft. A star ground topology minimizes potential EMC problems between the instruments and the use three full layers makes it easier to design and route high speed digital signals needed for the communication between the DPU and instrument

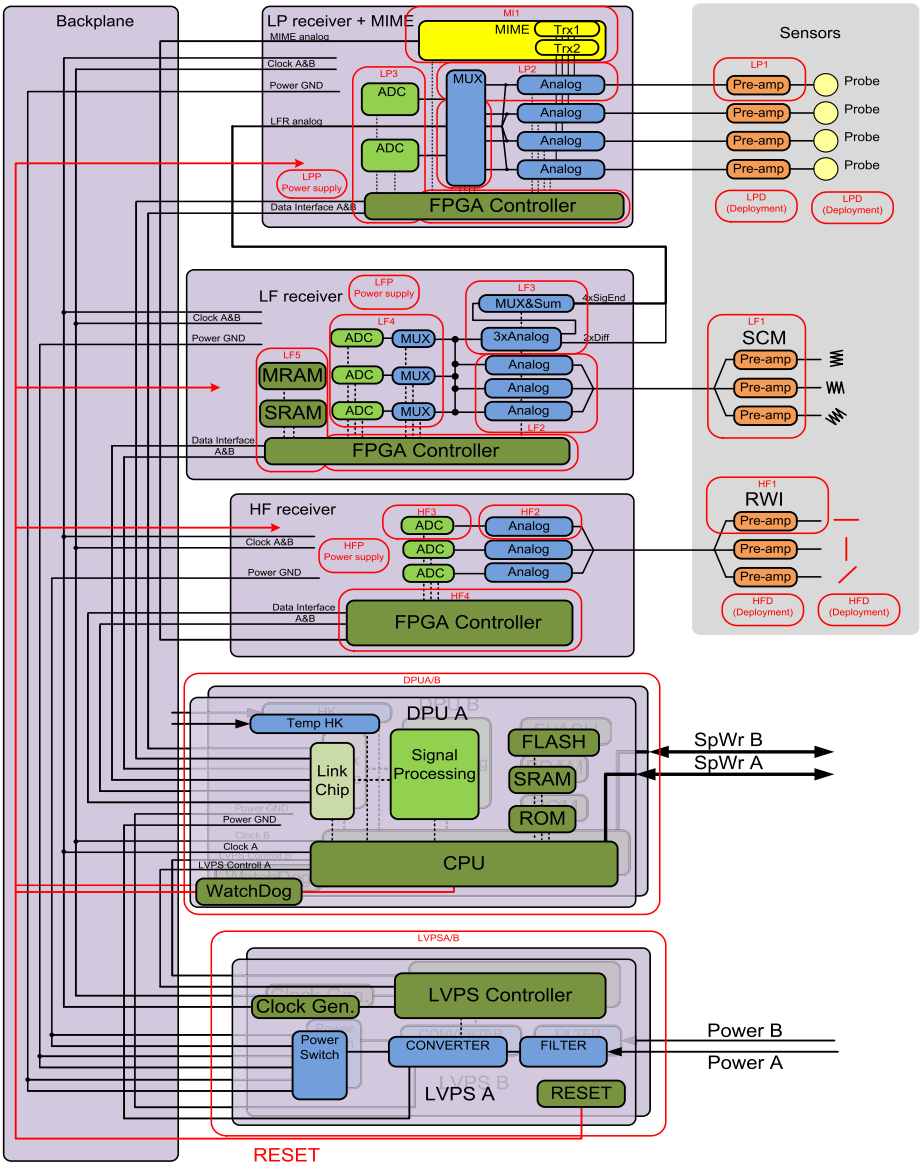

Fig. 33 RPWI functional block diagram. Red marked texts correspond to instrument single point failure chains

PCBs. In addition, care has been taken to avoid crosstalk on the backplane. Analogue signals are all contained in strip-lines with coplanar ground borders with via stitching. Noisy nets, such as digital nets, were kept well separated on the other half of the backplane from any analogue nets.

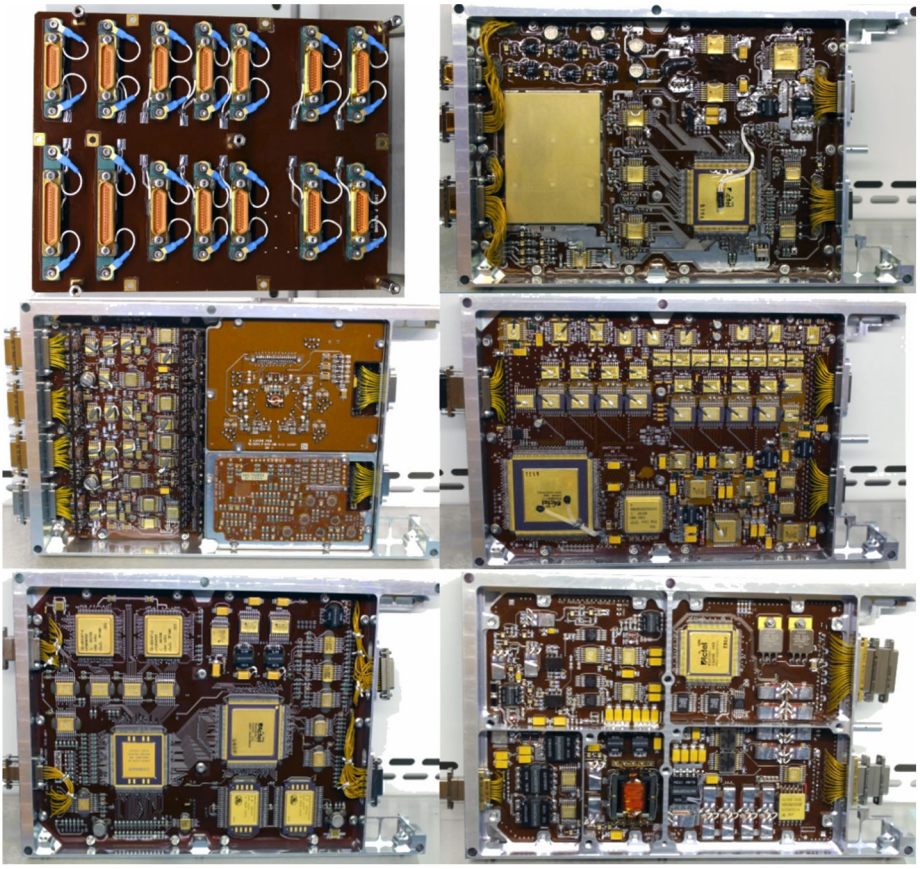

Fig. 34 EBOX PFM PCBs, Backplane (top left), HF (top right), LP-MIME (middle left), LF (middle right), DPU (Bottom left) and LVPS (bottom right)

4.2.2 Harness

A block diagram of the harness is shown in Fig. 36. The whole LP-PWI harness system is matched in length using analogue signals.

The different harnesses are parts of the sensor subsystems (LP-PWI, SCM, and RWI). The harnesses have been constructed in such a way as to minimize EMC impact to adjacent signals in the same harness as well as to nearby harnesses. To achieve this, differential signals make use of twisted pairs with an overall shield and single ended low-level signals use coaxial cables. Special care has also been taken when designing harness for any heaters and power supply lines to external sensors, twisting the source with return to minimize current loops. In addition, the routing of harnesses has been made to try minimizing pickup of noise, especially cables routed to the external sensors, where potential noise may contaminate the signals RPWI intend to measure.

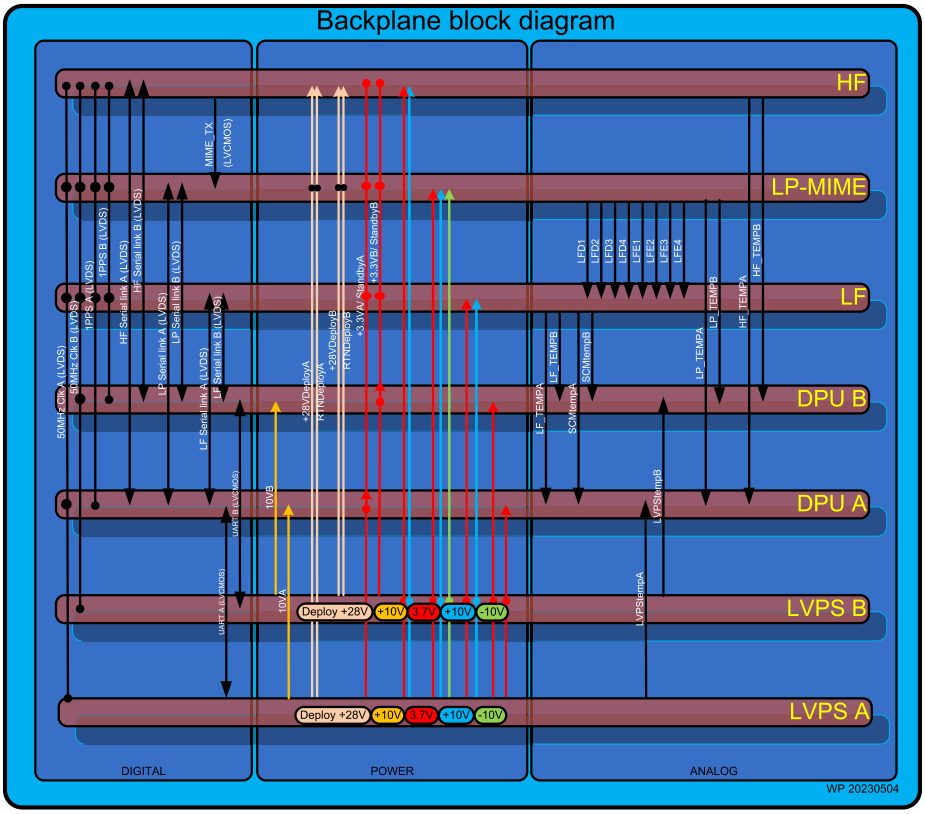

Fig. 35 Internal EBOX backplane block diagram

4.2.3 LVPS

The RPWI power generation is secured by the dedicated Low Voltage Power Supply, comprising of two independent DC/DC converters isolating the S/C PCDU out of the RPWI subsystems power inputs, Power Distribution Unit and Housekeeping Monitors (voltage, current sensing on both primary and secondary sides of the converter). Insight to the concept of the LVPS is given in block diagram in Fig. 37.

The converter is based on the step-down converter (Buck regulator) serving as a constant voltage feed pre-stage for the push-pull driver of the main power transformer. Thus, the converter topology is called Voltage-Fed Isolated Push-Pull Converter. Due to a lack of proper rad-hard semiconductors intended for isolated DC feedback on the market, the converter works with fixed duty cycle without any secondary to primary feedback loop, taking the output and internal parasitic resistance as acceptably low to provide the output load variation between required boundaries. This directly leads to positive impact on PCB footprint, mass savings and increased reliability (no optocouplers used, etc.).

The over-voltage and over-current protection are applied on both input circuitry as well as all outputs, except for the DPU, which needs to stay biased after start-up with all other loads implicitly set to OFF. Short circuit protection of dedicated loads or the ON/OFF switching are based on solid state MOSFET switches with low resistance between Drain and Source

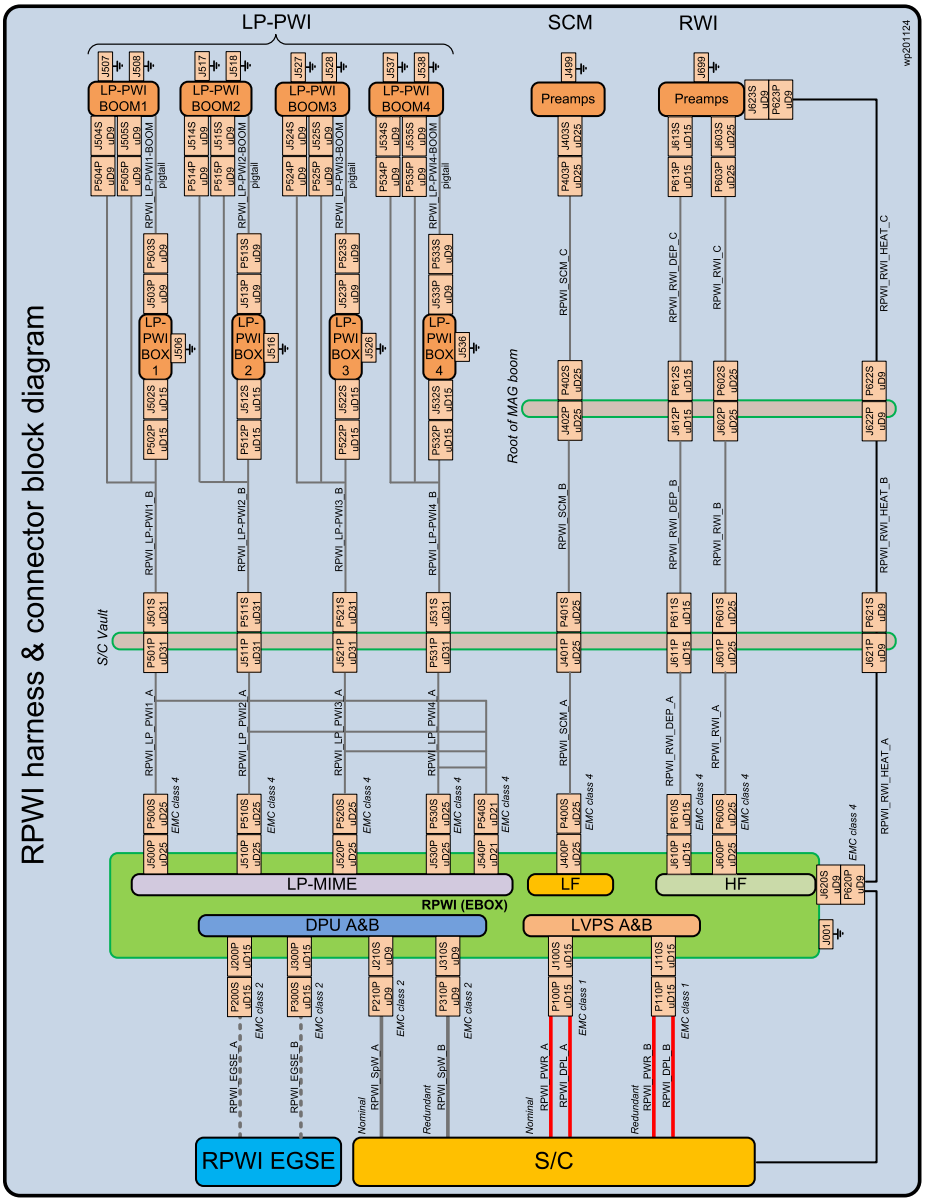

Fig. 36 RPWI Harness and interconnections

when turned ON (R_{DSon}). The analogue current sensing circuitry is used to limit the maximum output current per each output, whilst is continuously measured via FPGA. In case the limit is reached, for a limited amount of time, the current mode is activated. Dedicated digital current sensing then decides with at least three consecutive samples over the threshold to switch off the line permanently or keep ON.

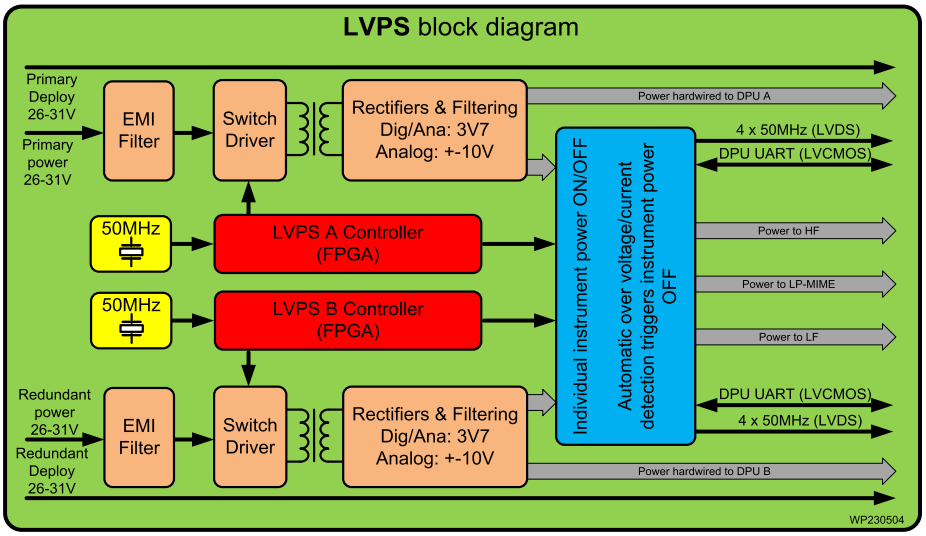

Fig. 37 LVPS block diagram

The whole RPWI package is synchronized to a 50 MHz low jitter crystal oscillator clock source distributed to all subsystems via LVDS bus, further divided locally to a switching frequency of 250 kHz by the FPGA. The switching clock is then back fed to the primary side via pulse transformer and replaces the startup R/C oscillator, once sync clock is available. An artificial delay of ∼300 ms is introduced to let the RC network stabilize and bias the LVPS core circuitries, prior the clock synchronization takeover is initiated. Housekeeping measurements and TM/TC engine is realized as FPGA softcore. Isolation of the clock signal and DPU-LVPS data link is based on dedicated LVDS driver to prevent the FPGA against the failure propagation from any other instrument subsystem, even if the LVDS peripherals are available in target FPGA at appropriate voltage/timing levels.

Two cold redundant LVPS power converters contain a switch matrix to fulfil the ON/FF function for dedicated lines for each RPWI subsystem separately. Output of both redundant parts are interconnected together as a summing circuitry making it a single point failure free design on ideal diode principle. Moreover, fast solid-state switches are used as a current chopper, controlled by the pulse trains (quasi PWM) delivered by the FPGA with duty cycle and length variable on the fly via telecommand. A series of pulses controlling the MOSFET line switch decrease the initial start-up current into bulk capacitances (order of millifarads) on the load side resulting in damped inrush currents observed on the main 28 V S/C power bus.

Difficulties with high current distribution of low voltage lines (1.5 V and 1.8 V) are covered locally at each subsystem by dedicated Point-of-Load (PoL) or Low Drop Out (LDO) regulators to produce the required voltages (CPU/FPGA core voltages). These PoLs and LDOs are powered from the 3.7 V rail to save power needed for their quiescent currents when not loaded by full computational load. Switch Mode PoL regulators are synchronized to 1 MHz clock derived from the distributed 50 MHz LVDS signal to minimize the frequency random walk of PoL's internal oscillators. The isolation between primary and secondary power lines in the RPWI are $\geq$ 1Mohm, 150nF. Power required for DPU, and instruments is routed via LVPS frame to the backplane to each of the subsystems. The deployment power

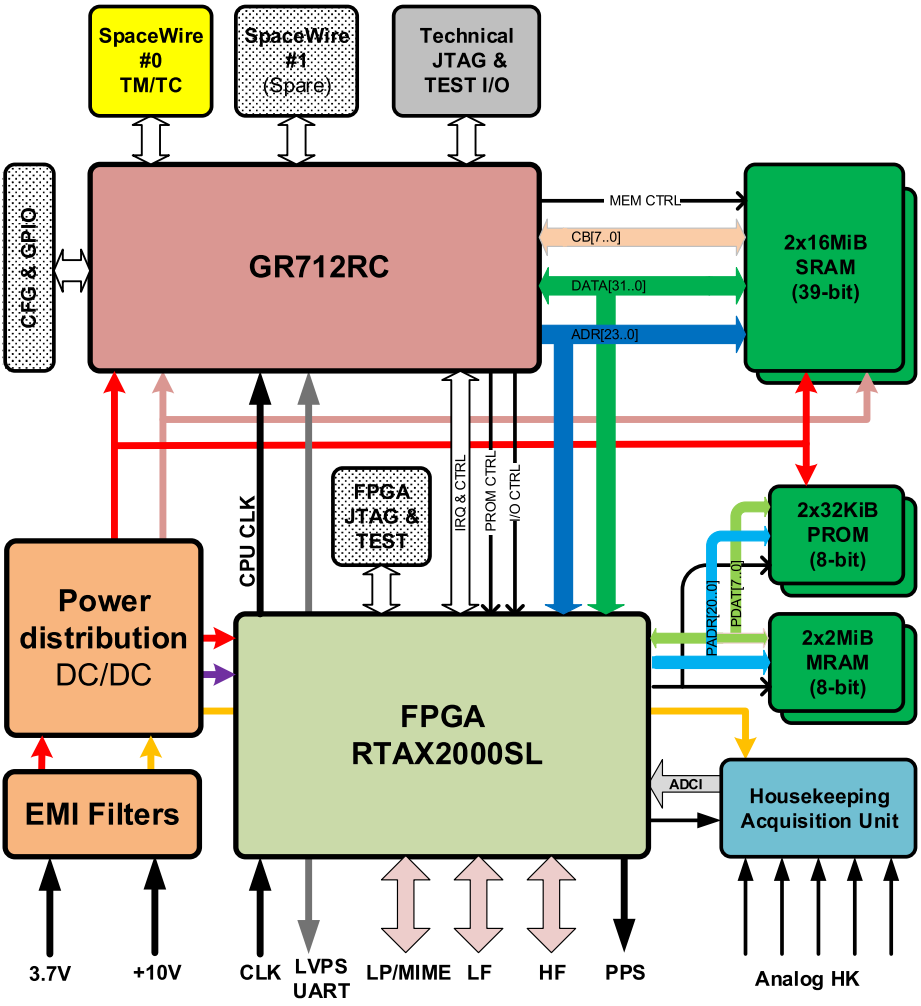

Fig. 38 DPU block diagram

is not controlled by the LVPS, however the 28 V is routed straight through the LVPS to the backplane and made available to the LP and HF PCBs.

4.2.4 DPU

The Digital Processing Unit (DPU) provide all required RPWI instrument control, health checkout, monitoring and high-level data processing functions. A block diagram of the DPU is shown in Fig. 38. To avoid "Single Point Failure" the RPWI instrument include two separate and fully autonomous DPU modules (primary A, redundant B). DPU A is supplied from LVPS A and DPU B is supplied from LVPS B, i.e., without commutation or crossing. Each DPU module communicate independently with the satellite on board data handling (OBDH) system TM interfaces. However, only one of the DPU modules is switched on at any given time, following the Hot/Cold rule. The DPU module can be silted into several

functional blocks as depicted in the high-level block diagram shown in Fig. 38. The DPU architecture is centred around a fault tolerant ASIC (the dual core GR712 RC from Aeroflex Geisler) which implements a LEON3 FT SPARC V8 processor core and several required peripheries, working as Board Supervisor Unit (BSU) The BSU features cover all functions required for minimum instrument functionality. TC & TM are supplied by SpW from the S/C where the LVDS buffers are powered with overvoltage protected 3.3 V to avoid failure propagation to the S/C in case of buffer failure.

The tasks to be handled by the on-board software are:

- Internal mode control.
- Switching and commanding of measurements measurement modules and LVPS.
- Tele command (TC) verification, validation, and execution.
- Software patch download, verification, and execution.
- Data collection and buffering (reduced functionality).
- Telemetry (TM) packet formatting and sending.
- Housekeeping data collection.

Some parts of this unit have been implemented in the FPGA together with supervisor part. The base 50 MHz clock is used to generate the reference time pulses (PPS) which are PLLed to the external S/C SpW time pulses. These time pulses are used by the other instrument boards to synchronize the sampling and time keeping.

There are three fully independent cores for communication with LP, LF or HF modules. Each one includes command and data FIFOs implemented inside the FPGA. The FIFO was based on RAM blocks and behavioral VHDL written FIFO controller. FIFOs will be 32-bit wide and 2048 words depth to optimize data transfer time (to or from CPU) and simplify CPU interfacing. The I/O registers access is always 32-bit wide. Data FIFO will be able to hold whole transmitted packet. So, no CPU involvement is required during one (requested or pushed) data packet transmission.

The Housekeeping acquisition unit (HKU) performs all functionality required to acquire data from analogue and thermistor instrument check points. The HKU is controlled by the BSU and includes ramp-compare ADC and analogue electrical interfaces to resistive or voltage sensors. This solution reduces the radiation sensitive of analogue hardware parts significantly since the ADC counter and control logic is implemented in an RTAX2000 FPGA (BSU processor peripheral). The sensor interface input circuitry can be unified to only a few types as presented in Table 11.

The analogue to digital conversion is based on comparison of measured values to generated voltage ramp signal by a Delta-Sigma DAC core implemented in FPGA. When the ramp starts, a timer starts counting to the ramp voltage until it matches the input. A comparator then fires, and the current ramp value is recorded.

The implemented method of data acquisition is useful only for signals that are changing at a slow rate. If the analogue input voltage changes during the sampling process, it effectively causes the sample point to move randomly. This adds a noise component, which becomes larger as the input frequency increases. However, most of the HK “checkpoints” values changes relatively slow (like temperature).

The memory unit is one of the units in every processor-based system that is sensitive to single event upset errors. In the DPU, external (from the viewpoint of the FPGA embedded processor) memory is used for storing:

- Application software code
- Application data structures
- Configuration and calibration tables

Table 11 HK sensor types (Voltage and Temperature) and interfaces

Sensor	Range	Interface
Voltage	0 - 5.0 V	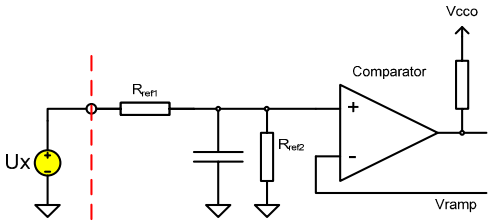
Temperature	−65 °C to 100 °C (NTC sensors) and −200 °C to 200 °C (PT1000 sensor)	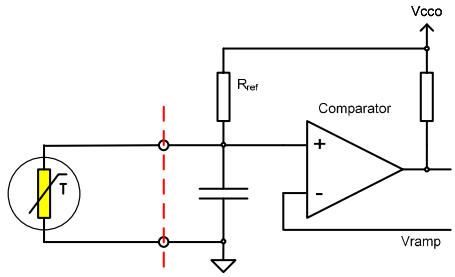

- Software patches
- Configuration bit streams of DPU FPGA
- Telemetry packet buffer

Data stored in memory are sensitive to errors induced by radiation. For instance, application software code, data structures, parameters, lookup tables, etc, are very sensitive and any content alteration may end up with catastrophic errors. On the other hand, information such as data samples, buffered TM packets, etc, are not as sensitive and may not require the same amount of error protection. To avoid complete software reloading, the flight software code is resident in ROM and FLASH and copied to RAM for execution. This implementation offers the advantage of allowing executable code modifications during the mission and autonomous code error corrections without restarting of program execution. For the code and data RAM memory segment, a "Correct Always" structure is used (EDAC-protected using a (39,7) BCH code). A block diagram of the memory module is depicted in Fig. 39.

The Boot SW can run directly from PROM (slow access time) or can be copied into RAM (fast access time) and executed from there. The BSW, loaded to SRAM or executed directly from PROM, cover all functions required for minimum instrument functionality.

Application specific software (ASW) will be stored in a rewritable MRAM memory bank that hold at least two images of complete code. The internal MRAM EDAC will be transparent for DPU design instead software image correctness will be controlled by segmented CRC or EDAC support for 8-bit memory provided by the LEON memory controller. This implementation offers the advantage of allowing executable code modifications during the mission and autonomous code error corrections without restarting of program execution.

The PROM and MRAM memory could be switched OFF (stays unpowered) when copied and run from SRAM (external or On-chip) to power saving at normal operation.

The Signal Processing is carried out by the dual core CPU (GR712RC). It includes data stream processing IP cores dedicated to each measurement module. The implemented

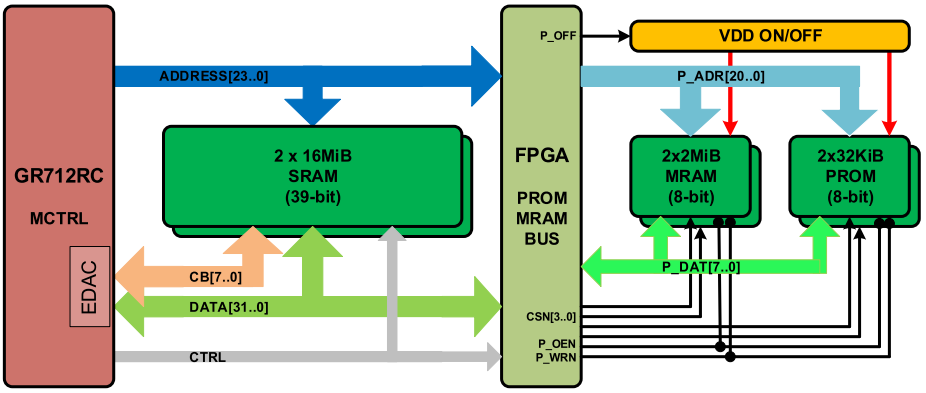

Fig. 39 DPU memory module block diagram

processing algorithms cover data accumulation, signal filtering and spectral analysis (Fast Fourier Transform).

The DPUs support the following Space Wire link characteristics.

- Supported link speed is 100 Mbps.
- Maximum packet size supported is 4kBytes.
- Minimum TM buffer size 100 kByte supporting 100 ms latency.
- Peak data traffic 2MByte/s.
- Traffic profile average rate is <40kByte/s during typical measurement cycles.

4.2.5 LP-MIME Transceiver

The LP-MIME transceiver consists of the LP receiver and the MIME driver circuits for filtering, switching and transmission. MIME and LP are two sandwiched boards that together make up one in the frames of the EBOX. A block diagram of the LP analogue section is shown in Fig. 40. The LP-MIME digital block diagram is shown in Fig. 41.

Up to four selected analogue signals are captured by the ADCs and routed to the FPGA for further filtering, mixing, and processing. The data is then sent to the DPU for further processing and storing. Each ADC has the possibility to choose from a subset of eight analogue signals (differential, single ended, E-field or Density).

The basic principles underlying plasma density (Langmuir probe – LP) and electric field (E-field) measurements with the LP receiver are identical to that of a digital multi-meter measuring in current and voltage mode, respectively (see Fig. 41). The plasma density is a scalar quantity, and one probe measurement is sufficient to obtain the local density at the probe. The E-field, on the other hand, is a vector quantity, which requires a minimum of four probes since one E-field component is obtained as the potential difference between two probes divided by the separation distance. The LP receiver employs four spherical probes, 10 cm in diameter, mounted at the tips of 3-meter-long deployable booms. The booms are allocated on the spacecraft such that three-dimensional E-field measurements are enabled. Each probe can be individually configured in Density or E-field mode; to support all expected sciences modes.

The spacecraft will become charged due to its interaction with the environment. The final surface potential of the spacecraft depends on the characteristics of the environment, but for many environments the potential difference between two insulated conductive spacecraft

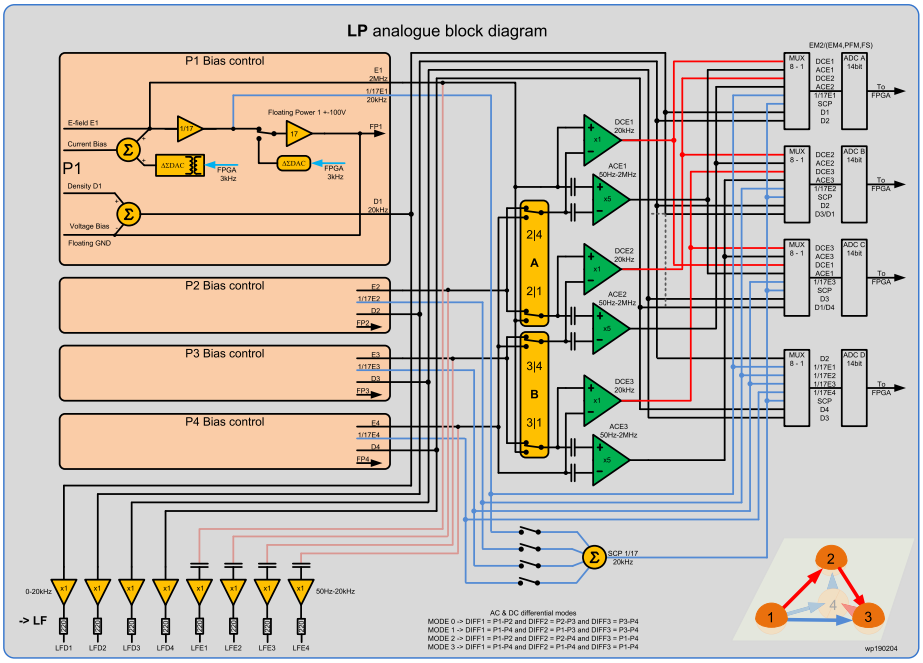

Fig. 40 LP-MIME transceiver block diagram

surfaces can be several tens of volts (Holmberg 2020; Bochet et al. 2023; Holmberg et al. 2024). Probe electronics must cope with those potential differences. That is achieved by using floating power supply techniques for the first stages of both E-field and LP electronics.

The probe potential in E-field mode is anchored tightly to the local plasma potential (reference potential in the plasma) and do not depend on the plasma parameters. To achieve this, a constant bias current is injected into the plasma, moving the probe quiescent point as close as possible to the plasma potential. In Density mode, the probe bias voltage is set to a preferable quiescent point on the local Langmuir curve.

A sweep of current in E-field mode or voltage in Density mode is used to obtain correct quiescent point settings for all probes. Traditional Langmuir sweeps are used to obtain local plasma parameters.

MIME is an active multi-pole instrument, which measures plasma impedance (Z). The experiment is composed of different transmission and reception electrodes, a sine wave generator, and a receiver.

The measurement principle is based on Ohm's law Z=V/I applied to the system formed by the electrodes and the surrounding plasma. By applying a sinusoidal signal at a given frequency on one or two transmission electrodes, an AC current (I) is forced inside the plasma. The sine wave generator transmits a signal of constant amplitude over several periods. After plasma stabilization, MIME measures the potential difference (V) between two reception electrodes to get access to the mutual impedance (Z) at the transmitted frequency, as illustrated on Fig. 42. The transmitted signal and reception signal are internally synchronized inside the FPGA of the receiver, which gives us the knowledge of the phase of the mutual impedance, a piece of important information to derive the plasma parameters. When MIME

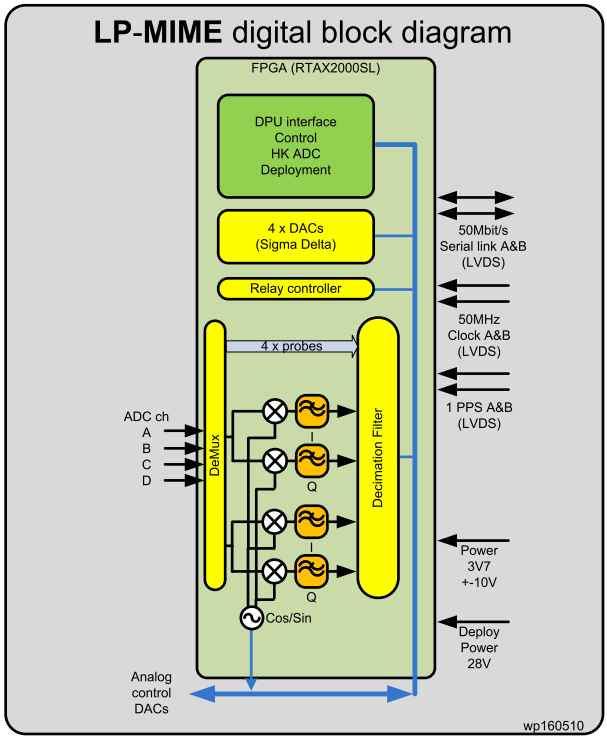

Fig. 41 LP-MIME digital block diagram

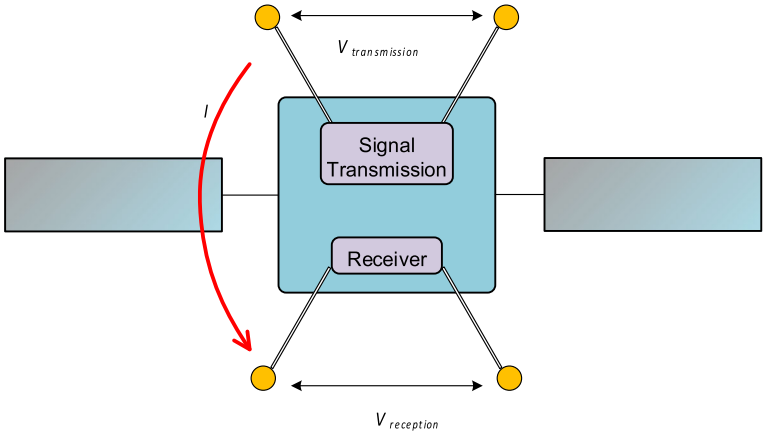

Fig. 42 MIME measurement principle

uses two transmission electrodes, the same signal, but in phase opposition, is sent to both transmitters.

By sweeping the transmitted frequency over a frequency interval containing the plasma resonances, MIME constructs a frequency impedance spectrum whose features reflect the plasma characteristics. After post-processing of the raw data by the DPU, the impedance spectra are sent to the ground where they can be analyzed to derive the properties of the

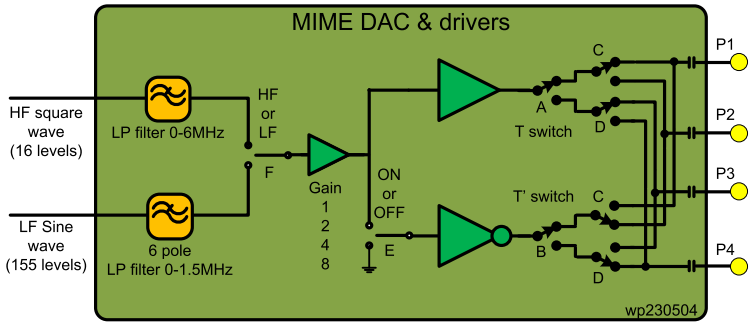

Fig. 43 MIME transmitter drivers

thermal component of the plasma such as electron density and, in certain conditions, electron temperature.

For low and medium frequency measurement (3 kHz up to 1.5 MHz), MIME uses the four Langmuir probes as transmitting/receiving electrodes together with the LP-MIME receiver to generate the transmission signal and perform the potential differential measurements.

Internally to the LP-MIME board, the transmission signal is generated and sent to the MIME transceiver. The MIME transceiver is a part of the LP-MIME receiver. The purpose of this sub-system is to filter the high frequency, amplify (4 gains) the signal, create the 180° phase shift for the second transmission signals (if used) and route the signals to one or two corresponding transmission Langmuir probes (see Fig. 43).

As shown in Fig. 44, for low and medium frequency measurement, there are two ways to carry out measurements by using the LP-MIME receiver. In case (A), the transmission signal is sent to one pair of Langmuir probes (red) and received by the other pair of Langmuir probes (green). In case (B), the transmission signal is sent to only one Langmuir probe (red) and received by one or two pairs formed by the other Langmuir probes (green).

The bandwidth can be extended to higher frequencies (from 80 kHz to 3 MHz) by using the RWI receiver and RWI antennas as follows. The RWI receiver generates the transmission signal which is routed to LP-MIME board to MIME transceiver to send the signal to the Langmuir probes (transmission sensors), while the measurement is performed on RWI antennas (reception sensors).

As shown in Fig. 45, there are two ways to perform high frequency measurements using the LP-MIME receiver as transmitter and RWI receiver. In case (C), the transmission signal from RWI receiver is sent to one pair of Langmuir probes (red) and received by one, two or three RWI antennas (green). In case (D), the transmission signal is sent to only one Langmuir probe (red) and received by one, two or three RWI dipolar antennas (green).

To ensure optimal modularity and enable MIME to easily adapt to the various scientific objectives of RPWI, it is possible to select any probes in transmission and reception. This results in a total of 96 possible antenna configurations (LP + RWI). In regular MIME operations, only a few configurations are expected to be used for science purposes.

Finally, although the Langmuir probes and the RWI antennas are the primary sensors used by MIME, any magnetic or electric field sensor can be employed. Therefore, the reception signal can be sampled by the LP, LF, and HF receivers and used for internal RPWI calibration purposes.

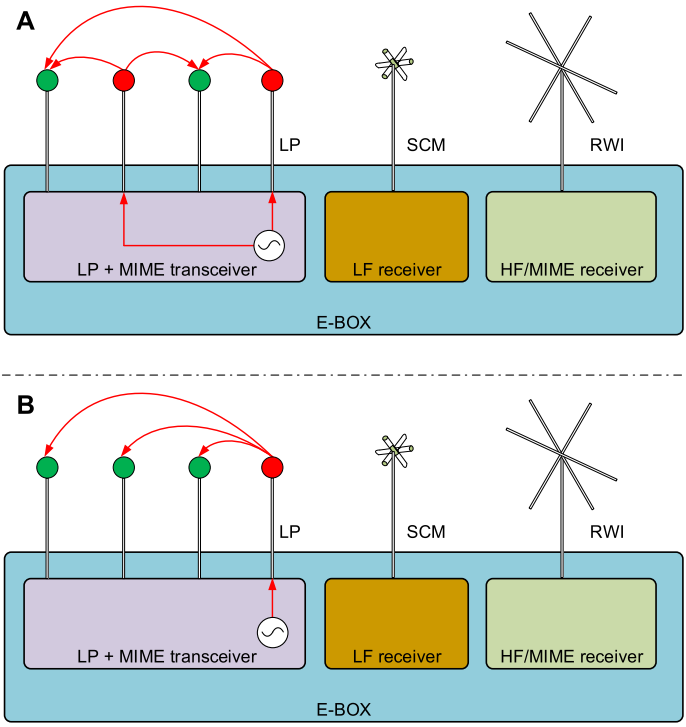

Fig. 44 MIME transmission/reception modes in low and medium frequency mode: (A) transmission (red) on one pair of Langmuir probes, reception (green) on one pair of Langmuir probes. (B) transmission (red) on one Langmuir probe, reception (green) on one or two pairs of Langmuir probes

4.2.6 LF Receiver

The LF receiver subsystem implements multidimensional onboard analysis of signals generated by the SCM and LP-PWI sensors at frequencies below 20 kHz (Fig. 46). The purpose of the LF receiver is to digitize and pre-process these signals for obtaining information on power, polarization, and propagation properties of fluctuating electromagnetic field and plasma parameters in the Jovian magnetosphere, in vicinity of Jovian icy moons and, especially, in the magnetosphere of Ganymede. The LF receiver performs computationally intense first stage onboard processing in an FPGA, while the more sophisticated second stage processing is implemented by a dedicated part of the RPWI flight software executing on the DPU. This two-stage processing yields a compressed data flow, effectively using the scarce telemetry resources.

The on-board analysis of low-frequency signals by the LF receiver is based on three magnetic field input signals from SCM, and on signals from the four Langmuir probes routed to LF from the LP-PWI subunit (density mode and electric field more signals are routed independently). Before digitization, all the signals are low pass filtered by identical 4th order analogue anti-aliasing filters with a cut-off at approximately 50 kHz. Furthermore, the LP-PWI signals are high-pass filtered with a cut-off of about 50 Hz to remove low frequency signal variations.

Digitization of the signals is performed by eight 14-bit analogue-to-digital converters (ADC). While the three SCM inputs are directly allocated to specific ADCs, the LP inputs

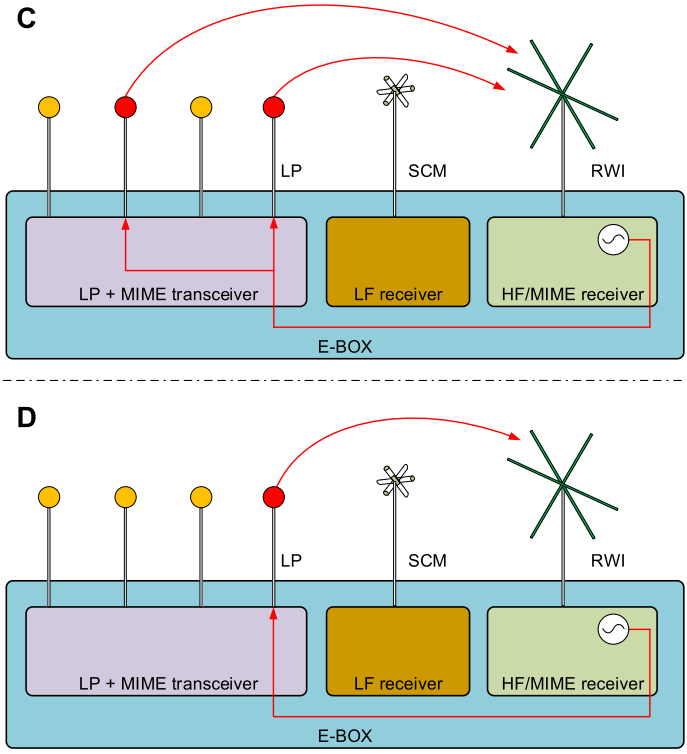

Fig. 45 MIME transmission modes in high-frequency mode: (C) transmission (red) on one pair of Langmuir probes and reception (green) on RWI antennas, (D) transmission (red) on one Langmuir probe and reception (green) on RWI antennas

(E-field and Density) are routed through a bank of analogue multiplexers and differential amplifiers allowing a variety of input signals to be sampled by the remaining 5 ADCs. The LF can thus sample combinations of E or D signals, an analogue sum of several probe potentials or differential E-field signals (differential voltages between pairs of LP probes).

All signals are oversampled at a base frequency of 781,250 Hz and further decimated and filtered in the FPGA to gain a better dynamic range. For D/E/B signals, a combination of cascaded integrator–comb (CIC) and FIR filters with a combined factor of 16 or 32 is used to obtain the final digital signal at 48,828 or 24,414 samples per second. The LF receiver allows to capture a snapshot of this waveform (up to 262,144 samples per channel) and store it in an internal memory to be later transmitted to the RPWI DPU. This same time series is then used to calculate averaged Fourier spectral matrices composed of auto-spectra and cross spectra of the 8 components. This calculation is done in the FPGA using a 2048 point fixed precision FFT, followed by cross-spectra calculation and averaging both in time and in frequency into a set of predefined frequency bands configurable by a telecommand. The LF FPGA also implements further decimation of the signals by another combination of CIC and FIR filters to obtain a continuous low frequency waveform sampled at 762.9 samples per second.

The second-stage data processing layer implemented in the application software of the RPWI DPU further treats the intermediate data products from the LF board to produce

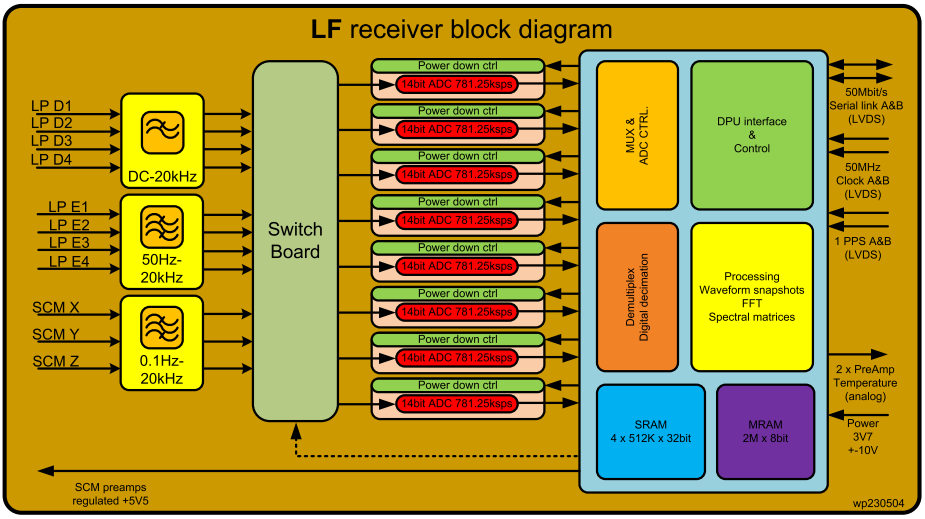

Fig. 46 LF receiver block diagram

the final science telemetry in an efficient format. See Sect. 5.6 for a description of the LF software.

4.2.7 HF Receiver

The HF receiver covers the highest frequency end of the RPWI, which implements analysis of the three-dimensional electric field vector in the 0.08 – 45 MHz range. The received signals are generated by the three orthogonal electric dipole antennas (RWI, see Sects. 4.2.12 and 4.2.13). As shown in the block diagram in Fig. 47, the HF receiver consists of two parts, HF-Analogue and HF-Digital.

HF-Analogue implements the analogue signal chain with low-path filter (8th order Butterworth, 45-MHz cut-off). After that the signal is amplified with +9 dB, which enables to see the RWI preamp noise floor with a few dB margin.

HF-Digital is a direct sampling, software defined radio (SDR), which implements the analogue to digital conversion, down mixing, and decimation filtering. First, the analogue signal chain gets digitized by 14-bit ADCs running at 90 Msps. Digitalized data stream gets multiplied with the two numeric local oscillator (NCO) signals, Cosine and Sine, to bring the centre frequency of interest to baseband (0 Hz). The signal is now complex valued and contains both positive and negative frequencies. The real (I) and imaginary (Q) parts of the signals are thereafter processed through CIC decimation, and later, FIR filters, where the final output sample rate can be adjusted stepwise from 298 ksps down to 18.6 ksps. The sample rate (and output bandwidth) is reduced by a factor of two in each step and the dynamic range is increased to 100 dB or better. The 20-bit signed I & Q output data is buffered and sent as packets over the serial link to the DPU board.

The problem of this HFR design is the high-power consumption associated with high sampling rate. If we try to operate continuous sampling, the peak power becomes ∼7 W, which impacts the operating temperature of the HF FPGA and ADCs. In most of the observations, the sampling is as sparse as possible (once per 10 – several 10 seconds) and the 90-MHz clock and ADC are stopped between this term. In this ‘standby-mode’, HFR only

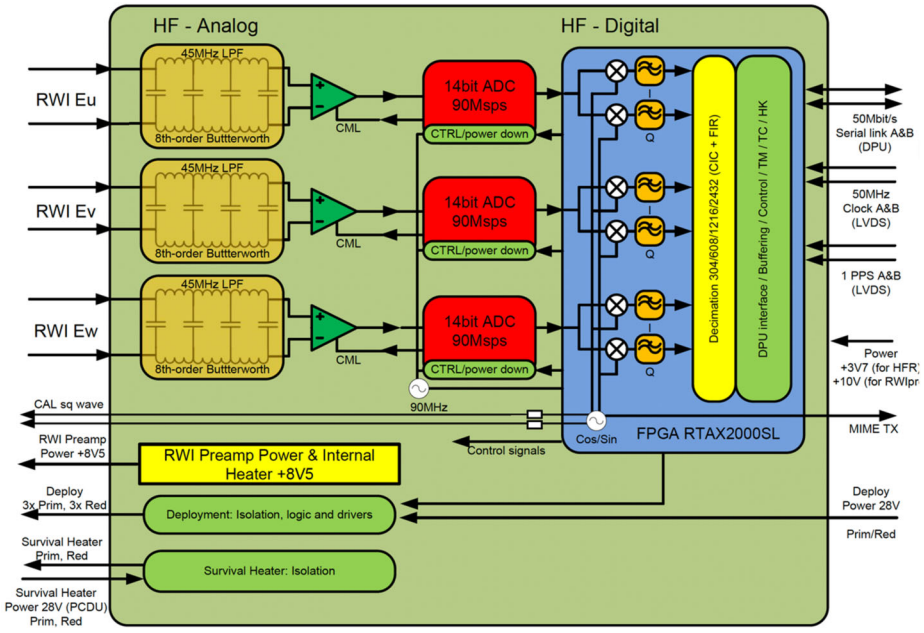

Fig. 47 HF receiver block diagram

consumes ∼0.5 W so that the semi-continuous long-term monitoring can be operated. With this operation, we will operate the HFR with the averaged power of ∼0.7 W in the normal magnetosphere monitoring, <1 W for the passive radar observations of icy moon crusts, and a few W for the radio occultation of icy moon ionospheres.

The HF system (JENRAGE) also contains the HF software (HF-DPU) installed into the DPU for further processing of the down-converted I and Q signals. Since raw telemetry from HFR is huge, further telemetry processing by the DPU-HF software is critical for a compressed data flow. See Sect. 5.8 for a description of the HF software.

As shown in Fig. 47, the HFR provides the driving power, the internal heater-power, and the calibration signals to the RWI preamp (see Sect. 4.2.13). The HFR also provides the route and control of the deployment power and the survival heater power to the RWI antennas (28 V).

MIME HF measurement from 80 kHz up to 3 MHz (as described Sect. 4.2.7) make use of the Langmuir probes to transmit a signal and reception with the RWI antennas. To synchronize the MIME HF measurements, the HF receiver sends its mixer frequency (MIME Tx) to the MIME subsystem, which is located on the LP-PWI transceiver board.

4.2.8 LP-PWI Booms & Probes

LP-PWI consists of four identical deployable booms located individually on various sides of the JUICE S/C. Each consists of two composite CFRP limbs connected with hinges and has ultra-light mass of 1.2 kg (Ossowski et al. 2021). Due to the low mass budget, the booms are actuated by the drive springs without a damper, and therefore they utilize their elasticity to compensate for the residual end deployment shock energy. They deploy and position each of four Langmuir Probes three meters from the spacecraft at a 135-degree angle from the initial position.

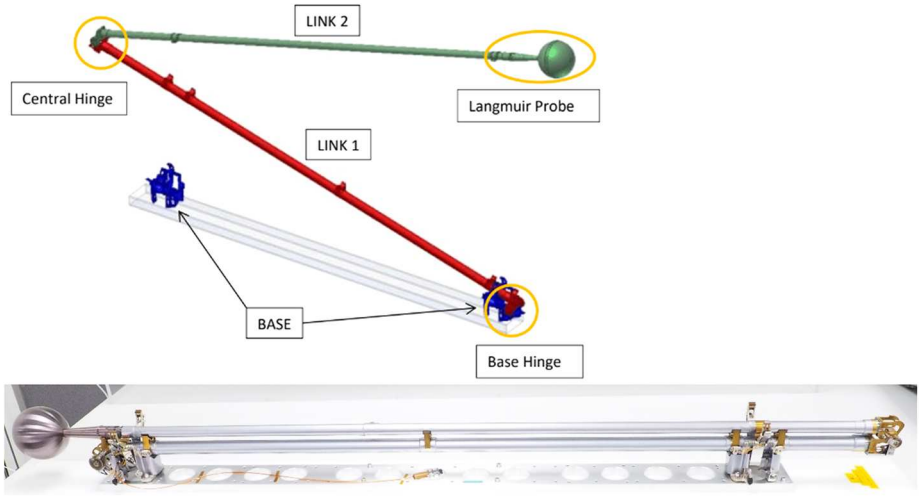

Fig. 48 (Top) LP-PWI Boom subassemblies in a deployment phase. (Bottom) One of the as-built flight models in the stowed configuration

The LP-PWI unit consists of four major subassemblies: Base (which consists of two Hold Down Release Mechanisms – HDRMs), Link 1, Link 2, and the sensor – the Langmuir Probe Assembly. There are connections between these subassemblies: the Base Hinge, which connects Base and Link 1, and the Central Hinge, which connects Link 1 and Link 2. The configuration of subassemblies is shown in Fig. 48. In the stowed configuration, shown at the bottom of the Figure, the links are held by HDRMs utilizing Vectran string and thermal knife technology. Once released on the orbit, the CFRP links start to deploy in a proper sequence (first central hinge, then base hinge) ensured by the selection of torques and energies in the drive springs.

The sensor – the Langmuir Probe (LP) – is a 100 mm diameter sphere at the end of the ∼100 mm long stub. The LP consists of two hemispheres (0.4 mm thick). A hollowed stiffening cone (also 0.4 mm thick) is tightened to both hemispheres in place of their contact to provide high probe stiffness. To reduce the sphere's mass, the central coupler is in the form of a hollowed stiffening cone. The whole LP structure is made of titanium grade 5 alloy, and the external surface is covered with sputtered TiAlN coating (see Fig. 49). From an electrical point of view, the sphere and the stub are insulated from each other. Inside the sphere, there are custom-made and qualified purposely for this mission electric RC components. The resistor consists of a ceramic washer with resistive paths, while the capacitance is provided by an additional layer of conductive sleeve on the cable next to the resistor (also seen in the Fig. 49). The LP is mounted at the end of the deployable boom enabling it to extend from the spacecraft body. A total of four LP booms are extended from the S/C body in different directions.

4.2.9 LP-PWI Preamplifiers

The purposes of the LP-PWI Preamplifiers are to support plasma density and E-field measurements as well as active mutual impedance measurements (MIME). The preamplifier contains switches and amplifiers for the density and E-field modes. A block diagram is shown in Fig. 50. The preamplifier housing (see Fig. 31) is made of aluminium with an added Tantalum plate for radiation protection.

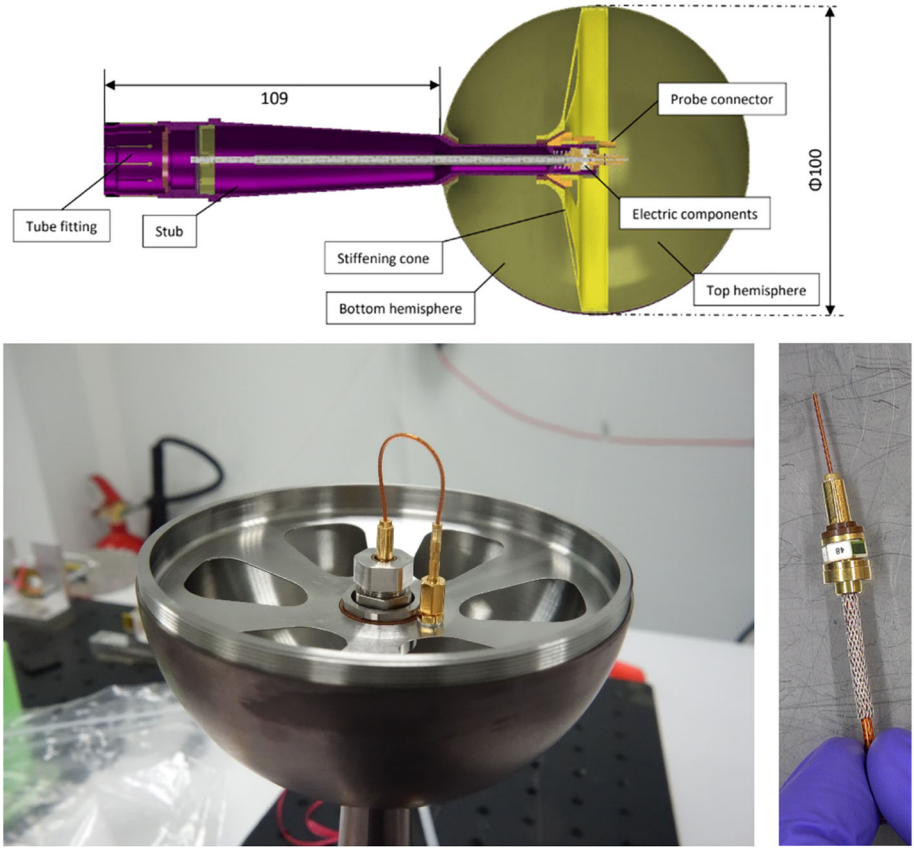

Fig. 49 (Top) Langmuir probe assembly. (Bottom, left) The Langmuir Probe during assembly with exposed RC circuit elements. (Bottom, right) The details of RC elements

4.2.10 Langmuir Probe (LP) Coating Design, Tests, and Considerations

The RPWI Langmuir probes and stubs are uniformly coated with a 0.6 μm layer of sputtered $Ti_{50}Al_{50}$ N with a detailed cleanliness procedure carried out at Linköping University. The choice was made after extensive testing of several different surface materials with different test-methods and will be described elsewhere. The RPWI Langmuir probe coatings were grown in a CemeCon AG CC800/9 magnetron sputter deposition system, using four TiAl cathodes, each operating at 6 kW in DC sputtering mode in a N_2/Ar atmosphere with a purity better than 99.999% (see Fig. 51). Prior to deposition, the probes and stubs are subject to a pre-treatment where the substrates are periodically immersed in a high-density Ar^+ plasma jet to (i) effectively clean the surface from residual contaminants and (ii) activate the surface sites to provide better bonding to the TiAlN layer. Throughout the pre-treatment and the deposition, the probe parts are subject to a negative pulsed potential of −650 V at 240 kHz to achieve ion assisted film growth utilizing the magnetron plasma, while eliminating detrimental charge accumulation/discharge effects. The substrate temperature was kept at 475 °C (using resistive radiative heaters at 8 kW) to degas the surfaces during the pre-treatment and during deposition to provide sufficient mobility at the growing film surface, which is necessary to obtain dense and hard coatings with good adhesion. The probe hemispheres were

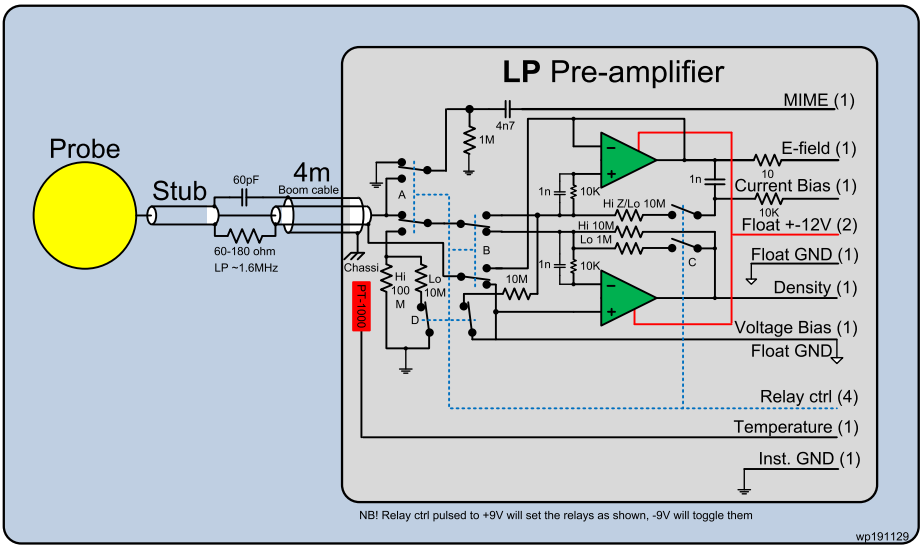

Fig. 50 LP-PWI Preamplifier block diagram. If the relay control (blue dashed) is set to positive voltage the relays are set to the positions shown, if set to negative voltage the relays flip to the other position

coated one by one assembled to a full sphere, allowing them to rotate freely on two concentric stainless-steel rings placed around the centre of the sputtering system (the rail system shown in Fig. 51). During the entire process, the rails rotate relative to each other causing the probe to roll in a quasi-random manner, giving the entire sphere's surface equal average exposure time to the deposition flux. This ensures a uniform coating and effective masking of all surfaces of the sphere's parts that are not to be coated. To avoid scratching of the pristine Ti-spheres during the pre-treatment stage, any (harder) TiAlN coating is removed from the (softer) steel rails, in-between each deposition. Other parts, such as the stubs were coated separately, and were rotated by a double planetary motion in the chamber during deposition.

During the development process, monitor samples of the same material were simultaneously coated and then tested for surface roughness (<300 nm), electrical work function (<0.03 eV rms), chemical composition (X-ray photoelectron spectroscopy, <0.1 atom %), surface reflectance (before and after high temperature annealing, optical properties, $\alpha/\varepsilon < 1.7$), adhesion (tape testing in accordance with ISO 9211-4: 2006 (E), including on an irradiated sample, a sample subjected to thermal vacuum cycling, and a sample subjected to thermal shock) and repeatability across batches. Equivalent monitor samples from the flight depositions were characterised through the same surface reflectance and electrical work function measurements.

Prior to selection of surface coating material and deposition methods, several different candidate coating materials were developed at the Ångström Laboratory of Uppsala University (UU) and the Swedish Institute of Space Physics in Uppsala (IRF-U), and at the Centre for Nanoscale Materials (CNM) at Argonne National Laboratory (USA). A few of the test samples, deposited with Nitrogen doped Ultra Nano Crystalline Diamond (N-UNCD), are shown to the left in Fig. 52 and all candidate coating materials are listed in Table 12.

The electrical performance of these coatings and their sensitivity to contaminations were investigate during a one-week long test campaign at ONERA in Toulouse, using their large, 9 m^3, IONospheric Atmosphere Simulator (JONAS) plasma chamber. The JONAS facility

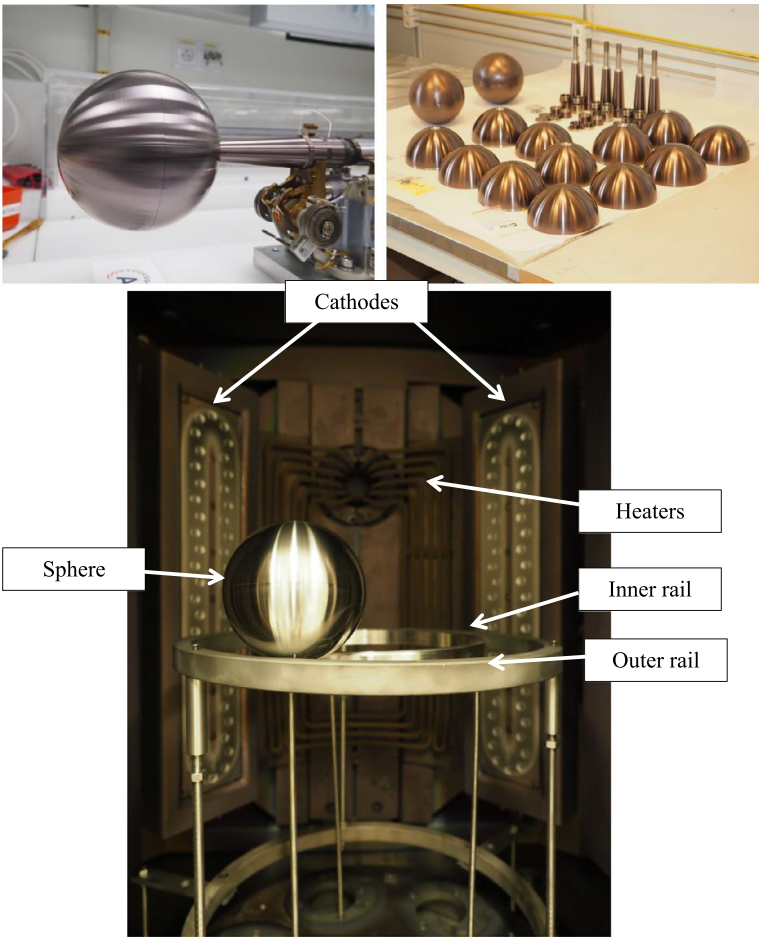

Fig. 51 Langmuir probes in flight configuration (top left), dis-assembled (two spares and four in-flight, top right), and one spherical probe on the rotating rail manipulator in the sputter deposition chamber

simulates ionospheric conditions in LEO, with plasma densities in the $10^5 - 10^6$ cm^{-3} range and electron and ion temperatures in the 0.1 – 0.2 eV range. As shown to the right in Fig. 52 twelve Langmuir probe surfaces (2 cm diameter Titanium plates with different coatings) were mounted on a carousel inside the plasma chamber on large aluminum plates, acting as guards. A resistor for probe cleaning, by heating, and a thermistor (PT1000) for temperature monitoring were installed on the backside of each probe. The carousel itself was driven by a stepper motor, which allowed to put the Langmuir probe under test directly in front of the plasma source. The electrical performance was evaluated from the current drawn by the Langmuir probes in response to the bias voltage, applied to the probe during the Langmuir probe sweep. Bias voltage sweeps from −5 V to +5 V (up) and from +5 V to −5 V (down) were used during the tests.

Contamination can only be estimated qualitatively by observing the hysteresis effect when performing double (up and down) voltage sweeps. Hysteresis indicates that the probe is contaminated, while no hysteresis means that the probe is clean. In the first attempts to

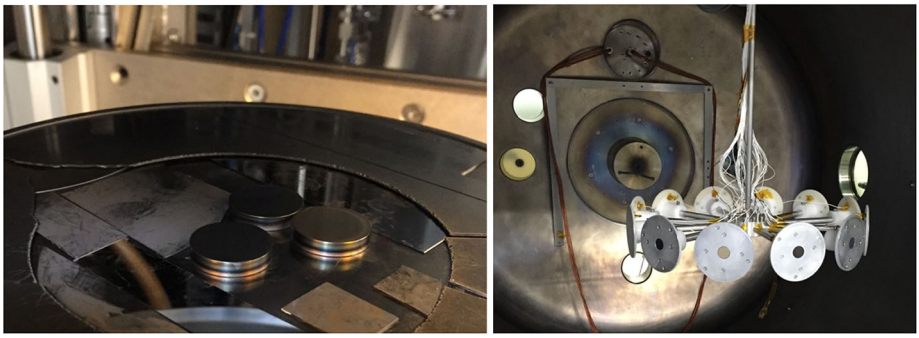

Fig. 52 Left. Test Langmuir probes surfaces after being deposited with Nitrogen doped Ultra Nano Crystalline Diamond (N-UNCD) at Centre for Nanoscale Materials (CNM). Right: Carrousel with all test Langmuir probes inside the JONAS plasma chamber at ONERA. The plasma source is in the center of the chamber wall

Table 12 Test sample coating: Nitrogen doped Ultra Nano Crystalline Diamond (N-UNCD), monolayer graphene annealed on N-UNCD, Boron doped Nano Crystalline Diamond (B-NCD), manufactured using Chemical Vapor Deposition, sputtered Au, TiAlN, TiN, and baked TiN. Samples with different doping concentrations are not listed here for brevity

Material	Thickness	Process	Provider
N-UNCD	200 nm	Microwave plasma CVD	CNM
Graphene on N-UNCD	200 nm + monolayer	Annealing/Microwave plasma CVD	CNM
B-NCD	1 and 2 um	CVD	UU
Au	650 nm	Sputter	UU
TiAlN	650 nm	Sputter	UU
TiN	650 nm	Sputter	UU
TiN	650 nm	Baked	IRF-U

clean the probes, they were heated to about +150 °C, but this turned out to be a very time consuming and inefficient method. A much better method was found to be electron sputtering. As shown in Fig. 53 and Fig. 54, very efficient cleaning was achieved in only 1 1/2 hour, by setting the probe bias voltage to constant +32 V and letting the electrons sputter the probes clean.

The best electrical properties were shown for a 200 nm Graphene monolayer. However, the energetic oxygen radical environment near the icy moons of Jupiter may easily react with a Graphene layer. Instead, the second-best coating material was selected, i.e., sputtered TiAlN. Another consideration is that while it is comparably easy to deposit smooth surface coatings on small flat samples, this is not straight-forward for the large 10 cm diameter spherical Langmuir probes. The sputtering chamber facility at Linköping University facilitated this. The heritage from our previous development of sputtered TiAlN coating for the MEFISTO instrument onboard BepiColombo (Blomberg et al. 2006a,b) was also an important factor during the final selection process. Furthermore, thanks to the good results of probe cleaning with electron sputtering at ONERA, this method has been implemented for probe cleaning in in-flight. During the inner cruise phase, probe cleaning operations at +80 V for several days will be performed at least twice a year before payload checkouts and planetary gravity assist maneuvers.

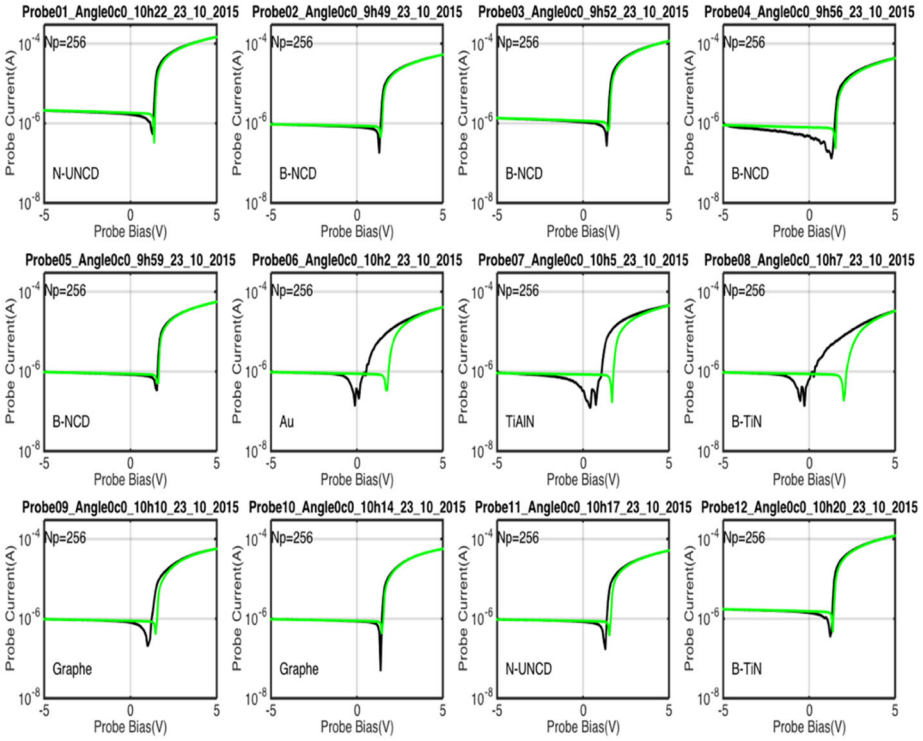

Fig. 53 Langmuir probe sweeps performed on 23 October 2015 at ONERA before probe cleaning by electron sputtering

When searching for long term durable conductive surface coatings for the Langmuir probes for the Cassini RPWS-LP instrument in the 1990 s, titanium nitride was identified as a suitable candidate due to its high mechanical durability and chemical inertness. An extreme degree of adhesion was achieved by using a process of "baking", i.e., conversion of the upper layers of a Ti sample to TiN by immersion in a nitrogen atmosphere at high temperature. Laboratory tests verified the general conclusions but showed that the probe would become very hot when passing Venus (Wahlström et al. 1992; Veszelei and Veszelei 1993).

During its lifetime, Cassini saw as wide a range of plasma conditions as JUICE will do, ranging from the very dense ionospheric plasmas during the Titan flybys and (even more) the end-of-mission orbits into Saturn's own ionosphere to the low-density regions of the Kronian magnetotail. The plasma density derived from RPWS-LP measurements, either by direct evaluation of probe bias sweeps or by a proxy method using the observed spacecraft potential, agrees very well with independent estimates using wave methods or particle integration (Wahlund et al. 2005, 2009, 2017; Morooka et al. 2009; Edberg et al. 2010, 2011, 2013; Holmberg et al. 2012, 2017, 2021). We consider the successful Cassini RPWS-LP as validating the use of a nitride coating for a Langmuir probe in conditions relevant to JUICE.

Two reasonable analogues for the RPWI electric field measurements are provided by Rosetta and Solar Orbiter. On Rosetta, RPC-LAP included two Langmuir probes, separated by 5 m that has been used in electric field mode, either with application of a bias current

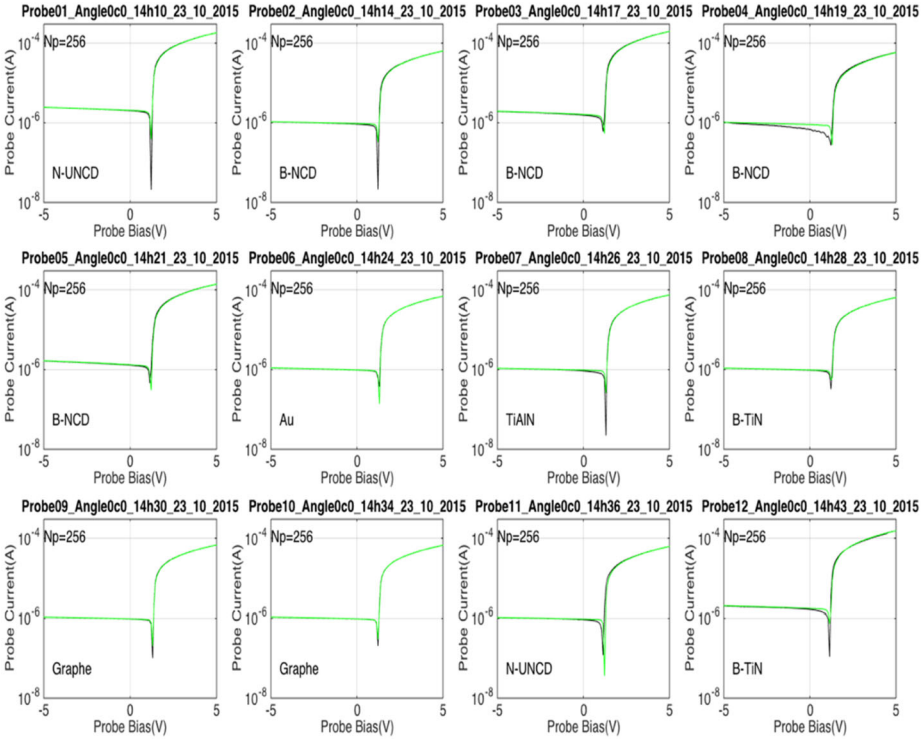

Fig. 54 Langmuir probe sweeps performed on 23 October 2015 at ONERA after probe cleaning by electron sputtering

or as floating probes (Eriksson et al. 2007, 2017; Odelstad et al. 2017). The electric field mode data were calibrated to particle measurements for monitoring the spacecraft potential (Odelstad et al. 2017) and has been used for studies of lower hybrid and ion acoustic waves (Karlsson et al. 2017; André et al. 2017; Gunell et al. 2017a,b). The Solar Orbiter RPW instrument includes three antennas, which has been used with a bias current as low frequency electric field probes with effective baselines of 7 m (comparable to the JUICE LPs, see Table 5) in two directions. The electric field measurements could be calibrated and verified by comparison to magnetic field and plasma drift measurements (Steinvall et al. 2021) while the spacecraft potential is used for studying plasma density variations (Khotyaintsev et al. 2021).

For the MEFISTO instrument on the BepiColombo magnetospheric orbiter (MMO), use of TiN, as on Cassini and Rosetta, was not possible due to the excessive equilibrium temperature at Mercury. A study for finding a thermally acceptable surface with the TiN durability resulted in identifying sputtered TiAlN as a suitable coating (Brogren et al. 2000; Larsson and Wahlund 2004; Blomberg et al. 2006a,b). Application by sputtering provided the additional advantage of a smoother surface, which is easier to keep clean, as well as a more controlled and repeatable process. Note that the mechanical durability is more than sufficient for space needs also for nitriding by sputtering, with commercial use including the hardening of cutting surfaces (Chauhan and Rawal 2014).

4.2.11 SCM

Figure 55 shows the SCM flight unit and its PCB which includes the ASIC pre-amplifier. Each SCM sensor is made of a high permeability rectangular nanocrystalline ferromagnetic core (VP800 from VaccumSchmeltze) allowing high amplification at low temperature. The ferromagnetic core is inserted into a mandrel (made with PEEK GF30). Two high turn number copper wires are coiled around this mandrel, the first one to collect the flux into the ferromagnetic core and the second one for the feedback and calibration signal. The so obtained sensor is surrounded by an electrostatic shielding and inserted into a protection tube. The sensor is filled with a low-density potting material (Mapsil 213-B) to ensure mechanical vibration stiffness.

The voltage across the winding is amplified by a dedicated ASIC two-stages low noise preamplifier (see Fig. 55). Since this sensor exhibits a natural resonance, the first stage output voltage is used to feedback the secondary coil magnetically coupled to the primary one through the ferromagnetic core, allowing to flatten the transfer function response without any noise degradation. The ASIC preamplifier mounted on a thin PCB has been inserted into the mechanical structure. Three sensors are mandatory to retrieve the magnetic field vector. They are maintained orthogonally thanks to a dedicated mechanical structure. This mechanical structure is attached to the MAG-boom. The boom is shared with fluxgate magnetometers positioned at a distance such that EMC disturbances from the spacecraft as well as the fluxgates are minimized. The tri-axis antenna is wrapped with MLI to filter temperature variation and to maintain coldest temperature within an acceptable operational range (>77 °K and <150 °C).

SCM low noise and low power ASIC preamplifier is designed in AMS CMOS 0.35 µm technology. The amplifier is supplied through a voltage regulator based on bandgap circuit, which has been implemented to guarantee regulated voltage stability over a wide temperature range [−200 °C; +100 °C] while increasing supply rejection. The first stage is optimised to get low noise while the next stage provides the required gain to adjust the signal to the 14 bits digitization provided by LF receiver (see Sect. 4.2.6) and first order low-pass filtering (20 kHz). A calibration signal, connected to the ASIC preamplifier is provided by LF receiver to check the transfer function over temperature and time in flight. The calibration signal varies from few Hz up to 20 kHz, with at least one frequency per decade and duration of each sine is higher than 100 ms. Calibration will be done a couple of times per orbit in burst mode. The ASIC has been tested at temperature as low as 77 K and proved radiation ability higher than 400 kRad|Si] at low dose rate. As the transfer function of SCM may varies smoothly with temperature and aging, an internal calibration can be performed in flight when high precision data are requested.

4.2.12 RWI Antenna System

RWI consists of three pairs of mutually orthogonal tubular booms (called SDAs, Single Dipole Antennas) assembled with an electronic preamplifier box and located far out (8.6 m) of the JUICE S/C on the last segment of the MAG boom (Fig. 56; Grygorczuk et al. 2023). When stored, the tubular booms possess potential energy that actuates their deployment and needs to be additionally damped by a patented miniaturized oscillatory damper inside the storage reel. RWI has a mass of 2.2 kg and deploys to a relatively large distance of 2.5 m (tip-to-tip). During the launch, the antenna reels are held by locking arms secured by a Vectran string and is released in flight via a thermal knife principle (like LP-PWI).

All three dipoles are directly fixed to their common electronics box (called the RWI Box, Fig. 57) with a thickness of 3 mm, which houses the three preamplifier PCBs, each assigned

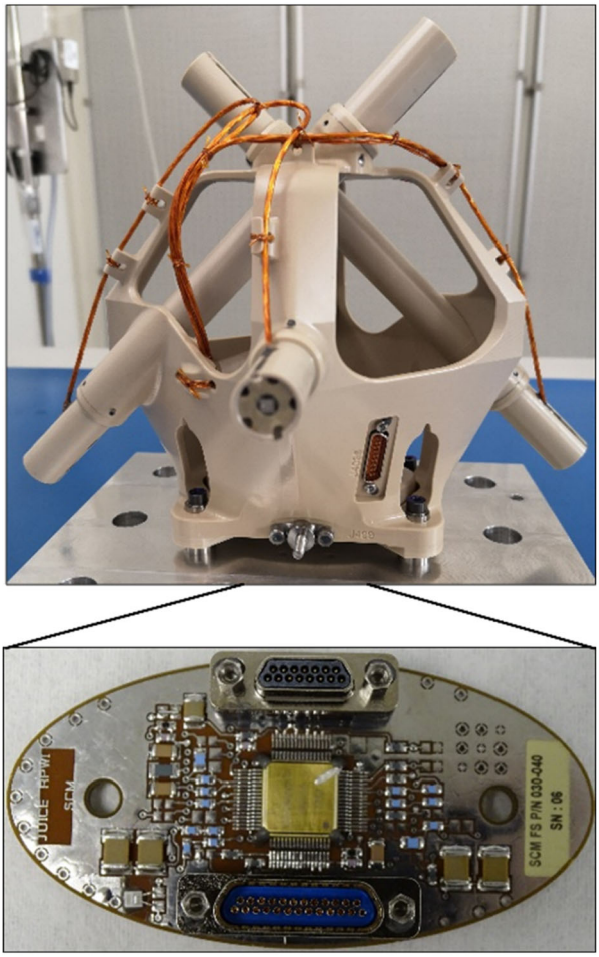

Fig. 55 Top: the SCM flight unit mounted on its mechanical test interface plate. Bottom: the SCM PCB including the ASIC low noise pre-amplifier

to one of the dipoles. Since the assembly on the MAG Boom is exposed directly to the space, the chassis components constitute thermal (together with two additional MLI blankets) and radiation protection for the electronics.

As mentioned above, the functional principle of the SDA is based on a tubular boom mechanism. The tubular boom strip is stored on a reel in the stowed configuration. When deployed, it forms a cylindrical tube with a diameter of c.a. 10 mm of a given length. The unquestionable advantage of the implemented solution is the lack of any motor drive and design simplicity. The deployment is based on energy accumulated in winded tape and its self-release during the transformation of the flat input profile to the original round one (Fig. 58). Notably, the selected material for the tubular booms is the Berrylium bronze alloy, which is non-magnetic (a strict requirement due to the proximity of the MAG boom experiment) and possesses unique strength properties, allowing for forming the tubes in a patented process. To meet the maximum allowable temperatures of the tubes, they are covered with sputtered DLC coating qualified for the mission and provide the necessary emissivity to absorptivity ratio.

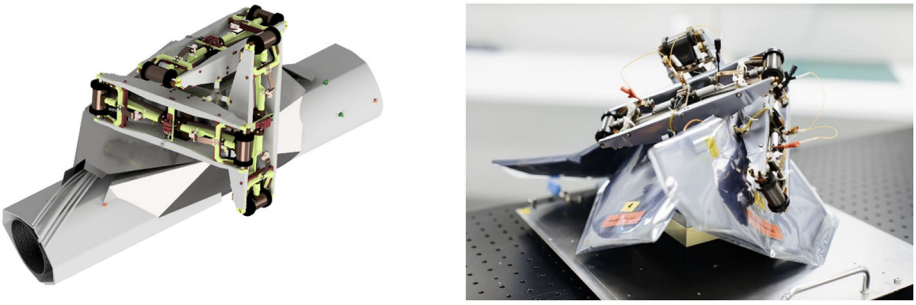

Fig. 56 (Left) Visualization of RWI dipole system on MAG Boom in stowed configuration. (Right) the actual Flight model of RWI antenna in stowed configuration before shipment to Airbus

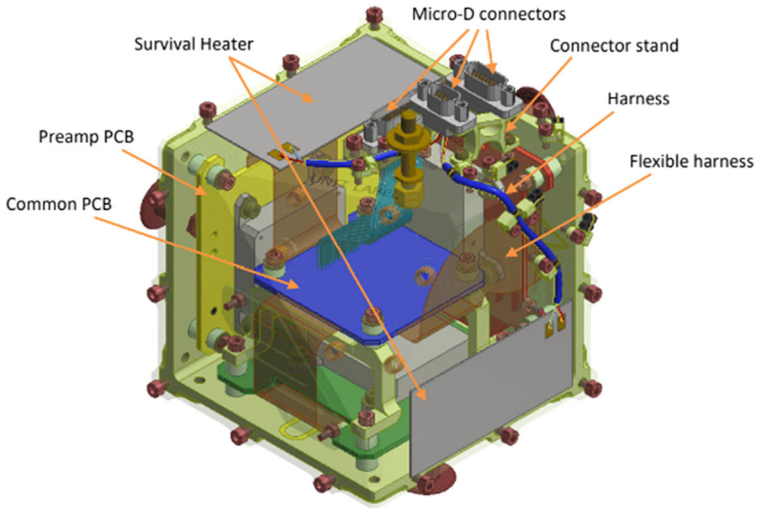

Fig. 57 Visualization of RWI chassis depicting details of its interior (three of the walls are transparent)

4.2.13 RWI Preamplifiers

A block diagram of the RWI preamplifier is shown in Fig. 59. The whole assembly is found in Figs. 31 and 56. RWI preamp consists of three identical differential amplifiers connected to U, V, and W SDA dipole antennas, respectively. At the input, signal clipping diodes are mounted at each amplifier input to mitigate the possibility of damage due to electric discharges. In parallel, the resister of 1 Mohm connects between the antenna line to the ground for the leak of charging.

Those amplifiers have high raw gain of $\sim$10 dB in 100 kHz – 25 MHz with the low noise floor of $\sim$10 nV/Hz$^{1/2}$. To keep high efficiency coupling with the SDA, the design aims the low base capacity, which achieves $\sim$25 pF including the amp input capacity itself, the wiring capacity between the antenna to the preamplifier input, and the stray capacity. The output signals are transferred to the HFR via the long HF-RWI harness along the MAG Boom with the length of 17 m. Although we use low-loss coaxial harness for the signal line, its loss becomes $-0.3 \sim -3.0$ dB in 100 kHz – 25 MHz and the phase difference between U, V, and W, are also distorted by this long harness.

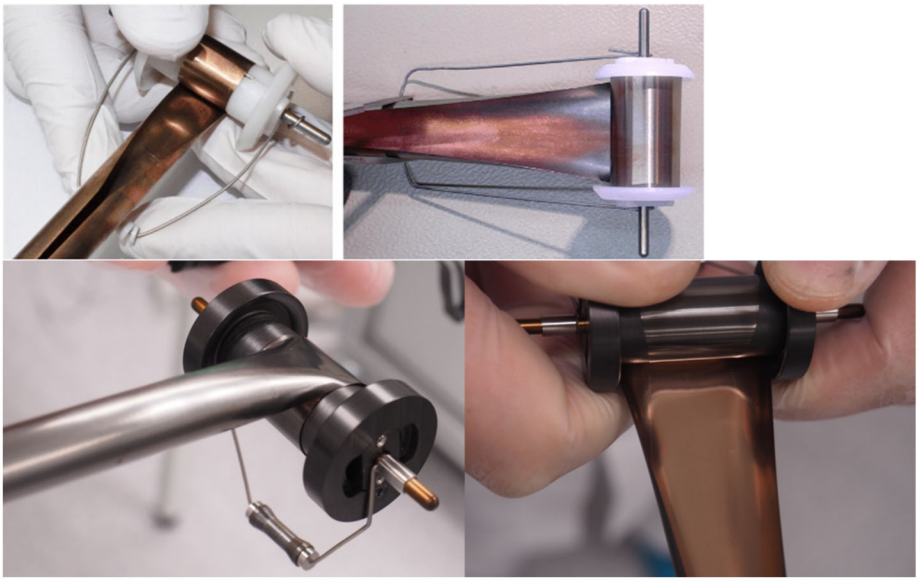

Fig. 58 Final tubular boom during rolling on storage reel

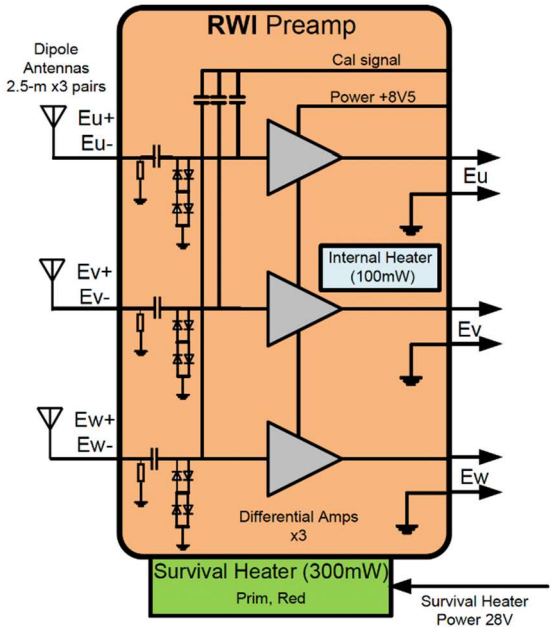

Fig. 59 RWI antenna preamplifier

The most important task for the JENRAGE experiment is the first achievement of high-precision polarization and the direction of arrival (DOA) measurements of the Jovian radio emissions. Those are disturbed by circuit characteristics (e.g., the RWI preamplifier characteristics, long RWI-HF harness, and the HFR). Including them, the practical electric field

sensitivity will be determined with the antenna. Unfortunately, the antenna length, 2.5 m tip-to-tip, is shorter than previous ones which visited the Jovian system like Voyager, Ulysses, Galileo, and Cassini. The reduced sensitivity by the short antenna with the expected capacity of <10 pF and the effective length of <1.0 m will be calibrated during the cruise and flyby observations, which utilizes natural radio sources like solar radio bursts in all frequency ranges and the terrestrial AKR below 1 MHz. In addition, HF also provides a calibration (CAL) signal to the RWI preamplifiers, to check the effects of temperature changes and degradations caused by radiation. The results will be summarized in a forthcoming paper on the JENRAGE calibration after the first Earth flyby.

As shown in Fig. 59, the RWI preamplifier has three preamplifier PCBs and one common PCB connected by flexible harness. Those are located inside the RWI chassis (Al, 3-mm thickness), and the active parts on each PCB are also covered by its own shield (Ta, 1.3-mm thickness) for protection against the harsh radiation in the Jovian environment. In the pre-launch analyses, the expected TID would be $\sim$100 krad. To endure this level, all the active components used by the RWI preamplifiers are specified by the manufacturer to withstand 300 kRad of TID.

Although we established the preamp will work for -180 °C $\sim +90$ °C, the gain is gradually reduced below -140 °C. To keep the preamplifier temperature even in the cold Jovian environment, the RWI preamp PCBs are thermally decoupled from the RWI chassis, by the PEEK supporters etc. By this effect, during the turn-on with $\sim$500 mW power dissipation of $+8.5$ V, the RWI preamplifier temperature was kept as $\sim$ 20 °C from the RWI chassis (i.e., $\sim$RWI preamplifier temperature is ~ -140 °C when RWI-chassis temperature is -160 °C). As a backup, RWI PCB can also activate an internal heater which provides additional 100 mW on the PCB next to the active parts. On the other hand, in the higher temperature environment like the flyby at Venus, this temperature difference reduces to $\sim$5 °C (i.e., $\sim$75 °C when RWI-chassis temperature is $+70$ °C), because higher radiation coupling between the PCBs and the chassis wall can be.

However, it means that the RWI preamp could be in very low temperature as the RWI chassis when its power is off. The gain becomes less when PCB temperature is lower than -140 °C, and it takes several 10 s min to reach the operational temperature and thermal equilibrium after the turn on. To avoid such unnecessary thermal cycling and for the emergencies, the S/C provides two survival heaters (nominal and redundant) attached on the outside of the RWI chassis. Once the S/C is beyond Mars and reaches the Jupiter orbit, when RWI is powered off, this heater can be activated by the S/C system (28 V) and continuously heat the RWI chassis with 300 mW. It can keep the RWI chassis at a reasonable temperature (>-160 °C) around the Jovian environment. This heater power is supplied from the System, but this path is through the HFR with a relay system. When this heater is off, the relay connects the survival heater lines to the RPWI EBOX chassis ground, to reduce the possible noise from the system power supply. This design is equivalent to the RWI deployment lines.

4.3 RPWI Mass, Power, Telemetry

4.3.1 Mass (Table 13)

- The orientation bracket for RWI is **not** included, with measured mass of 322.3 g.
- The MLI mass for RWI and SCM (which reside on the MAG boom) is included.

Table 13 RPWI sub-unit mass

Unit ((P)FM)	Measured [g]
EBOX (2 mm structure + 6 mm rad shield + internal PCBs)	8518
LP-PWI (booms+sensors)	4973
LP-PWI (preamp box + washers + stand-offs)	944
SCM (sensors+amps+MLI)	631
RWI (antennas+amps+MLI)	1797
RPWI total mass (with shielding)	**16,863**
Margin[%] (allocated 19.1 kg incl. shielding)	**13.3%**

Table 14 Subsystem representative maximum power usage when active. The numbers will vary with used operation modes for each sub-system. The modes in the top row are RPWI OFF (OFF), RPWI start up (Init), RPWI Standby and Safe modes, and RPWI max power science mode. Nominally the RPWI power consumption during science sampling will be around 12 W and significantly less than 21.8 W

Power modes [mW]	**OFF**	**Init**	**Standby**	**Safe**	**Science (max)**
LP-PWI sensors	0	0	0	0	528
SCM sensors	0	0	0	0	279
RWI sensors	0	0	0	0	556
MIME drivers	0	0	0	0	4
LP-MIME	0	0	0	0	2987
LFR	0	0	0	0	2658
HFR	0	0	0	0	7058
DPU	0	1883	1718	1718	1883
LVPS 77% eff. + 1100mW		1100	1100	1100	1100
EBOX (dissipated)	0	3547	3333	3333	20477
Total Power (Nom)	**0**	**3547**	**3333**	**3333**	**21839**

4.3.2 Power (Table 14)

4.3.3 Telemetry

The TM rate and Power will depend on the used operation mode of RPWI (there are many). Nominally the TM rate varies between 2.3 kbps – 65.7 kbps with a power of nominal power of 13.9 W. If the HF measures in radio burst or PSSR modes, then the TM rate and power may increase up to 1.6 Mbps and 21.8 W. RPWI also have a special low TM mode for downlink and spacecraft eclipse cases. See Sect. 6 for telemetry details of different operation modes.

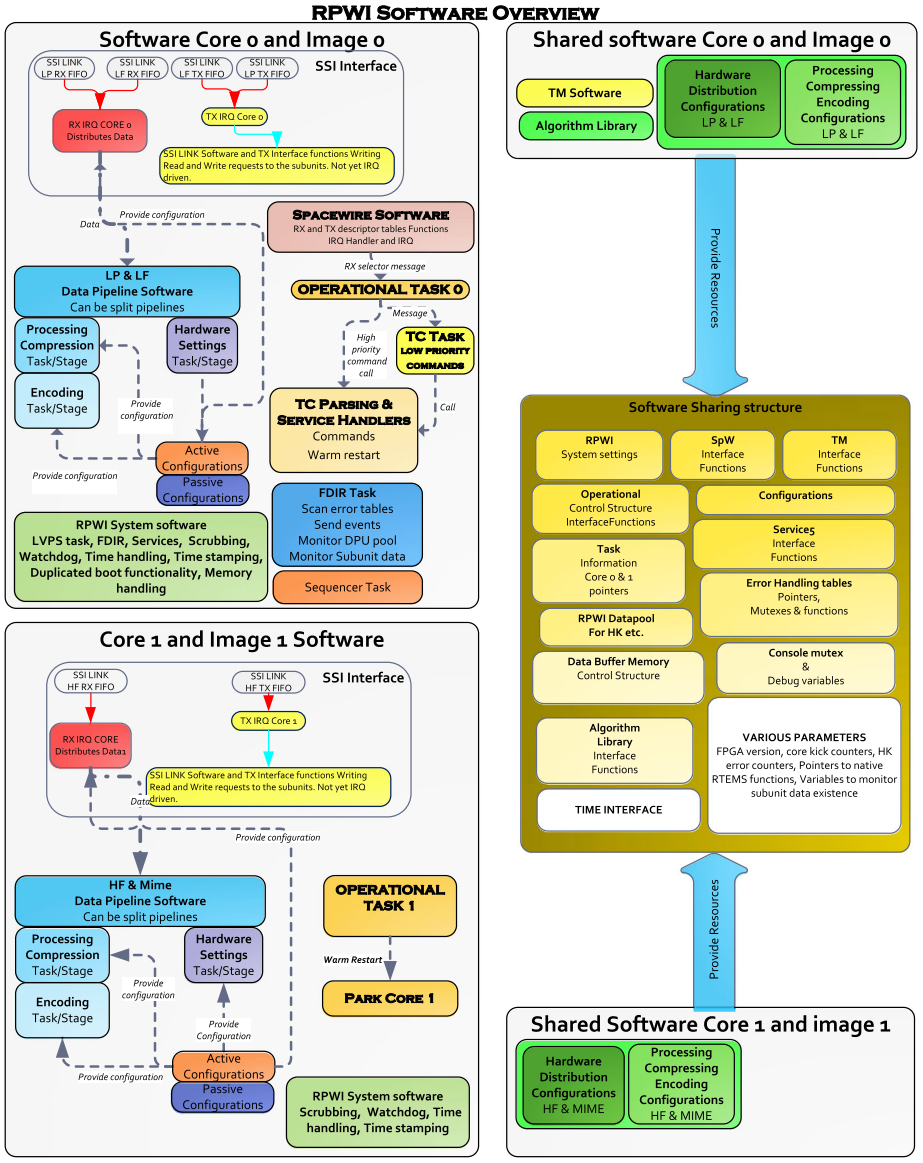

Fig. 60 Overview of the RPWI DPU software

5 Flight Software

5.1 General Design Goals & Architecture

The RPWI flight software run on the DPU, which has a dual core. Other flight software (VHDL for FPGAs) that run on the different subsystems is called firmware, as it is tightly linked to the hardware. The firmware and special receiver related application software (ASW) is described in Sects. 5.4 (LP), 5.6 (LF), and 5.8 (HF). The RPWI flight software

runs on a LEON3FT processor at a clock speed of 50 MHz. To handle the load of the most intensive science modes, both cores (referred to as Core 0 and Core 1) are utilised. Most core functionality, together with LF and LP DPU Software run on Core 0. Meanwhile, HF and MIME DPU Software run on Core 1, together with their required drivers and those required for inter-core communication. No work-sharing is done between the cores. An overview of the RPWI software is displayed in Fig. 60.

The software is built on top of the real-time operating system (RTOS) RTEMS. The software is written in the C programming language, using assembler strictly only when needed for small segments of code. It uses an event-driven task switching model to enable high priority tasks to interrupt lower priority tasks without taking away execution time when there is no high priority event to service. Non-blocking mutex locks are used to synchronise access to shared resources from multiple tasks. The boot loader is not using RTOS. The DPU software has several interfaces to the hardware. There are four to five internal data input links, interrupt signals and two space wire output links. Memory mapped I/O and interrupts will be used to communicate with the internal data links, DMA tables and interrupts will be used to communicate with the space wire links. We divide the software into logical blocks as follows (note that the blocks do overlap):

- Boot loader
- Overall control system
  - o Operational modes, science, and maintenance etc.
  - o Sequencing and duty cycling
  - o Kicking watchdog
  - o Etc. . .
- Receiving telemetry
- Parsing telecommands
- Sending telemetry
- Data pipelines
- Packaging of telemetry
- Science algorithms
- Spacecraft services
  - o Memory patching
  - o Memory dumping
  - o Event reporting
  - o Critical limits checking
  - o Etc. . .
- Housekeeping generation and transmission
- Time stamping and time handling
- Error handling software

These blocks are mapped to different PUS services described at the end of this Section. They also map to different tasks in the RTEMS task model. Task priorities are assigned in this order (TC, LVPS, FDIR and sequencer tasks only run on Core 0) and no two tasks share the same priority value:

1. Operational task – handle high priority telecommands, DPU hardware control
2. TC task – handle medium and low priority telecommands
3. LVPS tasks – control LVPS, handle LVPS telemetry
4. FDIR task – detect out of limit sensor or status values, perform appropriate actions
5. Sequencer task – run the operational sequencer
6. Subunit hardware tasks – control sub-experiment hardware

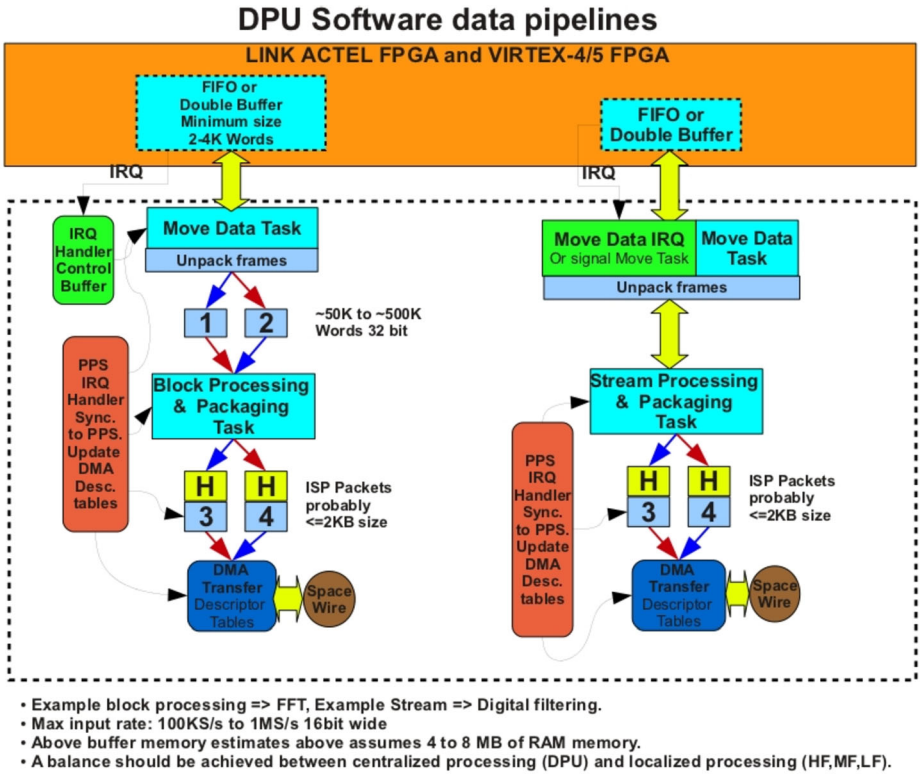

Fig. 61 DPU software data pipelines

7. Data pipeline tasks – process, compress and encode sub-experiment data, see below

Main task – kick watchdog, send housekeeping, perform routine maintenance

The core component of the software is the data pipelines describing the dataflow. The data pipelines in Fig. 61 describe two different examples of stream processing and block processing; both of which are used in the RPWI software. Block processing is used when all data need to be present before the processing starts, while stream processing will be used when you can start immediately. In both examples above data enters from the top coming from the instruments and exiting at the bottom to the spacecraft. The numbers 1, 2, 3 and 4 describe double buffers, where the arrows represent data flows and the colours red and blue represent different phases in time, blue could be the present state and red the next cycling back to blue and so on. The Pulse Per Second (PPS) represents a pulse generated each second and defines the highest rate a single pipeline can create output data packets.

Each of the sub-experiments (MIME, JENRAGE, GANDALF, SAMWISE) have their own pipeline consisting of one or more branches. Each branch has three stages: processing, compression and encoding. The processing stage is responsible for processing and packaging raw science data to produce the science products defined by the current instrument configuration. This includes the compression stage, after the processing part of each unit, responsible for compressing the science products for efficient storage and transfer. The encoding stage is responsible for preparing the compressed science products to be sent over SpaceWire by splitting up large packages and adding AUX headers.

Each pipeline branch stage is represented as its own task. In most cases, later pipeline stage tasks are given higher priority than their previous stages to ensure data flow even under a heavy load on the processing stage. However, MIME, which samples a large amount of data but only under a very short period, inverts this order to allow a higher acquisition rate than the maximum processing throughput by letting data buffer up in the pipeline and then process it later. Since no two tasks are assigned the same priority under our task model, LP tasks are prioritised higher than LF tasks and HF tasks are prioritised higher than MIME tasks.

The produced science data is divided into two categories: rich data and survey data. Rich data consists of high-resolution data which is produced at a greater rate than can be downloaded to Earth. Survey data generally consists of low-resolution data created through filtering and down-sampling of rich data to reach a data rate small enough to allow downloading all of it.

For the download of rich data, there exists two strategies: triggers and selective downlink. Triggers are programmed conditions for selecting which rich data to keep or discard based on what is detected in the science data. By limiting the number of times, a trigger can happen within a period, the amount of rich data sent to Earth can be kept within the bandwidth limits of the downlink. Selective downlink, on the other hand, is the practice of saving all rich data to the spacecraft mass memory and then select from Earth which time periods to download based on the information in the survey data. During the cruise phase of the mission close to Earth, all data (including rich data) will be downlinked without the need of Selective downlink.

The primary instrument control mechanism within the software is the sequencer. The mission timeline is another control mechanism. The sequencer provides 20 sequence tables, with each table capable of holding a sequence up to 64 lines long. Each PPS, the sequencer reads the current line in the current sequence table and executes it. Every line in the table describes certain actions the flight software will take when that line is executed, most notably selecting when to switch sub-instrument configurations and which configurations to switch to. Each line also describes which line to execute next and includes an optional repetition counter, thereby making it possible to create both finite and infinite loops within the sequence. If the sequencer reaches the end of the sequence table, it will restart from the top.

Each sub-instrument has 16 configuration sets containing all parameters required to define its operation, such as power settings, sweep tables and decimation values, as well as any other values which cannot be inferred at runtime, such as number of pipeline branches and their buffer sizes. Each configuration set is double buffered to allow updating a configuration while it is running.

For communication with the spacecraft and Earth, the flight software provides the following standard Packet Utilisation Standard (PUS) services for telecommand and telemetry handling:

- Service 1 – request verification
- Service 3 – housekeeping
- Service 5 – event reporting
- Service 6 – memory management
- Service 8 – function management
- Service 9 – time management
- Service 17 – test

In addition, the software provides the following mission-specific services:

- Service 145 – updates from J-MAG and reaction wheels

- Service 146 – enable/disable remote memory access protocol (RMAP) and destination logical addresses
- Service 204 – science data reporting
- Service 205 – telecommand echoing

5.2 DPU Application S/W

Each RPWI experiment and compression has application software (ASW) installed in the DPU (see relevant Sections below).

5.3 Compression

Data compression aims to represent the output from a sensor or onboard process as compactly as possible without loss of significant information. Compression methods may be classed either as 'loss-less' in which the original digital data may be recovered exactly, or 'lossy' which aims to preserve significant information, but does not recover exactly the original data, in effect reducing the precision of the measurements. With loss-less compression, the resulting data volume depends on the characteristics of the data, and no amount of compression can be guaranteed. However, on typical data a 2:1 ratio or better can often be achieved. When the available data storage (or telemetry bandwidth) is not sufficient to contain the compressed data, the options are either to store (or transmit) less samples, or to represent the samples less precisely.

The compression implemented for RPWI is normally loss-less, with an option to reduce precision to achieve a specified data volume by discarding the least significant bits. The compression is based on CCSDS standard 121.0-B-3 (CCSDS 2020), which comprises:

- A pre-processor which applies a reversible function to reduces the information content (numerical entropy) of the data as much as possible.
- An entropy coder which codes that information in the smallest number of bits.

The choice of pre-processor is the key to achieving good compression. RPWI employ both the unit delay predictor, where each sample is replaced by the difference between its value and that of the previous sample using modular arithmetic, and Linear Predictive Coding (LPC), where the difference from a prediction based on a linear combination of N previous samples is made. In the RPWI implementation LPC is applied to a single data component or a single spectrum using contiguous previous samples. Whilst it is in principle possible to use multiple components or spectra, thus exploiting inter-channel correlations, tests showed that for a given number of prediction coefficients the single channel implementation gave the best results. It is also considerably faster as the Levinson–Durbin method of matrix inversion may be used to calculate the coefficients, rather than Gaussian Elimination.

The standard specifies that the Rice algorithm (Rice et al. 1993) shall be used as the entropy coder, with exceptions including no compression and run length encoding when these result in a smaller data volume. This is an optimum way to encode data with a geometric distribution, which the pre-processor aims to achieve. The Rice algorithm has a single 'tuning' parameter k which is chosen to achieve the smallest data volume. The standard specifies this will be done by trying each value in turn, which is computationally expensive. Instead, the RPWI implementation uses a method described by Kiely (2004) based on the mean value (μ) of the input ($k = \text{floor}(\log_2(\mu + 0.382))$). In our tests Kiely's method selects the optimum value in 95% of cases with the remainder being border line cases unlikely to affect compression efficiency if an adjacent value were used.

Data compression for RPWI has two important requirements:

- The processing time must have a well-defined upper bound so we can be sure that the data will be processed in the time available.
- Spacecraft telemetry systems are not 100% reliable. Loss of data can occur during marginal link conditions. The data must therefore be processed in self-contained blocks, such that no other data are required to perform the decompression.

Both pre-processor implementations are primarily intended for application to linear numerical representations of physical quantities such as a voltage applied to an analogue to digital converter. Special considerations are needed for other source data formats. For RPWI these include the raw output data from the receivers' FPGAs, and floating-point data produced in the DPU tasks.

FPGA data may be processed simply as an array of bytes using the 'unit delay' pre-processor. Each byte within the data frame is processed as a separate component, with differences taken with respect to the same byte position in the previous frame. The use of modular arithmetic means this works efficiently even if the bytes are part of a larger numerical quantity.

Floating point data is handled by noting that the IEEE floating point format used (including the mini-float variants) when cast to an integer is effectively a piece wise approximation to the logarithm of the original data. In general, the integer representation shows three distinct ranges corresponding to negative, zero, and positive float values. These ranges need to be translated so they appear adjacent when applied to the compression (to avoid large difference values when transitioning from one range to another).

5.4 LP Receiver DPU Software

The LP part of the DPU software is responsible for configuration and control of the LP receiver hardware, as well as handling and processing data produced by the same. LP software is also responsible for calculating the spacecraft potential from electrical field data and sending it to the JUICE on-board computer for further distribution to other instruments. LP software is incompatible with MIME DPU software and must not interact with the LP receiver hardware while MIME software is active.

The core component of the LP configuration is the LP sequencer table. Each table row consists of a command with two arguments. The commands can select what LP software sub-mode to run, write a value directly to a LP receiver hardware register, generate new sweep tables, or tell LP software to wait for a set amount of time or for certain triggers. The LP sequencer table can contain at most 50 commands, which are executed when LP is enabled via the operational sequencer or via telecommand. Commands are executed one after another in order, and LP software will infer most of its behaviour from the written hardware register values. This grants fine control over the LP software and receiver hardware, but care must be taken to ensure no timing or order invariants are violated.

While LP allows a wide range of possible configurations, default implementations focus on a few specific categories of data products:

1. DE763 & DE24 – This category features time series of plasma density or electrical field data measured at a rate of 763 samples per second. This rich data product is passed through a low pass FIR filter and decimated to produce a parallel survey data product of 23.8 samples per second. A configuration flag allows for disabling the rich data product during periods of especially strict bandwidth constraints.
2. Voltage sweeps with hardware or software decimation – This category features plasma density sweeps, either between ± 10 V or ± 80 V, and optionally with some probes configured for measuring electrical field or plasma density with a fixed bias. A configuration

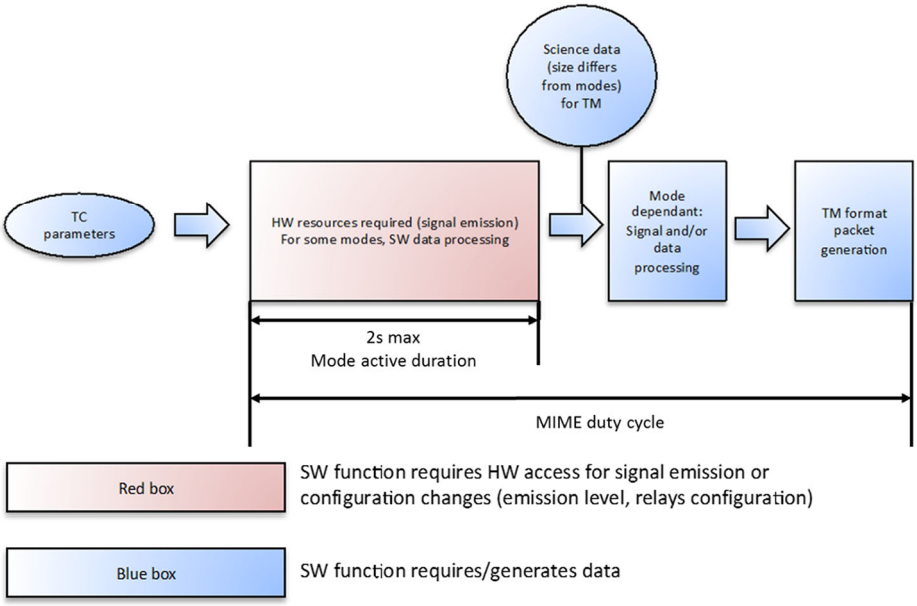

Fig. 62 MIME basic operations philosophy

flag allows running either single or double sweeps, where the latter runs the two available sweep tables back-to-back. Due to hardware limitations, the LP receiver hardware will discard an equal number of samples to remove the step response regardless of whether the channel is sweeping or not. To counteract this, a configuration value can enable LP software to perform this decimation only the sweeping channels.

3. E694k – This category features electrical field snapshots, typically containing 16,384 samples, with a sample rate of 694,000 samples per second. The data follows a special raw data format where each sample has a lower resolution (14 bits instead of 21) and carries a minimal number of metadata, meaning this data product must be timestamped by LP software using the DPU clock instead of by LP hardware.
4. D49k – This category features plasma density sweeps, typically containing 32,768 samples, measured with a sample rate of roughly 48,800 samples per second.
5. Frequency sweeps – This category features complex electrical field data measured with the mixer active and centre frequencies taken from an automatically generated sweep table. Each step in the table shifts the centre frequency by 75% of the sample frequency to create overlapping bins suitable for FFT analysis. The full sweep typically covers the bandwidth 0 – 1.54 MHz.

5.5 MIME DPU Software

The main tasks of the MIME DPU software are (see also Fig. 62):

- To configure the instrument. MIME has two fundamental antenna configurations. Either the four Langmuir probes are used for emission/reception (LP/LP), or the Langmuir probes are used for emission and the RWI antennae are used for reception (LP/RWI).

- To generate a sinusoidal signal at a frequency determined from a frequency sweep table. This signal is then applied to one or two Langmuir probes for both configurations (LP/LP and LP/RWI).
- To synchronously analyse the received signal, which is carried out in the DPU in two different ways depending on the instrument configuration (LP/LP or LP/RWI). The products of the analysis are the amplitude and the phase spectra of the electric field.

MIME performs two different types of measurement: passive and active. In active measurements, MIME synchronously performs signal transmission and reception while in passive measurements, there is no transmission and only a reference signal is acquired. On one hand, active measurement relies on an on-board frequency table to construct the spectrum by successively transmitting at different frequencies and analysing the received signal around these frequencies. On the other hand, passive measurement is carried out over the entire frequency range of interest by taking samples through a filter all along the frequency span. An FFT with amplitude averaging is then applied to produce the passive spectrum.

The MIME ASW has four science modes, which all have a maximum active duration of 2 seconds:

- **Wide sweep mode:**

This mode performs sweeps in the entire low and high-frequency bandwidth with the aim to measure the plasma frequency f_{pe} with a fixed resolution. This mode produces two passive and two active spectra: 1 passive and 1 active sweep is produced from 3 kHz to 1.5 MHz in LP-LP configuration, and 1 passive and 1 active sweep is produced from 80 kHz to 3 MHz in LP-RWI configuration. The mode only uses 1 channel in LP-LP mode and 1 channel in LP-RWI mode.

- **Nominal Sweep mode:**

This mode performs sweeps on a selected frequency bandwidth with the aim to measure the plasma frequency f_{pe} with a chosen resolution. The mode has 8 sub-modes that can use either 1, 2 or 3 reception channels (dipoles). Each sub-mode uses a defined number of channels (dipoles), performs a defined number of sweeps, and generates a defined number of frequencies. The configuration of dipoles is given by hardware switch positions.

In addition, there are two additional sub-modes. A relaxation mode, which performs a mutual impedance measurement, waiting for the plasma to "relax" and performing a measurement on the residual amplitude. It only uses the LP/LP configuration. The second sub-mode is the slow mode, usable when the amount of TM available for MIME is low. It consists of a nominal passive sweep and an active sweep with a reduced number of frequencies.

- **Tracking mode:**

This mode determines local density gradients by following the short time-scale evolution of the plasma frequency f_{pe}. This mode carries out a measurement on either LP-LP or LP-RWI. A passive sweep is performed followed by an active sweep on the entire corresponding frequency span. A search algorithm is then run on the data to determine the frequency of the maximum amplitude in the spectrum. A series of active sweeps are then successively performed over a narrower frequency band encompassing that value.

- **B-field mode:**

This mode determines the magnitude of the static magnetic field. It is an experimental technological mode. This mode consists of performing a linear sweep in the frequency

range of 3 kHz to 100 kHz, performing computation on the data measured to determine the electron gyro frequency and performing other sweeps around the electron gyro frequency harmonics. The second sweeps will use a specific hardware mode called "wide noise" that offers the possibility to emit on a wide range of frequencies. As a result, the obtained signal corresponds to a large spectrum with a resolution proportional to the emission duration. In addition, as an extra functionality, this mode can also be used to measure the plasma frequency at high resolution within this frequency range. Indeed, the processing to obtain the gyro frequency and the plasma frequency is very similar so the functionalities implemented in this mode can be multipurpose.

The mutual impedance spectra reflect the characteristics of the equivalent electric circuit (composed by the transmission and reception devices and the surrounding plasma) as a function of the frequency and depending on the plasma local properties. They are then analysed on the ground to infer the main plasma response and, when possible, derive the electron density and the electron temperature.

5.6 LF Receiver DPU Software

The LF part of the RPWI application software takes care of configuration and control of the LF receiver as well as handling and processing of the raw data transmitted by the LF receiver to the DPU. This software layer is highly configurable and allows to adjust the set of components to be transmitted, snapshot length, frequency axis of the spectral products as well as details of the spectral processing and waveform snapshot triggering – an algorithm to automatically detect plasma waves and dust impacts in the LF data. The LF software is compatible with the sequencer cycle of RPWI but does not use this cycle to control the configuration of the hardware. Instead, the LF receiver is configured to a desired configuration on entering science mode and remains in the same configuration until powered off or until a new configuration is set by a telecommand.

The LF software handles the incoming data from the LF receiver in three parallel pipelines implemented in separate RTEMS tasks: one pipeline for the decimated waveform at 762.9 sps (DWF), one for spectral matrices (SM) and one for the full resolution waveform snapshots (WFS).

The following data products can be generated after post processing of LF data by the software.

Waveform data products:

- A continuous time series of magnetic field fluctuations (SCM) from E/D signals (LP) sampled at a rate of $762.9/2^N$ samples per second, where N is configurable between 0 and 5. For values of $N > 0$, the decimation of the raw DWF data is performed in software by an FIR filter of order 512.
- Waveform snapshots sampled at 762.9 samples per second. These snapshots of up to 16,384 samples per second are extracted from the DWF data stream.
- Snapshots of time series sampled at 48.8 kHz or 24.4 kHz of up to 262,144 samples per component. These snapshots are taken by the LF receiver periodically and if triggering is enabled (see below), the software selects which snapshot will be sent to the ground and which snapshots are discarded.

All the waveform products above are transmitted as 16-bit integer values and the number and configuration of field components can be chosen arbitrarily by a telecommand. For some

products, only the three SCM signals are typically selected, while for others a set of 7 (3 magnetic and 4 electric field and/or density) components is sent to the ground.

Spectral data products:

- Averaged cross-spectral density matrices of selected components. These are averaged in the LFR board FPGA and the result is then further averaged in time in the software and compressed to an efficient form. An arbitrary frequency axis can be defined, typical configurations use a logarithmic frequency axis of up to 128 bins.
- Propagation and polarization parameters calculated on-board from spectral matrices. These include the intensity of the electric and magnetic field fluctuations, ellipticity, sense of polarization (left- or right-), degree of polarization (coherency), wave vector, and Poynting vector for a set of preselected frequency bands. This is a highly compressed product with minimum telemetry requirements. Two version of the product exist (BP1 which is effectively a more compressed version of the spectral matrix and requires 16 bytes per frequency bin and BP2 which contains the on-board calculated wave properties condensed into 4 bytes per frequency bin. Magnetic field vectors provided to RPWI on-board by the J-MAG instrument are used in the calculation of the wave parameters. They are used to transform the SCM data to field aligned coordinates before averaging and allow to evaluate projection of the Poynting vector to magnetic field direction. Due to the efficient form, these products can be generated at a high time resolution. The cadence of this data product is configurable from 250 ms to 30 seconds while its frequency axis is shared with the cross-spectral matrix data products, but can be reduced by summing together 2, 4 or 8 adjacent spectral bins.

Statistical data, triggering and event detection:
The LF software also implements several internal algorithms for event detection and snapshot triggering. The baseline triggering algorithm operates on each WFS snapshot taken by LF receiver. The instrument can be configured to collect and process up to 1 snapshot of 16,384 samples per second, corresponding to a 33% duty cycle. If longer snapshots are configured, they must be taken less frequently not to exceed this duty cycle limit imposed by the required processing load on the RPWI CPU. The detection algorithm calculates peak amplitude, median absolute value, RMS amplitude as well as a number of sign changes (Z_x) for a selected component. The classification of the snapshot is then performed by comparing the ratio R_{pm} of peak amplitude to median absolute value and the number of sign changes to predefined thresholds. Events can either be classified as waves for large Z_x and small R_{pm} or as dust impact spikes for the opposite case. An additional decision criterion is the RMS power in magnetic components; it is assumed that only plasma waves can have a significant magnetic component.

The triggering algorithm records the results of the processing of each snapshot and transmits characteristics such as a number of waves, dust impacts, peak and RMS amplitudes in the form of a short statistical data packet. The classification also assigns a quality factor to each snapshot and the highest quality snapshot is stored in a temporary buffer and transmitted to the spacecraft at the end of the RPWI sequence cycle. A second triggering algorithm based on spectral matrices and wave parameters is also implemented, but this only allows to detect waves and not dust.

5.7 S-WPIA

Software-type Wave-Particle Interaction Analyzer (S-WPIA) is a software function that can run in the DPU but is currently considered to be run on ground only. S-WPIA computes

physical quantities using wave electromagnetic fields and velocity vectors of plasma particles to measure the energy transfer between plasma waves and particles directly and quantitatively (Katoh et al. 2017, 2018). The significance of WPIA has been demonstrated by recent spacecraft observation in the terrestrial magnetosphere (Kitamura et al. 2018; Asamura et al. 2021; Shoji et al. 2021). The prime target of S-WPIA in JUICE is ion cyclotron waves (∼1 Hz) and related wave-particle interactions occurring in the region close to Ganymede and other Jovian satellites.

S-WPIA uses waveform of wave electromagnetic field sampled by GANDALF and/or SAMWISE, and particle counts measured on-board by PEP/JDC and transferred on-board by a link to RPWI. S-WPIA also uses the background magnetic field vector $\boldsymbol{B}_0$ measured by J-MAG. S-WPIA uses the wave and particle data sampled in the region of interest during the same time interval. The in-flight S-WPIA computation significantly reduces the data volume to be downlinked to the ground, but the computation can be carried out on ground as well as all data is currently planned to be downlinked.

S-WPIA collects the wave and particle raw data sampled in the region of interest during the same time interval. The raw data measured by PEP/JDC and J-MAG can be transferred to RPWI through inter-instruments communication. PEP/JDC data consists of the number of particles counts C as a function of energy (K), azimuth (φ), elevation (α), and mass-per-charge (m/q) with a time-tag showing the timing of the measurement. S-WPIA collects electromagnetic waveforms and the background magnetic field vectors measured simultaneously with the particle data and packs them into 1 data-unit. The stored high-resolution raw data will be transferred to the ground for detailed analysis.

The variation of the kinetic energy K of a charged particle can be obtained by computing the inner product of wave electric field $\boldsymbol{E}$ and velocity vector $\boldsymbol{v}_i$ to obtain $W_i = q_i\ \boldsymbol{E} \bullet \boldsymbol{v}_i = dK_i/\mathrm{d}t$. By accumulating W for particles detected during a certain time interval to obtain $W_{int} = \sum W_i$, we obtain the amount of energy transferred between plasma waves and particles.

S-WPIA uses $C\ (K,\ \varphi, \alpha, m/q)$ and electromagnetic waveform $\boldsymbol{E}(t)$ and $\boldsymbol{B}(t)$ to compute $W_{int}\ (K,\ \theta, \zeta, m/q)$, where θ is the pitch angle, ζ is the relative phase angle between wave magnetic field and particle velocity vector, θ and ζ are computed from φ, α, $\boldsymbol{B}$, and $\boldsymbol{B}_0$. The number of particles N and the standard deviation σ of the computed W_{int} are also obtained. We integrate the output matrices of S-WPIA, $W_{int}\ (K,\ \theta, \zeta, m/q)$, $N\ (K,\ \theta, \zeta, m/q)$, and $\sigma\ (K,\ \theta, \zeta, m/q)$, for ζ and/or θ to reduce the data size to be transferred to the ground in a later stage as well as to measure the energy exchange with the statistical significance. The S-WPIA output matrices indicate the region where strong wave-particle interaction occurs and can be referred to in selecting the full downlink of the stored high-resolution raw data.

5.8 HF Receiver DPU Software

The HF receiver DPU Software treats the command to, the housekeeping (HK) from, and the telemetry from the HF receiver. The commands sent from the spacecraft are received by the HF DPU software and sent to the HF receiver triggered by PPS pulse. Those are sent to the HF FPGA and set the hardware and raw telemetry modes. The HK are taken from the HF receiver and the DPU HF software itself. Those are sent to the spacecraft once per 1 second.

The HF receiver telemetry includes the whole properties of radio waves produced by many different radio sources at Jovian polar region and atmosphere, the Jovian magnetosphere and the Io torus, and the vicinity of the icy moons, including Ganymede's magnetosphere (cf. Sects. 2.5, 3.14 and 3.15). Those data also contain the occulted, refracted, and

Table 15 Maximum lengths of continuous wave form HFR

Decimation	Data rate (−3 dB)	Effective bandwidth	Max data length [msec] 65,536 samples / data rate
304	296 ksps	224 kHz	221
608	148 ksps	112 kHz	422
1216	74 ksps	56 kHz	885
2432	37 ksps	28 kHz	1771

reflected waves via the ionospheres, surfaces, and sub-surfaces of icy moons (cf. Sects. 2.5 and 3.3). The data stored in the spacecraft are transferred to the ground fully or partially after the selection. We summarize here the data flow, including the raw data transferred from the HF receiver, the processing in the DPU, and the produced data telemetries.

5.8.1 Raw Data Transferred from the HF Receiver

From the HF receiver, the DPU can receive the down-converted waveform at arbitral frequencies between 80 kHz – 45 MHz, at stepped central frequencies. The data is taken based on 'the sweep table' stored in the DPU. The start of each frequency sweep is triggered at the timing of PPS pulse sent to the HF receiver.

The sweep table contains the list of central frequency steps and the number of down-converted waveform samples for each step. The number of the frequency step can be set as 1 – 512, and the number of samples in each frequency step is set as 1 – 65,536. The output waveform also depends on the decimation (Table 15). Those parameters can be flexibly selected with telemetry modes.

5.8.2 HF Data Telemetries Produced from the HF DPU Software

The raw data stream from the HF receiver is stored in the data buffer in the DPU with the size of 10 MB. The HF software reads this data and produces the telemetry which contains power, polarization, cross spectra information or waveforms. The processes include the averaging in the frequency and time regimes, the calculations of auto and cross correlations, and the rejection of noises and interferences generated by the spacecraft.

For the telemetry production, the HF software has the following sequence: (1) HF receiver FPGA setting, to set the sweep table, to set CAL ON/OFF, etc., (2) Software setting, to set the data processing mode, (3) Data acquisition from the HF receiver, (4) to process the data, and (5) to transfer the telemetry into the compress and encoding.

The following HF data telemetry modes currently exist, (1) Radio-Full mode, (2) Radio-Burst mode (rich/survey), (3) PSSR-1 mode (rich/survey), (4) PSSR-2 mode (rich/survey), and (5) PSSR-3 mode (rich/survey). In total, HF produces five major modes of telemetries plus a Test (RAW) mode which transfers the HF receiver raw I/Q waveforms directly. During the cruise phase, the implementation of the final HF operation modes will depend on the results from calibrations and the trial of artificial noise rejections.

(1) The 'Radio-Full' mode

Radio-full mode is used for long-term monitoring of radio waves, intended mostly for the Jovian orbiting phase to study the general variability of the magnetosphere. Down-converted I/Q waveforms is sent from the HF receiver, where the central frequency is swept once per sequence cycle (usually 30 – 600 s), with logarithmic 256 steps from 80 kHz to 45 MHz.

There exist several sub-modes; (a) power spectrum, 3 components, (b) spectral matrix, 9 components, (c) spectral matrix with polarization separation (linear, right- and left-handed), 28 components, and (d) 3D spectral matrix, 21 components. Nominally the spectral matrix mode (b) is used and samples a 3-channel (U, V, W) spectral matrix with 9 components. Before the frequency averaging (all modes), line noise rejection (RFI mitigation) is applied. It is based on the 'RFI frequency mask pattern' uploaded from the ground.

(2) The 'Radio-burst' mode for Occultations

Radio-burst mode is primary used during occultations of Jovian radio emission by icy moons and their ionospheres. This mode is activated during the flybys of ice moons and on orbits around Ganymede (twice per orbit), when JUICE can see the Jovian HOM radio source above the northern and southern auroral oval through the icy moons' ionosphere on the limb. Total time of measurement of single run can be 10 min. To observe frequency dependent cut-off of the radio emission by the radio occultation, spectral matrix of Jovian radio emissions below ∼2 MHz is measured. The mode is focused on fine time and frequency resolutions to trace the cut-off frequency changes associated with the spacecraft-limb relative motion.

The current plan is to sample down-converted waveform with 37 kHz bandwidth by the HF receiver. Its central frequency is swept with 72 steps, 28 kHz interval from 80 kHz to 2096 kHz. To track the variation of spectral features the data is taken with fine time and spectral resolutions (dt = 0.2, 0.5, 1, or 2 seconds and df = ∼30 kHz) respectively. In the DPU, these waveforms are converted from raw I/Q waveforms to complex spectrum. The waveforms from three channels (U, V and W) are processed for each sweep step. The spectral matrix with 9 independent components (three auto correlations and six cross correlation components) are created. The 3D spectral matrix with 21 independent components can also be as an option. RFI mitigation is not applied in this mode, because it consumes the processing time and has an impact to the time resolution. The rich data transfer to the Earth is after the selection based on the survey data. The survey data product contains one-tenth samples of the rich data. All of them will be transferred to the Earth as a quick-look data sets of the rich data product.

(3) The passive sub-surface radar (PSSR) modes

PSSR has three modes to measure the electric characteristics of the surfaces and subsurfaces of Europa, Ganymede, and Calisto by reflections of Jovian radio emissions. PSSR1 and PSSR2 is based on the frequency domain characteristics, and it requires the DPU onboard processes. PSSR3 sends the raw down-converted waveforms for further analyses on the ground.

A. PSSR1 mode

PSSR1 mode is used to detect interferometry pattern appearing in a frequency-time spectrogram of Jovian radio emission. If the Jovian radiation is seen as a coherent and continuous radio source, an interferometry pattern can arise from a mixture of Jovian radio waves (directly from source regions near Jupiter) and those reflected from the icy moon surface and subsurface structures. PSSR1 tries to resolve this fine interferometry patterns in the spectral matrix with 2.3 kHz spectral resolution.

The current plan is to produce a single data set by down-converted waveforms scanned by the HF receiver with 296 kHz bandwidth (2048 data points for each waveform, selectable) at 45 frequency steps for 10 MHz span with 222 kHz interval. It consists of short waveforms with the duration of 6.92-msecond at each frequency, and full duration is < 1 sec per sequence. In the DPU, these waveforms are converted from I/Q waveforms to complex spectrum as Radio-Full mode. The waveforms from two channels among U, V and W are processed for each sweep step. After RFI mitigation an averaged spectral matrix are produced.

The rich data product contains 4 spectral matrix components for 4320 frequency channels. The survey data product contains power spectrum of 540 frequency channels. The data transfer to Earth occurs after a selection based on the survey data.

B. PSSR2 mode

PSSR2 mode is like PSSR1, but for non-continuous Jovian short radio burst, S-burst, a part of the Io decametric radiation (Io-DAM). S-burst has dispersive fine spectral structures so its short duration of several milliseconds can be potentially used like Chirp radar signals. If the S-burst signals reflected from surface and subsurface structures are included in the received signals, the arrival time of the reflected waves will be delayed compared to the direct wave from Jupiter. PSSR2 will operate as a "Doppler-radar" through onboard auto-correlation analysis of the S-burst signals and their reflection shorter than the transmission time (>500 km·2/c ≈ 1.6 ms).

In the current plan a single data set is produced by down-converted waveforms scanned by HF receiver with 296 kHz bandwidth (2048 data points for each waveform) at 45 frequency steps (+3 dummies for EMC checks). It consists of short waveforms with the duration of 6.92 ms at each frequency. In the DPU, these waveforms are converted to complex spectrum with FFT, their power spectrum, and finally the auto-correlation functions with inverse FFT. The rich data product contains 16 auto-correlation functions from the U, V, or W-channel (one channel among three) with fine lag-time resolution (2048 steps). Those are selected from measured 45+3 frequency channels, based on the greater auto-correlation values at the zero lag-time (i.e., total signal power). The data transfer to the Earth is after the selection based on the survey data.

C. PSSR3 mode

PSSR3 mode obtains raw down-converted waveforms, which are the mixture of direct waves coming from Jupiter and reflected waves from icy moon surface and subsurface structures. The plan is to sample a single data set for about 10 seconds/sequence cycle, with a set of 128 waveforms during 11.2 ms each in intervals of 77.8 ms. The data samples a single centre frequency at several 100 kHz to a few MHz, for the correlation analyses on the ground.

The rich data product is the down-converted I/Q waveforms in U, V, and W with 296 kHz bandwidth (2048 data points for each waveform). This data is transferred to the Earth without any further processing in DPU. The single data is large, 54 Mbit per sequence cycle. Therefore, the data transfer occurs to Earth after a selection based on the survey data.

The survey data product is the auto-correlation function in U, V, and W, with 128 lag-time steps for short waveforms in the rich data. For this product, the DPU converts raw I/Q waveforms to complex spectrum with FFT, makes their power spectrum, and produces the final auto-correlation functions with inverse FFT. The single data is not large, 61 kbit (with 10-sec duration). This data will be fully transferred to the Earth as a quick-look data sets of the rich data product.

6 RPWI Operations

6.1 Concept of RPWI Operations

The RPWI operations are designed to meet the overall science objectives of the JUICE mission (see JUICE Science Working Team 2014). This means a continuous sampling of the near DC electric field is required, so is the monitoring of all electromagnetic and plasma

Table 16 Current solid state mass memory allocation to RPWI

RPWI SSMM allocation	Gbit
Selector 1 (In-Situ)	10
Bulk 1 (In-Situ)	170
Selector 2 (Radio)	5
Bulk 2 (Radio)	15
Selected (S/C control)	2

wave modes and the dynamics of the thermal plasma. Below we describe briefly the common RPWI operation modes, while a more detailed description would be found in the continuously maintained operation mode documents of RPWI. It is therefore recommended that a contact is made with the PI institute when analysing the data to understand possible features of how the instrument is operated at a given time.

6.2 SSMM Partition and Selective Downlink

The science operations at Jupiter are based on the selective downlink method to gain high quality data. The Solid-State Mass Memory (SSMM) onboard JUICE and its partition for RPWI is given in Table 16 (can be changed in-flight).

The allocation is based on calculated RPWI TM rates at Jupiter and expected operation sequences, where a couple of examples are presented in Sect. 6.3 below. The selector (or survey) data is always downlinked. The table numbers assume a 4-week (28 days) turnaround period for selecting high resolution (Bulk or rich) data time periods for downlink. The time-periods of bulk data selection to be downlinked are made by an RPWI scientist on duty continuously analysing the selector data. The selector data consist of the continuous electric field (24 sps), the Langmuir probe sweeps from 2 probes, basic wave spectral parameters, dust signals, and radio spectral matrix components. During early cruise operations close to Earth, all RPWI data (selector + bulk) will be downloaded by ESA MOC (i.e., no selective downlink active).

6.3 RPWI Science Modes

The RPWI can be run in many operation mode configurations. Some of the more common currently implemented are listed in Table 17. All are run in operation cycles with a common length of 30 seconds, but can be longer, e.g., 600 seconds to reduce TM needs (e.g., in the Jovian magnetosphere).

6.3.1 Sequence Cycle Examples

Nominally a set of RPWI measurements will be run in a specific sequence cycle scheme. An example is illustrated below (Table 18). The duration of a sequence cycle can be varied but is here set to default 30 seconds (to fit at least 16,384 samples at 763 samples/s). It can be set to be longer to save TM (e.g., 600 s). Most often the Langmuir probes (LP) will measure the waveform electric field in lowpass and various bandpass bands. The exception is the voltage sweeps once per sequence cycle. The electric field measurements are differential between probe-pairs, while the single ended probe measurements monitor the spacecraft potential. The 24 samples-per-second (sps) signal is a down-sampling of the 763 sps data.

Table 17 Some common operation modes by receiver/active mode

Data product	Samples	Duration	Data type	Res.	Output TM[1]
HF receiver					
Radio Full	3 ant. 256 freq.	1 sweep/cycle	Spectrum matrix 9 components	12bit	27.6 kb
Radio Burst (for limb radio occultation)	3 ant. 72 freq.	Continuous 1 sweep/0.2 s	Spectrum matrix 9 components	12bit	7.8 kb/0.2 s
PSSR-1	2 ant.	1 sweep/cycle	Spectrum matrix 12 components 4320 freq	12bit	6.22 Mb
PSSR-2	1 ant.	Once/cycle	Auto corr. 16 freq 2048 samples	16bit	5.3 Mb
PSSR 3	3 ant. waveform	Continuous during 10 s/cycle	Waveform 11 ms 3328 samples ×128	128bit	54.5 Mb
MIME Sweep					
Nominal sweep	LP-LP or LP-RWI	2 s/cycle	1 passive & 1 – 4 active sweeps dep. on sub-mode		13.3 kb
Slow sub-mode	LP-LP or LP-RWI	2 s/cycle	1 passive sweep 1 active sweep		3.9 kb
Relaxation sub-mode	LP-LP	2 s/cycle	1 passive sweep 1 active sweep		13.3 kb
Wide Sweep	1 LP-LP 1 LP-RWI	2 s/cycle	2 passive sweeps 2 active sweeps		13.3 kb
Tracking	LP-LP or LP-RWI	2 s/cycle	1 passive sweep 1 active sweep 6 active sweeps around freq. of max amplitude		13.3 kb
Track B-field	LP-LP	2 s/cycle	1 passive sweep 1 active sweep 3 wide noise measurements around f_{gyro} harmonics		11.8 kb
LP Sweep					
Nominal sweep	2 probes ±80 V	2 seconds 256 samples	LP sweep	21bit	21.5 kb
Dense sweep	2 probes ±10 V	2 seconds 512 samples up-down sweep	Double sweep	21bit	43 kb
Complete sweep (cal)	4 probes ±80 V	2 seconds 20*512 samples	LP sweep	21bit	860 kb

Table 17 (*Continued*)

Data product	Samples	Duration	Data type	Res.	Output TM[1]
E-field (LP)					
DC **E**	4 probes 3diff+1 single-end	Continuous 763 sps (or 24 sps)	Waveform	21bit	64 kbps (1.9 Mb/30 s)
Medium δ**E**	4 probes 3diff+1 single-end	16 ksamples 49 ksps	Waveform	16bit	1 Mb
		High pass 50 Hz			
High δ**E**	4 probes	16 ksamples	Waveform	14bit	896 kb
	3diff+1 single-end	694 ksps			
δ**E** power sweep	4 probes	Freq. sweep	Power spectrum	21bit	1.8 Mb
	2 diff	40 kHz window			
		128 freq.			
		$<$ 1.5 MHz			
LF SCM					
δ**B**	3 coils	Continuous 763 sps (or 24 sps)	Waveform	16bit	36.6 kbps (1.1 Mb/30 s)
Medium δ**B**	3 coils	16 ksamples	Waveform	16bit	768 kb
		49 ksps			
LF (Parameters with use of LP E-field probes and SCM data)					
Dust param:s	4 probes	Continuous trigger 49 ksps	Dust count		
Spectral matrix	4 probes + 3 coils	Continuous 49 ksps	Spectral parameters		

[1)] Before compression & assuming a sequence cycle length (usually 30 – 600 s) where applicable.

As can be seen from Table 18 a RPWI measurement cycle gains substantial information about the plasma and electromagnetic environment. The cycles are repeated continuously and at Jupiter the lower TM survey data (always downloaded) will be used to select on ground the full set of measurements cycles to be downlinked. In this way RPWI will be able to select rich data where interesting events for science occur, i.e., higher science quality data will be kept.

A special thermal plasma density mode can be run where the targets are higher density cases ($>$100 cm^{-3} plasma), like during low altitude $<$500 km icy moons flybys, or in orbit around Ganymede. The purpose is to gain high time resolution plasma density (and dust population charge state). The 763 sps (and 24 sps) sampling is then run with a voltage bias and the Langmuir probes sample instead the current giving the density. The voltage bias can be either positive (sampling electrons) or negative (sampling ions) to be sensitive to regions with substantial amounts of negative ions/dust (if existing). There is also the possibility of running all four Langmuir probes in a δn/n interferometry mode at 49 ksps. The bias voltage is set to $+4$ V or -4 V in all these cases sampling electrons and positive ions respectively.

Table 18 Example of a RPWI sequence cycle of 30 seconds (given in top row). JENRAGE (yellow, HF), MIME (grey, LP, Tx/*Rx*), GANDALF (brown, LP) and SAMWISE (orange, LP and SCM) measure in electric field (e, sand-colour, LP), magnetic field (b, green, SCM) or in current sampling modes (blue, LP) where voltage sweeps (*vs*) occur. Certain SAMWISE output products use both electric and magnetic field measurements (light green)

Receiver	Product	+0	+2	+4	+5	+6	+7 +30 s
HF	**Radio Full** (3 RWI antenna)			e, 1 freq. sweep			
LP	**MIME Nominal sweep**		Tx/Rx				
LP	**LP Sweep** (P1, ±80V)	vs					
	LP Sweep (P2, ±80V)	vs					
	E-field (diff P3/P4 & P4)	e					
	DC E 24sps 3diff + 1x single ended P4				e		
	DC E_763sps 3diff + 1x single ended P4				e		
LF/SCM	**B_763sps**	b					
	B_49ksps snaps, 16k					b	
LF	**E_49ksps** snaps (all probes), 16k					e	
	Dust parameters (all probes)				e		
	Spectral Matrix (all probes)				e+b		
	Survey Wave params (all probes)				e+b		
LP	**E_694ksps** snaps, 16k, 3 diff + 1x single ended P4			**e**			

6.4 RPWI in-Flight Calibration and Activities

This includes routine health checks of the instrument parts, Langmuir probe surface decontamination, cross-sensor/receiver inter-calibrations, routine calibration signals, tests of uploaded new operation modes, and interference runs with all S/C and other instruments.

The cross-comparisons of independently determined data by RPWI is carried out to verify and improve the interpretation of the data in terms of physical quantities such as density, vector electric field, wave intensity, wave direction finding etc. It also aims to compensate for sensitivity drifts during changing temperatures of all sensors/pre-amps + receivers during different mission phases. The Langmuir probe surface decontamination is run intermittently to sputter the LP sensor surfaces with electrons at +80 V for a continuous time duration of a few days.

The RPWI in-flight calibration activities also includes more complex and dedicated S/C manoeuvres and payload operations, often with simultaneous J-MAG and PEP operations. Three specific types of activities will be mentioned here, all carried out before insertion into Jupiter orbit of JUICE in 2031. These are:

- GANDALF in-flight calibration with full 3D S/C rolls in the solar wind.
- JENRAGE in-flight calibration with partial S/C rolls near Earth.
- Calibration in known plasma and electromagnetic environments near Earth.

6.4.1 GANDALF in-Flight Calibration with S/C Rolls

The main purpose of these S/C rolls over an extended time is to gain a complete information of the S/C environment electric and plasma response obtained over the full spacecraft pointing range within the reasonably well-known solar wind environment. This allows for

a determination of the photoelectron and plasma ram wake environment response near the spacecraft and makes it possible to do an accurate near DC electric field calibration to be used during the Jovian phases. The calibration therefore needs measurements of the near DC E-field and plasma environment for the full range of S/C attitudes with respect to the Sun. Simultaneous J-MAG and PEP observations will help characterize the space environment. The activity is planned to occur in the solar wind beyond 1.36 AU due to thermal constraints.

6.4.2 JENRAGE in-Flight Calibration with Partial S/C Rolls

The JENRAGE experiment needs in-flight calibration versus foremost Earth's Auroral Kilometric Radiation (AKR) together with S/C rolls (around the axis of the HGA). The calibration activity is used to find the effective RWI antenna pattern and polarization capability with use of the known AKR source in the frequency range 100 – 800 kHz. When JUICE is not too far from the Earth, solar type-III radio burst in >1 MHz will also be used for effective RWI antenna length calibration together with observations from ground-based radio observatory and Earth-orbiting spacecraft like Arase, Wind, etc. The calibration facilitates the sensitivity and direction finding with the JENRAGE experiment. Currently all three JUICE Earth flybys within 300 R_{Earth} are considered for this activity.

6.4.3 Calibration in Known Plasma and Electromagnetic Environments Near Earth

The processing chain implemented in the RPWI experiments have so far relied primarily on internal calibration signals. The onboard processing needs to be calibrated, verified, and validated in a known plasma and electromagnetic environment during in-flight during the Earth flybys, and these are therefore a necessary component for a successful science mission. It needs an extended period starting when JUICE is within the solar wind near Earth, before entering the known Earth space environments, and back in the solar wind. Simultaneous J-MAG and PEP observations will help characterize the space environment. The Earth (and lunar) flybys also give us an opportunity to calibrate the on-board dust counting algorithm for spacecraft impact generated electric signals propagating to and detected by the Langmuir probes. These electric pulses of dust hits on the spacecraft are recorded by all probes in their waveforms.

7 RPWI Data Products

7.1 Ground Segment Data Processing Pipeline & Archiving

7.1.1 Introduction

The JUICE/RPWI ground segment data pipeline software will process raw and opaque TM files, i.e., CCSDS packets which are generated by the RPWI FSW and handled by various spacecraft and ESA ground station systems, and then convert them into user-friendly datasets in the form of CDF files. This processing covers (1a) RPWI HK and (1b) event data (packets), both for which the format is described wholly by the RPWI MIB, and (2) RPWI science data, which is partly described by the RPWI MIB and partly by the RPWI FSW.

Every science dataset will be generated on one of a set of standardized and ordered processing levels (or "archiving levels"): L1a, L1b, L2, or L3. In general, science datasets will be derived from one or multiple science datasets on the immediately lower processing

level and possibly also from HK datasets. HK datasets and science datasets on the lowest level, L1a, will be generated from TM files. In this manner, science data will be processed in steps from CCSDS packets into more and more refined data products: first to uncalibrated L1a datasets which use non-dimensional TM/ADC units, then to calibrated L1b datasets which use the physical units of the physical instrument, and then further to L2 and L3 which use various calibrated and "derived" quantities, such as e.g., plasma density and E–field using physical units. Datasets can also potentially be derived from combinations of RPWI datasets and datasets from other JUICE experiments when beneficial.

The full pipeline will be split into separate software components that process data for different steps in this chain, and which can be independently operated, as detailed below. In addition, the RPWI GS will also supply software for generating quick looks for RPWI datasets. The "TM2RAW" component will use RPWI TM files as input to produce uncalibrated L1a datasets, while the "RAW2CAL" component will use uncalibrated L1a datasets as input to produce L1b science-quality calibrated datasets. Further processing of L1b datasets to produce L2 and L3 datasets will be performed by a "High-level pipeline". All datasets will be compliant with both the PDS4 and ISTP archiving standards. All datasets will be validated and archived by the ESA PSA. The TM2RAW and RAW2CAL components of the pipeline will be delivered to SOC either in the form of docker images or git repos (for generating docker images). SOC will then execute the s/w components inside docker containers in order to process RPWI TM files into L1a and L1b datasets for immediate official archiving. Official L2 and L3 data generation will be handled by the pipeline at IRF.

The full pipeline, from TM to the highest processing levels, is at the time of writing not yet complete. The TM2RAW component was successfully used during RPWI commissioning for the purposes of near real time conversion of TM to usable CDFs for all HK and event data, and for most types of RPWI science data. It has further been successfully used internally for verifying the functioning of both the physical instrument as well as the RPWI FSW (including FSW upgrades), as well as for miscellaneous ancillary tasks such as estimating granular TM volumes. The major remaining features to be implemented for TM2RAW are: support for time conversion from s/c clock to UTC using SPICE kernels, RPWI-specific time adjustments of science data, support for remaining science data products, various compliance with archiving standards (ISTP, PDS4 labels), and compliance with interface specifications for running the software at SOC.

7.1.2 TM2RAW Implementation and Features

The TM2RAW is implemented (see Fig. 63) from scratch in Python 3.8 except for the support for decompression of RPWI science data which is implemented in C though accessed through a Python wrapper. TM2RAW is constituted of six standard Python distribution packages, each one installable using the standard Python tool "pip". It has been developed using CI/CD in the form of git/GitLab combined with automated tests and style checks.

The main TM2RAW distribution package, developed at IRF, handles all CCSDS packets as far as they are described by CCSDS standard and the RPWI MIB and also writes the output CDF files (datasets). The RPWI-specific compression of science data is handled by a separate Python distribution package. The processing of custom-formatted science data is delegated to four separate "plugins" to the main software, separately referred to as Science Data Unpacking Softwares (SDUS's) and each one implemented as a separate Python distribution package. There is one SDUS for each of four physical subsystems: LP, LF, HF, and MIME. TM originating from the RPWI SCM subsystem is handled by the LF SDUS.

The main TM2RAW distribution package identifies and parses all CCSDS packets as far as possible using the CCSDS standard and the RPWI MIB. For science data specifically,

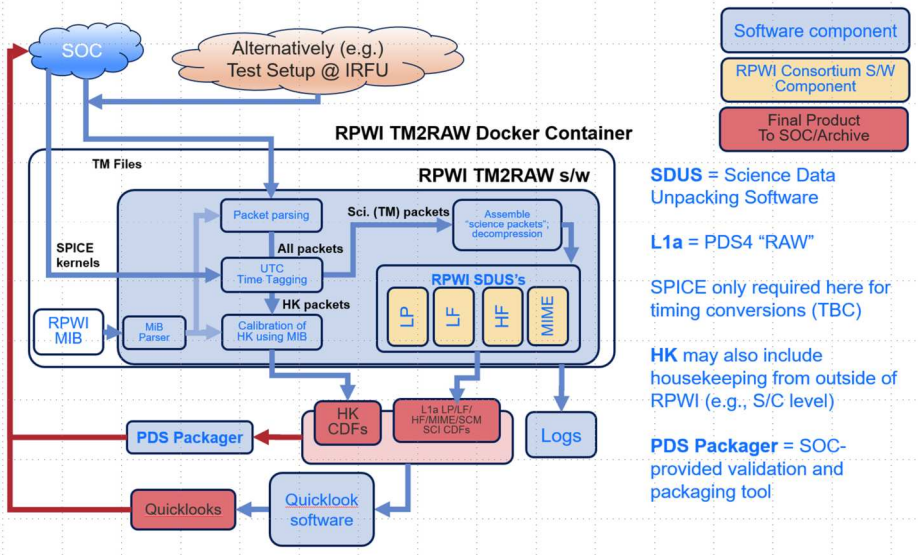

Fig. 63 An overview over the separate conceptual modules that make up the TM2RAW part of the RPWI ground segment pipeline, plus the RPWI quick look software and the SOC-provided PDS packager. All the components in the figure will be run by SOC

it uses the CCSDS packet sequence control to reconstruct and extract "science packets" (longer units of science data constructed by the RPWI FSW) from the TM. These science packets are then used as input to the SDUS's. The SDUS's in turn return in-memory data structures that describe the bulk content of the corresponding datasets (CDF files), including explicit CDF variables and custom metadata. This delegation of processing to the SDUS's makes it possible to outsource the de-commutation of custom-formatted science data, as well as outsource the corresponding dataset design to those consortium partners who are responsible for the corresponding hardware, while simultaneously minimizing the development efforts required by those consortium partners.

Additional TM2RAW features include logging, sophisticated built-in statistics of the TM and processing which is used for debugging and monitoring TM and SDUS's, support for multiple TM file formats and packet headers, a powerful system for layered incremental configurations of the software, and the capacity to generate additional unofficial datasets for debugging, e.g., global lists of all CCSDS packets and science packets respectively. It also contains special features for mitigating shortcomings and known bugs in the first version of the RPWI FSW.

7.1.3 RAW2CAL and High-Level Pipeline

The "RAW2CAL" s/w component (L1a-to-L1b) will use uncalibrated L1a datasets as input to produce L1b science-quality calibrated datasets. This component will be developed and tested during the JUICE cruise phase. The specifics of the calibration, e.g., of LP measurements, will be covered in future papers. Broadly speaking, every L1a data product will be directly calibrated using standard techniques to generate a corresponding L1b data product. Higher-level products, L2 and L3, are more likely to be derived from multiple L1b datasets, e.g., combining electric and magnetic field data to determine Poynting flux, processing of LP current voltage sweeps to determine electron density and temperature, and so forth.

Table 19 Summarized data products to be generated by RPWI, showing the originating subsystems and sensors, processing levels and other salient information

Name	Subunit	Sensor	Measurements	Processing level	Comment
LP Sweeps	LP	LP-PWI	Current-Voltage sweeps	L1a, L1b	
Probe potentials	LP	LP-PWI	Probe voltages (single ended, differential)	L1a, L1b	Survey + Snapshot
E field vectors	LP	LP-PWI	Electric field components	L1b L2 w. analysis	Survey + Snapshot
Frequency sweep products	LP	LP-PWI	Spectral matrix	L1a, L1b L2 w. analysis	
LP Sweep products	LP	LP-PWI	Electron & ion density, electron temperature, ion drift speed	L2	
Spacecraft potential	LP	LP-PWI	Spacecraft potential	L2	
Density fluctuations	LP	LP-PWI	δn/n(t)	L2	Survey + Snapshot
Interferometry	LP	LP-PWI	Group speed from δE or δn/n	L2 L3 w. J-MAG	
Ocean properties	LP	LP-PWI	Interior conductivity / impedance with depth maps	L3 w. J-MAG	
Poynting flux	LP+LF	LP-PWI + SCM	Combined **E** and **B** vectors	L2 L3 w. J-MAG	
Polarization	LP+LF	LP-PWI + SCM	Combined **E** and **B** vectors	L2 L3 w. J-MAG	
Dust counts products	LF	LP-PWI	Amplitude, duration	L2	
HF spectral matrix	HF	RWI	Spectral matrix	L1a, L1b L2	
HF time series	HF	RWI	Electric field components	L1a, L1b L2	
Ice crust properties	HF	RWI	Depth maps	L3	
MIME sweep spectra	MIME	LP + RWI	Spectral matrix	L1a, L1b	
MIME sweep products	MIME	LP + RWI	Electron density, scalar magnetic field	L2	

7.2 RPWI Data Products

A summary of the intended data products to be produced is given in Table 19. Each row in the table corresponds to a dataset to be generated and archived as part of the relevant PDS4 archive "bundle". Full descriptions of the final datasets will be contained alongside the datasets themselves within the archive bundles, an RPWI data user's handbook, and in the metadata contained within the CDF files and the PDS4 label files.

8 Conclusions

The Radio & Plasma Wave Investigation (RPWI) onboard the ESA JUpiter ICy moons Explorer (JUICE) is described here. The information presented herein can be used as a library look-up source for the future when using the RPWI science data. More than 10,000 pages of further technical information of the RPWI instrument will be stored at ESA and the Swedish Institute of Space Physics (IRF) in Uppsala, and so will the in-flight development of the operations and related modes as they become available. It is therefore wise to keep a contact with the PI institute when analysing the RPWI data. All RPWI data will be available as CDF and PDS data after some propriety period. The RPWI provides a complete set of highly sensitive plasma and fields instrumentation, and related science investigations, for all JUICE project phases until completion. Together, the integrated RPWI system can carry out an ambitious planetary science investigation in and around the Galilean icy moons and the Jovian space environment. RPWI focuses, apart from cold plasma studies, on the understanding of how, through electrodynamic and electromagnetic coupling, the momentum and energy transfer occur with the icy Galilean moons, their surfaces and salty conductive sub-surface oceans. The RPWI instrument is planned to be operational during most of the JUICE mission, during the cruise phase, in the Jovian magnetosphere, during the icy moon flybys, and in particular Ganymede orbit, and will hopefully deliver data from the near surface during the final crash orbit.

Acknowledgements The extensive implementation work of the RPWI system on board JUICE have been supported by the following national and international space agencies, which we are thoroughly thankful for: The Swedish National Space Agency (SNSA, lead agency for RPWI), Swedish Institute of Space Physics (IRF), Japan Aerospace Exploration Agency (JAXA), Centre National d'Etudes Spatiales (CNES) and Centre National de la Recherche Scientifique (CNRS), PRODEX Committees for Poland and Czech Republic and ESA PRODEX Office, Austrian National Agency (FFG), and ESA JUICE project has supported the JUICE/RPWI implementation. We give special recognition to the engineering support from Airbus Defence and Space (ADS) in Toulouse and Friedrichshafen as well as the ESA JUICE project. MH's, LC's, and CMJ's work at DIAS is supported by Science Foundation Ireland Grant 18/FRL/6199. MH is also supported by an ESA OSIP fellowship. Work performed at the Center for Nanoscale Materials, a U.S. Department of Energy Office of Science User Facility, was supported by the U.S. DOE, Office of Basic Energy Sciences, under Contract No. DE-AC02-06CH11357.

The following companies have contributed to the RPWI implementation: RUAG Space (now Beyond Gravity), ESSDE Teknik, ÅAC Clyde Space, Matra Électronique, Creotech Instruments S.A., Microtec High-Rel Electronics, G. L. Electronics, Alter Technology TÜV Nord, TESAT-Spacecom, Habia Cable AB, Söderfors, Sweden, Invent GmbH, Braunschweig, Germany, Johann Maier GmbH, Stuttgart, Germany, Swedish Space Corporation (SSC), Your Special Delivery Service (YSDS), and Airbus Poland (PZL). Finally, we thank wholeheartedly the reviewers of this manuscript.

Funding Open access funding provided by Uppsala University.

Declarations

Competing Interests The authors declare no competing interests.

References

Achilleos N, André N, Blanco-Cano X, et al (2015) Transport of mass, momentum and energy in planetary magnetodisc regions. Space Sci Rev 187:229–299. https://doi.org/10.1007/s11214-014-0086-y

Addison P, Liuzzo L, Arnold H, Simon S (2021) Influence of Europa's time-varying electromagnetic environment on magnetospheric ion precipitation and surface weathering. J Geophys Res Space Phys 126:e2020JA029087. https://doi.org/10.1029/2020JA029087

Alfvén H (1942) Existence of electromagnetic-hydrodynamic waves. Nature 150:405–406. https://doi.org/10.1038/150405d0

Alfvén H (1958) On the theory of magnetic storms and Aurorae. Tellus 10:104–116. https://doi.org/10.1111/j.2153-3490.1958.tb01991.x

Allegrini F, Gladstone GR, Hue V, Clark G, Szalay JR, Kurth WS, et al (2020b) First report of electron measurements during a Europa footprint tail crossing by Juno. Geophys Res Lett 47(18):e2020GL089732. https://doi.org/10.1029/2020GL089732

Allegrini F, Mauk B, Clark G, Gladstone GR, Hue V, Kurth WS, et al (2020a) Energy flux and characteristic energy of electrons over Jupiter's main auroral emission. J Geophys Res Space Phys 125:e2019JA027693. https://doi.org/10.1029/2019JA027693

Allegrini F, Bagenal F, Ebert RW, Louarn P, McComas DJ, Szalay JR, et al (2022) Plasma observations during the 7 June 2021 Ganymede flyby from the Jovian Auroral Distributions Experiment (JADE) on Juno. Geophys Res Lett 49:e2022GL098682. https://doi.org/10.1029/2022GL098682

Alm L, Marklund GT, Karlsson T (2014) In situ observations of density cavities extending above the auroral acceleration region. J Geophys Res Space Phys 119:5286–5294. https://doi.org/10.1002/2014JA019799

Alm L, Li B, Marklund GT, Karlsson T (2015) Statistical altitude distribution of the auroral density cavity. J Geophys Res Space Phys 120:996–1006. https://doi.org/10.1002/2014JA020691

André M, Koskinen H, Matson L, Erlandson R (1988) Local transverse ion energization in and near the polar cusp. Geophys Res Lett 15(1):107–110. https://doi.org/10.1029/GL015i001p00107

André M, Odelstad E, Graham DB, Eriksson AI, Karlsson T, Stenberg Wieser G, Vigren E, Norgren C, Johansson FL, Henri P, Rubin M, Richter I (2017) Lower hybrid waves at comet 67P/Churyumov-Gerasimenko. Mon Not R Astron Soc 469(Suppl_2):S29–S38. https://doi.org/10.1093/mnras/stx868

Arce A, Rodriguez D (2019) JUICE magnetometer boom subsystem. In: Proc. 18. European space mechanisms and tribology symposium 2019, Munich, Germany. https://esmats.eu/esmatspapers/pastpapers/pdfs/2019/arce.pdf

Arnold H, Liuzzo L, Simon S (2019) Magnetic signatures of a plume at Europa during the Galileo E26 flyby. Geophys Res Lett 46:1149–1157. https://doi.org/10.1029/2018GL081544

Asamura K, Shoji M, Miyoshi Y, Kasahara Y, Kasaba Y, Kumamoto A, Tsuchiya F, Matsuda S, Matsuoka A, Teramoto M, Kazama Y, Shinohara I (2021) Cross-energy couplings from magnetosonic waves to electromagnetic ion cyclotron waves through cold ion heating inside the plasmasphere. Phys Rev Lett 127:245101. https://doi.org/10.1103/PhysRevLett.127.245101

Aubier MG, Meyer-Vernet N, Pedersen BM (1983) Shot noise from grain and particle impacts in Saturn's ring plane. Geophys Res Lett 10:5–8. https://doi.org/10.1029/GL010i001p00005

Bagenal F, Dols V (2020) The space environment of Io and Europa. J Geophys Res Space Phys 125:e2019JA027485. https://doi.org/10.1029/2019JA027485

Bagenal F, Sullivan JD (1981) Direct plasma measurements in the Io torus and inner magnetosphere of Jupiter. J Geophys Res 86(A10):8447–8466. https://doi.org/10.1029/JA086iA10p08447

Bagenal F, Sidrow E, Wilson RJ, Cassidy TA, Dols V, Crary FJ, Steffl AJ, Delamere PA, Kurth WS, Paterson WR (2015) Plasma conditions at Europa's orbit. Icarus 261:1–13. https://doi.org/10.1016/j.icarus.2015.07.036

Bagenal F, Wilson RJ, Siler S, Paterson WR, Kurth WS (2016) Survey of Galileo plasma observations in Jupiter's plasma sheet. J Geophys Res, Planets 121:871–894. https://doi.org/10.1002/2016JE005009

Bagenal F, Adriani A, Allegrini F, Bolton SJ, Bonfond B, Bunce EJ, et al (2017b) Magnetospheric science objectives of the Juno mission. Space Sci Rev 213:219–287. https://doi.org/10.1007/s11214-014-0036-8

Bagenal F, Dougherty LP, Bodisch KM, Richardson JD, Belcher JM (2017a) Survey of Voyager plasma science ions I: Analysis method. J Geophys Res, Planets 122. https://doi.org/10.1002/2016JA023797

Barabash et al (2025) Space Sci Rev. in preparation

Béghin C, Kolesnikova E (1998) Surface-charge distribution approach for modeling of quasi-static electric antennas in isotropic thermal plasma. Radio Sci 33(3):503–516. https://doi.org/10.1029/97RS03588

Belyaev PP, Polyakov SV, Rapoport VO, Trakhtengerts VY (1990) The ionospheric Alfvén resonator. J Atmos Terr Phys 52(9):781–788. https://doi.org/10.1016/0021-9169(90)90010-K

Bergman JES, Carozzi TD (2007) Systematic characterization of low frequency electric and magnetic field data applicable to Solar Orbiter, proceedings of the 'The second Solar Orbiter workshop' in Athens, Greece (ESA SP-641). ESA Publications Division ESTEC, Noordwijk. ISBN 92-9291-205-2. Preprint.https://arxiv.org/abs/physics/0611073

Bergman S, Stenberg Wieser G, Wieser M, Johansson FL, Eriksson A (2020) The influence of spacecraft charging on low-energy ion measurements made by RPC-ICA on Rosetta. J Geophys Res Space Phys 125(1):e27478. https://doi.org/10.1029/2019JA027478

Bhattacharyya D, Clarke JT, Montgomery J, Bonfond B, Gérard J-C, Grodent D (2018) Evidence forauroral emissions from Callisto'sfootprint in HST UV images. J Geophys Res Space Phys 123:364–373. https://doi.org/10.1002/2017JA024791

Block LP (1972) Potential double layers in the ionosphere. Cosm Electrodyn 3:349

Block LP, Fälthammar C-G (1968) Effects of field-aligned currents on the structure of the ionosphere. J Geophys Res 73(15):4807–4812. https://doi.org/10.1029/JA073i015p04807

Blöcker A, Saur J, Roth L (2016) Europa's plasma interaction with an inhomogeneous atmosphere: development of Alfvén winglets within the Alfvén wings. J Geophys Res Space Phys 121(10):9794–9828. https://doi.org/10.1002/2016JA022479

Blomberg LG, Wahlund J-E, Cumnock JA, Marklund GT, Lindqvist P-A, Morooka M, André M, Eriksson AI (2005) Electric field diagnostics in the Jovian system: brief scientific case and instrumentation overview. In: Proceedings of the 6th IAA International Conference on Low-Cost Planetary Missions, 11–13 October 2005, Kyoto, pp 335–340

Blomberg LG, Cumnock JA, Kasaba Y, Matsumoto H, Kojima H, Omura Y, Moncuquet M, Wahlund J-E (2006a) Electric fields in the Hermean environment. Adv Space Res 38:627–631. https://doi.org/10.1016/j.asr.2005.02.034

Blomberg LG, Matsumoto H, Bougeret J-L, Kojima H, Yagitani S, Cumnock JA, Eriksson AI, Marklund GT, Wahlund J-E, Bylander L, Åhlén L, Holtet JA, Ishisaka K, Kallio E, Kasaba Y, Matsuoka A, Moncuquet M, Mursula K, Omura Y, Trotignon J-G (2006b) MEFISTO - an electric field instrument for BepiColombo/MMO. Adv Space Res 38:672. https://doi.org/10.1016/j.asr.2005.05.032

Bochet M, Bergman S, Holmberg MKG, Wieser M, Wieser GS, Wittmann P, et al (2023) Perturbations of JUICE/JDC ion measurements caused by spacecraft charging in the Jovian magnetosphere and the ionosphere of Ganymede. J Geophys Res Space Phys 128:e2023JA031377. https://doi.org/10.1029/2023JA031377

Boehm MH, Carlson CW, McFadden JP, Clemmons JH, Mozer FS (1990) High-resolution sounding rocket observations of large-amplitude Alfvén waves. J Geophys Res 95(A8):12157–12171. https://doi.org/10.1029/JA095iA08p12157

Bonfond B, et al (2015) The far-ultraviolet main auroral emission at Jupiter - Part 1: Dawn-dusk brightness asymmetries. Ann Geophys 33:1203

Bonfond B, Saur J, Grodent D, Badman SV, Bisikalo D, Shematovich V, Gérard J-C, Radioti A (2017) The tails of the satellite auroral footprints at Jupiter. J Geophys Res Space Phys 122:7985–7996. https://doi.org/10.1002/2017JA024370

Bonfond B, Yao Z, Grodent D (2020) Six pieces of evidence against the corotation enforcement theory to explain the main aurora at Jupiter. J Geophys Res Space Phys 125:e2020JA028152. https://doi.org/10.1029/2020JA028152

Borovsky JE, Delzanno GL, Valdivia JA, Moya PS, Stepanova M, Birn J, Blum LW, Lotko W, Hesse M (2020) Outstanding questions in magnetospheric plasma physics: the Pollenzo view. J Atmos Sol-Terr Phys 208:105377. https://doi.org/10.1016/j.jastp.2020.105377

Boström R (1964) A model of the auroral electrojets. J Geophys Res 69(23):4983–4999. https://doi.org/10.1029/JZ069i023p04983

Boudouma A, Zarka P, Magalhães FP, Marques MS, Louis CK, Echer E, Lamy L, Prangé R (2023) Localisation of the main HOM source in the dusk side of the Jovian magnetosphere. In: Louis CK, Jackman CM, Fischer G, Sulaiman AH, Zucca P (eds) Planetary, solar and heliospheric radio emissions IX. DIAS, TCD. https://doi.org/10.25546/103094.

Bougeret J-L, et al (1995) WAVES: The radio and plasma wave investigation on the WIND spacecraft. Space Sci Rev 71:231–263. https://doi.org/10.1007/BF00751331

Brogren M, Harding GL, Karmhag R, Ribbing CG, Niklasson GA, Stenmark L (2000) Titanium–aluminum–nitride coatings for satellite temperature control. Thin Solid Films 370(1–2):268–277. https://doi.org/10.1016/S0040-6090(00)00914-7

Brown S, Janssen M, Adumitroaie V, Atreya S, Bolton S, Gulkis S, Ingersoll A, Levin S, Li C, Li L, Lunine J, Misra S, Orton G, Steffes P, Tabataba-Vakili F, Kolmasova I, Imai M, Santolik O, Kurth W, Hospodarsky G, Gurnett D, Connerney J (2018) Prevalent lightning sferics at 600 megahertz near Jupiter's poles. Nature 558:87–90. https://doi.org/10.1038/s41586-018-0156-5

Bruzzone L, Alberti G, Catallo C, Ferro A, Kofman W, Orosei R (2011) Subsurface radar sounding of the Jovian moon Ganymede. In: Proceedings of the IEEE, vol 99, pp 837–857. https://doi.org/10.1109/JPROC.2011.2108990

Bruzzone L et al (2025) Space Sci Rev. in preparation

Bucciantini L, Henri P, Wattieaux G, Califano F, Vallières X, Randriamboarison O (2022) In situ space plasma diagnostics with finite amplitude active electric experiments: non-linear plasma effects and instrumental performance of mutual impedance experiments. J Geophys Res Space Phys 127:e2022JA030813. https://doi.org/10.1029/2022JA030813

Bucciantini L, Henri P, Wattieaux G, Lavorenti F, Dazzi P, Vallières X (2023) Space plasma diagnostics and spacecraft charging. The impact of plasma inhomogeneities on mutual impedance experiments. J Geophys Res Space Phys 128:e2023JA031534. https://doi.org/10.1029/2023JA031534

Buccino DR, Parisi M, Gramigna E, Gomez-Casajus L, Tortora P, Zannoni M, Caruso A, Park RS, Withers P, Steffes P, Hodges A, Levin S, Bolton S (2022) Ganymede's ionosphere observed by a dual-frequency radio occultation with Juno. Geophys Res Lett. https://doi.org/10.1029/2022GL098420

Burke BF, Franklin KL (1955) Observations of a variable radio source associated with the planet Jupiter. J Geophys Res 60(2):213–217. https://doi.org/10.1029/JZ060i002p00213

Carberry Mogan SR, Tucker OJ, Johnson RE, Roth L, Alday J, Vorburger A, et al (2022) Callisto's atmosphere: first evidence for H_2 and constraints on H_2O. J Geophys Res, Planets 127:e2022JE007294. https://doi.org/10.1029/2022JE007294

Carnielli G, Galand M, Leblanc F, Leclercq L, Modolo R, Beth A, Huybrighs HLF, Jia X (2019) First 3D test particle model of Ganymede's ionosphere. Icarus 330:42–59. https://doi.org/10.1016/j.icarus.2019.04.016

Carnielli G, Galand M, Leblanc F, Modolo R, Beth A, Jia X (2020a) Constraining Ganymede's neutral and plasma environments through simulations of its ionosphere and Galileo observations. Icarus 343:113691. https://doi.org/10.1016/j.icarus.2020.113691

Carnielli G, Galand M, Leblanc F, Modolo R, Beth A, Jia X (2020b) Simulations of ion sputtering at Ganymede. Icarus 351:113918. https://doi.org/10.1016/j.icarus.2020.113918

Carozzi TD, Karlsson R, Bergman JES (2001) Parameters characterizing electromagnetic wave polarization. Phys Rev E 61(2):2024–2028. https://doi.org/10.1103/PhysRevE.61.2024

Carrer L, Schroeder DM, Romero-Wolf A, Ries PA, Bruzzone L (2020) Analysis of temporal and structural characteristics of Jovian radio emissions for passive radar sounding of Jupiter's Icy Moons. IEEE Trans Geosci Remote Sens 59(5):3857–3874

CCSDS standard 121.0-B-3 - LOSSLESS DATA COMPRESSION, Consultative Committee for Space Data Systems, 2020. https://public.ccsds.org/Pubs/121x0b3.pdf

Cecconi B (2013) Goniopolarimetric techniques for low-frequency radio astronomy in space. In: Huber MCE, et al (eds) Observing photons in space. Scientific Report Series, vol 9. Springer, New York. https://doi.org/10.1007/978-1-4614-7804-1_15

Cecconi B, Zarka P (2005) Direction finding and antenna calibration through analytical inversion of radio measurements performed using a system of 2 or 3 electric dipole antennas. Radio Sci 40:RS3003. https://doi.org/10.1029/2004rs003070

Cecconi B, Bougeret J-L, Dekkali M, Lamy L, Zarka P, André N (2010). EJSM Electro-Magnetic Sensor Study (1.7). Zenodo. https://doi.org/10.5281/zenodo.2532436

Cecconi B, Hess S, Hérique A, Santovito MR, Santos-Costa D, Zarka P, Alberti G, Blankenship D, Bougeret J-L, Bruzzone L, Kofman W (2012) Natural radio emission of Jupiter as interferences for radar investigations of the icy satellites of Jupiter. Planet Space Sci 61:32–45. https://www.doi.org/10.1016/j.pss.2011.06.012

Cecconi B, Louis CK, Crego CM, Vallat C (2021) Jovian auroral radio source occultation modelling and application to the JUICE science mission planning. Planet Space Sci 209:1–34. https://doi.org/10.1016/j.pss.2021.105344

Chané E, Saur J, Poedts S (2013) Modeling Jupiter's magnetosphere: influence of the internal sources. J Geophys Res Space Phys 118:2157–2172. https://doi.org/10.1002/jgra.50258

Chasseriaux JM, Debrie R, Renard C (1972) J Plasma Phys 8:231–253. https://doi.org/10.1017/S0022377800007108

Chaston CC, Peria WJ, Carlson CW, Ergun RE, McFadden JP (2001) FAST observations of inertial Alfvén waves and electron acceleration in the dayside aurora. Phys Chem Earth, Part C, Sol-Terr Planet Sci 26(1–3):201–205. https://doi.org/10.1016/S1464-1917(00)00108-2

Chaston CC, Salem C, Bonnell JW, Carlson CW, Ergun RE, Strangeway RJ, McFadden JP (2008) The turbulent Alfvénic aurora. Phys Rev Lett 100:175003. https://doi.org/10.1103/PhysRevLett.100.175003

Chauhan KV, Rawal SK (2014) A review paper on tribological and mechanical properties of ternary nitride based coatings. Proc Technol 14(supplement c):430–437. https://doi.org/10.1016/j.protcy.2014.08.055

Chave AD, Jones AG (2012) The magnetotelluric method: theory and practice. Cambridge University Press, Cambridge

Chmyrev VM, Berthelier A, Jorjio NV, Berthelier JJ, Bosqued JM, Galperin YuI, Kovrazhkin RA, Beghin C, Mogilevsky MM, Bilichenko SV, Molchanov OA (1989) Non-linear Alfven wave generator of auroral particles and ELF/VLF waves. Planet Space Sci 37(6):749–759. https://doi.org/10.1016/0032-0633(89)90044-5

Chust T, Louarn P, Volwerk M, de Feraudy H, Roux A, Wahlund J-E, Holback B (1998) Electric fields with a large parallel component observed by the Freja spacecraft: artifacts or real signals? J Geophys Res 103(A1):215–224. https://doi.org/10.1029/97JA02587

Clark G, Tao C, Mauk BH, Nichols J, Saur J, Bunce EJ, et al (2018) Precipitating electron energy flux and characteristic energies in Jupiter's main auroral region as measured by Juno/JEDI. J Geophys Res Space Phys 123:7554–7567. https://doi.org/10.1029/2018JA025639

Clarke JT, et al (2009) Response of Jupiter's and Saturn's auroral activity to the solar wind. J Geophys Res 114:A05210. https://doi.org/10.1029/2008JA013694

Collet B, Lamy L, Louis CK, Zarka P, Prangé P, Louarn P, Sulaiman A, Kurth WSK (2023) Characterization of Jovian hectometric sources with Juno: statistical position and generation by shell-type electrons. In: Louis CK, Jackman CM, Fischer G, Sulaiman AH, Zucca P (eds) Dublin institute for advanced studies, planetary, solar and heliospheric radio emissions IX. https://doi.org/10.25546/103095

Connerney JEP, Timmins S, Oliversen RJ, Espley JR, Joergensen JL, Kotsiaros S, et al (2022) A new model of Jupiter's magnetic field at the completion of Juno's prime mission. J Geophys Res, Planets 127:e2021JE007055. https://doi.org/10.1029/2021JE007055

Constable S, Parker R, Constable C (1987) Occam's inversion: a practical algorithm for generating smooth models from electromagnetic sounding data. Geophysics 52:289–300. https://doi.org/10.1190/1.1442303

Cook AF, Duxbury TC, Hunt GE (1979) First results on Jovian lightning. Nature 280:794. https://doi.org/10.1038/280794a0

Cowley SWH, Bunce EJ (2001) Origin of the main auroral ovel in Jupiter's coupled magnetosphere-ionosphere system. Planet Space Sci 49:1067–1088. https://doi.org/10.1016/S0032-0633(00)00167-7

Cowley SWH, Deason A, Bunce EJ (2008) Auroral current systems in Jupiter's magnetosphere: predictions for the Juno mission. Ann Geophys 26:4051–4074. https://doi.org/10.5194/angeo-26-4051-2008

Cravens TE, McNutt RL, Waite JH, Robertson IP, Luhmann JG, Kasprzak W, Ip W-H (2009) Plume ionosphere of Enceladus as seen by the Cassini ion and Neutral Mass Spectrometer. Geophys Res Lett 36:L08106. https://doi.org/10.1029/2009GL037811

Cully CM, Angelopoulos V, Auster U, Bonnell J, Le Contel O (2011) Observational evidence of the generation mechanism for rising-tone chorus. Geophys Res Lett 38:L01106. https://doi.org/10.1029/2010GL045793

de Kleer K, Milby Z, Schmidt C, Camarca M, Brown ME (2023) The optical aurorae of Europa, Ganymede, and Callisto. Planet Sci J 4:37. https://doi.org/10.3847/PSJ/acb53c

DeForest SE (1972) Spacecraft charging at synchronous orbit. J Geophys Res 77(4):651–659. https://doi.org/10.1029/JA077i004p00651

Di Paolo F, Lauro SE, Cosciotti B, Mattei E, Pettinelli E (2020) Radar sounding of Ganymede: attenuation and volume scattering losses estimation. EPSC Abstracts 14:EPSC2020-EPSC291. https://doi.org/10.5194/epsc2020-291

Dols VJ, Bagenal F, Cassidy TA, Crary FJ, Delamere PA (2016) Europa's atmospheric neutral escape: importance of symmetrical O2 charge exchange. Icarus 264:387–397. https://doi.org/10.1016/j.icarus.2015.09.026

Dong Y, Hill TW, Ye S-Y (2015) Characteristics of ice grains in the Enceladus plume from Cassini observations. J Geophys Res Space Phys 120:915–937. https://doi.org/10.1002/2014JA020288

Dougherty MK, Khurana KK, Neubauer FM, Russell CT, Saur J, Leisner JS, Burton ME (2006) Identification of a dynamic atmosphere at Enceladus with the Cassini magnetometer. Science 311(5766):1406–1409. https://doi.org/10.1126/science.1120985

Dougherty et al (2025) Space Sci Rev. in preparation

Drell SD, Foley HM, Ruderman MA (1965) Drag and propulsion of large satellites in the ionosphere: an Alfvén propulsion engine in space. J Geophys Res 70:13. https://doi.org/10.1103/PhysRevLett.14.171

Duling S, Saur J, Wicht J (2014) Consistent boundary conditions at nonconducting surfaces of plane- tary bodies: applications in a new Ganymede MHD model. J Geophys Res Space Phys 119:4412–4440. https://doi.org/10.1002/2013JA019554

Edberg NJT, Wahlund J-E, Ågren K, Morooka MW, Modolo R, Bertucci C, Dougherty MK (2010) Electron density and temperature measurements in the cold plasma environment of Titan – implications for atmospheric escape. Geophys Res Lett 37:L20105. https://doi.org/10.1029/2010GL044544

Edberg NJT, Ågren K, Wahlund J-E, Morooka MW, Andrews DJ, Cowley SWH, Wellbrock A, Coates AJ, Bertucci C, Dougherty MK (2011) Structured ionospheric outflow during the Cassini T55–T59 Titan flybys. Planet Space Sci 59(8):788–797. https://doi.org/10.1016/j.pss.2011.03.007

Edberg NJT, Andrews DJ, Shebanits O, Ågren K, Wahlund J–E, Opgenoorth HJ, Cravens TE, Girazian Z (2013) Solar cycle modulation of Titan's ionosphere. J Geophys Res Space Phys 118:5255–5264. https://doi.org/10.1002/jgra.50463

Egbert GD, Erofeeva SY (2002) Efficient inverse modelling of barotropic ocean tides. J Atmos Ocean Technol 19:183-204. https://doi.org/10.1175/1520-0426(2002)019<0183:EIMOBO>2.0.CO;2

Engelhardt IAD, Wahlund J-E, Andrews DJ, Eriksson AI, Ye S, Kurth WS, Gurnett DA, Morooka MW, Farrell WM, Dougherty MK (2015) Plasma regions, charged dust and field-aligned currents near Enceladus. Planet Space Sci 117:453–469. https://doi.org/10.1016/j.pss.2015.09.010

Ergun RE, Carlson CW, McFadden JP, Mozer FS, Delory GT, Peria W, Chaston CC, Temerin M, Roth I, Muschietti L, Elphic R, Strangeway R, Pfaff R, Cattell CA, Klumpar D, Shelley E, Peterson W, Moebius E, Kistler L (1998) FAST satellite observations of large-amplitude solitary structures. Geophys Res Lett 25(12):2041–2044. https://doi.org/10.1029/98GL00636

Ergun RE, Andersson L, Main D, Su Y-J, Newman DL, Goldman MV, Carlson CW, McFadden JP, Mozer FS (2002) Parallel electric fields in the upward current region of the aurora: numerical solutions. Phys Plasmas 9:3695–3704. https://doi.org/10.1063/1.1499121

Ergun RE, Andersson L, Main D, Su Y-J, Newman DL, Goldman MV, Carlson CW, Hull AJ, McFadden JP, Mozer FS (2004) Auroral particle acceleration by strong double layers: the upward current region. J Geophys Res 109:A12220. https://doi.org/10.1029/2004JA010545

Eriksson AI, Wahlund J-E (2006) Charging of the Freja satellite in the auroral zone. IEEE Trans Plasma Sci 34:2038–2045. https://doi.org/10.1109/TPS.2006.883373

Eriksson AI, Boström R, Gill R, et al (2007) RPC-LAP: the Rosetta Langmuir probe instrument. Space Sci Rev 128:729–744. https://doi.org/10.1007/s11214-006-9003-3

Eriksson I, Engelhardt IAD, André M, Boström R, Edberg NJT, Johansson FL, Odelstad E, Vigren E, Wahlund J-E, Henri P, Lebreton J-P, Miloch WJ, Paulsson JJP, Simon Wedlund C, Yang L, Karlsson T, Jarvinen R, Broiles T, Mandt K, Carr CM, Galand M, Nilsson H, Norberg C (2017) Cold and warm electrons at comet 67P/Churyumov-Gerasimenko. Astron Astrophys 605:A15. https://doi.org/10.1051/0004-6361/201630159

Eriksson AI, Wedin LJ, Wahlund J-E, Holback B Analysis of Freja Charging Events: Modelling of Freja observations by spacecraft charging codes, SPEE-WP 120-TN, under ESA contract 11974/96/NL/JG(SC), IRF Sci. Report 252, 1999, ISSN 0284-1703

Evans S (1965) Dielectric properties of ice and snow - a review. J Glaciol 5:773–792. https://doi.org/10.3189/S0022143000018840

Eviatar A, Vasyliunas VM, Gurnett DA (2001) The ionosphere of Ganymede. Planet Space Sci 49:327–336. https://doi.org/10.1016/S0032-0633(00)00154-9

Fahleson U, Fälthammar C-G, Pedersen A (1974) Ionospheric temperature and density measurements by means of spherical double probes. Planet Space Sci 22:41–66

Farrell WM, Kaiser ML, Desch MD (1999) A model of the lightning discharge at Jupiter. Geophys Res Lett 26:2601–2604. https://doi.org/10.1029/1999GL900527

Farrell WM, Kurth WS, Tokar RL, Wahlund J-E, Gurnett DA, Wang Z, MacDowall RJ, Morooka MW, Johnson RE, Waite JH (2010) Modification of the plasma in the near-vicinity of Enceladus by the enveloping dust. Geophys Res Lett 37:20202. https://doi.org/10.1029/2010GL044768

Farrell WM, Wahlund J-E, Morooka M, Gurnett DA, Kurth WS, MacDowall RJ (2012) The electromagnetic pickup of submicron-sized dust above Enceladus's northern hemisphere. Icarus 219:498–501. https://doi.org/10.1016/j.icarus.2012.02.033

Farrell WM, Wahlund J-E, Morooka M, Gurnett DA, Kurth WS, MacDowall RJ (2014) An estimate of the dust pickup current at Enceladus. Icarus 239:217–221. https://doi.org/10.1016/j.icarus.2014.05.034

Farrell WM, Wahlund J-E, Morooka M, Kurth WS, Gurnett DA, MacDowall RJ (2017) Ion trapping by dust grains: simulation applications to the Enceladus plume. J Geophys Res, Planets 122:729–743. https://doi.org/10.1002/2016JE005235

Fatemi S, Poppe AR, Khurana KK, Holmström M, Delory GT (2016) On the formation of Ganymede's surface brightness asymmetries: kinetic simulations of Ganymede's magnetosphere. Geophys Res Lett 43:4745–4754. https://doi.org/10.1002/2016GL068363

Feldman PD, McGrath MA, Strobel DF, Moos HW, Retherford KD, Wolven BC (2000) HST/STIS ultraviolet imaging of polar aurora on Ganymede. Astrophys J 535:1085. https://doi.org/10.1086/308889

Fischer G, Gurnett DA, Kurth WS, Akalin F, Zarka P, Dyudina UA, Farrell WM, Kaiser ML (2008) Atmospheric electricity at Saturn. Space Sci Rev 137:271–285. https://doi.org/10.1007/s11214-008-9370-z

Fischer G, Panchenko M, Macher W, Kasaba Y, Misawa H, Tokarz M, Wisniewski L, Cecconi B, Bergman J, Wahlund J-E (2021) Calibration of the JUICE RWI antennas by numerical simulation. Radio Sci 56:e2021RS007309. https://doi.org/10.1029/2021RS007309

Fleshman BL, Delamere PA, Bagenal F (2010) Modeling the Enceladus plume–plasma interaction. Geophys Res Lett 37:L03202. https://doi.org/10.1029/2009GL041613

Fletcher LN, Cavalié T, Grassi D, et al (2023) Jupiter science enabled by ESA's JUpiter ICy moons Explorer. Space Sci Rev 219:53. https://doi.org/10.1007/s11214-023-00996-6

Frank LA, Paterson WR, Ackerson KL, Bolton SJ (1997) Outflow of hydrogen ions from Ganymede. Geophys Res Lett 24:2151. https://doi.org/10.1029/97GL01744
Fujita S, Matsuoka T, Ishida T, Matsuoka K, Mae S (2000) A summary of the complex dielectric permittivity of ice in the megahertz range and its applications for radar sounding of polar ice sheets. Physics of Ice Core Records, 185–212. http://hdl.handle.net/2115/32469
Galand M, Carnielli G, Jia X (2025) Ganymede's ionosphere. In: Volwerk M, McGrath M, Jia X, Spohn T (eds) Ganymede. Cambridge planetary science. Cambridge University Press, Cambridge.
Galli A, Vorburger A, Carberry Mogan SR, Roussos E, Stenberg Wieser G, Wurz P, et al (2022) Callisto's atmosphere and its space environment: prospects for the particle environment package on board JUICE. Earth Space Sci 9:e2021EA002172. https://doi.org/10.1029/2021EA002172
Galopeau PHM, Boudjada MY (2016) An oblate beaming cone for Io-controlled Jovian decameter emission. J Geophys Res Space Phys 121:3120–3138. https://doi.org/10.1002/2015JA021038
Gassot O, Herique A, Kofman W, Witasse O (2021) Passive radar probing of the Galilean Moons (No. EPSC2021-521). Copernicus Meetings
Gautier A-L (2013) Étude de la propagation des ondes radio dans les environnements planétaires. (Doctoral dissertation), Observatoire de Paris. https://theses.hal.science/tel-01145651v2
Génot V, et al (2018) Science data visualization in planetary and heliospheric contexts with 3DView. Planet Space Sci 150:111–130. https://doi.org/10.1016/j.pss.2017.07.007
Gerekos C, Bruzzone L, Imai M (2019) A coherent method for simulating active and passive radar sounding of the Jovian icy moons. IEEE Trans Geosci Remote Sens 58(4):2250–2265
Gershman DJ, Connerney JEP, Kotsiaros S, DiBraccio GA, Martos YM, F.-Viñas A, et al (2019) Alfvénic fluctuations associated with Jupiter's auroral emissions. Geophys Res Lett 46:7157–7165. https://doi.org/10.1029/2019GL082951
Gilet N, Henri P, Wattieaux G Cilibrasi M, Beghin C (2017) Electrostatic potential radiated by a pulsating charge in a two-electron temperature plasma. Radio Sci 52:1432
Gilet N, Henri P, Wattieaux G, Myllys M, Randriamboarison O, Béghin C, Rauch J-L (2019) Mutual impedance probe in collisionless unmagnetized plasmas with suprathermal electrons - application to BepiColombo. Front Astron Space Sci 6:16. https://doi.org/10.3389/fspas.2019.00016
Gilet N, Henri P, Wattieaux G, Traoré N, Eriksson AI, Vallières X, Moré J, Randriamboarison O, Odelstad E, Johansson FL, Rubin M (2020) Observations of a mix of cold and warm electrons by RPC-MIP at 67P/Churyumov-Gerasimenko. Astron Astrophys 640:A110
Giono G, Roth L, Ivchenko N, Saur J, Retherford K, Schlegel S, Ackland M, Strobel D (2020) An analysis of the statistics and systematics of limb anomaly detections in HST/STIS transit images of Europa. Astrophys J 159(4):155. https://doi.org/10.3847/1538-3881/ab7454
Gissinger C, Petitdemange L (2019) A magnetically driven equatorial jet in Europa's ocean. Nat Astron 3:401–407. https://doi.org/10.1038/s41550-019-0713-3
Goertz CK (1984) Kinetic Alfvén waves on auroral field lines. Planet Space Sci 32(11):1387–1392. https://doi.org/10.1016/0032-0633(84)90081-3
Graham DB, Khotyaintsev YV, Norgren C, Vaivads A, André M, Drake JF, et al (2019) Universality of lower hybrid waves at Earth's magnetopause. J Geophys Res Space Phys 124. https://doi.org/10.1029/2019JA027155
Grard RJL (1969) Coupling between two electric aerials in a warm plasma. Alta Freq 38:97–101
Grayver AV, Olsen N (2019) The magnetic signatures of the $M2$, $N2$, and $O1$ Oceanic tides observed in swarm and CHAMP satellite magnetic data. Geophys Res Lett 46:4230–4238. https://doi.org/10.1029/2019GL082400
Grayver AV, Schnepf NR, Kuvshinov AV, Sabaka TJ, Manoj C, Olsen N (2016) Satellite tidal magnetic signals constrain Oceanic lithosphere-asthenosphere boundary. Sci Adv 2(9):e1600798
Grayver AV, Munch FD, Kuvshinov AV, Khan A, Sabaka TJ, Tøffner-Clausen L (2017) Joint inversion of satellite-detected tidal and magnetospheric signals constrains electrical conductivity and water content of the upper mantle and transition zone. Geophys Res Lett 44:6074–6081. https://doi.org/10.1002/2017GL073446
Greathouse TK, Gladstone GR, Molyneux PM, Versteeg MH, Hue V, Kammer JA, et al (2022) UVS observations of Ganymede's aurora during Juno orbits 34 and 35. Geophys Res Lett 49:e2022GL099794. https://doi.org/10.1029/2022GL099794
Grimm RE, et al (2020) A magnetotelluric instrument for probing the interiors of Europa and other worlds. Adv Space Res. https://arxiv.org/abs/2101.06730
Grimm R, Castillo-Rogez J, Raymond C, Poppe AR (2021) Feasibility of characterizing subsurface brines on Ceres by electromagnetic sounding. Icarus 362:114424. https://doi.org/10.1016/j.icarus.2021.114424
Grygorczuk J, Tokarz M, Wisniewski L, Kucinski T, Ossowski M, Bochra K, Bogonski M, Jarzynka S, Palma P, Ryszawa E, Jarocki K, Wahlund J-E, Bergman J, Kasaba Y, Le Letty R (2023) RWI tubular boom antennas – lessons learned from the development of a flight model for the ESA JUICE Mission, ESMAT

Gunell H, Goetz C, Eriksson A, Nilsson H, Simon Wedlund C, Henri P, Maggiolo R, Hamrin M, De Keyser J, Rubin M, Stenberg Wieser G, Cessateur G, Dhooghe F, Gibbons A (2017a) Plasma waves confined to the diamagnetic cavity of comet 67P/Churyumov-Gerasimenko. Mon Not R Astron Soc 469(Suppl_2):S84–S92. https://doi.org/10.1093/mnras/stx1134

Gunell H, Nilsson H, Hamrin M, Eriksson A, Odelstad E, Maggiolo R, Henri P, Vallieres X, Altwegg K, Tzou C-Y, Rubin M, Glassmeier K-H, Stenberg Wieser G, Simon Wedlund C, De Keyser J, Dhooghe F, Cessateur G, Gibbons A (2017b) Ion acoustic waves at comet 67P/Churyumov-Gerasimenko. Astron Astrophys 600:A3. https://doi.org/10.1051/0004-6361/201629801

Gunell H, Goetz C, Odelstad E, Beth A, Hamrin M, Henri P, Johansson FL, Nilsson H, Stenberg Wieser G (2021) Ion acoustic waves near a comet nucleus: Rosetta observations at comet 67P/Churyumov-Gerasimenko. Ann Geophys 39:53–68. https://doi.org/10.5194/angeo-39-53-2021

Gurnett DA, Frank LA (1977) A region of intense plasma wave turbulence on auroral field lines. J Geophys Res 82(7):1031–1050. https://doi.org/10.1029/JA082i007p01031

Gurnett DA, Show RR, Anderson RR, Kurth WS, Scarf FL (1979) Whistlers observed by Voyager 1: detection of lightning on Jupiter. Geophys Res Lett 6:511–514. https://doi.org/10.1029/GL006i006p00511

Gurnett DA, Grün E, Gallagher D, Kurth WS, Scarf FL (1983b) Micron-sized particles detected near Saturn by the Voyager plasma wave instrument. Icarus 53(2):236–254. https://doi.org/10.1016/0019-1035(83)90145-8

Gurnett D, Kurth W, Scarf F (1983a) Narrowband electromagnetic emissions from Jupiter's magnetosphere. Nature 302:385–388. https://doi.org/10.1038/302385a0

Gurnett DA, Kurth WS, Scarf FL, Burns JA, Cuzzi JN, Grün E (1987) Micron-sized particle impacts detected near Uranus by the Voyager 2 plasma wave instrument. J Geophys Res 92(A13):14959–14968. https://doi.org/10.1029/JA092iA13p14959

Gurnett DA, Kurth WS, Granroth LJ, Allendorf SC, Poynter RL (1991) Micron-sized particles detected near Neptune by the Voyager 2 plasma wave instrument. J Geophys Res 96(S01):19177–19186. https://doi.org/10.1029/91JA01270

Gurnett D, Kurth W, Roux A, et al (1996) Evidence for a magnetosphere at Ganymede from plasma-wave observations by the Galileo spacecraft. Nature 384:535–537. https://doi.org/10.1038/384535a0

Gurnett DA, Kurth WS, Roux A, Bolton SJ, Thomsen EA, Groene JB (1998) Galileo plasma wave observations near Europa. Geophys Res Lett 25(3):237–240. https://doi.org/10.1029/97GL03706

Gurnett DA, Persoon AM, Kurth WS, Roux A, Bolton SJ (2000) Plasma densities in the vicinity of Callisto from Galileo plasma wave observations. Geophys Res Lett 27(13):1867–1870. https://doi.org/10.1029/2000GL003751

Gurnett DA, Kurth WS, Kirchner DL, Hospodarsky GB, Averkamp TF, Zarka P, Lecacheux A, Manning R, Roux A, Canu P, Cornilleau-Wehrlin N, Galopeau P, Meyer A, Boström R, Gustafsson G, Wahlund J-E, Åhlén L, Rucker HO, Ladreiter HP, Macher W, Woolliscroft LJC, Alleyne H, Kaiser ML, Desch MD, Farrell WM, Harvey CC, Louarn P, Kellogg PJ, Goetz K, Pedersen A (2004) The Cassini Radio and Plasma Wave Investigation. Space Sci Rev 114:395–463. https://doi.org/10.1007/s11214-004-1434-0

Gurnett DA, et al (2011) Auroral hiss, electron beams and standing Alfvén wave currents near Saturn's moon Enceladus. Geophys Res Lett 38:L06102. https://doi.org/10.1029/2011GL046854

Gustafsson G, Wahlund J-E (2010) Electron temperatures in Saturn's plasma disc. Planet Space Sci 58:1018–1025. https://doi.org/10.1016/j.pss.2010.03.007

Haerendel G (2011) Six auroral generators: a review. J Geophys Res 116:A00K05. https://doi.org/10.1029/2010JA016425

Hall DT, Strobel DF, Feldman PD, McGrath MA, Weaver HA (1995) Detection of an oxygen atmosphere on Jupiter's moon Europa. Nature 373(6516):677–681. https://doi.org/10.1038/373677a0

Hall DT, Feldman PD, McGrath MA, Strobel DF (1998) The far-ultraviolet oxygen airglow of Europa and Ganymede. Astrophys J 499:475. https://doi.org/10.1086/305604

Harris CDK, Jia X, Slavin JA, Toth G, Huang Z, Rubin M (2021) Multi-fluid MHD simulations of Europa's plasma interaction under different magnetospheric conditions. J Geophys Res Space Phys 126:e2020JA028888. https://doi.org/10.1029/2020JA028888

Harris CDK, Jia X, Slavin JA (2022) Multi-fluid MHD simulations of Europa's plasma interaction: effects of variation in Europa's atmosphere. J Geophys Res Space Phys 127:e2022JA030569. https://doi.org/10.1029/2022JA030569

Hartkorn O, Saur J (2017) Induction signals from Callisto's ionosphere and their implications on a possible subsurface ocean. J Geophys Res Space Phys 122:11,677–11,697. https://doi.org/10.1002/2017JA024269

Hartkorn O, Saur J, Strobel DF (2017) Structure and density of Callisto's atmosphere from a fluid-kinetic model of its ionosphere: comparison with Hubble Space Telescope and Galileo observations. Icarus 282:237–259. https://doi.org/10.1016/j.icarus.2016.09.020

Hartogh P, Ilyushin YA (2016) A passive low frequency instrument for radio wave sounding the subsurface oceans of the Jovian icy moons: an instrument concept. Planet Space Sci 130:30–39
Hasegawa A (1976) Particle acceleration by MHD surface wave and formation of aurora. J Geophys Res 81(28):5083–5090. https://doi.org/10.1029/JA081i028p05083
Hess S, Mottez F, Zarka P (2007) Jovian S-bursts generation by Alfvén waves. J Geophys Res 112:A11212
Hess S, Mottez F, Zarka P, Chust T (2008) Generation of the Jovian radio decametric arcs from the Io flux tube. J Geophys Res 113:A03209
Hess SLG, Echer E, Zarka P, Lamy L, Delamere PA (2014) Multi-instrument study of the Jovian radio emissions triggered by solar wind shocks and inferred magnetospheric subcorotation rates. Planet Space Sci 99:136–148
Hill TW (1975) Inertial limit on corotation. J Geophys Res 84:6554. https://doi.org/10.1029/JA084iA11p06554
Hill TW (1979) Inertial limit on corotation. J Geophys Res 84(A11):6554–6558. https://doi.org/10.1029/JA084iA11p06554
Hill TW (2001) The Jovian auroral oval. J Geophys Res 106(A5):8101–8810. https://doi.org/10.1029/2000JA000302
Hill TW, et al (2012) Charged nanograins in the Enceladus plume. J Geophys Res 117:A05209. https://doi.org/10.1029/2011JA017218
Hillier JK, Green SF, McBride N, Schwanethal JP, Postberg F, Srama R, Kempf S, Moragas-Klostermeyer G, McDonnell JAM, Grün E (2007) The composition of Saturn's E ring. Mon Not R Astron Soc 377:1588–1596. https://doi.org/10.1111/j.1365-2966.2007.11710.x
Holmberg MKG (2020) JUICE spacecraft charging analysis. ESA Technical note JUI-EST-SYS-TN-026
Holmberg MKG, Wahlund J-E, Morooka MW, Persoon AM (2012) Ion densities and velocities in the inner plasma torus of Saturn. Planet Space Sci 73:151–160. https://doi.org/10.1016/j.pss.2012.09.016
Holmberg MKG, Shebanits O, Wahlund J-E, Morooka MW, Vigren E, André N, Garnier P, Persoon AM, Génot V, Gilbert LK (2017) Density structures, dynamics, and seasonal and solar cycle modulations of Saturn's inner plasma disk. J Geophys Res Space Phys 122:12,258–12,273. https://doi.org/10.1002/2017JA024311
Holmberg MKG, Cipriani F, Nilsson T, Hess S, Huybrighs HLF, Hadid LZ, et al (2021) Cassini-plasma interaction simulations revealing the Cassini ion wake characteristics: implications for in-situ data analyses and ion temperature estimates. J Geophys Res Space Phys 126:e2020JA029026. https://doi.org/10.1029/2020JA029026
Holmberg MKG, Jackman CM, Taylor MGGT, Witasse O, Wahlund J-E, Barabash S, et al (2024) Surface charging of the Jupiter Icy Moons Explorer (JUICE) spacecraft in the solar wind at 1 AU. J Geophys Res Space Phys 129:e2023JA032137. https://doi.org/10.1029/2023JA032137
Holmgren G, Kintner PM (1990) Experimental evidence of widespread regions of small-scale plasma irregularities in the magnetosphere. J Geophys Res 95(A5):6015–6023. https://doi.org/10.1029/JA095iA05p06015
Huscher E, Bagenal F, Wilson RJ, Allegrini F, Ebert RW, Valek PW, et al (2021) Survey of Juno observations in Jupiter's plasma disk: density. J Geophys Res Space Phys 126:e2021JA029446. https://doi.org/10.1029/2021JA029446
Imai M, Kolmasova I, Kurth WS, Santolik O, Hospodarsky GB, Gurnett DA, Brown ST, Bolton SJ, Connerney JEP, Levin S (2019) Evidence for low density holes in Jupiter's ionosphere. Nat Commun 10. https://doi.org/10.1038/s41467-019-10708-w
Jacome HRP, Marques MS, Zarka P, Echer E, Lamy L, Louis C (2022) Search for Jovian DAM emissions induced by Europa on the extensive Nançay decameter array's catalog. Astron Astrophys 665:A67. https://doi.org/10.1051/0004-6361/202244246
Janhunen P, Olsson A, Laakso H (2002) Altitude dependence of plasma density in the auroral zone. Ann Geophys 20:1743–1750. https://doi.org/10.5194/angeo-20-1743-2002
Jia X, Walker RJ, Kivelson MG, Khurana KK, Linker JA (2009) Properties of Ganymede's magnetosphere inferred from improved three-dimensional MHD simulations. J Geophys Res 114:A09209. https://doi.org/10.1029/2009JA014375
Jia X, Kivelson MG, Khurana KK, et al (2018) Evidence of a plume on Europa from Galileo magnetic and plasma wave signatures. Nat Astron 2:459–464. https://doi.org/10.1038/s41550-018-0450-z
Johansson FL, et al (2021) Plasma densities, flow, and solar EUV flux at comet 67P a cross-calibration approach. Astron Astrophys 653:A128. https://doi.org/10.1051/0004-6361/202039959
Johnson RE, Burger MH, Cassidy TA, Leblanc F, Marconi M, Smyth WH (2009) Composition and detection of Europa's sputter-induced atmosphere. In: Pappalardo RT, McKinnon WB, Khurana KK (eds) Europa. University of Arizona Press, Tucson, p 507
Jones GH, et al (2009) Fine jet structure of electrically charged grains in Enceladus' plume. Geophys Res Lett 36:L16204. https://doi.org/10.1029/2009GL038284

JUICE Science Working Team (2014) JUICE definition study report (Red Book). ESA/SRE(2014)1. European Space Agency. https://sci.esa.int/web/juice/-/54994-juice-definition-study-report
Karlsson T, Eriksson AI, Odelstad E, André M, Dickeli G, Kullen A, Lindqvist P-A, Nilsson H, Richter I (2017) Rosetta measurements of lower hybrid frequency range electric field oscillations in the plasma environment of comet 67P. Geophys Res Lett 44:1641–1651. https://doi.org/10.1002/2016GL072419
Karlsson T, Andersson L, Gillies DM, et al (2020) Quiet, discrete auroral arcs – observations. Space Sci Rev 216:16. https://doi.org/10.1007/s11214-020-0641-7
Kasahara Y, et al (2018) The plasma wave experiment (PWE) on board the Arase (ERG) satellite. Earth Planets Space 70:86. https://doi.org/10.1186/s40623-018-0842-4
Katoh M, Fujimoto M, Kawaguchi H, Tsuchiya K, Ohmi K, Kaneyasu T, Taira Y, Hosaka M, Mochihashi A, Takashima Y (2017) Angular momentum of twisted radiation from an electron in spiral motion. Phys Rev Lett 118:094801. https://doi.org/10.1103/PhysRevLett.118.094801
Katoh Y, Kojima H, Hikishima M, et al (2018) Software-type wave–particle interaction analyzer on board the arase satellite. Earth Planets Space 70:4. https://doi.org/10.1186/s40623-017-0771-7
Keiling A, Wygant JR, Cattell C, Peria W, Parks G, Temerin M, et al (2002) Correlation of Alfvén wave Poynting flux in the plasma sheet at 4-7 RE with ionospheric electron energy flux. J Geophys Res 107(A7):1132. https://doi.org/10.1029/2001JA900140
Keiling A, Thaller S, Wygant J, Dombeck J (2019a) Assessing the global Alfvén wave power flow into and out of the auroral acceleration region during geomagnetic storms. Sci Adv 5(6):eaav8411. https://doi.org/10.1126/sciadv.aav8411
Keiling A, Thaller S, Wygant J, Dombeck J (2019b) Global Alfvén wave power in the auroral zone in relation to the AE index. J Geophys Res Space Phys 124:8637–8646. https://doi.org/10.1029/2019JA026805
Kempf S, Beckmann U, Srama R, Horanyi M, Auer S, Grün E (2006) The electrostatic potential of E ring particles. Planet Space Sci 54:999–1006. https://doi.org/10.1016/j.pss.2006.05.012
Kempf S, Beckmann U, Moragas-Klostermeyer G, Postberg F, Srama R, Economou T, Schmidt J, Spahn F, Grün E (2008) The E ring in the vicinity of Enceladus. I: Spatial distribution and properties of the ring particles. Icarus 193:420–437. https://doi.org/10.1016/j.icarus.2007.06.027
Kempf S, Beckmann U, Schmidt J (2010) How the Enceladus dust plume feeds Saturn's E ring. Icarus 206(2):446–457. https://doi.org/10.1016/j.icarus.2009.09.016
Kennel CF, Coroniti FV (1975) Is Jupiter's magnetosphere like a pulsar's or Earth's. Space Sci Rev 17:857–883. https://doi.org/10.1007/BF00777259
Khotyaintsev YV, Cully CM, Vaivads A, André M, Owen CJ (2011) Plasma jet braking: energy dissipation and nonadiabatic electrons. Phys Rev Lett 106:16500. https://doi.org/10.1103/PhysRevLett.106.165001
Khotyaintsev YV, Graham DB, Norgren C, Vaivads A (2019) Collisionless magnetic reconnection and waves: progress review. Front Astron Space Sci 6:70. https://doi.org/10.3389/fspas.2019.00070
Khotyaintsev YuV, et al (2021) Density fluctuations associated with turbulence and waves – first observations by Solar Orbiter. Astron Astrophys 656:A19. https://doi.org/10.1051/0004-6361/202140936
Khurana KK, Kivelson MG (1999) Inner Jovian magnetosphere: mass-loading near Europa. Eos 80:F875
Khurana K, Kivelson M, Stevenson D, et al (1998) Induced magnetic fields as evidence for subsurface oceans in Europa and Callisto. Nature 395:777–780. https://doi.org/10.1038/27394
Khurana KK, Vasyliūnas V, Mauk B, Frank L, Paterson B, Kivelson M, Krupp N, Woch J, Lagg A, Kurth B (2004) The configuration of Jupiter's magnetosphere. In: Bagenal F, Dowling TE, McKinnon WB (eds) Jupiter: the planet, satellites and magnetosphere. Cambridge University Press, Cambridge, pp 593–616
Kiely A (2004) Selecting the Golomb Parameter in Rice Coding. IPN Progress Report 42-159. https://ipnpr.jpl.nasa.gov/progress_report/42-159/159E.pdf
Kim TK, Ebert RW, Valek PW, Allegrini F, McComas DJ, Bagenal F, et al (2020) Survey of ion properties in Jupiter's plasma sheet: Juno JADE-I observations. J Geophys Res Space Phys 125:e2019JA027696. https://doi.org/10.1029/2019JA027696
Kimura T, Cecconi B, Zarka P, Kasaba Y, Tsuchiya F, Misawa H, Morioka A (2012) Polarization and direction of arrival of Jovian quasi-periodic bursts observed by Cassini. J Geophys Res 117:A11209
Kintner PM, et al (1987) Detection of spatial density irregularities with the viking plasma wave interferometer. Geophys Res Lett 14(4):467–470. https://doi.org/10.1029/GL014i004p00467
Kitamura N, et al (2018) Direct measurements of two-way wave-particle energy transfer in a collisionless space plasma. Science 361:1000–1003. https://doi.org/10.1126/science.aap8730
Kivelson MG, Southwood DJ (2005) Dynamical consequences of two modes of centrifugal instability in Jupiter's outer magnetosphere. J Geophys Res Space Phys 110:A12209
Kivelson MG, Khurana KK, Russell CT, et al (1996) Discovery of Ganymede's magnetic field by the Galileo spacecraft. Nature 384:537–541. https://doi.org/10.1038/384537a0
Kivelson MG, Warnecke J, Bennett L, Joy S, Khurana KK, Linker JA, Russell CT, Walker RJ, Polanskey C (1998) Ganymede's magnetosphere: magnetometer overview. J Geophys Res 103(E9):19963–19972

Kivelson MG, Khurana KK, Stevenson DJ, Bennett L, Joy S, Russell CT, Walker RJ, Zimmer C, Polanskey C (1999) Europa and Callisto: induced or intrinsic fields in a periodically varying plasma environment. J Geophys Res 104(A3):4609–4625. https://doi.org/10.1029/1998JA900095

Kivelson MG, Khurana KK, Russell CT, Volwerk M, Walker RJ, Zimmer C (2000) Galileo magnetometer measurements: a stronger case for a subsurface ocean at Europa. Science 289:1340–1343. https://doi.org/10.1126/science.289.5483.1340

Kivelson MG, Khurana KK, Volwerk M (2002) The permanent and inductive magnetic moments of Ganymede. Icarus 157(2):507–522. https://doi.org/10.1006/icar.2002.6834

Kivelson MG, Bagenal F, Kurth WS, Neubauer FM, Paranicas C, Saur J (2004) Magnetospheric interactions with satellites. In: Bagenal F, Dowling TE, McKinnon WB (eds) Jupiter: the planet, satellites and magnetosphere. Cambridge University Press, Cambridge, pp 513–536

Kivelson MG, Khurana KK, Volwerk M (2009) In: Pappalardo RT, McKinnon WB, Khurana KK (eds) Europa. University of Arizona Press, Tucson, pp 545–570

Kliore AJ (1998) Satellite atmospheres and magnetospheres. In: Andersen J (ed) Highlights of astronomy. International astronomical union / union astronomique internationale, vol 11B. Springer, Dordrecht. https://doi.org/10.1007/978-94-011-4778-1_138

Kliore AJ, Hinson DP, Flasar FM, Nagy AF, Cravens TE (1997) The ionosphere of Europa from Galileo radio occultations. Science 277(5324):355–358. https://doi.org/10.1126/science.277.5324.355

Kliore AJ, Anabtawi A, Herrera RG, Asmar SW, Nagy AF, Hinson DP, Flasar FM (2002) Ionosphere of Callisto from Galileo radio occultation observations. J Geophys Res 107(A11):1407. https://doi.org/10.1029/2002JA009365

Knight S (1973) Parallel electric fields. Planet Space Sci 21:741–750. https://doi.org/10.1016/0032-0633(73)90093-7

Kolmašová I, Imai M, Santolík O, Kurth WS, Hospodarsky GB, Gurnett DA, Connerney JEP, Bolton S (2018) Discovery of rapid whistlers close to Jupiter implying lightning rates similar to those on Earth. Nat Astron 2:544–548. https://doi.org/10.1038/s41550-018-0442-z

Kolmašová I, Santolík O, Imai M, et al (2023) Lightning at Jupiter pulsates in a similar rhythm as in-cloud lightning at Earth. Nat Commun 14:2707. https://doi.org/10.1038/s41467-023-38351-6

Kotsiaros S, Connerney JEP, Clark G, et al (2019) Birkeland currents in Jupiter's magnetosphere observed by the polar-orbiting Juno spacecraft. Nat Astron 3:904–909. https://doi.org/10.1038/s41550-019-0819-7

Kriegel H, Simon S, Motschmann U, Saur J, Neubauer FM, Persoon AM, Dougherty MK, Gurnett DA (2011) Influence of negatively charged plume grains on the structure of Enceladus' Alfvén wings: hybrid simulations versus Cassini magnetometer data. J Geophys Res 116:A10223. https://doi.org/10.1029/2011JA016842

Krivov AV, Krüger H, Grün E, Thiessenhusen K-U, Hamilton DP (2002) A tenuous dust ring of Jupiter formed by escaping ejecta from the Galilean satellites. J Geophys Res 107:E1. https://doi.org/10.1029/2000JE001434

Krüger H, et al (1999) Analysis of the sensor characteristics of the Galileo dust detector with collimated Jovian dust stream particles. Planet Space Sci 47:1015–1028. https://doi.org/10.1016/S0032-0633(99)00027-6

Krüger H, Horányi M, Grün E (2003) Jovian dust streams: probes of the Io plasma torus. Geophys Res Lett 30:1058. https://doi.org/10.1029/2002GL015920

Krupp N, Roussos E, Kollmann P, Paranicas C, Mitchell DG, Krimigis SM, Rymer A, Jones GH, Arridge CS, Armstrong TP, Khurana KK (2012) The Cassini Enceladus encounters 2005–2010 in the view of energetic electron measurements. Icarus 218(1):433–447. https://doi.org/10.1016/j.icarus.2011.12.018

Kumamoto A, Kasaba Y, Tsuchiya F, Misawa H, Kita H, Puccio W, Kobayashi T (2018) Feasibility of the exploration of the subsurface structures of Jupiter's icy moons by interference of Jovian hectometric and decametric radiation, in Planetary Radio Emissions VIII. ISBN 978-3-7001-8263-4 or ISBN 978-3-7001-8392-1, Online Edition https://doi.org/10.1553/PRE8

Kurita S, Miyoshi Y, Cully CM, Angelopoulos V, Le Contel O, Hikishima M, Misawa H (2014) Observational evidence of electron pitch angle scattering driven by ECH waves. Geophys Res Lett 41:8076–8080. https://doi.org/10.1002/2014GL061927

Kurth WS, Gurnett DA, Roux A, Bolton SJ (1997) Ganymede: a new radio source. Geophys Res Lett 24(17):2167–2170. https://doi.org/10.1029/97GL02249

Kurth WS, Gurnett DA, Persoon AM, Roux A, Bolton SJ, Alexander CJ (2001) The plasma wave environment of Europa. Planet Space Sci 49(3–4):345–363. https://doi.org/10.1016/S0032-0633(00)00156-2

Kurth WS, Averkamp TF, Gurnett DA, Wang Z (2006) Cassini RPWS observations of dust in Saturn's E Ring. Planet Space Sci 54(9–10):988–998. https://doi.org/10.1016/j.pss.2006.05.011

Kurth WS, Sulaiman AH, Hospodarsky GB, Menietti JD, Mauk BH, Clark G, et al (2022) Juno plasma wave observations at Ganymede. Geophys Res Lett 49:e2022GL098591. https://doi.org/10.1029/2022GL098591

Kurth WS, Wilkinson DR, Hospodarsky GB, Santolik O, Averkamp TF, Sulaiman AH, Menietti JD, Connerney JEP, Allegrini F, Mauk BH, Bolton SJ (2023) Juno plasma wave observations at Europa. Geophys Res Lett 50:e2023GL105775. https://doi.org/10.1029/2023GL105775
LaBelle J, Kintner PM, Kelley MC (1986) Interferometric phase velocity measurements in the auroral electrojet. Planet Space Sci 34(12):1285–1297. https://doi.org/10.1016/0032-0633(86)90065-6
Lamy L, Colomban L, Zarka P, Prangé R, Marques MS, Louis C, Kurth W, Cecconi B, Girard J, Griessmeier J-M, Yerin S (2022) Determining the beaming of Io decametric emissions: a remote diagnostic to probe the Io-Jupiter interaction. J Geophys Res 127:e2021JA030160. https://doi.org/10.1029/2021JA030160
Lamy L, Duchêne A, Mauduit E, Zarka P, Yerin S, Louis C, Griessmeier J-M, Girard J, Theureau G (2023) Probing Jupiter-satellite interactions from the beaming of their decametric emissions: the case of Europa and Ganymede. Louis CK, Jackman CM, Fischer G, Sulaiman AH, Zucca P (eds) Dublin institute for advanced studies, planetary, solar and heliospheric radio emissions IX. https://doi.org/10.25546/103097
Larsson AL, Wahlund J-E (2004) Low-temperature coatings for instruments on the BepiColombo mission to Mercury. Swedish Institute of Space Physics, IRF-report
Leblanc Y, Rubio M (1982) A narrow-band splitting at the Jovian decametric cutoff frequency. Astron Astrophys 111(2):284–294
Leblanc F, Oza AV, Leclercq L, Schmidt C, Cassidy T, Modolo R, Chaufray JY, Johnson RE (2017) On the orbital variability of Ganymede's atmosphere. Icarus 293:185–198. https://doi.org/10.1016/j.icarus.2017.04.025
Leblanc F, Roth L, Chaufray JY, Modolo R, Galand M, Ivchenko N, Carnielli G, Baskevitch C, Oza A, Werner ALE (2023) Ganymede's atmosphere as constrained by HST/STIS observations. Icarus 399:115557. https://doi.org/10.1016/j.icarus.2023.115557
Lecacheux A (1988) Polarization aspects from planetary radio emissions. In: Rucker HO, Bauer SJ, Pedersen BM (eds) Planetary radio emissions II. Austrian Acad. Sci. Press, Vienna, pp 299–314
Lecacheux A, Boischot A, Boudjada MY, Dulk GA (1991) Spectra and complete polarization state of two, Io-related, radio storms from Jupiter. Astron Astrophys 251(1):339–348
Leclercq L, Modolo R, Leblanc F, Hess S, Mancini M (2016) 3D magnetospheric parallel hybrid multi-grid method applied to planet-plasma interactions. J Comput Phys 309:295–313. https://doi.org/10.1016/j.jcp.2016.01.005
Leisner JS, Hospodarsky GB, Gurnett DA (2013) Enceladus auroral hiss observations: implications for electron beam locations. J Geophys Res Space Phys 118:160–166. https://doi.org/10.1029/2012JA018213
Li J, Gudipati MS, Yung YL (2020) The influence of Europa's plumes on its atmosphere and ionosphere. Icarus 352:113999. https://doi.org/10.1016/j.icarus.2020.113999
Lindkvist J, Holmström M, Khurana KK, Fatemi S, Barabash S (2015) Callisto plasma interactions: hybrid modeling including induction by a subsurface ocean. J Geophys Res Space Phys 120:4877–4889. https://doi.org/10.1002/2015JA021212
Lindqvist P-A, Marklund GT (1990) A statistical study of high-altitude electric fields measured on the viking satellite. J Geophys Res 95(A5):5867–5876. https://doi.org/10.1029/JA095iA05p05867
Liu X, Schmidt J (2019) Dust in the Jupiter system outside the rings. Astrodynamics 3:17–29. https://doi.org/10.1007/s42064-018-0031-z
Louarn P, Wahlund J-E, Chust T, de Feraudy H, Roux A, Holback B, Dovner PO, Eriksson AI, Holmgren G (1994) Observation of kinetic Alfvén waves by the FREJA spacecraft. Geophys Res Lett 21(17):1847–1850. https://doi.org/10.1029/94GL00882
Louarn P, Paranicas CP, Kurth WS (2014) Global magnetodisk disturbances and energetic particle injections at Jupiter. J Geophys Res Space Phys 119:4495–4511. https://doi.org/10.1002/2014JA019846
Louarn P, André N, Jackman CM, Kasahara S, Kronberg EA, Vogt MF (2015) Magnetic reconnection and associated transient phenomena within the magnetospheres of Jupiter and Saturn. Space Sci Rev 187:181–227. https://doi.org/10.1007/s11214-014-0047-5
Louarn P, et al (2017) Generation of the Jovian hectometric radiation: first lessons from Juno. Geophys Res Lett 44:4439–4446. https://doi.org/10.1002/2017GL072923
Louis CK, Lamy L, Zarka P, Cecconi B, Hess SLG (2017) Detection of Jupiter decametric emissions controlled by Europa and Ganymede with Voyager/PRA and Cassini/RPWS. J Geophys Res 122:9228–9247. https://doi.org/10.1002/2016JA023779
Louis CK, Hess SLG, Cecconi B, Zarka P, Lamy L, Aicardi S, Loh A (2019a) ExPRES: an exoplanetary and planetary radio emissions simulator. Astron Astrophys 627:A30. https://doi.org/10.1051/0004-6361/201935161
Louis CK, Prangé R, Lamy L, Zarka P, Imai M, Kurth WS, Connerney JEP (2019b) Jovian auroral radio sources detected in situ by Juno/Waves: comparisons with model auroral ovals and simultaneous HST FUV images. Geophys Res Lett 46. https://doi.org/10.1029/2019GL084799
Louis CK, Zarka P, Dabidin K, Lampson P-A, Magalhaes FP, Boudouma A, Marques MS, Cecconi B (2021) Latitudinal beaming of Jupiter's radio emissions from Juno/waves flux density measurements. J Geophys Res 126(10):e29435. https://doi.org/10.1029/2021JA029435

Louis CK, Jackman CM, Hospodarsky G, O'Kane Hackett A, Devon-Hurley E, Zarka P, et al (2023) Effect of a magnetospheric compression on Jovian radio emissions: in situ case study using Juno data. J Geophys Res Space Phys 128:e2022JA031155. https://doi.org/10.1029/2022JA031155
Lysak RL (2023) Kinetic Alfvén waves and auroral particle acceleration: a review. Rev Mod Plasma Phys 7(1):6. https://doi.org/10.1007/s41614-022-00111-2
Lysak RL, Lotko W (1996) On the kinetic dispersion relation for shear Alfvén waves. J Geophys Res 101(A3):5085–5094. https://doi.org/10.1029/95JA03712
Lysak RL, Echim MM, Karlsson T, Marghitu O, Rankin R, Song Y, Watanabe T (2020) Quiet, discrete auroral arcs: acceleration mechanisms. Space Sci Rev 216:1–31. https://doi.org/10.1007/s11214-020-00715-5
Lysak RL, Song Y, Elliott S, Kurth W, Sulaiman AH, Gershman D (2021) The Jovian ionospheric Alfvén resonator and auroral particle acceleration. J Geophys Res Space Phys 126:e2021JA029886. https://doi.org/10.1029/2021JA029886
MacDowall RJ, Kaiser ML, Desch MD, Farrell WM, Hess RA, Stone RG (1993) Quasiperiodic Jovian radio bursts: observations from the Ulysses radio and plasma wave experiment. Planet Space Sci 41(11/12):1059–1072
Manners H, Masters A (2020) The global distribution of ultralow-frequency waves in Jupiter's magnetosphere. J Geophys Res Space Phys 125:e2020JA028345. https://doi.org/10.1029/2020JA028345
Marklund G, Ivchenko N, Karlsson T, et al (2001) Temporal evolution of the electric field accelerating electrons away from the auroral ionosphere. Nature 414:724–727. https://doi.org/10.1038/414724a
Marklund GT, et al (2011) Evolution in space and time of the quasi-static acceleration potential of inverted-V aurora and its interaction with Alfvénic boundary processes. J Geophys Res 116:A00K13. https://doi.org/10.1029/2011JA016537
Marques MS, Zarka P, Echer E, Ryabov VB, Alves MV, Denis L, Coffre A (2017) Statistical analysis of 26 years of observations of decametric radio emissions from Jupiter. Astron Astrophys 604:A17. https://doi.org/10.1051/0004-6361/201630025
Marzok A, Schlegel S, Saur J, Roth L, Grodent D, Strobel DF, Retherford KD (2022) Mapping the brightness of Ganymede's ultraviolet aurora using Hubble Space Telescope observations. J Geophys Res, Planets 127:e2022JE007256. https://doi.org/10.1029/2022JE007256
Masters A, Modolo R, Roussos E et al. (2024) Magnetosphere and plasma ccience with the Jupiter icy moons explorer. Space Sci Rev
Mauduit E, Zarka P, Lamy L, Hess SLG (2023) Drifting discrete Jovian radio bursts reveal acceleration processes related to Ganymede and the main aurora. Nat Commun. https://doi.org/10.1038/s41467-023-41617-8
Mauk BH, Mitchell DG, Krimigis SM, Roelof EC, Paranicas CP (2003) Energetic neutral atoms from a trans-Europa gas torus at Jupiter. Nature 421(6926):920–922. https://doi.org/10.1038/nature01431
Mauk BH, Clark G, Gladstone GR, Kotsiaros S, Adriani A, Allegrini F, et al (2020) Energetic particles and acceleration regions over Jupiter's polar cap and main aurora: a broad overview. J Geophys Res Space Phys 125:e2019JA027699. https://doi.org/10.1029/2019JA027699
McGrath MA, Hansen CJ, Hendrix AR (2009) Observations of Europa's tenuous atmosphere. In: Pappalardo RT, McKinnon WB, Khurana KK (eds) Europa. University of Arizona Press, Tucson, pp 485–506
McGrath MA, Jia X, Retherford K, Feldman PD, Strobel DF, Saur J (2013) Aurora on Ganymede. J Geophys Res Space Phys 118:2043–2054. https://doi.org/10.1002/jgra.50122
McNutt R, Belcher J, Sullivan J, et al (1979) Departure from rigid co-rotation of plasma in Jupiter's dayside magnetosphere. Nature 280:803. https://doi.org/10.1038/280803a0
Meyer-Vernet N, Lecacheux A, Pedersen BM (1996) Constraints on Saturn's E Ring from the Voyager 1 radio astronomy instrument. Icarus 123(1):113–128. https://doi.org/10.1006/icar.1996.0145
Meyer-Vernet N, Maksimovic M, Czechowski A, et al (2009) Dust detection by the wave instrument on STEREO: nanoparticles picked up by the solar wind? Sol Phys 256:463–474. https://doi.org/10.1007/s11207-009-9349-2
Modolo R, et al (2018) The LatHyS database for planetary plasma environment investigations: overview and a case study of data/model comparisons. Planet Space Sci 150:13–21. https://doi.org/10.1016/j.pss.2017.02.015
Molyneux PM, Nichols JD, Bannister NP, Bunce EJ, Clarke JT, Cowley SWH, et al (2018) Hubble Space Telescope observations of variations in Ganymede's oxygen atmosphere and aurora. J Geophys Res Space Phys 123:3777–3793. https://doi.org/10.1029/2018JA025243
Morioka A, Nozawa H, Misawa H, Tsuchiya F, Miyoshi Y, Kimura T, Kurth W (2006) Rotationally driven quasi-periodic radio emissions in the Jovian magnetosphere. J Geophys Res 111:A04223. https://doi.org/10.1029/2005JA011563
Morooka MW, André M, Wahlund J-E, Buchert SC, Fazakerley AN, Winningham JD, Re`me H, Dandouras I, Lavraud B, Balogh A, Igenbergs K (2004) Cluster observations of ULF waves with pulsating electron beams above the high latitude dusk-side auroral region. Geophys Res Lett 31:L05804. https://doi.org/10.1029/2003GL017714

Morooka MW, Modolo R, Wahlund J-E, André M, Eriksson AI, Persoon AM, Gurnett DA, Kurth WS, Coates AJ, Lewis GR, Khurana KK, Dougherty M (2009) The electron density of Saturn's magnetosphere. Ann Geophys 27:2971. http://www.ann-geophys.net/27/2971/2009/

Morooka MW, Wahlund J-E, Eriksson AI, Farrell WM, Gurnett DA, Kurth WS, Persoon AM, Shafiq M, André M, Holmberg MKG (2011) Dusty plasma in the vicinity of Enceladus. J Geophys Res 116:A12221. https://doi.org/10.1029/2011JA017038

Mott-Smith HM, Langmuir I (1926) The theory of collectors in gaseous discharges. Phys Rev 28:727. https://doi.org/10.1103/PhysRev.28.727

Mottez F, Hess SLG, Zarka P (2010) Explanation of dominant oblique radio emission at Jupiter and comparison to the Terrestrial case. Planet Space Sci 58:1414–1422

Mozer FS, Bruston P (1967) Electric field measurements in the auroral ionosphere. J Geophys Res 72(3):1109–1114. https://doi.org/10.1029/JZ072i003p01109

Mozer FS, Kletzing CA (1998) Direct observation of large, quasi-static, parallel electric fields in the auroral acceleration region. Geophys Res Lett 25(10):1629–1632. https://doi.org/10.1029/98GL00849

Mozer FS, Carlson CW, Hudson MK, Torbert RB, Parady B, Yatteau J, Kelley MC (1977) Observations of paired electrostatic shocks in the polar magnetosphere. Phys Rev Lett 38:6. https://doi.org/10.1103/PhysRevLett.38.292

Mozer FS, et al (2022) Core electron heating by triggered ion acoustic waves in the solar wind. Astrophys J Lett 927:L15. https://doi.org/10.3847/2041-8213/ac5520

Neubauer F (1980) Nonlinear standing Alfvén wave current system at Io: theory. J Geophys Res 85(A3):1171–1178. https://doi.org/10.1029/JA085iA03p01171

Neubauer FM (1998) The sub-Alfvénic interaction of the Galilean satellites with the Jovian magnetosphere. J Geophys Res 103(E9):19843–19866. https://doi.org/10.1029/97JE03370

Neubauer FM (1999) Alfvén wings and electromagnetic induction in the interiors: Europa and Callisto. J Geophys Res 104(A12):28671–28684. https://doi.org/10.1029/1999JA900217

Newell PT, Sotirelis T, Wing S (2009) Diffuse, monoenergetic, and broadband aurora: the global precipitation budget. J Geophys Res 114:A09207. https://doi.org/10.1029/2009JA014326

Ni B, Thorne RM, Horne RB, Meredith NP, Shprits YY, Chen L, Li W (2011) Resonant scattering of plasma sheet electrons leading to diffuse auroral precipitation: 1. Evaluation for electrostatic electron cyclotron harmonic waves. J Geophys Res 116:A04218. https://doi.org/10.1029/2010JA016232

Nichols JD (2011) Magnetosphere-ionosphere coupling in Jupiter's middle magnetosphere: computations including a self-consistent current sheet magnetic field model. J Geophys Res 116:A10232. https://doi.org/10.1029/2011JA016922

Nimmo F, Schenk P (2008) Stereo and photoclinometric comparisons and topographic roughness of Europa. Lunar Planet Sci

Nishimura Y, Donovan EF, Angelopoulos V, Nishitani N (2020) Dynamics of auroral precipitation boundaries associated with STEVE and SAID. J Geophys Res Space Phys 125:e2020JA028067. https://doi.org/10.1029/2020JA028067

Odelstad E, Stenberg-Wieser G, Wieser M, Eriksson AI, Nilsson H, Johansson FL (2017) Measurements of the electrostatic potential of Rosetta at comet 67P. Mon Not R Astron Soc 469(Suppl_2):S568–S581. https://doi.org/10.1093/mnras/stx2232

Ono T, Kumamoto A, Kasahara Y, Yamaguchi Y, Yamaji A, Kobayashi T, Oshigami S, Nakagawa H, Goto Y, Hashimoto K, Omura Y, Imachi T, Matsumoto H, Oya H (2010) The lunar radar sounder (LRS) onboard the KAGUYA (SELENE) spacecraft. Space Sci Rev 154:145–192. https://doi.org/10.1007/s11214-010-9673-8

Ossowski M, Borys M, Palma P, Wisniewski L, Tokarz M, Kuciński T, Ryszawa E, Bochra K, Duda M, Grygorczuk J (2021) Development of deployable RWI and LP-PWI mechanisms for JUICE mission – quality and product assuarance aspects. In: European conference on spacecraft structures, materials and environmental. Testing (ECSSMET 2021)

Panchenko M, Rucker HO, Kaiser ML, St. Cyr OC, Bougeret J-L, Goetz K, Bale SD (2010) New periodicity in Jovian decametric radio emission. Geophys Res Lett 37:L05106. https://doi.org/10.1029/2010GL042488

Panchenko M, Rucker HO, Farrell WM (2013) Periodic bursts of Jovian non-Io decametric radio emission. Planet Space Sci 77:3–11. https://doi.org/10.1016/j.pss.2012.08.015

Panchenko M, Rošker S, Rucker HO, Brazhenko A, Zarka P, Litvinenko G, Shaposhnikov VE, Konovalenko AA, Melnik V, Franzuzenko AV, Schiemel J (2018) Zebra pattern in decametric radio emission of Jupiter. Astron Astrophys 610:A69

Paschmann G, Haaland S, Treumann R (eds) (2003) Auroral plasma physics. Space sciences series of ISSI, vol 15. Springer, Dordrecht. https://doi.org/10.1007/978-94-007-1086-3

Persoon AM, Gurnett DA, Peterson WK, Waite JH, Burch JL, Green JL (1988) Electron density depletions in the nightside auroral zone. J Geophys Res 93(A3):1871–1895. https://doi.org/10.1029/JA093iA03p01871

Petkaki P, Dougherty MK (2001) Waves close to the crossover frequency in the Jovian middle magnetosphere. Geophys Res Lett 28(2):211–214. https://doi.org/10.1029/2000GL012029

Polyakov SV (1976) On properties of ionospheric Alfvén resonator. In: Symposium KAPG on solar-terrestrial physics. Theses of reports. Part III. Nauka, Moscow, pp 72–73

Pontius DH, Hill TW (2006) Enceladus: a significant plasma source for Saturn's magnetosphere. J Geophys Res 111:A09214. https://doi.org/10.1029/2006JA011674

Poppe AR, Fatemi S, Khurana KK (2018) Thermal and energetic ion dynamics in Ganymede's magnetosphere. J Geophys Res Space Phys 123:4614–4637. https://doi.org/10.1029/2018JA025312

Porco CC, Helfenstein P, Thomas PC, Ingersoll AP, Wisdom J, West R, Neukum G, Denk T, Wagner R, Roatsch T, Kieffer S, Turtle E, McEwen A, Johnson TV, Rathbun J, Veverka J, Wilson D, Perry J, Spitale J, Brahic A, Burns JA, DelGenio AD, Dones L, Murray CD, Squyres S (2006) Cassini observes the active south pole of Enceladus. Science 311:1393–1401. https://doi.org/10.1126/science.1123013

Postberg F, Kempf S, Schmidt J, et al (2009) Sodium salts in E-ring ice grains from an ocean below the surface of Enceladus. Nature 459:1098–1101. https://doi.org/10.1038/nature08046

Postberg F, Schmidt J, Hillier J, et al (2011) A salt-water reservoir as the source of a compositionally stratified plume on Enceladus. Nature 474:620–622. https://doi.org/10.1038/nature10175

Postberg F, Khawaja N, Abel B, Choblet G, Glein CR, Gudipati MS, Henderson BL, Hsu HW, Kempf S, Klenner F, Moragas-Klostermeyer G, Magee B, Nölle L, Perry M, Reviol R, Schmidt J, Srama R, Stolz F, Tobie G, Trieloff M, Waite JH (2018) Macromolecular organic compounds from the depths of Enceladus. Nature 558(7711):564–568. https://doi.org/10.1038/s41586-018-0246-4

Postberg F, Sekine Y, Klenner F, et al (2023) Detection of phosphates originating from Enceladus's ocean. Nature 618:489–493. https://doi.org/10.1038/s41586-023-05987-9

Pryor W, Rymer A, Mitchell D, et al (2011) The auroral footprint of Enceladus on Saturn. Nature 472:331–333. https://doi.org/10.1038/nature09928

Rabia J, Hue V, Szalay JR, André N, Nénon Q, Blanc M, et al (2023) Evidence for non-monotonic and broadband electron distributions in the Europa footprint tail revealed by Juno in situ measurements. Geophys Res Lett 50:e2023GL103131. https://doi.org/10.1029/2023GL103131

Callingham JR, Vedantham HK, Shimwell TW, et al (2021) The population of M dwarfs observed at low radio frequencies. Nat Astron 5:1233–1239

Reiner MJ, Fainberg J, Stone RG, Kaiser ML, Desch MD, Manning R, Zarka P, Pedersen BM (1993) Source characteristics of Jovian narrow-band kilometric radio emissions. J Geophys Res, Planets 98:13163–13176

Reiner M, et al (1995) Elliptically polarized bursty radio emissions from Jupiter. Geophys Res Lett 22:345–348

Rice RF, Yeh P-S, Miller WH (1993) Algorithms for high-speed universal noiseless coding. In: Proceedings of AIAA computing in aerospace, IX, October 19-21, 1993, San Diego, CA. AIAA, Reston. https://doi.org/10.2514/6.1993-4541

Roberts TM, Romero-Wolf A, Bruzzone L, Carrer L, Peters S, Schroeder DM (2021) Conditioning Jovian Burst Signals for Passive Sounding Applications. IEEE Trans Geosci Remote Sens

Romero-Wolf A, Vance S, Maiwald F, Heggy E, Ries P, Liewer K (2015) A passive probe for subsurface oceans and liquid water in Jupiter's icy moons. Icarus 248:463–477

Roth L (2021) A stable H_2O atmosphere on Europa's trailing hemisphere from HST images. Geophys Res Lett 48:e2021GL094289. https://doi.org/10.1029/2021GL094289

Roth L, et al (2014a) Transient water vapor at Europa's south pole. Science 343:171–174. https://doi.org/10.1126/science.124705

Roth L, Retherford KD, Saur J, Strobel DF, Feldman PD, McGrath MA, Nimmo F (2014b) Orbital apocenter is not a sufficient condition for HST/STIS detection of Europa's water vapor aurora. Proc Natl Acad Sci 111(48):E5123–E5132. https://doi.org/10.1073/pnas.1416671111

Roth L, Smith HT, Yoshioka K, Becker TM, Blöcker A, Cunningham NJ, Ivchenko N, Retherford KD, Saur J, Velez M, Tsuchiya F (2023) Constraints on Europa's water group torus from HST/COS observations. Planet Sci J 4:87. https://doi.org/10.3847/PSJ/accddd

Sandahl I, Eliasson L, Lundin R (1980) Rocket observations of precipitating electrons over a pulsating aurora. Geophys Res Lett 7:309–312. https://doi.org/10.1029/GL007i005p00309

Sarrailh P, Matéo-Vélez J-C, Hess SLG, Roussel J-F, Thiébault B, Forest J, Payan D (2015) SPIS 5: new modeling capabilities and methods for scientific missions. IEEE Trans Plasma Sci 43(9):2789–2798. https://doi.org/10.1109/TPS.2015.2445384

Sato T (1978) A theory of quiet auroral arcs. J Geophys Res 83(A3):1042–1048. https://doi.org/10.1029/JA083iA03p01042

Saur J, Strobel DF, Neubauer FM (1998) Interaction of the Jovian magnetosphere with Europa: constraints on the neutral atmosphere. J Geophys Res 103(E9):19947–19962. https://doi.org/10.1029/97JE03556

Saur J, Neubauer FM, Schilling N (2007) Hemisphere coupling in Enceladus' asymmetric plasma interaction. J Geophys Res 112:A11209. https://doi.org/10.1029/2007JA012479
Saur J, Neubauer FM, Glassmeier K-H (2010) Induced magnetic fields in Solar System bodies. Space Sci Rev 152:391–421. https://doi.org/10.1007/s11214-009-9581-y
Saur J, Feldman PD, Roth L, Nimmo F, Strobel DF, Retherford KD, Mc Grath MA, Schilling N, Gérard J-C, Grodent D (2011) Hubble Space Telescope/advanced camera for surveys observations of Europa's atmospheric ultraviolet emission at eastern elongation. Astrophys J 738:2. https://doi.org/10.1088/0004-637X/738/2/153
Saur J, et al (2015) The search for a subsurface ocean in Ganymede with Hubble Space Telescope observations of its auroral ovals. J Geophys Res Space Phys 120:1715–1737. https://doi.org/10.1002/2014JA020778
Saur J, Janser S, Schreiner A, Clark G, Mauk BH, Kollman P, et al (2018) Wave-particle interaction of Alfvén waves in Jupiter's magnetosphere: auroral and magnetospheric particle acceleration. J Geophys Res Space Phys 123:9560–9573. https://doi.org/10.1029/2018JA025948
Schroeder DM, Romero-Wolf A, Carrer L, Grima C, Campbell BA, Kofman W, Blankenship DD (2016) Assessing the potential for passive radio sounding of Europa and Ganymede with RIME and REASON. Planet Space Sci 134:52–60
Schukla P, Stenflo L (2000) Generalized dispersive Alfvén waves. J Plasma Phys 64(2):125–130. https://doi.org/10.1017/S0022377800008412
Seyler CE, Clark AE, Bonnell J, Wahlund J-E (1998) Electrostatic broadband ELF wave emission by Alfvén wave breaking. J Geophys Res 103(A4):7027–7041. https://doi.org/10.1029/97JA02297
Shafiq M, Wahlund J-E, Morooka MW, Kurth WS, Farrell WM (2011) Characteristics of the dust–plasma interaction near Enceladus' South Pole. Planet Space Sci 59(1):17–25. https://doi.org/10.1016/j.pss.2010.10.006
Shoji M, Miyoshi Y, Kistler LM, et al (2021) Discovery of proton hill in the phase space during interactions between ions and electromagnetic ion cyclotron waves. Sci Rep 11:13480. https://doi.org/10.1038/s41598-021-92541-0
Shprits YY, Menietti JD, Drozdov AY, et al (2018) Strong whistler mode waves observed in the vicinity of Jupiter's moons. Nat Commun 9:3131. https://doi.org/10.1038/s41467-018-05431-x
Simon S, Saur J, van Treeck SC, Kriegel H, Dougherty MK (2014) Discontinuities in the magnetic field near Enceladus. Geophys Res Lett 41:3359–3366. https://doi.org/10.1002/2014GL060081
Simpson F, Bahr K (2005) Practical magnetotellurics. Cambridge University Press, Cambridge
Smith T, Mitchell DG, Johnson RE, Mauk BH, Smith JE (2019) Europa neutral torus confirmation and characterization based on observations and modeling. Astrophys J 871(1):69. https://doi.org/10.3847/1538-4357/aaed38
Soja RH, Altobelli N, Krüger H, Sterken VJ (2013) Dust environment predictions for the ESA L-class mission JUICE. Planet Space Sci 75:117–128. https://doi.org/10.1016/j.pss.2012.11.010
Soucek J, Píša D, Kolmasova I, Uhlir L, Lan R, Santolík O, Krupar V, Kruparova O, Baše J, Maksimovic M, Bale SD, Chust T, Khotyaintsev YuV, Krasnoselskikh V, Kretzschmar M, Lorfèvre E, Plettemeier D, Steller M, Štverák Š, Vaivads A, Vecchio A, Bérard D, Bonnin X (2021) Solar Orbiter radio and plasma waves – time domain sampler: in-flight performance and first results. Astron Astrophys 656:A26. https://doi.org/10.1051/0004-6361/202140948
Spahn F, et al (2006) Cassini dust measurements at Enceladus and implications for the origin of the E Ring. Science 311:1416–1418. https://doi.org/10.1126/science.1121375
Sparks WB, Hand KP, McGrath MA, Bergeron E, Cracraft M, Deustua SE (2016) Probing evidence of plumes on Europa with HST/STIS. Astrophys J 829:2. https://doi.org/10.3847/0004-637X/829/2/121
Spitale JN, Porco CC (2007) Association of the jets of Enceladus with the warmest regions on its south-polar fractures. Nature 449(7163):695–697. https://doi.org/10.1038/nature06217
Stasiewicz K, Bellan P, Chaston C, Kletzing C, Lysak R, Maggs J, Pokhotelov O, Seyler C, Shukla P, Stenflo L, Streltsov A, Wahlund J-E (2000b) Small scale Alfvénic structure in the Aurora. Space Sci Rev 92:423–533. https://doi.org/10.1023/A:1005207202143
Stasiewicz K, Khotyaintsev Y, Berthomier M, Wahlund J-E (2000a) Identification of widespread turbulence of dispersive Alfvén waves. Geophys Res Lett. https://doi.org/10.1029/1999GL010696
Steinbrugge G, Schroeder DM, Haynes MS, Hussmann H, Grima C, Blankenship DD (2018) Assessing the potential for measuring Europa's tidal Love number h2 using radar sounder and topographic imager data. Earth Planet Sci Lett 482:334–341. https://doi.org/10.1016/j.epsl.2017.11.028
Steinvall K, Khotyaintsev YuV, Cozzani G, Vaivads A, Yordanova E, Eriksson AI, Edberg NJT, Maksimovic M, Bale SD, Chust T (2021) Solar wind current sheets and deHoffmann-Teller analysis – first results from Solar Orbiter's DC electric field measurements. Astron Astrophys 656:A9. https://doi.org/10.1051/0004-6361/202140855
Stone RG, et al (1992) Ulysses radio and plasma wave observations in the Jupiter environment. Science 257:1524–1531. https://doi.org/10.1126/science.257.5076.1524

Storey L, Aubry L, Meyer P (1969) In: Measurement techniques in space plasmas - fields. Geophysical monograph series, vol 103, p 155. https://doi.org/10.1029/GM103p0155
Streltsov AV, Karlsson T (2008) Small-scale, localized electromagnetic waves observed by cluster: result of magnetosphere-ionosphere interactions. Geophys Res Lett 35:L22107. https://doi.org/10.1029/2008GL035956
Sulaiman AH, Kurth WS, Hospodarsky GB, Averkamp TF, Ye S-Y, Menietti JD, et al (2018) Enceladus auroral hiss emissions during Cassini's grand finale. Geophys Res Lett 45:7347–7353. https://doi.org/10.1029/2018GL078130
Sulaiman AH, Mauk BH, Szalay JR, Allegrini F, Clark G, Gladstone GR, et al (2022) Jupiter's low-altitude auroral zones: fields, particles, plasma waves, and density depletions. J Geophys Res Space Phys 127:e2022JA030334. https://doi.org/10.1029/2022JA030334
Szalay JR, Allegrini F, Bagenal F, Bolton SJ, Bonfond B, Clark G, et al (2020b) Alfvénic acceleration sustains Ganymede's footprint tail aurora. Geophys Res Lett 47:e2019GL086527. https://doi.org/10.1029/2019GL086527
Szalay JR, Bagenal F, Allegrini F, Bonfond B, Clark G, Connerney JEP, et al (2020a) Proton acceleration by Io's Alfvénic interaction. J Geophys Res Space Phys 125(1):e2019JA027314. https://doi.org/10.1029/2019JA027314
Szalay JR, Smith HT, Zirnstein EJ, McComas DJ, Begley LJ, Bagenal F, et al (2022) Water-group pickup ions from Europa-genic neutrals orbiting Jupiter. Geophys Res Lett 49:e2022GL098111. https://doi.org/10.1029/2022GL098111
Tao C, Sahraoui F, Fontaine D, de Patoul J, Chust T, Kasahara S, Retinò A (2015) Properties of Jupiter's magnetospheric turbulence observed by the Galileo spacecraft. J Geophys Res Space Phys 120:2477–2493. https://doi.org/10.1002/2014JA020749
Temerin M, Roth I (1986) Ion heating by waves with frequencies below the ion gyrofrequency. Geophys Res Lett 13(11):1109–1112. https://doi.org/10.1029/GL013i011p01109
Thiessenhusen K-U, Krüger H, Spahn F, Grün E (2000) Dust grains around Jupiter—the observations of the Galileo dust detector. Icarus 144(1):89–98. https://doi.org/10.1006/icar.1999.6277
Tokar RL, Johnson RE, Hill TW, Pontius DH, Kurth WS, Crary FJ, Young DT, Thomsen MF, Reisenfeld DB, Coates AJ, Lewis GR, Sittler EC, Gurnett DA (2006) The interaction of the atmosphere of Enceladus with Saturn's plasma. Science 311(5766):1409–1412. https://doi.org/10.1126/science.1121061
Tokar RL, et al (2008) Cassini detection of water-group pick-up ions in the Enceladus torus. Geophys Res Lett 35:L14202. https://doi.org/10.1029/2008GL034749
Tokar RL, Johnson RE, Thomsen MF, Wilson RJ, Young DT, Crary FJ, Coates AJ, Jones GH, Paty CS (2009) Cassini detection of Enceladus' cold water-group plume ionosphere. Geophys Res Lett 36:L13203. https://doi.org/10.1029/2009GL038923
Toledo-Redondo S, André M, Aunai N, Chappell CR, Dargent J, Fuselier SA, et al (2021) Impacts of ionospheric ions on magnetic reconnection and Earth's magnetosphere dynamics. Rev Geophys 59:e2020RG000707. https://doi.org/10.1029/2020RG000707
Tosi F, Roatsch T, Galli A, et al (2024) Characterization of the surfaces and near-surface atmospheres of Ganymede, Europa and Callisto by JUICE. Space Sci Rev 220:59. https://doi.org/10.1007/s11214-024-01089-8
Tóth G, Jia X, Markidis S, Peng IB, Chen Y, Daldorff LKS, Tenishev VM, Borovikov D, Haiducek JD, Gombosi TI, et al (2016) Extended magnetohydrodynamics with embedded particle-in-cell simulation of Ganymede's magnetosphere. J Geophys Res Space Phys 121:1273–1293. https://doi.org/10.1002/2015JA021997
Tyler RH, Boyer TP, Minami T, et al (2017) Electrical conductivity of the global ocean. Earth Planets Space 69:156. https://doi.org/10.1186/s40623-017-0739-7
Valek PW, Waite JH, Allegrini F, Ebert RW, Bagenal F, Bolton SJ, et al (2022) In situ ion composition observations of Ganymede's outflowing ionosphere. Geophys Res Lett 49:e2022GL100281. https://doi.org/10.1029/2022GL100281
Van Hoolst T, Tobie G, Vallat C, et al (2024) Geophysical characterization of the interiors of Ganymede, Callisto and Europa by ESA's JUpiter ICy moons Explorer. Space Sci Rev 220:54. https://doi.org/10.1007/s11214-024-01085-y
Veszelei M, Veszelei E (1993) Optical properties and equilibrium temperatures of titanium-nitride-and graphite-coated Langmuir probes for space application. Thin Solid Films 236(1–2):46–50. https://doi.org/10.1016/0040-6090(93)90640-B
Viberg H, Khotyaintsev YuV, Vaivads A, André M, Pickett JS (2013) Mapping HF waves in the reconnection diffusion region. Geophys Res Lett 40:1032–1037. https://doi.org/10.1002/grl.50227
Vines SK, Fuselier SA, Trattner KJ, Burch JL, Allen RC, Petrinec SM, Russell CT (2017) Magnetospheric ion evolution across the low-latitude boundary layer separatrix. J Geophys Res Space Phys 122:10,247–10,262. https://doi.org/10.1002/2017JA024061

Volwerk M, Louarn P, Chust T, Roux A, de Feraudy H, Holback B (1996) Solitary kinetic Alfvén waves: a study of the Poynting flux. J Geophys Res 101(A6):13335–13343. https://doi.org/10.1029/96JA00166
Volwerk M, Khurana K, Kivelson M (2007) Europa's Alfvén wing: shrinkage and displacement influenced by an induced magnetic field. Ann Geophys 25:905–914. https://doi.org/10.5194/angeo-25-905-2007
Vorburger A, Wurz P (2021) Modeling of possible plume mechanisms on Europa. J Geophys Res Space Phys 126:e2021JA029690. https://doi.org/10.1029/2021JA029690
Vorburger A, Fatemi S, Galli A, Liuzzo L, Poppe AR, Wurz P (2022) 3D Monte-Carlo simulation of Ganymede's water exosphere. Icarus 375:114810. https://doi.org/10.1016/j.icarus.2021.114810
Vozoff K (1991) The magnetotelluric method. In: Nabighian MN (ed) Electromagnetic methods in applied geophysics, vol 2, pp 1943–1961. https://doi.org/10.1190/1.9781560802686.ch8
Wahlström MK, Johansson E, Veszelei E, Bennich P, Olsson M, Hogmark S (1992) Improved Langmuir probe surface coatings for the Cassini satellite. Thin Solid Films 220(1–2):315–320. https://doi.org/10.1016/0040-6090(92)90591-X
Wahlund J-E, Louarn P, Chust T, de Feraudy H, Roux A, Holback B, Dovner PO, Holmgren G (1994) On ion acoustic turbulence and the nonlinear evolution of kinetic Alfvén waves in aurora. Geophys Res Lett 21:1831–1834. https://doi.org/10.1029/94GL01289
Wahlund J-E, Eriksson AI, Holback B, Boehm MH, Bonnell J, Kintner PM, Seyler CE, Clemmons JH, Eliasson L, Knudsen DJ, Norqvist P, Zanetti LJ (1998) Broadband ELF plasma emission during auroral energization 1. Slow ion acoustic waves. J Geophys Res 103(A3):4343. https://doi.org/10.1029/97JA02008
Wahlund J-E, Wedin LJ, Carrozi T, Eriksson AI, Holback B, Andersson L, Laakso H Analysis of Freja Charging Events: Statistical Occurrence of Charging Events. SPEE-WP 130-TN, under ESA contract 11974/96/NL/JG(SC), IRF Sci. Report 253, 1999b, ISSN 0284–1703
Wahlund J-E, Wedin LJ, Eriksson AI, Holback B, Andersson L Analysis of Freja Charging Events: Charging Events Identification and Case Study, SPEE-WP 110-TN, under ESA contract 11974/96/NL/JG(SC), IRF Sci. Report 251, 1999a, ISSN 0284-1703
Wahlund J-E, Yilmaz A, Backrud M, Sundkvist D, Vaivads A, Winningham D, André M, Balogh A, Bonnell J, Buchert S, Carozzi T, Cornilleau N, Dunlop M, Eriksson AI, Fazakerley A, Gustafsson G, Parrot M, Robert P, Tjulin A (2003) Observations of auroral broadband emissions by CLUSTER. Geophys Res Lett 30:1563. https://doi.org/10.1029/2002GL016335
Wahlund J-E, Blomberg LG, Morooka M, André M, Eriksson AI, Cumnock JA, Marklund GT, Lindqvist P-A (2005b) Cold plasma diagnostics in the Jovian system: brief scientific case and instrumentation overview. In: Proc. Int. conf. On low-cost planetary missions, Kyoto, 11-13 October 2005, pp 341–346
Wahlund J-E, Blomberg LG, Morooka M, Cumnock JA, André M, Eriksson AI, Kurth WS, Gurnett DA, Bale SD (2005a) Science opportunities with a double Langmuir probe and electric field experiment for JIMO. Adv Space Res 36(11):2110–2119
Wahlund J-E, Boström R, Gustafsson G, Gurnett DA, Kurth WS, Averkamp T, Hospodarsky GB, Persoon AM, Canu P, Pedersen A, Desch MD, Eriksson AI, Gill R, Morooka MW, André M (2005) The inner magnetosphere of Saturn: Cassini RPWS cold plasma results from the first encounter. Geophys Res Lett 32:L20S09. https://doi.org/10.1029/2005GL022699
Wahlund J-E, et al (2009) Detection of dusty plasma near the E-ring of Saturn. Planet Space Sci 57:1795–1806. https://doi.org/10.1016/j.pss.2009.03.011
Wahlund J-E, Morooka MW, Hadid LZ, Persoon AM, Farrell WM, Gurnett DA, Hospodarsky G, Kurth WS, Ye S-Y, Andrews DJ, Edberg NJT, Eriksson AI, Vigren E (2017) In situ measurements of Saturn's ionosphere show it is dynamic and interacts with the rings. Science. https://doi.org/10.1126/science.aao4134
Waite JH Jr, Combi MR, Ip WH, Cravens TE, McNutt RL Jr, Kasprzak W, Yelle R, Luhmann J, Niemann H, Gell D, Magee B, Fletcher G, Lunine J, Tseng WL (2006) Cassini ion and Neutral Mass Spectrometer: Enceladus plume composition and structure. Science 311(5766):1419–1422. https://doi.org/10.1126/science.1121290
Wattieaux G, Gilet N, Henri P, Vallières X, Bucciantini L (2019) RPC-MIP observations at comet 67P/ChuryumovGerasimenko explained by a model including a sheath and two populations of electrons. Astron Astrophys 630:A41. https://doi.org/10.1051/0004-6361/201834872
Wattieaux G, Henri P, Gilet N, Vallières X, Deca J (2020) Plasma characterization at comet 67P between 2 and 4 AU from the Sun with the RPC-MIP instrument. Astron Astrophys 638:A124. https://doi.org/10.1051/0004-6361/202037571
Whipple EC Jr (1965) The equilibrium electric potential of a body in the upper atmosphere and in the interplanetary space. PhD thesis, NASA, Goddard Space Flight Center, Greenbelt, Maryland. https://ntrs.nasa.gov/api/citations/19660007937/downloads/
Winterhalder TO, Huybrighs HLF (2022) Assessing JUICE's ability of in situ plume detection in Europa's atmosphere. Planet Space Sci 210:105375. https://doi.org/10.1016/j.pss.2021.105375
Witasse O et al (2025) Space Sci Rev. in preparation

Yahnin AG, Popova TA, Demekhov AG, Lubchich AA, Matsuoka A, Asamura K, et al (2021) Evening side EMIC waves and related proton precipitation induced by a substorm. J Geophys Res Space Phys 126:e2020JA029091. https://doi.org/10.1029/2020JA029091
Ye S-Y, Gurnett DA, Kurth WS, Averkamp TF, Kempf S, Hsu HW, et al (2014) Properties of dust particles near Saturn inferred from voltage pulses induced by dust impacts on Cassini spacecraft. J Geophys Res Space Phys 119:6294–6312. https://doi.org/10.1002/2014ja020024
Ye S-Y, Kurth WS, Hospodarsky GB, Averkamp TF, Gurnett DA (2016) Dust detection in space using the monopole and dipole electric field antennas. J Geophys Res Space Phys 121:11,964–11,972. https://doi.org/10.1002/2016JA023266
Ye S-Y, Vaverka J, Nouzák L, Sternovsky Z, Zaslavsky A, Pavlu J, et al (2019) Understanding Cassini RPWS antenna signals triggered by dust impacts. Geophys Res Lett 46:10,941–10,950. https://doi.org/10.1029/2019GL084150
Ye S-Y, Averkamp TF, Kurth WS, Brennan M, Bolton S, Connerney JEP, Joergensen JL (2020) Juno waves detection of dust impacts near Jupiter. J Geophys Res, Planets 125:e2019JE006367. https://doi.org/10.1029/2019JE006367
Yoneda M, Nozawa H, Misawa H, Kagitan M, Okano S (2010) Jupiter's magnetospheric change by Io's volcanoes. Geophys Res Lett 37:L11202. https://doi.org/10.1029/2010GL043656
Yoneda M, Tsuchiya F, Misawa H, Bonfond B, Tao C, Kagitani M, Okano S (2013) Io's volcanism controls Jupiter's radio emissions. Geophys Res Lett 40:671–675. https://doi.org/10.1002/grl.50095
Zarka P (1985) On detection of radio bursts associated with Jovian and Saturnian lightning. Astron Astrophys 146:L15–L18
Zarka P (1998) Auroral radio emissions at the outer planets: observations and theories. J Geophys Res 103:20159–20194. https://doi.org/10.1029/98JE01323
Zarka P (2000) Radio emissions from the planets and their moons. In: Stone RG, Weiler KW, Goldstein ML, Bougeret J-L (eds) Radio astronomy at long wavelengths. Geophysical Monograph Series, vol 119. AGU, Washington DC, pp 167–178. https://doi.org/10.1029/GM119p0167
Zarka P, Farges T, Ryabov BP, Abada-Simon M, Denis L (1996) A scenario for Jovian S-bursts. Geophys Res Lett 23:125–128
Zarka P, Cecconi B, Kurth WS (2004) Jupiter's low frequency radio spectrum from Cassini/RPWS absolute flux density measurements. J Geophys Res 109:A09S15. https://doi.org/10.1029/2003JA010260
Zarka P, Marques MS, Louis C, Ryabov VB, Lamy L, Echer E, Cecconi B (2018) Jupiter radio emission induced by Ganymede and consequences for the radio detection of exoplanets. Astron Astrophys 618:A84. https://doi.org/10.1051/0004-6361/201833586
Zarka P, Magalhaes FP, Marques MS, Louis CK, Echer E, Lamy L, Cecconi B, Prangé R (2021) Jupiter's auroral radio emissions observed by Cassini: rotational versus solar wind control, and components identification. J Geophys Res 126(10):e29780. https://doi.org/10.1029/2021JA029780
Zaslavsky A, et al (2012) Interplanetary dust detection by radio antennas: mass calibration and fluxes measured by STEREO/WAVES. J Geophys Res 117:A05102. https://doi.org/10.1029/2011JA017480
Zaslavsky A, Mann I, Soucek J, Czechowski A, Píša D, Vaverka J, Meyer-Vernet N, Maksimovic M, Lorfèvre E, Issautier K, Babic KR, Bale SD, Morooka M, Vecchio A, Chust T, Khotyaintsev Y, Krasnoselskikh V, Kretzschmar M, Plettemeier D, Steller M, Štverák Š, Trávníc̆ek P, Vaivads A (2021) First dust measurements with the Solar Orbiter radio and plasma wave instrument. Astron Astrophys 656:A30. https://doi.org/10.1051/0004-6361/202140969
Zheng R, Wang Y, Li X, Wang C, Jia X (2023) Statistical study of the Jovian decametric radio emissions based on multiple-view observations from remote radio instruments. Astron Astrophys 673:A106. https://doi.org/10.1051/0004-6361/202244121
Zhou H, Tóth G, Jia X, Chen Y, Markidis S (2019) Embedded kinetic simulation of Ganymede's magnetosphere: improvements and inferences. J Geophys Res Space Phys 124:5441–5460. https://doi.org/10.1029/2019JA026643
Zhou H, Tóth G, Jia X, Chen Y (2020) Reconnection-driven dynamics at Ganymede's upstream magnetosphere: 3-D global Hall MHD and MHD-EPIC simulations. J Geophys Res Space Phys 125:e2020JA028162. https://doi.org/10.1029/2020JA028162

Authors and Affiliations

J.-E. Wahlund[1] · J.E.S. Bergman[1] · L. Åhlén[1] · W. Puccio[1] · B. Cecconi[2] · Y. Kasaba[3] · I. Müller-Wodarg[4] · H. Rothkaehl[5] · M. Morawski[5] · O. Santolik[6,7] · J. Soucek[6] ·

J. Grygorczuk[8] · Ł. Wisniewski[8] · P. Henri[9,10] · J.L. Rauch[9] · O. Le Duff[9] · A. Retinò[11] · M. Mansour[11] · S. Stverak[6,12] · J. Laifr[12] · D. Andrews[1] · M. André[1] · I. Benko[1] · M. Berglund[1] · V. Cripps[1] · C. Cully[1,13] · J. Davidsson[1] · A. Dimmock[1] · N.J.T. Edberg[1] · A.I. Eriksson[1] · J. Fredriksson[1] · R. Gill[1] · S. Gomis[1] · B. Holback[1] · S.-E. Jansson[1] · F. Johansson[1] · E.P.G. Johansson[1] · Y. Khotyaintsev[1] · B. Mårtensson[1] · M.W. Morooka[1] · T. Nilsson[1] · D. Ohlsson[1] · D. Pelikan[1] · L. Richard[1] · F. Shiwa[1] · E. Vigren[1] · H.C. Wong[1] · X. Bonnin[2] · J.N. Girard[2] · L. Grosset[2] · F. Henry[2] · L. Lamy[2,14] · J.-P. Lebreton[2] · P. Zarka[2] · Y. Katoh[3] · H. Kita[15] · A. Kumamoto[3] · H. Misawa[3] · F. Tsuchiya[3] · M. Galand[4] · T. Barcinski[5] · J. Baran[5] · T. Kowalski[5] · P. Szewczyk[5] · B. Grison[6] · J. Jansky[6] · I. Kolmasova[6,7] · R. Lan[6] · D. Pisa[6] · U. Taubenschuss[6] · L. Uhlir[6] · K. Bochra[8] · M. Borys[8] · M. Duda[8] · T. Kucinski[8] · M. Ossowski[8] · P. Palma[8] · M. Tokarz[8] · F. Colin[9] · P. Dazzi[9,2] · E. De Léon[9] · T. Hachemi[9] · A.-L. Millet[9] · O. Randrianboarisson[9] · O. Sene[9] · T. Chust[11] · O. Le Contel[11] · P. Canu[11] · L. Hadid[11] · F. Sahraoui[11] · Y. Zouganelis[11] · D. Alison[11] · N. Ba[11] · A. Jeandet[11] · M. Lebassard[11] · J.-D. Techer[11] · F. Mehrez[11] · L. Varizat[11,16] · A.V. Sumant[17] · G. Sou[16] · P. Hellinger[12] · P. Travnicek[12,18] · L. Bylander[19] · G. Giono[19] · N. Ivchenko[19] · A. Kullen[19] · L. Roth[19] · A. Vaivads[19,20] · K. Tanimoto[21] · H. Mizuno[21] · A. Sawamura[21] · T. Suzuki[21] · M. Namiki[21] · S. Fujishima[21] · K. Asai[21] · T. Shimoyama[21] · M. Fujii[21,22] · Y. Sato[22] · J. Birch[23] · B. Bakhit[23,24,25] · G. Greczynski[23] · P. Gare[26] · S. Landström[26] · R. LeLetty[26] · E. Ryszawa[26] · I. Torralba[26] · J.L. Trescastro[26] · S. Osipenco[27] · U. Wiklund[28] · A. Roos[28] · J.C. Söderström[28] · O. Björneholm[28] · G. Fischer[29] · T. Nyberg[30] · K.K. Kovi[31,17] · M. Balikhin[32] · K.H. Yearby[32] · M. Holmberg[33] · C.M. Jackman[33] · C.K. Louis[2,33] · A. Rhouni[16] · V. Leray[34] · N. Geyskens[35] · C. Berthod[35] · B. Lemaire[35] · A. Clémencon[35] · G. Wattieaux[36] · N. André[37,38] · P. Garnier[37] · V. Génot[37] · P. Louarn[37] · A. Marchaudon[37] · R. Modolo[39] · C.-A. Baskevitch[39] · L.G. Hess[40] · L. Leclercq[40] · J. Saur[41] · T. Kimura[42] · H. Kojima[43] · S. Yagitani[44] · Y. Miyoshi[45]

✉ J.-E. Wahlund
jwe@irfu.se

1 Swedish Institute of Space Physics (IRF), Box 537, 751 21 Uppsala, Sweden

2 Laboratoire d'Etudes Spatiales et Instrumentation en Astrophysique (LESIA), Observatoire de Paris-PSL, CNRS, Sorbonne Université, Université Paris Cité, 5 Place Jules Janssen, 92190 Meudon, France

3 Graduate School of Science, Tohoku University, Aramaki aza Aoba 6-3, Aoba-ku, Sendai 980-8578, Japan

4 Department of Physics, Imperial College London, London SW7 2AZ, UK

5 Space Research Centre of the Polish Academy of Sciences, 00-716 Bartycka 18A, Warsaw, Poland

6 Institute of Atmospheric Physics of the Czech Academy of Sciences, Boční II/1401, 14100 Prague 4-Sporilov, Czech Republic

7 Faculty of Mathematics and Physics, Charles University, Prague, Czech Republic

8 Astronika sp. z o.o., ul. Bartycka 18, 00-716 Warsaw, Poland

9 CNRS-LPC2E, Université d'Orléans, 3A, Avenue de la Recherche Scientifique, 45071 Orléans cedex, France

10 Laboratoire Lagrange, Observatoire de la Côte d'Azur, Université Côte d'Azur, CNRS, Nice, France

11 Laboratoire de Physique des Plasmas (LPP), UMR7648, CNRS, Sorbonne Université, UniversitéParis-Saclay, Observatoire de Paris, Ecole Polytechnique Institut Polytechnique de Paris, Palaiseau 91128, France

[12] Astronomical Institute of the Czech Academy of Sciences, Fričova 298, 25165 Ondřejov, Czechia

[13] University of Calgary, 2500 University Drive NW Calgary, Alberta T2N 1N4, Canada

[14] Aix Marseille Université, CNRS, CNES, LAM, Marseille, France

[15] Tohoku Institute of Technology, Yagiyama Kasumi-cho 35-1, Taihaku-ku, Sendai 982-8577, Japan

[16] GEEPS (laboratoire de Genie Electrique et Electronique de Paris), CNRS, Sorbonne Universite, 75252 Paris, France

[17] Center for Nanoscale Materials (CNM), Argonne National Laboratory (ANL), 9700 S. Cass Avenue, Lemont, IL, 60439, USA

[18] Space Sciences Laboratory, UC Berkeley, 94720 Berkeley, USA

[19] Royal Institute of Technology (KTH), Space & Plasma Physics, SE-100 44 Stockholm, Sweden

[20] Ventspils University of Applied Sciences, Inzenieru 101, Ventspils, LV-3601, Latvia

[21] Meisei Electric Co., Ltd., Naganuma-machi 2223, Isesaki, Gunma 372-8585, Japan

[22] FAM Science Co., Ltd, Kinunodai 2-8-8, Tsukubamirai, Ibaraki 300-2436, Japan

[23] Thin Film Physics Division, Department of Physics, Chemistry, and Biology (IFM), Linköping University, Linköping SE-58183, Sweden

[24] Present address: Department of Materials Science & Metallurgy, University of Cambridge, 27 Charles Babbage Rd, Cambridge CB3 0FS, UK

[25] Present address: Department of Engineering, University of Cambridge, 9 JJ Thompson Avenue, Cambridge CB3 0FA, UK

[26] ESA/ESTEC, Keplerlaan 1, 2201 AZ Noordwijk, The Netherlands

[27] Airbus, Friedrichshafen, Claude-Dornier-Straße, 88090 Immenstaad am Bodensee, Germany

[28] Uppsala University, Ångström Laboratory, Lägerhyddsvägen 1, 752 37 Uppsala, Sweden

[29] Space Research Institute, Austrian Academy of Sciences, Schmiedlstraße 6, 8042 Graz, Austria

[30] Division of Solid State Electronics, Department of Electrical Engineering, Uppsala University, Box 65, SE-751 03 Uppsala, Sweden

[31] AKHAN Semiconductor Inc, 940 Lakeside Drive, Gurnee, IL 60031, USA

[32] Department of Automatic Control and Systems Engineering, The University of Sheffield, Sheffield, S1 3JD, UK

[33] School of Cosmic Physics, DIAS Dunsink Observatory, Dublin Institute for Advanced Studies, Dublin 15, Ireland

[34] Hensoldt space consulting, Golf park – Bâtiment F, 1 rond-point du Général Eisenhower, 31100 Toulouse, France

[35] Division Technique de l'Institut National des Sciences de l'Univers, CNRS, Avenue de la Terrasse, 91198 Gif-sur-Yvette, France

[36] LAPLACE, CNRS / INP / Université Paul Sabatier, 118 route de Narbonne, 31062 Toulouse cedex 9, France

[37] Institut de Recherche en Astrophysique et Planétologie (IRAP), CNRS-Université Toulouse III-CNES, 9, Avenue du Colonel Roche, BP 44346, 31028 Toulouse Cedex 4, France

[38] Institut Supérieur de l'Aéronautique et de l'Espace (ISAE-SUPAERO), Université de Toulouse, Toulouse, France

[39] Laboratoire ATMOsphères, Observations Spatiales/IPSL, UVSQ Université Paris-Saclay, Sorbonne Université, CNRS, CNES, Guyancourt, France

[40] Office National d'Etudes et de Recherches Aérospatiales, BP74025 - 2 avenue Edouard Belin, FR-31055 Toulouse cedex 4, France

[41] University of Cologne, Cologne, Germany

[42] Faculty of Science Division I, Tokyo University of Science, Kagurazaka 1-3, Shinjuku-ku, Tokyo 162-8601, Japan

[43] Research Institute for Sustainable Humanosphere, Kyoto University, Gokasho, Uji, Kyoto, 611-0011, Japan

[44] School of Electrical and Computer Engineering, Kanazawa University, Kakuma-machi, Kanazawa 920-1192, Japan

[45] Institute for Space-Earth Environmental Research, Nagoya University, Furo-cho, Chikusa-ku, Nagoya 464-8601, Japan